# Università degli Studi di Ferrara

DOTTORATO DI RICERCA IN

SCIENZE DELLA TERRA

CICLO XXII

COORDINATORE Prof. Luigi Beccaluva

# Petrological features of Subei Basin (Eastern China) lithospheric mantle and their relationships with $H_2O$ contents in NAMs

Settore Scientifico Disciplinare **GEO07/GEO08**


**Dottorando**
Dott. Hao Yantao

**Tutore**
Prof. Coltorti Massimo

**Co-Tutori**
Prof. Xia Qunke

Dott. Dallai Luigi


Anni 2007/2009

## Acknowledgements

I would like to thank my PhD advisors, Professor Massimo Coltorti, Professor Qunke Xia and Doctor Luigi Dallai, Not only they fully support me during the period of three years on my PhD academic work but also my living and study in Ferrara, Pisa and Hefei. Qunke is also my master advisor; he is my guide into the road of scientific research. The first time I met Luigi was when he is visited China and gave an excellent lecture at my previous university. He is the first foreigner with whom I have a long conversation with, not in mother language. When I saw the picture of Massimo for the website of the Department, the first thing into my sight was a big pipe and a kindly feeling. And it's correct when I saw him in person. I thank all of them; from them I have learned not only how to make science but also how to be enthusiastic, energetic in the life.

I am also very grateful to Costanza Bonadiman, who spend lot of time on my thesis, discussion and correct the draft, as she said she spent so much time on my thesis even more than when she do her own. She is a funny advisor, her office always fill with laughing. I thank Barbara Faccini and Riccardo Boraso; they help me to solve lot of tiny but important troubles, from preparing rock powder, to filling the documents of different bureaucracy. I also thank Renzo Tassinari, the chief of our department laboratory, for helping me on the whole rock analysis and to discuss analyses of FeO contents.

I thank Xiaozhi Yang and Pei Li , they help me a lot with measurement in FTIR experiments; we had good period in discussing data. I thank Professor Rucheng Wang and researcher Wenlan Zhang in Nanjing University for EMPA. I thank professor Theodoros Ntaflos in Vienna University for the hospitality

during EGU2007 and permission to use his lab for analyses. I also thank Professor Zhi Xie and Zhenhui Hou in University of Science and Technology of China for their assistance in the experiments

I would like to thank my former roommate Tao Su and other Chinese students in Ferrara, we have spent a happy time, important when you study abroad in Italy.

I also thank my friends (too many to list here but you know who you are!) for providing the support and the friendship I needed.

I also thank my wife Yanqun Zhen, she give me the courage to face lonely and filled my heart with full love. I especially thank my mom and dad. My hard-working parents give me life and bring me up. They have sacrificed their lives for me; I thank all the things they do. I love them so much, and I would not have made it this far without them.

## Abstract

The Subei basin is located east of the Tanlu fault, a major discontinuity which separates the Archean North China Craton from the Proterozoic Yangtze Craton. South-West of the Tanlu fault the two cratonic blocks collided during Triassic time, originating the well-known UHP (Ultra-High Pressure) belt of Dabie Shan.

Central-eastern China experienced widespread basaltic volcanism during Cenozoic, probably related to extensive lithospheric thinning and mantle upwelling along weak zones of the Archean-Proterozoic lithospheric roots. This volcanism was particular intense in the Subei basin, where it included minor tholeiitic eruptions in the early Paleogene, and more extensive, xenolith-bearing alkali basalt activity in the Neogene. Three localities, Panshishan (PSS), Lianshan (LS) and Fangshan (FS), about 30 km apart, were sampled in the Subei basin and more than 60 peridotite xenoliths were collected. Volcanism in the last locality has been dated at about 9 Ma.

Most of the xenoliths are rounded and small to moderate in size (typically 5–10 cm in diameter), Most of the xenoliths are lherzolites ranging from highly fertile (16-23 vol% of clinopyroxene) to cpx-poor lherzolites (with cpx modal content of 6-9%), although few harzburgites, olivine-websterite and dunites are also found. No hydrous nor metasomatic secondary phases were observed. Textures vary from coarse-grained protogranular (~70% of total samples) through porphyroclastic (~20%) to equigranular (~10%) type. Rarely metasomatic textures, mainly spongy clinopyroxene, were observed.

Using two pyroxenes geothermometer (Brey and Kohler, 1990), Panshishan and Lianshan show quite low equilibrium temperature (T=816-1010℃), whereas Fangshan samples show temperature between 1011°C and 1208°C,

Pressure estimates on the basis of Ca-exchange between olivine and clinopyrossene, range between 12 to 25, 11 to 23 and 11 to 33 Kbar for Panshishan, Lianshan and Fangshan lherzolites, respectively. $f_{O2}$ conditions calculated for Panshishan and Fangshan samples range over four orders of magnitude from log $f_{O2}$~ -4.12 to 0.25 FMQ and from 2.26 to -2.13 FMQ, respectively; Lianshan samples present a more restricted range, with log $f_{O2}$ from 0.55 to -2.4 FMQ.

FTIR analyses of nominally anhydrous minerals (NAMs) have been carried out for these xenoliths. Water content in olivines is very low; frequently it reaches the instrument detective limitation (less then 2ppm). Water content varies from 37 to 183 ppm for cpx and 13 to 74 ppm for opx. Fangshan xenoliths have the highest water content for both opx and cpx compare to other two localities, while Panshisan have the lowest water content in opx, leading to anomalously high $DH_2O$cpx/opx ratios.

Panshishan xenoliths show $\delta^{18}O$ values ranging from 5.28 to 5.78 ‰ in olivine, 5.87 to 6.53 ‰ in opx, 5.18 to 6.15 ‰ in cpx, and 4.11 to 5.37 ‰ in sp. The results are similar to those reported by Yu et al. (2005), although these authors refer a broader range of $\delta^{18}O$ values for ol, opx and cpx. In Lianshan xenoliths, $\delta^{18}O$ values range from 5.42 to 5.96 ‰ in olivine, 6.01 to 6.67 ‰ in opx, 5.77 to 6.34 ‰ in cpx, and 4.52 to 5.58 ‰ in sp. In xenoliths from Fangshan $\delta^{18}O$ values range from 5.12 to 6.32 ‰ in ol, 5.79 to 6.57 ‰ in opx, 5.33 to 6.31 ‰ in cpx, and 4.37 to 5.39 ‰ in sp.

On the basis of the cpx REE patterns the 47 measured xenoliths are subdivided into five different groups. Group I, with LREE-depleted pattern; Group II, with upward convex pattern, Group III, with flat REE pattern; Group IV, with LREE-enriched pattern; and Group V, with spoon-shape pattern.

Group I samples reflect low degree of mantle melting process (F less than 10%) and group IV samples has been strong modified during mantle metasomatic event/s.

Comparing water content of peridotite minerals (NAMs) with geochemical parameters, such as major and trace element compositions of minerals, melting index (i.e. Mg# value) for whole rock and minerals, oxygen isotopes, as well as physico-chemical parameters such as Temperature, Pressure and Oxygen Fugacity no correlation are envisaged. In conclusion, at least for the Subei Basin lithospheric mantle represented by xenoliths of Panshinshan, Linshan and Funshan water contents in NAMs are not related to the main depletion/enrichment processes occurring in the upper mantle, but it appears as an intrinsic (pristine?) feature of different mantle domains.

# Riassunto

Il bacino di Subei si trova a est della faglia Tanlu, una discontinuità importante che separa il cratone Archeano della Cina del Nord dal Cratone Proterozoico di Yangtze. A sud-ovest della faglia Tanlu i due blocchi cratonici collidono durante il periodo Triassico, dando luogo alla nota UHP (Ultra-High Pressure) cintura del Dabie Shan.

Durante il Cenozoico la Cina centro-orientale vede un estensiva attività vulcanica, probabilmente correlata al vasto assottigliamento litosferico e alla risalita del mantello lungo le zone di debolezza delle radici litosferiche archeane-proterozoiche. Questa attività vulcanica è stata particolarmente intensa nel bacino Subei, includendo anche limitate eruzioni toleiitiche nel Paleogene inferiore, ed una cospiqua attività alcali-basaltica, ricca di xenoliti di mantello nel Neogene. Tre località noodulifere nel Subei Basin (Panshishan (PSS), Lianshan (LS) e Fangshan (FS)) tutte nl raggio di 30 km, sono state campionate per questa tesi e più di 60 noduli peridotitici sono stati raccolti. Il vulcanismo dell'ultima località è stato datato a circa 9 Ma.

La maggior parte degli xenoliti sono arrotondati e generalmente di dimensioni da centimetriche a decimetriche (5-10 centimetri di diametro). Questi sono principalmente lherzoliti (cpx modale 16-23%) e lherzoliti povere in cpx (cpx modale 6-9%); sono comunque presenti alcune harzburgiti, olivine-websterite e duniti. Non sono state rilevate fasi idrate, né fasi metasomatiche secondarie. La tessitura più frequente (~70% dei campioni totali) è la protogranulare a grana grossa, ma gradazioni verso la porfiroclastica (~ 20%) e equigranulare (~ 10%) sono comunque osservate. Tessiture

metasomatiche sono rare e principalemente caratterizzate da clinopirosseno spongy.

Utilizzando il geotermometro a due pirosseni (Brey e Kohler, 1990), gli xenoliti di Panshishan e Lianshan registrano temperature di equilibrio relativamente basse (T = 816-1.010℃) per un mantello sublitosferico, mentre i noduli di Fangshan mediamente presentano temperature di equilibrio più alte tra i 1011 °C e 1208°C. Stime di pressioni, calcolate usando la distribuzione del Ca tra olivina e clinopyrosseno, variano rispettivamente da 12 a 25, da 11 a 23 e da 11 a 33 Kb in Panshishan, Lianshan and Fangshan.

I campioni di Panshishan e Fangshan mostrano un ampio range di valori di $f_{O2}$ (fino a 4 ordini di grandezza), rispettivamente da ~ -4.12 a 0.25 FMQ e da 2.26 a -2.13 FMQ, mentre i campioni di Lianshan resigrano un range di $f_{O2}$ molto più ristretto: da 0.55 a -2.4 FMQ.

Misure FTIR in minerali nominalmente anidri (NAMs) sull'intera campionatura di noduli, registrano contenuti d'acqua in olivina molto bassa vicina al limite di rivelabilità dello strumento (meno di 2 ppm). Il contenuto di acqua nei clinopirosseni varia da 37 a183 ppm mentre negli ortopirosseni varia da 13 a 74 ppm. Gli xenoliti di Fangshan hanno un contenuto di acqua superiore sia per cpx che per opx se confrontati con le altre due località, mentre gli xenoliti di Panshishan mostrano un contenuto in opx più basso a cui consegue un $D_{H2O}$cpx/opx anormalmente alto.

I noduli di Panshishan presentano $\delta^{18}O$ che varia da 5.28 a 5.78 ‰ nell'olivina, da 5.87 a 6.53 ‰ nell'opx, da 5.18 a 6.15 ‰ per cpx e da 4.11 a 5.37 ‰ per sp. I risultati ottenuti sono simili a quelli riportati da Yu et al. (2005), anche se i noduli oggetto di questa tesi, mostrano un range più ristretto di $\delta^{18}O$ per olivine e pirosseni. I noduli di Lianshan, presentano valori di δ18O

da 5.42 a 5.96 ‰ nelle olivine, 6.01-6.67 ‰ in opx, 5.77-6.34 ‰ per cpx, e 4.52-5.58 ‰ per sp. I noduli di Fangshan registrano δ18O che variano da 5.12-6.32 ‰ nell'olivina, da 5.79 a 6.57 ‰ nell'opx , da 5.33 a 6.31 ‰ nel cpx, e da 4.37 a 5.39 ‰ nello sp.

In base ai pattern di REE dei cpx, i 47 xenoliti analizzati sono stati suddivisi in cinque diversi gruppi. Gruppo I: con un pattern delle LREE impoverito; Gruppo II: con un pattern convesso verso l'alto; Gruppo III: con un pattern piatto di REE; Gruppo IV: con un pattern di LREE arricchito ed infine il Gruppo V: con un pattern di REE a cucchiao. I campioni del gruppo I possono essere modellizati per gradi di fusione parziale inferiore al 10% di un mantello primitivo, mentre i campioni del Gruppo IV riflettono composizioni di un mantello estensivamente modificato da processi metasomatici.

Confrontando il contenuto di acqua dei minerali peridotitici (NAMs) con i parametri geochimici, che includono gli elementi maggiori ed in traccia dei minerali, l'indici di fusione (i.e. Mg#) sia di roccia totale che di singoli minerali, e isotopi dell'ossigeno, unitamente a parametri fisico-chimici come Temperatura, Pressione e Fugacità di Ossigeno non è stata verificata nessuna correlazione. In conclusione si può affermare che, almeno per il mantello litosherico del Subei Basin rappresentato dagli xenoliti di Panshinshn, Linshan e Funshan, il contenuto d'acqua nel NAMS non sembra dipendere dai principali processi di impoverimento e di arricchimento che sono avvenuti nel mantello superiore. Questa tesi suggerisce invece che tale parametro possa essere una caratteristica intrinseca (primitiva?) dei diversi domini di mantello presenti nell'area.

# Table of Contents

Acknowledgements

Abstract

Riassunto

Table of Contents ..... ..... ..... ..... ..... .....i

List of Illustrations ..... ..... ..... ii

List of Tables (in Appendixes) ……..... .....v

Chapter 1 - Introduction and aim of the thesis …….1

Chapter 2 - Geological setting and previous works ……..7

Chapter 3 - Analytical method …..……27

Chapter 4 – Petrography ……... ……38

Chapter 5 – Geochemistry ……..50

Chapter 6 – P-T estimate and oxygen fugacity estimates ……..…….111

Chapter 7 - Water content in opx and cpx……118

Chapter 8 - Discussion and conclusions……132

References ...……..168

Appendixes……186

## List of Illustrations

<Chapter 2>

Fig. 2.1 - Simplified tectonic units of Eastern China and sample locality
Fig. 2.2 - Schematic illustration of the thermo-tectonic evolution of the lithospheric mantle beneath North China Craton (NCC) and related magmatism
Fig. 2.3 - Thermal (a) and tomography (b) structure of the upper mantle in eastern China
Fig. 2.4 - A 200Ma event history for the NCC
Fig. 2.5 - Crustal-detachment model for South China Craton (SCC) beneath Subei basin
Fig. 2.6 - Detailed map of sample locality and alkali basalt outcrops in the northern part of Jiangsu Province
Fig. 2.7 - $^{143}Nd/^{144}Nd$ vs $^{87}Sr/^{86}Sr$ for NE and SE China basalts
Fig. 2.8 - Outline of the mantle source components for the late Cenozoic basaltic rocks from East Asia

<Chapter 3>

Fig. 3.1 - Picture of the Nicolet 5700 FTIR spectrometer coupled with a microscope
Fig. 3.2 - Absorption diagram of the Nicolet 5700 FTIR spectrometer
Fig. 3.3 - Interference treatments from the instrumental absorption diagram

<Chapter 4>

Fig. 4.1 - General pictures of sample localities
Fig. 4.2 - Pictures of xenoliths from Panshishan and Lianshan
Fig. 4.3 - Textures in xenoliths from Subei basin
Fig. 4.4 – Petrographic classification for peridotite xenoliths from Subei basin

<Chapter 5>

Fig. 5.1 - Whole-rock major element: $SiO_2$ and $Al_2O_3$ contents vs Mg#
Fig. 5.2 - Whole-rock trace element: Cr, Ni, Sr, Y and V (ppm) vs Mg#
Fig. 5.3 - Whole-rock major element compositions (wt %) for the eastern China xenolith suite plotted in the Niu (1997) diagram

Fig. 5.4 – Whole-rock CaO vs $Al_2O_3$ (wt %) diagram
Fig. 5.5 - CaO and NiO in olivines vs Mg# diagrams
Fig. 5.6 – Diagram of Mg# vs Cr# in spinels
Fig. 5.7 - $SiO_2$, $TiO_2$, $Al_2O_3$, $Cr_2O_3$, and $Na_2O$ in orthopyroxene vs Mg# diagrams
Fig. 5.8 - $TiO_2$, $Al_2O_3$, $Cr_2O_3$, CaO and $Na_2O$ in clinopyroxene vs Mg# diagrams
Fig. 5.9 - REE and trace element patterns of clinopyroxenes from peridotite xenoliths from Panshishan
Fig. 5.10 - REE and trace element patterns of clinopyroxenes from peridotite xenoliths from Lianshan
Fig. 5.11 - REE and trace element patterns of clinopyroxenes from peridotite xenoliths from Fangshan
Fig. 5.12 - Simplified REE pattern with $(La/Sm)_N$ vs $(Sm/Yb)_N$ of Subei basin clinopyroxenes
Fig. 5.13 - Oxygen isotope composition for olivine, orthopyroxene and clinopyroxene in xenoliths from Subei basin

<Chapter 6>

Fig. 6.1 - Pressure vs equilibrium temperature of Subei basin xenoliths
Fig. 6.2 - Oxygen fugacity vs equilibrium temperature of Subei basin xenoliths
Fig. 6.3 - Oxygen fugacity vs Pressure of Subei basin xenoliths

<Chapter 7>

Fig. 7.1 - Representative IR spectra for cpx and opx in Panshishan peridotite xenolith
Fig. 7.2 - Representative IR spectra for cpx and opx in Lianshan peridotite xenolith
Fig. 7.3 - Representative IR spectra for cpx and opx in Fangshan peridotite xenolith
Fig. 7.4 - Representative IR spectra for ol in Panshishan peridotite xenolith
Fig. 7.5 - Profile analyses of H absorption in Lianshan opx
Fig. 7.6 - Water contents of cpx and opx in Panshishan, Lianshan and Fangshan xenoliths and NCC peridotite

<Chapter 8>

Fig. 8.1 – Melting modelling using both batch and fractional melting in spinel facies
Fig. 8.2 - Melting modelling using both batch and fractional melting in garnet facies
Fig. 8.3 - Modelling of REE patterns in spinel facies for clinopyroxenes from Subei basin xenoliths
Fig. 8.4 - Modelling of REE patterns in garnet facies for clinopyroxenes from Subei basin xenoliths
Fig. 8.5 - Melting modelling in garnet facies and re-equilibration in spinel facies
Fig. 8.6 - Modelling of REE patterns in garnet facies for Group II cpx
Fig. 8.7 - Batch and fractional melting models for Zr and Sr contents in clinopyroxenes from Subei basin
Fig. 8.8 – Inferred metasomatic melts in equilibrium with Group IV cpx
Fig. 8.9 - (La/Yb)N vs Ti/Eu ratios of clinopyroxene from Subei basin xenoliths
Fig. 8.10 - Correlation between $H_2O$ (ppm) and $Al_2O_3$ (%) in peridotite opx
Fig. 8.11 - MgO (wt %) versus (a) orthopyroxene and (b) clinopyroxene $H_2O$ content
Fig. 8.12 – $(Ce)_N$, $(Yb)_N$ and $(La/Yb)_N$ versus clinopyroxene $H_2O$ content
Fig. 8.13 - Opx $H_2O$ content (a) and cpx $H_2O$ content (b) versus $\Delta$FMQ
Fig. 8.14 - Cpx $H_2O$ content versus $\delta^{18}O$
Fig. 8.15 - Comparison of $H_2O$ content of cpx, opx and whole rock of the NCC peridotite xenoliths with that of craton and off-craton peridotites

## List of Tables (in Appendixes)

Table 2.1 - Mineral mode of Panshishan, Lianshan and Fangshan peridotite xenoliths

Table 5.1 - Whole rock composition of peridotite xenoliths from Subei basin

Table 5.2 - Olivine major element compositions in peridotite xenoliths from Subei basin

Table 5.3 - Orthopyroxene major element compositions in peridotite xenoliths from Subei basin

Table 5.4 - Clinopyroxene major element compositions in peridotite xenoliths from Subei basin

Table 5.5 - Spinel major element compositions in peridotite xenoliths from Subei basin

Table 5.6 - Clinopyroxene trace element analyses in peridotite xenoliths from Subei basin

Table 5.7 - Oxygen isotopic analyses of xenoliths form Subei basin

Table 6.1 - Temperature, Pressure and Oxygen fugacity estimates of peridotite xenoliths from Subei basin

Table 7.1 - Minerals and bulk rock water content of peridotite xenoliths from Subei basin

Table 8.1 - Xenolith phase modal proportions (vol %) used in the models

Table 8.2 - Crystal/Liquid partition coefficients for modeling calculations

Table 8.3 - Primitive mantle source and starting bulk composition (ppm) in spinel and garnet facies

# Chapter 1 - Introduction and aim of the thesis

## Mantle xenoliths

Until now it is difficult to access directly and get the information on the composition and evolution of the deeper part of the lithosphere, i.e. the lower crustal and upper mantle layers. Mantle-derived xenoliths provide a good chance to understand the nature of the mantle. Xenoliths can be transported by magma to the Earth's surface when volcano erupts. As the magma rise from its source (upper mantle) to the surface in a very short time (just few days or even few hours) the xenoliths represent almost a "quenched" product and most source information could be kept. Peridotite is the dominant rock of the upper part of the Earth's mantle. It is a dense, coarse-grained rock, consisting mostly of the minerals olivine (ol), orthopyroxene (opx), clinopyroxene (cpx), spinel (sp) and/or garnet (grt) and representing, in most cases, the residues of partial melting after the extraction of basaltic melts (e.g. Salters and Stracke, 2004; Workman and Hart, 2005). A system study of the peridotite xenoliths can make us better understanding the composition, structure, physical and chemical features of the upper mantle, to learn the past, now and even the future of our Earth.

## Water in nominally anhydrous minerals

Knowledge of the amount of water, or hydrogen species, inside the earth at present, and in the past, is a critical issue for understanding the petrological, geochemical, geophysical and dynamical processes of the Earth, as well as for constraining the segregation, accretion and evolution model of the planet and the whole cycle of hydrogen in its interior. This relies heavily on the

well-known fact that water, even in trace amounts, has a strong influence on many chemical and physical properties of its host silicate minerals/rocks, including mechanical and rheological strength (e.g. Griggs, 1967; Kronenberg et al., 1986; Hirth and Kohlstedt, 1996), rate of ionic diffusion (Goldsmith, 1987; Elphick et al., 1988), melting behavior (Kushiro, 1972; Arndt et al., 1998) and electrical conductivity (Karato, 1990); and, if extracted from minerals, it contributes to the formation of ore deposits and hydrous fluids, and even to the triggering of deep-seated earthquakes (Meade and Jeanloz, 1991). After the Griggs and Blacic (1965) and Martin and Donnay (1972) pioneering works and the early speculations of Fyfe (1970) – later reviewed by Ackermann et al. (1983) – who stated that OH-bearing anhydrous minerals might be a significant reservoir for water in the Earth's mantle, it has been gradually and widely accepted that nominally anhydrous minerals can commonly contain few to several thousand ppm of water ($H_2O$ by weight) in their lattice, predominated by OH and/or less molecular $H_2O$, and are the main hydrogen reservoir in the deep earth, especially in the upper mantle (Bell and Rossman, 1992a; Ingrin and Skogby, 2000; Bolfan-Casanova, 2005). Such water may play crucial but diversified roles on many properties and processes in the earth (e.g. Williams and Hemley, 2001; Keppler and Smyth, 2006). Recent works on quartz, garnet and igneous feldspars in the upper and middle crust demonstrate that they contain more than ~ 1200 ppm $H_2O$ as dispersed, structurally bound OH groups, molecular $H_2O$ and/or $NH^{4+}$ (Kronenberg, 1994; Johnson and Rossman, 2003, 2004). The upper mantle is dominated by ol, cpx and opx, so these nominally anhydrous minerals in principle can also incorporate some water/hydroxyl in them. A thorough investigation about water in peridotite xenoliths coupled with other geophysics/geochemistry information is therefore

necessary for a better understanding of the whole Earth system. Fourier transform infrared (FTIR) absorption spectroscopy is a highly sensitive, site-specific, high resolution (down to 20 μm), and non-destructive in situ method for the study of OH and molecular $H_2O$ in minerals. It can provide quantitative determination of the amount of structurally incorporated water and OH in the target minerals, although depending on the experimentally-calibrated absorption coefficients for given phases. (Rossman, 1996)

**Oxygen isotopes**

Oxygen is the most abundant element in silicate rock-forming minerals. Oxygen isotope composition of mantle may have been affected by processes such as removal or addition of melt and fluids, or the recycling of crustal component at subduction zones. Oxygen isotopes of mantle xenoliths have the potential to make important contributions to identify this heterogeneity. Importantly, the stable isotopes $^{18}O$ and $^{16}O$ are strongly fractionated in the low temperature geochemical environments prevailing at the Earth's surface. Therefore, tectonic processes that return to the mantle material that has at one time resided in surface or near-surface environments should provide an effective means of introducing oxygen of variable isotopic composition into the upper mantle.

**Aim of this work**

In the present PhD thesis a detailed work which includes petrography, major element and trace element composition of whole rock and minerals, oxygen isotope compositions for ol, opx, cpx and sp, coupled with water content measurements by FTIR on opx and cpx were carried out in Subei basin area,

thus representing the most complete studies of the area developed so far. The main aim of the work is to highlight the relationships between petrological features of the mantle peridotite and its water content.

**Structure of this study**

This thesis is subdivided into 8 chapters, starting with the general introduction presented here, followed by other Chapters.

Chapter 2 gives a brief introduction to the geological setting of the North China Craton and Dabie Shan-Sulu UHP (Ultra-High Pressure) belt with some available geological, tectonic, petrological, dynamic and chronological data. Then a summary of the previous works that have done in the Subei basin is reported.

Chapter 3 describes details of analytical methods which include whole-rock analysis by XRF, major and trace element contents in minerals obtained by EMPA and LA-ICP-MS, water content in NAMs acquired by FTIR and minerals oxygen isotopic composition using laser fluorination technology.

Chapter 4 gives a petrological picture of xenoliths from the three sampling localities, Panshishan, Lianshan and Fangshan in Subei basin. Textures of hand speciments and thin sections are described. Petrological classification for rock type is applied for xenoliths by mineral mode content estimates by more than 1600 points counting.

Chapter 5 shows the geochemistry of the sample, including major and trace element content for both whole rock and the four mineral phases (ol, opx, cpx and sp). Based on the pattern and distribution of rare earth elements, xenoliths have been divided into five groups: Group I, with LREE-depleted pattern; Group II, with upward convex pattern, Group III, with flat REE pattern; Group IV, with LREE-enriched pattern; and Group V, with spoon-shape pattern. At the end of the chapter, we report the oxygen isotopic composition of all the four minerals phases in the xenoliths.

After the discussion of single mineral major elements, in Chapter 6 equilibrium temperature, pressure and redox state of the Subei Basin mantle domain are determined.

Chapter 7 reports the results from the FTIR experiments for NAMs water contents. H species are confirmed in the spectra. Water contents for opx and cpx are calculated by integrating the absorption areas and whole rock water contents are evaluated.

Chapter 8 deals with the discussion. It is divided in: a) modelling depletion and enrichment processes that affect the sampled xenoliths; b) evaluating the possible relationships between petrological features of the Subei basin mantle and its water content; c) making comparison between NAMs water contents of minerals and whole rock with other localities.

The Appendix includes all the tables mentioned in the thesis and detailed information for EMPA results of mineral grains core and rim, and repeated

measurement for trace element by LA-ICP-MS. Some related publications are listed at the end of appendix.

# Chapter 2 - Geologic setting and previous works

## Geologic setting and sample localities

The North China Craton (NCC) is the Chinese part of the Sino-Korean Craton (SKC), named the North China Block in some literature. It is one of the most ancient cratons on the Earth, composed of early Archean and Proterozoic metamorphic rocks with the oldest recorded crustal ages >3.8 Ga (e.g. Liu et al., 1992), and is the largest craton in China, covering an area >1,700,000 $km^2$. It is separated from the Mongolian Block by the eastern Central Asian Orogenic Belt in the north, and from the Yangtze Craton, part of the South China Craton, by the Triassic Dabie Shan-Sulu UHP belt in the south and east (Fig. 2.1). In the west, it is separated from Tarim Craton by the Qilianshan Orogen. The NCC is crosscut by two large-scale geophysical and geological linear zones. In the west, it is cut by the NS trending Daxing'anling-Taihangshan Gravity Lineament (DTGL) (equiv. North–South Gravity Lineament (NSGL), which separates two topographically and tectonically different regions and probably related to the diachronous lithospheric thinning of the craton (Ma, 1989; Xu, 2007). In the east, it is traversed by the Tan-Lu Fault Zone (TLFZ), which is associated with significant Cenozoic and Mesozoic volcanism.

Based on the lithological assemblage, tectonic evolution and P-T-t paths of metamorphic rocks, the North China Craton can be divided into the Western and Eastern Blocks, separated by the central Orogenic Belt (equiv. Trans-North China Orogen Belt. Fig. 2.1: Zhao et al., 2000; 2001).

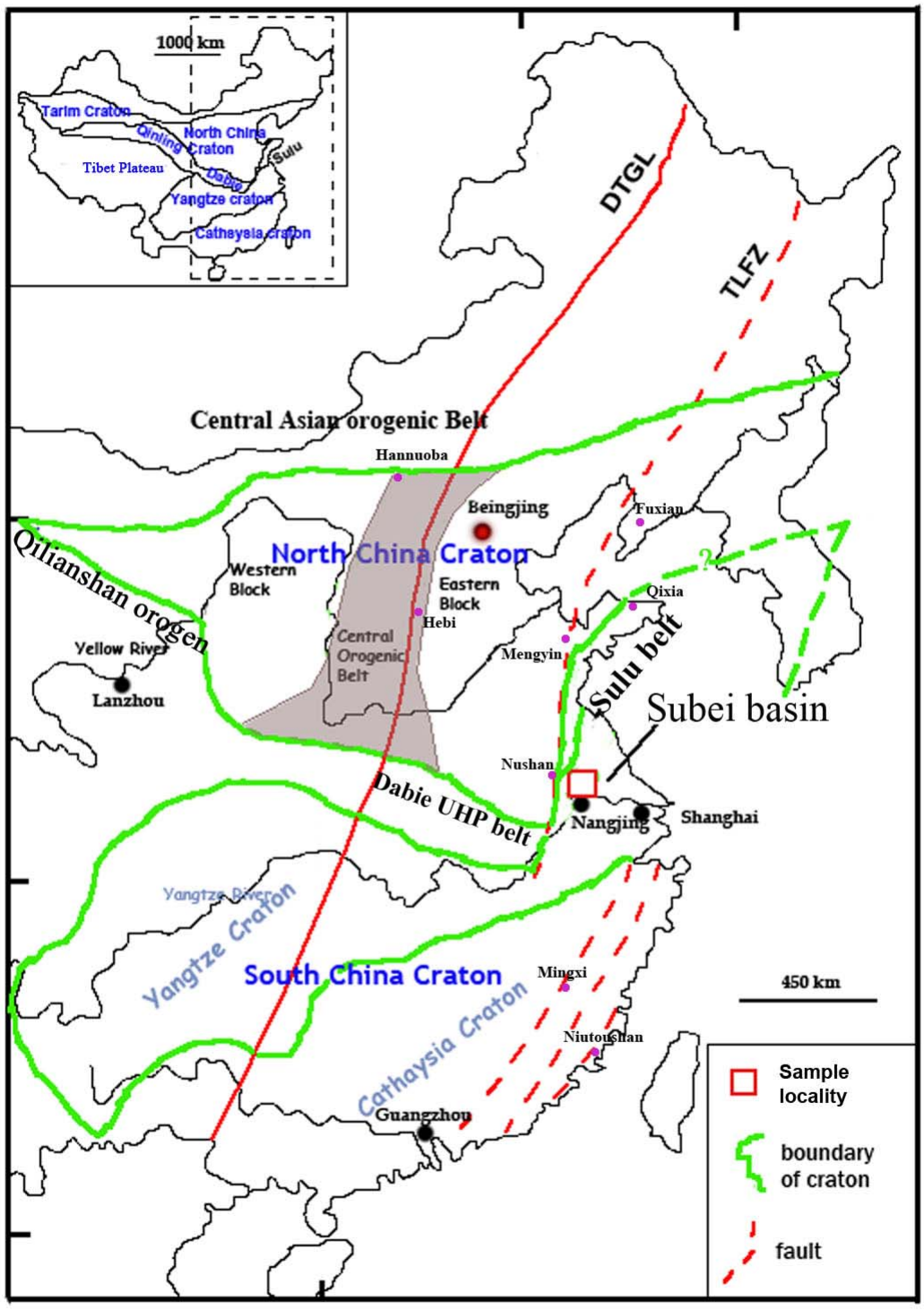


Fig. 2.1 - Simplified tectonic units of Eastern China and sample locality. (modified after Zhang et al., 2008)

The Western Block is composed of late Archean to early Proterozoic metasedimentary belts that unconformable overlie the Archean basement; the latter consists mainly of granulite facies gneiss and charnockite with small amounts of mafic granulites and amphibolites. The basement of the central Orogenic Belt consist of late Archean amphibolites and granulites, and 2.5 Ga granite-greenstone terrains, overlaid by 2.4-2.2 Ga bimodal volcanic rocks in the southern region and thick carbonate and terrigenous sedimentary rocks interlayered with thin basalt flows in the central region. The Eastern Block consists mainly of 3.5-2.5 Ga orthogneisses (dominated by tonalitic, trondhjemitic and granodioritic gneisses (TTGs)), 2.5 Ga granitoids and less amounts of ultramafic to mafic volcanics and sedimentary supracrustal rocks including banded iron formations. The collision between the Western and Eastern blocks may have led to the formation of the Central Orogenic Belt and represent the final amalgamation of the North China Craton. There are contrasting views regarding the timing of the collision between the Eastern and Western Blocks. Multi-grain zircon U-Pb age populations from TTG gneisses of the Central Orogenic Belt have upper intercept of 2.5-2.7 Ga and lower intercept of 1.8-2.0 Ga. These younger ages are consistent with Sm-Nd ages of garnets from the high-pressure granulites in this belt and $^{40}Ar/^{30}Ar$ ages of hornblendes in amphibolites and biotites in TTGs, along with SHRIMP zircon rim ages of the TTGs and supracrustal rocks (Zhao et al., 2000, 2001). The age of 1.8-2.0 Ga are interpreted as the age of metamorphic overgrowth. These, as well as near-isothermal decompressional clockwise P-T paths, led Zhao et al. (2000; 2001) to propose that collision occurred between the two Blocks at ~1.8 Ga. However, a 2.5 Ga ophiolite complex in the northern Central Orogenic

Belt was reported by Kusky et al., (2001). It implies a much older collisional event between these two blocks. Li et al. (2000; 2001) suggested a model that combines all these observations and assumes that collision occurred between the two blocks at ~2.5 Ga followed by rifting during the 2.3-2.4 Ga with subsequent collision at 1.8-2.0 Ga representing the final amalgamation/cratonization event.

The Dabie Shan-Sulu UHP belt lies between the North and South China Cratons, extending from east to west for ca. 2000 km in the central-eastern China (Fig. 2.1). It is separated into two terrenes by about 500 km of left-lateral strike-slip displacement along the TLFZ. The Sulu terrain in the east is segmented into a number of blocks by several NE-SW trending faults sub parallel to the TLFZ, and the Dabie Shan terrain in the west is the major segment bounded by the TLFZ to the east and separated into a series of continuous zones by several EW-trending faults of large scales. The formation of the Dabie Shan-Sulu UHP belt occurred mainly in the Triassic, caused by collision between the North China and Yangtze Cratons with peak metamorphism at ~ 245 Ma (Hacker et al., 1998). The basement of the Dabie Shan-Sulu UHP terranes is constituted by metamorphic rocks, such as schists, greenstones, gneisses, and rare quartzites, marbles, granulites, and eclogites, intruded by granitoids. The occurrence of eclogites first suggests that pressures of metamorphism were high. Discovery of coesite, diamond, and extreme $^{18}O$-depletion, as well as exsolution of clinopyroxene in orthopyroxene, rutile and apatite, in eclogites (e.g. Okay et al., 1989; Wang et al., 1989; Yui et al., 1995; Zheng et al., 1996; Ye et al., 2000) demonstrates that deep subduction of continental crust to the depths of about 200 km and the subsequent quick exhumation (see also a review by Zheng et al., 2003 and references therein) of

eclogites in Central Dabie Shan and the granulites in North Dabie Shan (after Zheng et al., 2003) occurred.

The NCC experienced widespread tectonothermal reactivation, beginning from the early Paleozoic but occurring mainly during the late Mesozoic and Cenozoic, as manifested by the emplacement of early Paleozoic kimberlites, voluminous late Mesozoic basaltic rocks and granites and Cenozoic alkali basalts (Fan et al., 2000; Zhang et al., 2002; Yang et al., 2003; Zhang et al., 2004; Wu et al., 2005). The NCC also experienced development of extensive sedimentary basins (most of the eastern portion of the craton is covered by Quaternary sediments) and presently has higher heat flow (60 $mW/m^2$: Hu et al., 2000) compared to other Archean and Proterozoic cratons (Nyblade et al., 1990; Jaupart and Mareschal, 2003). The changes in tectonic/magmatic activity are also reflected in a change in the type and composition of mantle xenoliths. Xenoliths carried in Ordovician kimberlites are deep-seated garnet-facies peridotites. These highly refractory xenoliths, together with the appearance of diamonds in the kimberlites, indicate a typical ancient cratonic lithospheric mantle which was thick (ca. 200 km) and cold (geotherm ca. 40$mW/m^2$) at least up to mid-Ordovician time (Wu et al., 2005; Zhang et al., 2008). By contrast, xenoliths hosted in late Cretaceous and Cenozoic basalts are dominated by fertile spinel peridotites, which record shallower (60-100 km) and hotter (mean geotherm ca. 80 $mW/m^2$) lithospheric mantle (Fan and Hooper, 1989; Xu et al., 1998; Zheng et al., 1998, 2001, 2006; Fan et al., 2000; Rudnick et al., 2004; Reisberg et al., 2005; Ying et al., 2006), in good agreement with an average present-day surface heat flow of 60 $mW/m^2$ and thin lithosphere of 60-80 km. These suggest that 80-140 km of cratonic lithosphere was removed or strongly modified during late Mesozoic-early

Cenozoic time (Menzies et al., 1993, 2007; Griffin et al., 1998; Xu, 2001, 2008b; Zheng et al., 2001, 2006; Gao et al., 2002, 2004, 2008; Zhang et al., 2002, 2005, 2008, 2009; Wu et al., 2003, 2005). Xu (2001) show a thermo-tectonic evolution of the lithospheric mantle beneath North China Craton and related magmatism (Fig. 2.2).

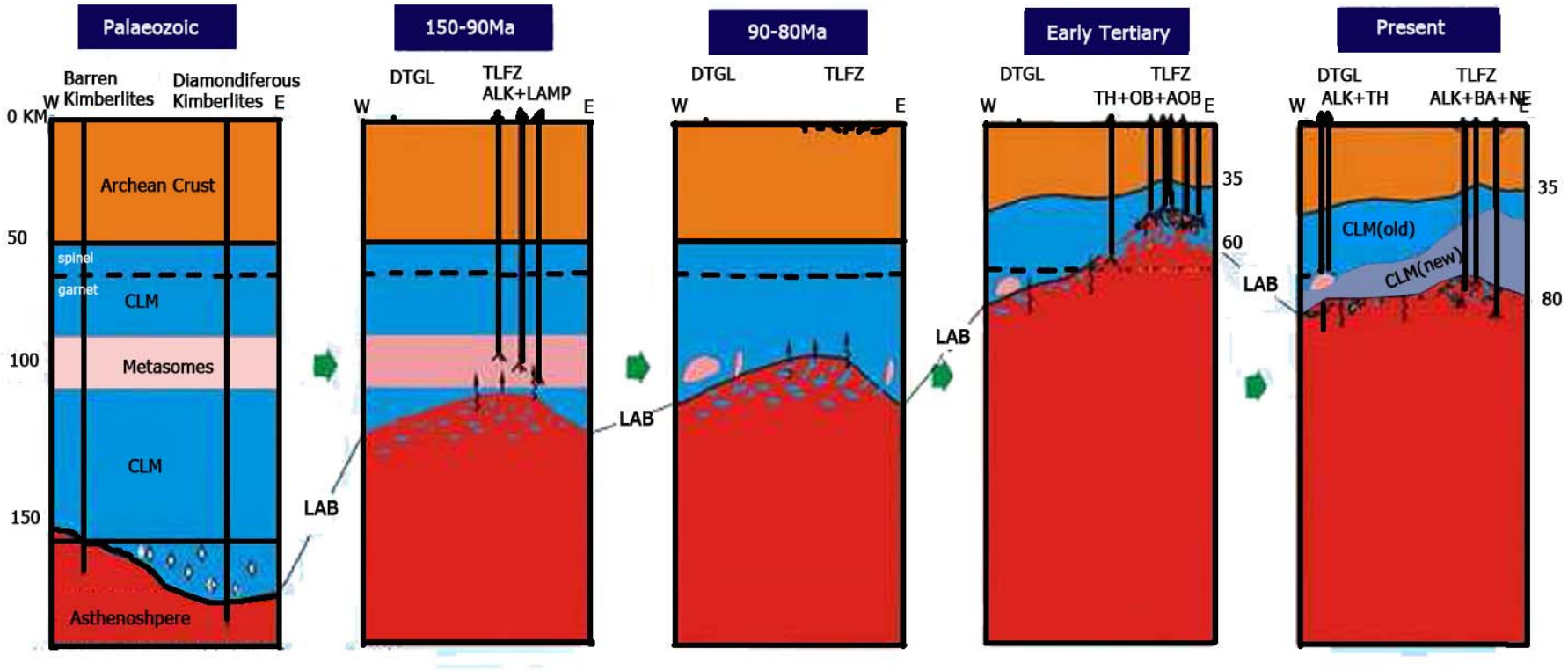


Fig. 2.2 - Schematic illustration of the thermo-tectonic evolution of the lithospheric mantle beneath North China Craton and related magmatism. CLM: Continental Lithospheric Mantle; LAB: Lithosphere Asthenosphere Boundary; ALK: alkali basalt; LAMP: lamprophyre basalt; TH: tholeiite basalt; OB+AOB: subalkali basalts; ALK+BA+NE: alkali and strongly alkali basalts).

(a) Paleozoic. A thick lithospheric keel existed under the NCC and extended into the diamond stability field. A metasome horizon was formed at 80 to 120 km through repeated infiltration of small melt batches derived from the convective asthenosphere (Menzies et al., 1993). The lithosphere was cold corresponding to ~40 mW/m$^2$.
(b) Jurassic to early Cretaceous. The low-temperature melting components in metasome zones were reactivated due to thermal perturbation associated with initial lithospheric erosion. These magmas show enriched mantle components.
(c) 90 to 80 Ma. Magmatism during this period was absent. The SCLM was essentially dry due to the exhaustion of fusible components during precedent magmatism. The solidus of dry peridotites was not intercepted by the thermal gradient.
(d) Early Tertiary. The lithosphere was significantly thinned (< 60 km) as a result of lithospheric extension and associated asthenospheric upwelling. The thermal gradient was as high as ~90 mW/m$^2$. The magmatism is mainly tholeiites (TH) and subalkali basalts (OB+AOB) with minor alkali basalt. The depleted mantle source involved in these rocks suggests that lithosphere erosion may have been accomplished by the end of the Cretaceous.
(e) Present. The lithosphere thickens (> 70 km) since the Miocene subsequent to the lowering of the LAB as a result of thermal decay (~ 65 mW/m$^2$). The declining in the partial melting degrees and the increase in the depth of partial melting result in the formation of alkali- and strongly alkaline basalts (ALK+BA+NE). New lithosphere was accreted below the old keel remnants. This lithostratigraphy is believed to vary from west to east with relics of the old keel being more important in the western part of the craton.

The lithospheric thinning in eastern China is a warmly and widely discussed topic in the last decade (Fan and Menzies, 1992; Menzies et al., 1993; Griffin et al., 1998; Menzies and Xu, 1998; Menzies et al., 2007). It is not clear, in fact, the scale, mechanism and timing, as well as tectonic controlling factors, of this geodynamical process. The scale for the lithospheric thinning involves both its spatial and vertical distribution, which indicates how wide and how thick the lithosphere has been removed, respectively. There is at present a general consensus that the NCC has experienced significant lithospheric thinning, especially in its eastern domain. Recent studies show that, not only the NCC, but also the north-east and south-east China are characterized by rather thin lithosphere relative to other ancient cratons on the Earth (Xu et al., 2000; Zou,

2001; Xu, 2002; Wu et al., 2003). Based on these works, it seems that the entire eastern China, to the east of the DTGL, has experienced lithospheric thinning. This can be further supported by the thermal structure (Fig. 2.3a; He et al., 2001) and seismic tomography (Fig. 2.3b; Priestley et al., 2006) of the upper mantle below eastern China. The issue for the vertical thinning involves the removal of the lithospheric mantle only or both the lower crust and the whole lithospheric mantle, which is still under debate (Menzies et al., 1993; Griffin et al., 1998; Menzies and Xu, 1998; Zheng, 1999; Xu, 2001; Wu et al., 2003; Gao et al., 2004; Xu et al., 2004; Menzies et al., 2007).

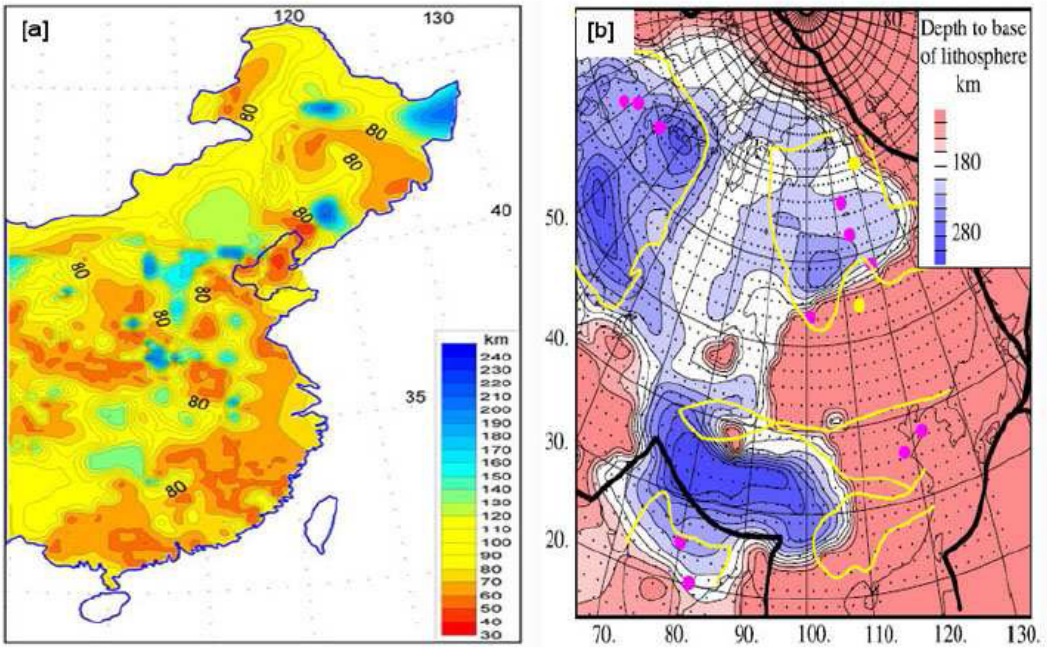


Fig. 2.3 - Thermal (a) and tomography (b) structure of the upper mantle in eastern China. (after He et al., 2001 and Priestley et al., 2006, respectively)

How the lithospheric keel below eastern China had been lost has been the subject of considerable debate during the past 20 years, among which previous

studies are largely concentrated on the eastern NCC. Various mechanisms have been proposed to explain this process below the NCC, the most prevailing are:

(1) Delamination in a short period (Yang et al., 2003; Gao et al., 2004). Yang et al. (2003) suggested that lithospheric delamination took place primarily in the early Cretaceous, based on the evidence for widespread crustal melting during 130-110 Ma which would require thinning of the lithosphere. By contrast, Gao et al. (2004) argued for Jurassic delamination of the lower crust, based on their discovery that Jurassic andesites, dacites and adakites from Xinglonggou (north NCC, Western Liaoning Province) have chemical signatures consistent with their derivation as partial melts of eclogites that interacted with mantle peridotite; in this case, they proposed that lithospheric thinning had reached such a stage by the late Jurassic that lower crustal rocks could be delaminated, converted to eclogites, incorporated into the convecting mantle and melted. The latter model, however, is difficult to reconcile with the fact that mafic and felsic Mesozoic magmatism peaked in the early Cretaceous (Yang et al., 2003; Xu et al., 2004; Wu et al., 2005) rather than the Jurassic; furthermore, rapid delamination is clearly at odds with the protracted Mesozoic magmatism (~100 Ma) in the NCC (e.g. Xu et al., 2004), and it is not easy to explain satisfactorily the linear thinning along the whole east China (Fig. 2.3a, Fig.2.3b).

(2) Thermal-mechanical erosion (e.g. Griffin et al., 1998; Xu, 2001). Within this scheme, lithospheric thinning proceeded by heat transport into the lithosphere and small-scale asthenospheric convection induced by extension. Once lithospheric mantle is thermally converted to asthenosphere, it can convectively mix with, and eventually be replaced by, asthenosphere (Davis, 1994). A recent hypothesis suggests that the lithospheric thinning has been

initiated with hydration which weakened the base of the old lithospheric mantle and transformed it into the convective asthenosphere. The water required for such a process may come from the dehydration of the subducted Paleo-Pacific lithosphere that lies horizontally in the 410-660 km transition zone beneath eastern China. The westward subduction of the Pacific plate caused an accumulation of eclogitic material above the 670 discontinuity with may coincide with the surface position of the DTGL as it has been recently observed by high-resolution seismic tomography (Huang and Zhao, 2006). Furthermore, the subduction may also explain the Bouguer gravity anomaly in eastern China and the formation of the DTGL in the early Cretaceous (e.g. Niu, 2005; Xu, 2007).

Although the lithospheric thinning in east China has been well recognized for more than a decade, debate continues on the time-scale of such destruction, especially in terms of its beginning, peak-period and ending. This, however, relies fundamentally, or at least in part, on the understanding of how the lithosphere keel could be removed. A short time interval of only 10-20 Ma, or even less, for delamination-induced thinning (Yang et al., 2003; Gao et al., 2004) is in strong contrast to that of over 100 Ma for erosion-induced thinning (Griffin et al., 1998; Xu, 2001; Xu et al., 2004). Some relevant geological, geochemical and geophysical data on a 200 Ma time scale for the NCC is summarized by Menzies et al. (2007) (Fig. 2.4) so that these events can be cross-correlated. The presence of mantle derived plutonic rocks around 180-190 Ma is believed to mark the reactivation of the cratonic lithosphere, the early Cretaceous is widely agreed to mark a key period, and the thinning is probably very weak, if any, in the Cenozoic (Menzies et al., 2007; and references therein).

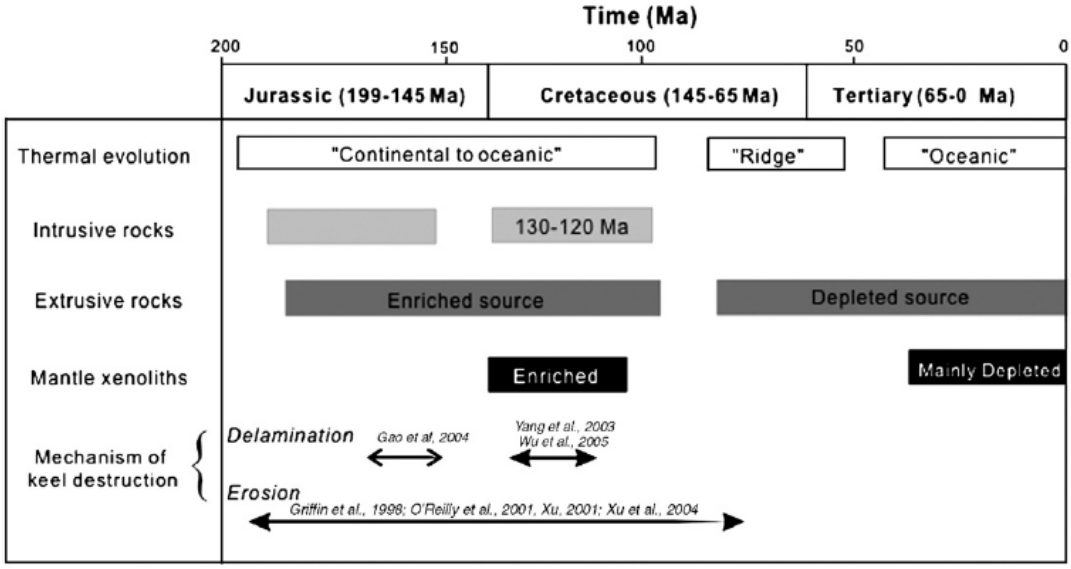


Fig. 2.4 - A 200Ma event history for the NCC (after Menzies et al., 2007). Thermal evolution "Continental to oceanic" geotherms based on basalt- and kimberlite-borne xenoliths and surface heat flow measurements. Note the temporal change that peaks in the Cenozoic. Intrusive rocks have a magmatic peak at 130–120Ma. Effusive rocks with a temporal change in mantle source from enriched to depleted largely inferred from Sr–Nd isotope variation (Xu, 2004). Mantle xenoliths primarily found in Cenozoic volcanic rocks with a characteristic "depleted" isotopic signature ( Xu et al., 1998). The timescale of keel delamination and lithospheric thinning is debated by Gao et al.(2004), Yang et al.(2003), Wu et al.(2005) suggest it occurred within a 10Ma, whereas Griffin et al.(1998), O'Reilly et al.(2001), Xu et al.(2004) believe it can occur over a period of 100Ma.

## Previous petrological work in the studied area

Subei basin is located at the south edge of NCC (Fig. 2.1), east of the TLFZ in east central China. This region is marked by the Triassic collision of NCC and the Yangtze Craton. West of the Tanlu fault, the collision zone is defined by the Dabie Shan UHP belt, but the location of the suture east of the fault is debated. The resemblance of petrologic and structural features between the Sulu and the Dabie Shan UHP belts may imply that the suture lies beneath or slightly north of the Sulu terrain. In this case the mantle lithosphere beneath the

Subei basin would belong to the Yangtze Craton. However, Li (1994) proposed a crustal-detachment model, based on the interpretation of linear aeromagnetic anomalies, surface geological observations, and deep seismic profiles. The model shows that during the mid-Mesozoic collision between the two continental blocks, the upper crust of the South China Craton (SCC, composed of the Yangtze Craton and the Cathaysia Craton) in the Subei-Yellow Sea region was detached from the lower crust and thrust over the NCC for more than 400 km, whereas the lower part of the lithosphere was subducted under the NCC along a subsurface suture running east of Nanjing (Fig. 2.5). Chung (1999) studied the trace element and isotope characteristics of Cenozoic basalts in Subei Basin and Shandong Province around Tanlu fault and inferred the same plate boundary between the NCC and SCC. The samples studied here come from just north of the proposed subsurface suture.

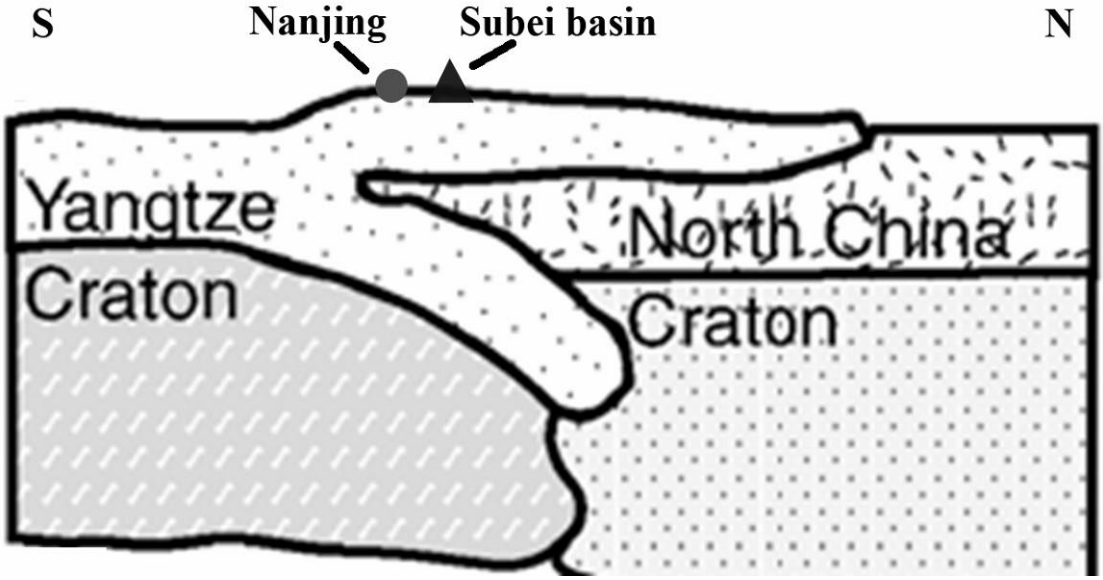


Fig. 2.5 - Crustal-detachment model for SCC beneath Subei basin (modified after Li 1994)

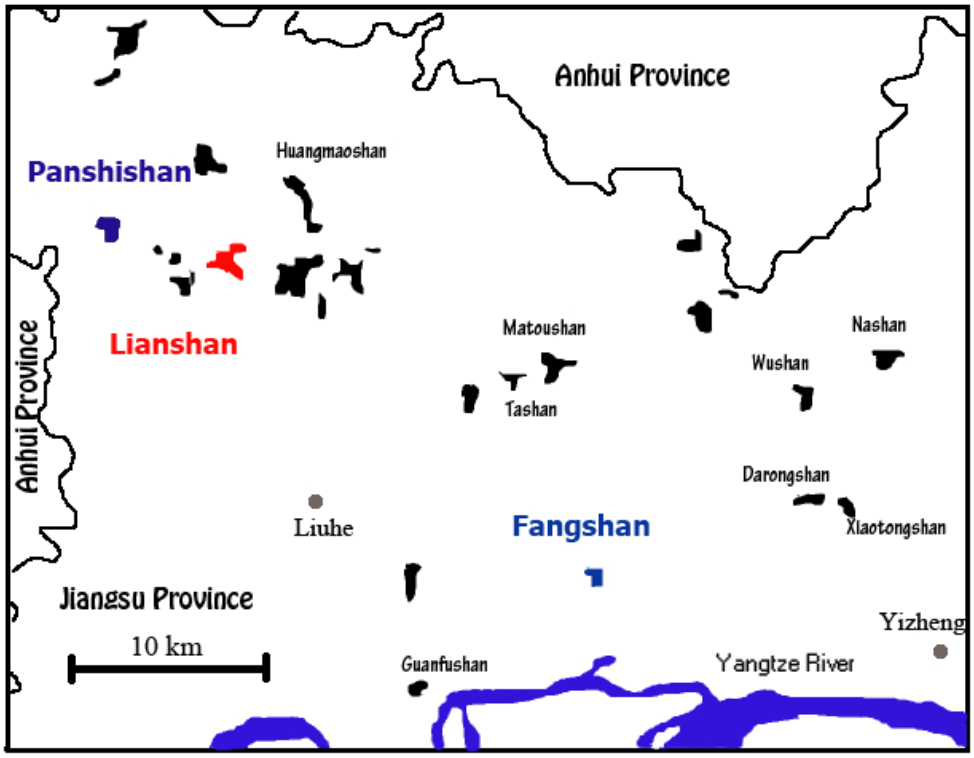


Fig. 2.6 - Detail map of sample locality and alkali basalt outcrops in the northern part of Jiangsu Province (modified after Zhi, 1991)

East central China experienced widespread Cenozoic basaltic volcanism, probably directly or indirectly related to the lithospheric thinning. This volcanism was particularly intense in the Subei basin, where it includes minor tholeiitic eruptions in the early Paleogene, and more extensive, xenolith-bearing alkali basalt activity in the Neogene (Fig. 2.6). Several works were carried out in the Subei basin area on both basalts and xenoliths.

A K-Ar ages and Sr, Pb isotopic characteristics of some Cenozoic volcanic rocks from Anhui and Jiangsu province were reported by early work of Chen and Peng (1988), According to this work the volcanism of Fangshan has been

dated at about 9 Ma, while Tashan, about 10km north Fangshan, has an age of 18Ma.

Sun et al. (1998) show that $^{187}Os/^{188}Os$ ratios for spinel lherzolite xenoliths from Panshishan range from 0.1241 to 0.1294. Most of them are lower than that of the primitive mantle (0.1290±9), suggesting that these xenoliths have slightly unradiogenic Os isotopic features. This result is concordant with the Sr and Nd isotopic characteristic in Panshishan reported by Chen and Wang (1994).

Zou et al. (2000) measured major, trace element, and Nd–Sr–Pb isotopic compositions of mantle xenolith-bearing Cenozoic basalts in southeastern China. Just two samples from Fangshan, and compared their results with those on NCC (Hannuoba, Datong, Kuandian, and Wudalianchi, Song et al., 1990; Basu et al., 1991; Zhang et al., 1991, 1995; Liu et al., 1992.). From Subei basin they found an increase in $^{87}Sr/^{86}Sr$ and a decrease in $^{143}Nd/^{144}Nd$ moving both Northward (Hannuoba, Datong, Kuandian, and Wudalianchi) and Southward (Mingxi, Xionglong, Longyou and Niutuo, Zou et al. 2000) (Fig. 2.7). They suggest that southeast China basalts result from a mixing between an asthenospheric mantle and an EM2 component, whereas the northeast China basalts reflect a mixing between an asthenospheric mantle and an EM1 component. The basalts in central-eastern China Nushan, Fangshan, and Tashan have the highest $^{143}Nd/^{144}Nd$ and the lowest $^{87}Sr/^{86}Sr$ and may represent the isotopic composition of the asthenospheric mantle (Fig. 2.8).

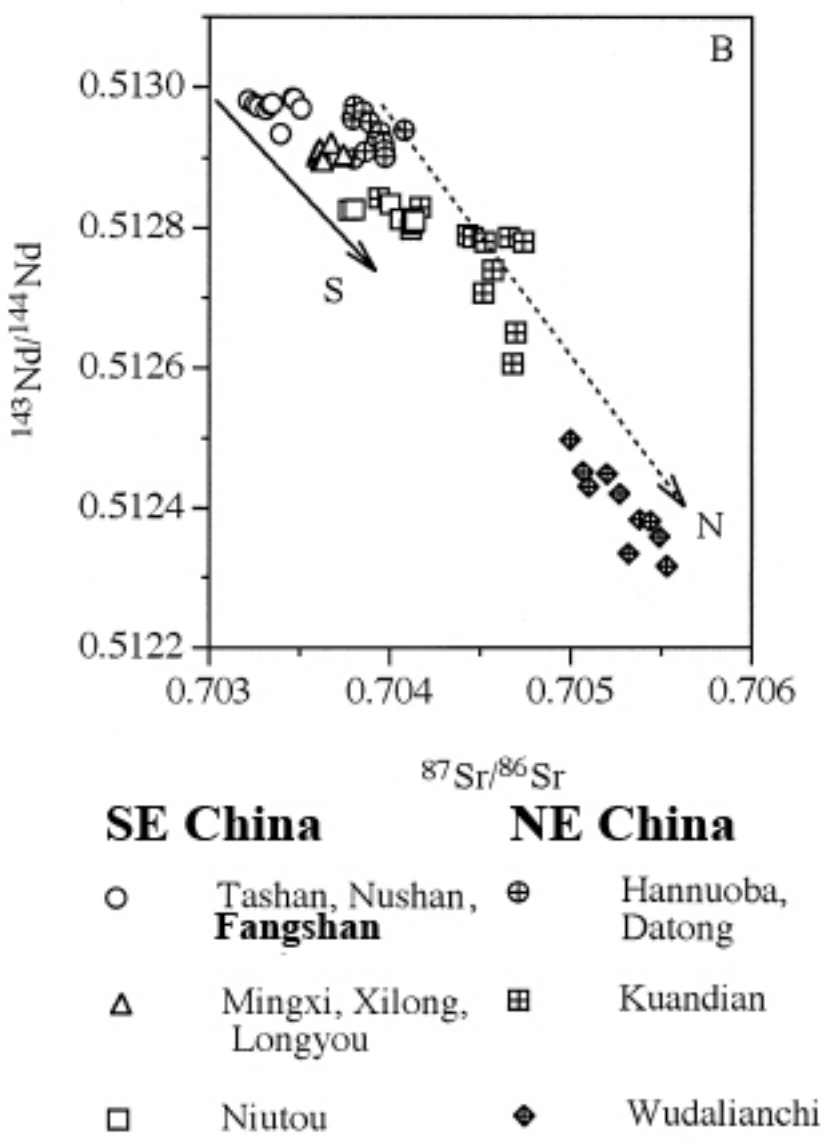


Fig. 2.7 - $^{143}Nd/^{144}Nd$ vs $^{87}Sr/^{86}Sr$ for NE and SE China basalts (modified after Zou et al., 2000)

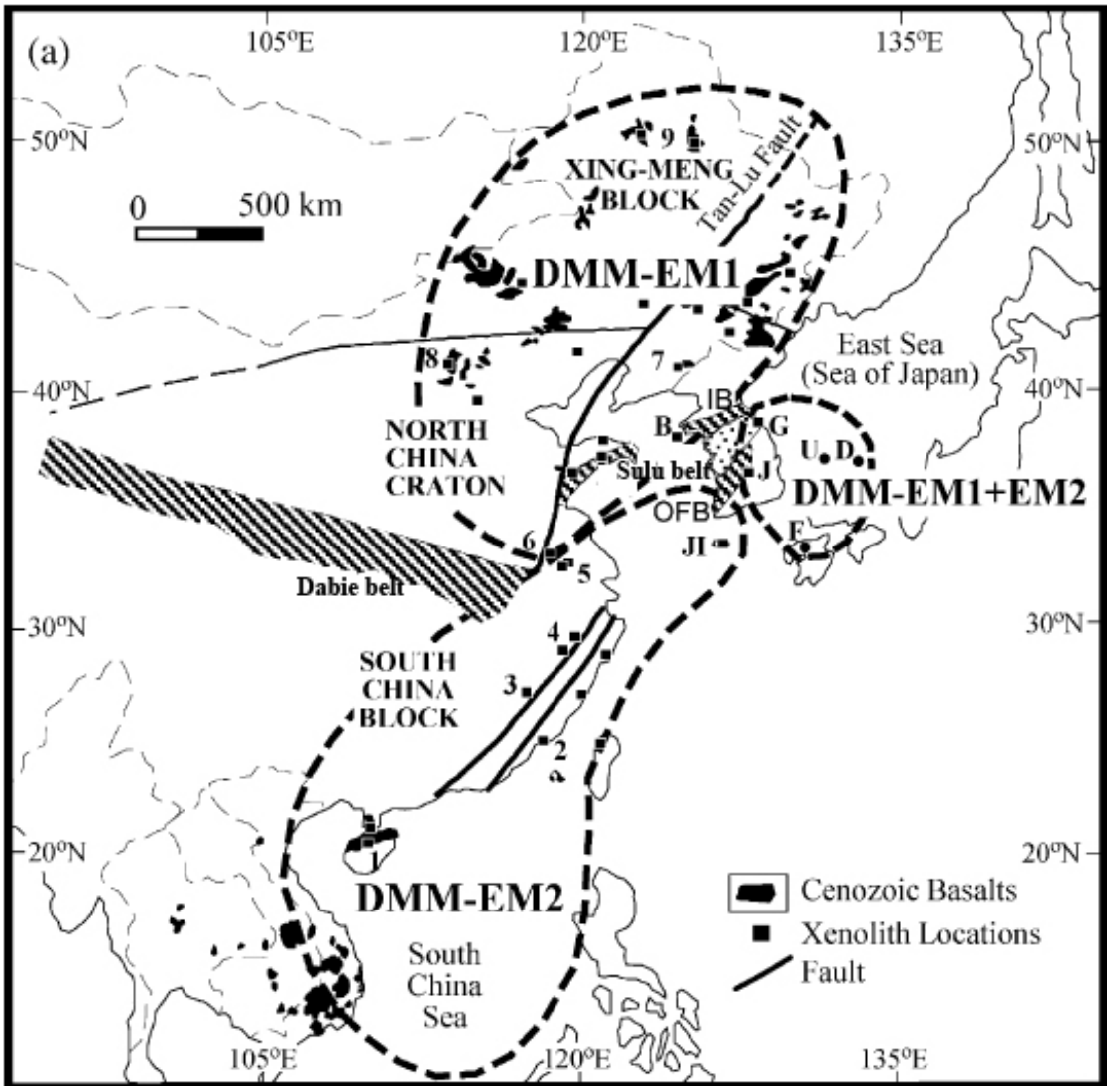


Fig. 2.8 - Outline of the mantle source components for the late Cenozoic basaltic rocks from East Asia (DMM = depleted mantle, EM1 and EM2 = enriched mantle type 1 and type 2, respectively). Distribution of the basalts and locations of mantle-derived xenoliths are after Hoang et al. (1996), Zou et al. (2000), and Choi et al. (2005). Tectonic boundaries between the North China Craton and the South China Block in South Korea are after Ree et al. (1996) and Chough et al. (2000). Xenolith Locations: 1 = Hainan Island, 2 = Niutoushan, 3 = Mingxi, 4 = Longyou and Xilong, 5 = Fangshan and Tashan, 6 = Nushan, 7 = Kuandian, 8 = Hannuoba, 9 = Erkeshan, Keluo, Nuominhe, Wudalianchi and Xiaogulihe.

Reisberg et al. (2005) have determined the whole-rock Os isotopic compositions and Re and Os concentrations for the ultramafic xenoliths from the Subei Basin (Panshishan, Lianshan and Fangshan). Re–Os analyses were coupled with whole rock major and trace element and S abundance determinations, and with characterization of rock textures, modal phase proportions and sulfide petrography. The two main sampling areas, Panshishan (eight xenoliths) and Lianshan (eighteen xenoliths) have similar textures and major and moderately incompatible lithophile trace element compositions. They show that Os isotopic ratios are related to Yb, thus suggesting an ancient melt extraction process which depleted the rocks in Re. These Os isotopic systematic suggest that both areas were affected by an early Proterozoic (~1.8 Ga) melt extraction event. Thus the two areas apparently shared the same long term lithospheric history. Nevertheless, the sulfide abundances and whole rock S, Os and Re concentrations are strikingly lower in Lianshan than in Panshishan, and the two localities have different incompatible lithophile trace element signatures. These differences resulted from contrasting melt percolation styles between the two areas. Panshishan experienced interaction with S-saturated possibly evolved melts that added Re, Cu and S, but had no affect on Os abundances, while Lianshan was affected by extensive percolation of sulfur undersaturated melts that removed Re, Os and S. On the basis of lack of correlation between $^{187}Os/^{188}Os$ and $^{187}Re/^{188}Os$, compared with the good correlation between $^{187}Os/^{188}Os$ and Yb, they speculated that the perturbation of the Re and Os concentrations was fairly recent, and perhaps related to Mesozoic or Cenozoic lithospheric thinning in eastern China.

On the other hand Xu et al.(2008a) obtained in situ Re–Os isotopic data for sulfide grains in mantle-derived peridotite xenoliths from Panshishan and

Tashan in Subei basin, They use $T_{RD}$ (Time of Re depletion model ages, which assume that all Re was depleted at the time of melting; these ages are more robust indications of the minimum age of melt depletion; Walker et al., 1989; Pearson et al., 1995a,b) and found that the sulfide populations in xenoliths from this area are dominated by grains that yield Neoproterozoic to Mesozoic ages. Archean ages are not recorded. The integration of sulfide and whole-rock Re–Os data suggests that the oldest part of the lithospheric mantle sampled beneath Subei basin may be Paleoproterozoic in age, and has been modified in Mesoproterozoic and Phanerozoic time.

For stable isotope, Zhi et al. (1996) use a conventional $BrF_5$ method for Oxygen isotope composition of mantle-derived materials from Anhui-Jiangsu basalt, while Li et al. (1999) measure oxygen isotope by the laser probe technique on mineral separates from mantle xenolith and megacryst in Cenozoic basalts, East China. Two samples from Panshishan are included. One $\delta^{18}O$ value of 4.97 for Ol was obtained, and $\delta^{18}O$ values are 5.67 and 5.25 for opx and 5.50 and 5.80 for cpx.

Yu et al. (2005) collected eight peridotite xenoliths from Panshishan, using ICP-MS measured trace elements of clinopyroxenes and systematic oxygen composition for ol, opx and cpx were measured using laser fluorination technology. The oxygen composition of minerals falls in the “normal” mantle range and achieved equilibrium between them. Clinopyroxene enrichment in incompatible elements indicates that some samples experienced a cryptic metasomatism.

A systematic work in Subei basin is still lacking. The previous works either have few samples, e.g. Li et al. (1999); Zhou et al. (2000) with just 2-3 samples, or just focus on certain elements or isotope composition, e.g. Sun et al. (1998)

on Os isotope, Reisberg et al. (2005) on whole rock Re-Os and Xu et al. (2008a) on sulfides Re-Os, Li et al. (1999) and Yu et al. (2005) on oxygen isotope.

# Chapter 3 - Analytical method

In this chapter, analytical method are described in detail. They include: whole rock major and trace elements obtained by XRF, in situ mineral major element measurements with electron microprobe (EMP), in situ mineral trace elements analysis with LA-ICPMS, in situ water contents of minerals using FTIR instrument, and oxygen isotopic ratios determination using a laser fluorination method.

## Whole rock - XRF

Whole rock X-ray Florescence (XRF) analyses were carried out at the Department of Earth Science, University of Ferrara, on a Philips PW 1400 spectrometer using standard procedures (Franzini et al., 1975; Leoni and Saitta, 1976). Fresh parts of xenoliths were selected, crashed and powdered. In order to keep the geometry of the tube-sample-detector assembly constant, the sample is normally prepared as a 1 cm thick disc, typically 50 mm in diameter. This is located at a standardized, small distance from the tube window. Because the X-ray intensity follows an inverse-square law, the tolerances for this placement and for the flatness of the surface must be very tight in order to maintain a repeatable X-ray flux. A further reason for obtaining a flat and representative sample surface is that the secondary X-rays from lighter elements often only emit from the top few micrometers of the sample. In order to further reduce the effect of surface irregularities, the sample is usually spun at 5-20 rpm. It is necessary to ensure that the sample is sufficiently thick to absorb the entire primary beam. For higher-Z materials, a few millimeters thickness is adequate, but for a light-element matrix such as coal, a thickness of

30-40 mm is needed. Major, minor and some trace elements (Ba, Co, Cr, Nb, Ni, Rb, Sr, V, Y and Zr) were analyzed. Typical uncertainties are <3% for Si, Ti, Fe, Ca and K, and 7% for Mg, Al, Mn, Na and P; uncertainties for trace elements (above 10ppm) are <7% for Rb, Sr and V and 15% for Ba, Ni, Co and Cr.

**Mineral major elements - EMPA**

Electronic microprobe analyses were performed at state key Laboratory for Mineral Deposits Research, Nanjing University and Institute of Petrology, Vienna University. In Nanjing University the mineral composition of samples was determined using a JOEL Superprobe (JXA 8100). Operating conditions were as follows: 15 kV accelerating voltage, 10 nA beam current and <5 μm beam diameter. Natural minerals and synthetic oxides were used as standards, and a program based on the ZAF procedure was used for data correction. Multi-point measurements were carried out from the core to the rim region of each mineral grain, and 3-4 grains of each mineral were measured in every sample.

In Vienna University the major element analyses of minerals were carried out on a Cameca SX100 electron microprobe, the operating conditions were 15 kV and 20 nA. In order to reduce alkali loss, glass analyses were performed using a defocused beam with a diameter of 5–10 μm at 15kV and 10nA. The error for all elements is below 5%, except for Na, which may be up to 10%. Natural and synthetic standards were used for calibration, and the PAP correction (Pouchou and Pichoir, 1991) was applied to the data.

**Water content in NAMs - FTIR**

Double-polished thin sections with a thickness of about 0.2 mm were prepared for the FTIR investigation (resin was used during the polishing treatment). The cleaning procedure of the sections prior to measurements included 10 to 20 hours dissolution in ethanol or acetone to remove the residual epoxy, followed by heating in an oven at ~ 100 °C for 3 to 10 hours to remove the surface absorbed water. Infrared spectra were obtained at wavelengths from 650 to 6000 cm-1 using a Nicolet® 5700 FTIR spectrometer (Fig. 3.1) coupled with a Continuμm microscope at the School of Earth and Space Sciences, University of Science and Technology of China (USTC) in Hefei. The principal advantages of such treatment are that: First, it is easy to observe the sample spot and to check the quality optically before the measurements; second, the liquid-$N_2$ cooled detector placed over the microscope is optimized for a focused beam; Third, the focused IR beam yields higher intensities than a measurement in the sample chamber of the spectrometer. The samples were measured by unpolarized radiation with an IR light source, KBr beam-splitter and liquid-nitrogen cooled MCT-A detector. A total of 128 or 256 scans were counted for each spectrum at a 4 $cm^{-1}$ or 8 $cm^{-1}$ resolution. Optically clean, inclusion- and crack-free areas, usually centered in the core region of each grain, were selected for the measurements with apertures of 30×30 or 50×50 μm, depending critically on the size and quality of the mineral grains.

Fig. 3.1 - Picture of the Nicolet 5700 FTIR spectrometer coupled with a microscope

Large and fresh grains were selected for the H-profile analysis. An accurate measurement of hydrogen-species in anisotropic minerals requires orientation of single crystals and use of polarized IR radiation (Libowitzky and Rossman, 1996). This is a very difficult technique to perfect and so an alternative technique using unpolarized determinations was performed and a statistically significant number of individual grains for each mineral in the same sample were chosen. Assuming that crystal orientation is randomly distributed within each sample (as evidenced by the variability in our FTIR results) an average value was used. Water contents were calculated by the modified form of Beer-Lambert Law: $\Delta=I\times c\times t\times\gamma$. where $\Delta$ is the integral absorption area ($cm^{-1}$) of absorption bands, I is the integral specific absorption coefficient ($ppm^{-1}\bullet cm^{-2}$), c are the contents of hydrogen species (ppm $H_2O$), t is the thickness of the section (cm), and $\gamma$ is the orientation factor discussed by

Paterson (1982). In this study, the integral region was 3000–3800 $cm^{-1}$, and the integral specific coefficients for cpx and opx were taken from Bell et al. (1995; 2003). Thickness was measured with a digital micrometer and reported as an average of 30~40 measurements covering the whole section; Baseline corrections were carried out with a spline-fit method by points outside the OH-stretching region.

Several factors have to be taken into consideration during the integration of IR spectra: (i) The Nicolet 5700 FTIR spectrometer occasionally suffers from an intrinsic problem, in that it can randomly produce positive, neutral or negative absorptions in 3700-3900 $cm^{-1}$, usually peaked at ~ 3740 and ~ 3850 $cm^{-1}$ (Fig. 3.2). These absorptions can change from one type to another in very short time, e.g. in less than a few minutes. Dehumidifiers were working all the time to keep the atmosphere in the labs dry and we try to less people in the room to avoid increase moisture. so that unstable of the background are probably caused by an artifact of the instrument, e.g. by the silicon carbide source, rather than by the instabilities of the background (ii) The application of liquid-$N_2$ on the coupled microscope can sometimes lead to the formation of invisible water film on the detector, and thus result in a weak absorption peak at about 3250 $cm^{-1}$. (iii) Some secondary phases even in trace amounts, e.g. invisible amphibole/mica lamellae, may contribute to the absorption of hydrogen-related species in the 3000-3700 $cm^{-1}$ region, e.g. a weak band at ~ 3660 $cm^{-1}$ observed in some Panshishan samples. (iv) Residual traces of epoxy on the sample wafers can generate minor absorptions between 2800 and 3000 $cm^{-1}$ because of influences from C-H bands; this contribution should not be included in the calculation of the total integrated OH absorbance, especially for some spectra which can extend down to ~ 2800 $cm^{-1}$. The influences from the above

mentioned 4 aspects are actually, in most cases, very little or negligible to the final total integrated area related with the absorption of OH/water molecular structurally bound to the host minerals; but there are a few occasions that their influences are so evident that they have to be treated separately. I attempted to resolve and fit the individual peaks manually on each background-subtracted spectrum, of which the bands from non-structural OH/$H_2O$ are notably visible (in this case, the contributions are mostly beyond 5%), by using the Peakfit V4.12 program (Jandel Scientific). The Gaussian form was used to fit the spectra, and the results were usually assured by $r^2 > 99.9\%$ at 95% confidence level. The above case (iii) is a little complicated, because altered hydrous products may produce, in addition to the ~ 3660 $cm^{-1}$ peak, absorption bands at other positions, which may superimpose on the typical peaks from structural hydrogen-species. In this case, it is impossible to separate the superimposed peak at present.

The interference from the FTIR spectrometer, mentioned above as artifact of the instrument, has fundamental influences on the baseline treatment of the IR spectra, in that it produces absorption in the 3700-3850 $cm^{-1}$ range (see also the later chapter for details). Therefore, this problem must be treated carefully. I try to resolve this by the following procedure illustrated in Fig. 3.3: firstly, a blank background spectrum was obtained (Fig. 3.3a); secondly, a subtraction was carried out on a normal spectrum with many noisy bands in the 3700-3850 cm-1 area (Fig. 3.3b) relative to the blank, and a new spectrum with very weak or relatively simple absorptions in this region was produced (Fig. 3.3c); finally, a linear replacement was performed on the yielded spectrum between ~ 3750 and 3900 $cm^{-1}$ for an approximation, which was processed by a “Straight Line” function provided in the Omnic software (Nicolet), and a relatively

high-quality spectrum was made (Fig. 3.3d), on which the band at ~ 3740 $cm^{-1}$, if present, can be easily resolved by Peakfit software. According to the curve trend of the spectrum (Fig. 3.3d), this approach, in most cases, contributes very little (e.g. < 2% or even less) uncertainty to the final calculated water content.

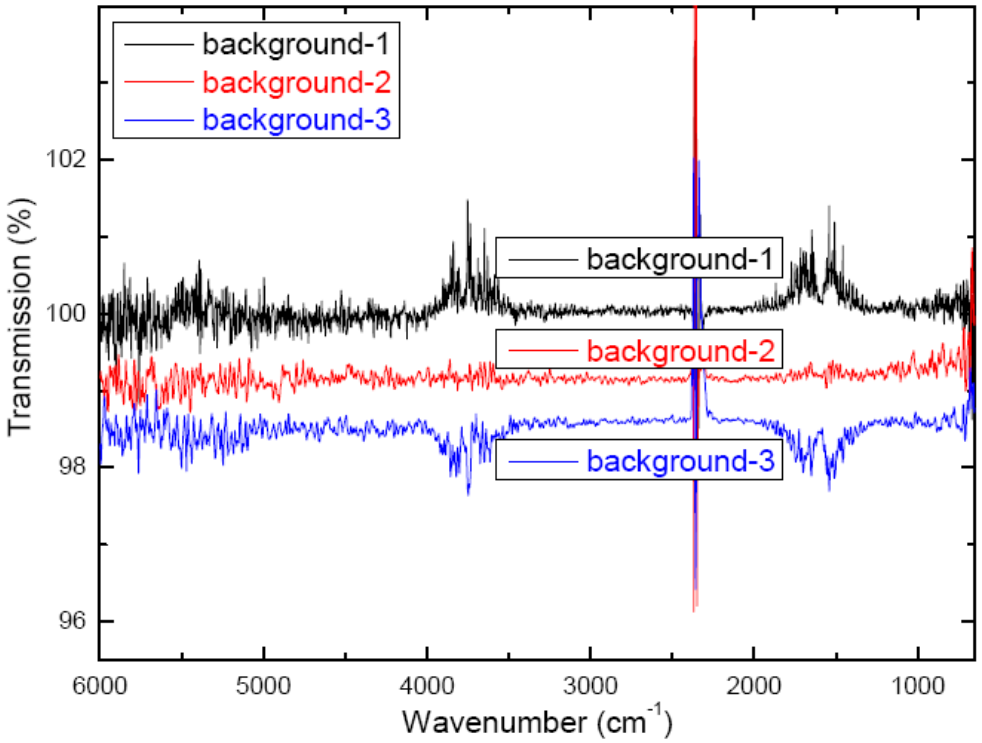


Fig. 3.2 - Absorption diagram of the Nicolet 5700 FTIR spectrometer (The spectra were obtained for a blank, and were vertically offset for the illustration)

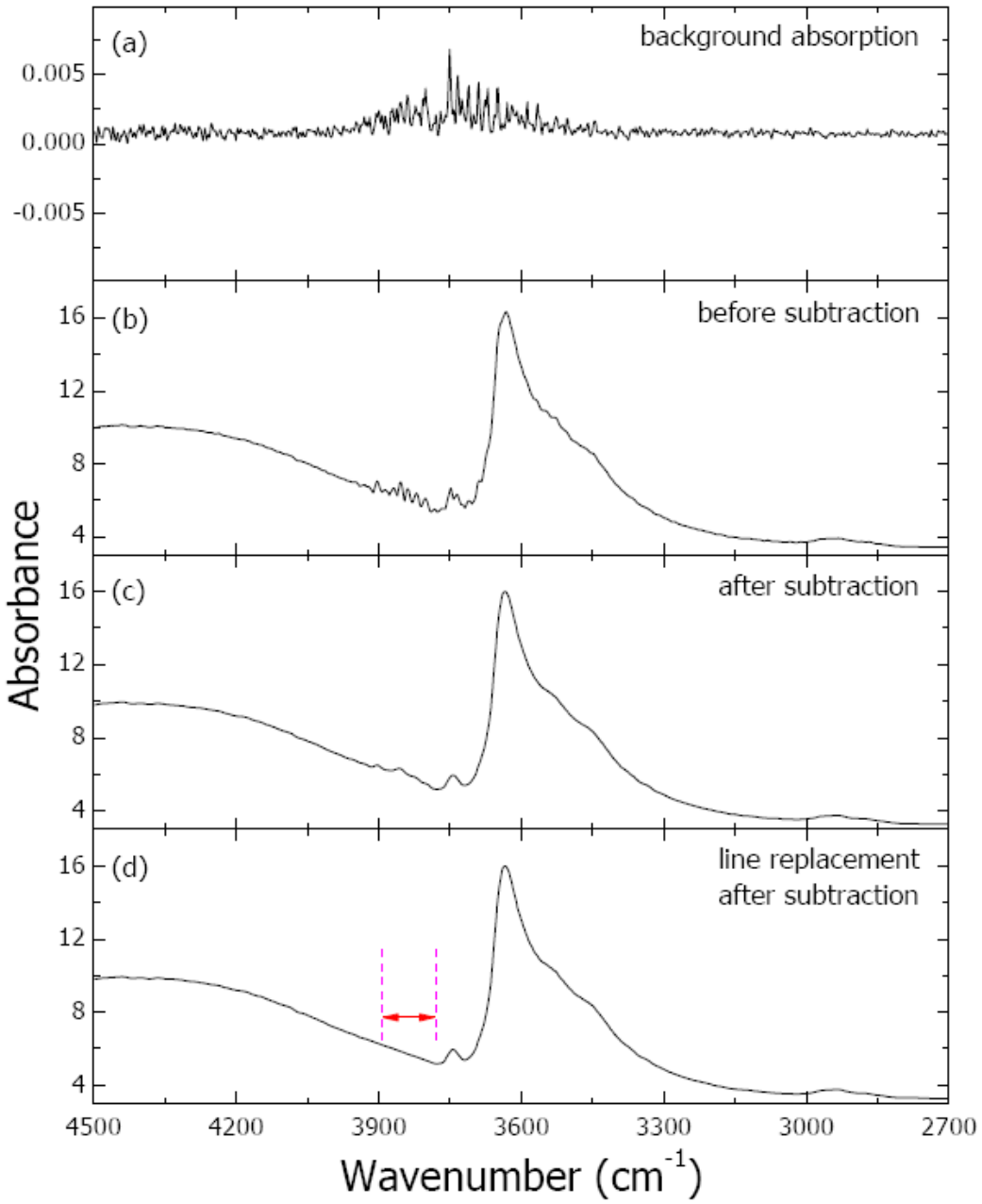


Fig. 3.3 - Interference treatments from the instrumental absorption diagram

Uncertainties in the obtained results derive from: (1) Unpolarized light. This is the main uncertainty during the analysis but it is estimated to be mostly less than 10% considering the applied procedures and the recent approach of

Asimow et al. (2006). (2) Baseline correction. Some strongly rising, non-linear baselines may be an intrinsic part of the spectrum in the OH region. These baselines commonly arise from $Fe^{2+}$ and may arise from silicate overtones in thick samples. A major, subjective source of uncertainty in IR measurements of OH in minerals remains the choice of baseline. Error introduced by different baseline corrections, e.g. spline-fit, polynomial-fit or slightly changing the points during the fitting is usually < 5%. (3) Variation of thin sections thickness. This was less then than 6% centered on the average value for each sample. (4) Absorption coefficients. There are slight differences between absorption coefficients in cpx and opx in my samples and those used to determine the mineral specific absorption coefficients (Bell et al., 1995), due to their different compositions and densities. These variations are estimated to be generally < 10%. On the whole, the total uncertainty, summing each single error, is estimated < 30%.

Detailed FTIR profile analysis performed at the USTC lab of two augite megacrysts hosted by Nushan Cenozoic basanites confirmed the homogeneity of their water content. These were used as standards to detect potential instrument shift during analysis. During the analytical period of all the NCC peridotites, the maximum difference for two augites is <4% both for peak height and integrated area within OH absorption area. The augites were also analyzed ay the LMTG lad (Toulouse, France). The maximum difference of peak height and integrated area within OH absorption area between the USTC lab and the LMTG [Toulouse, France] lab is <3% during cross-check analysis.

**Mineral trace element - LA-ICP-MS**

Trace element compositions of Cpx and a few Opx were carried out at LA-ICP-MS laboratory of University of Science and Technology of China. FTIR thin sections were broken and minerals grains were selected mounted in epoxy pellet and polished. Mineral grains were ablated in situ with Coherent company GeoLas pro ArF laser system with beam wavelength 193nm at 10 Hz repetition rate and 10J/cm$^2$ energy per plus. The ablation crater diameters are 60μm, and the sample aerosol was carried to ICPMS by high purity Helium with flow rate of 0.3L/min. A typical analysis consists of 80-100 replicates within 80-100s. PerkinElmer DRCII ICPMS was used to analysis the aerosol samples with the RF power 1350w and nebulized gas flow rate 0.7L/min. Sample analysis results processed with LaTEcalc software. The signal intensities (counts per ppm) for each element were calibrated against the NIST 610 silicate glass and the $^{44}$Ca content of samples was used as an internal standard. Typical analytical precision ranged from 2% to 5%.

**Mineral O isotope - LA- MS**

Oxygen isotope data were measured at the CNR-IGG of PISA by laser fluorination, reacting 1 to 1.5 mg ol, opx, cpx and sp fragments in $F_2$ gas atmosphere. I employed a 25 W $CO_2$ laser operating at a wavelength of 10.6 μm to irradiate the samples, and pure fluorine desorbed at 290°C from hexafluoropotassium-nickelate salt as a reagent. Three pre-fluorination steps were made before measuring new sets of analyses, in order to remove the moisture in the sample holder and the line. The $O_2$ produced during laser fluorination together with excess fluorine were passed through potassium chloride salt and excess fluorine was converted into a potassium-fluoride salt

and chlorine gas. A cryogenic trap cooled at liquid nitrogen temperature was used to freeze chlorine. After purification, $O_2$ was trapped over a cold finger filled with 13A zeolites, and then transferred to a Finnigan Delta Plus Mass Spectrometer for oxygen isotope analysis. QMS and NBS30 standard samples were measured at the beginning of each day of analysis; after the standard samples reached the accepted values, minerals samples sequence started. 5 to 6 standards were measured during each set of analyses. The average $\delta^{18}O$ value of QMS is 14.05 ±0.17 ‰ (1σ) and the $\delta^{18}O$ value of NBS30 is 5.24±0.15 ‰ (1σ). All $\delta^{18}O$ values are relative to SMOW. At least two fragments were analyzed for each mineral, and the variation within the same sample is less than the precision of standards.

# Chapter 4 - Petrography

The studied mantle xenoliths come from the three localities of Panshishan, Lianshan and Fangshan in Subei basin (Fig. 2.3). They are located in northwestern Jiangsu Province. Panshishan and Lianshan are separated by about 6 km, while Fangshan is about 20 km southwest of Lianshan. 14 samples from Panshishan, 22 from Lianshan, and 17 from Fangshan were investigated.

**Sample description**

The xenoliths from the three localities Panshishan, Lianshan and Fangshan are all hosted in alkali basalt lava flows (Fig. 4.1). Most of the xenoliths are rounded. Xenoliths from Panshishan and Lianshan are moderate in size (typically 5–10 cm in diameter), the largest ones (35cm in diameter) have been found in Panshishan and Lianshan (Fig. 4.2). Xenoliths from Fangshan are relative smaller than those of Panshishan and Lianshan. Textures vary from coarse-grained protogranular (~70% of total samples) through porphyroclastic (~20%) to equigranular (~10%) types. No hydrous phase or metasomatic secondary phases were observed. Samples from Panshishan are quite fresh, while those from Lianshan appear slightly altered in hand specimen. This difference is apparent in the olivine color, which varies from light green in the freshest samples, towards yellow, brown or even red in the most altered samples. The few samples from Fangshan showing textural evidence of host basalt infiltrations were disregarded. Fig. 4.3 shows some textures in the xenoliths, for each locality detail description are reported below.

Fig. 4.1 - General pictures of sample localities, from top to bottom Panshishan, Lianshan and Fangshan.

Fig. 4.2a - Picture of xenoliths from Panshishan

Fig. 4.2b - Picture of xenoliths from Lianshan

**Panshishan xenoliths**

The textures of Panshishan xenoliths were mostly protogranular and protogranular- porphyroclastic. Olivine (ol) and orthopyroxene (opx) are large (5–8mm), while clinopyroxene (cpx) and spinel (sp) are smaller (1–3 mm). Cpx and sp are always in direct contact with the large opx grains and sp commonly forms vermicular crystals inside opx or between opx and cpx. Occasional cpx exsolution lamellae are seen in opx. PSS07 is equigranular (Fig. 4.3), with small ol (2mm), opx (2mm), cpx (1mm) and sp (<1mm). Petrographic evidences for alteration are absent.

**Lianshan xenoliths**

The protogranular textures typical of most Lianshan xenoliths show no preferential orientation and crystals are not elongated. Olivine (ol) and orthopyroxene (opx) are large (4–7mm), while cpx and sp are smaller (1–3 mm). Cpx and sp are always in direct contact with the large opx grains and sp commonly forms vermicular crystals inside opx or between opx and cpx. Occasional cpx exsolution lamellae are seen in opx (Fig. 4.3). Sample LS05 is the only xenolith displaying a preferential orientation, with parallel elongated tabular olivine crystals (1*3mm). Holly-leaf sp grains and some triple junctions are present. This texture is transitional between porphyroclastic and tabular equigranular.

**Fangshan xenoliths**

The Fangshan xenoliths are all spinel-facies peridotites, dominantly spinel lherzolites with rare spinel harzburgites. Samples are mostly protogranular or porphyroclastic. Olivine (ol) and orthopyroxene (opx) are large (4-7mm), while clinopyroxene (cpx) and spinel (sp) are smaller (1-3mm). Occasional cpx exsolution lamellae are seen in opx, similar to the other localities.

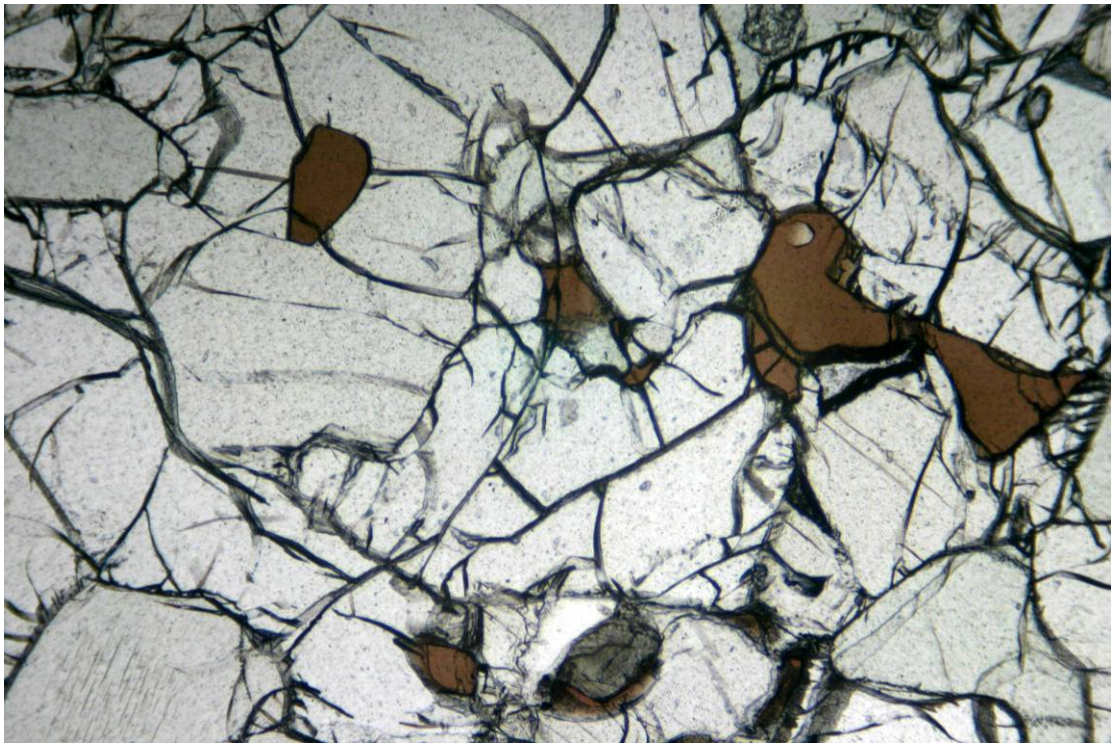

Fig. 4.3 - Texture of xenolith PSS07

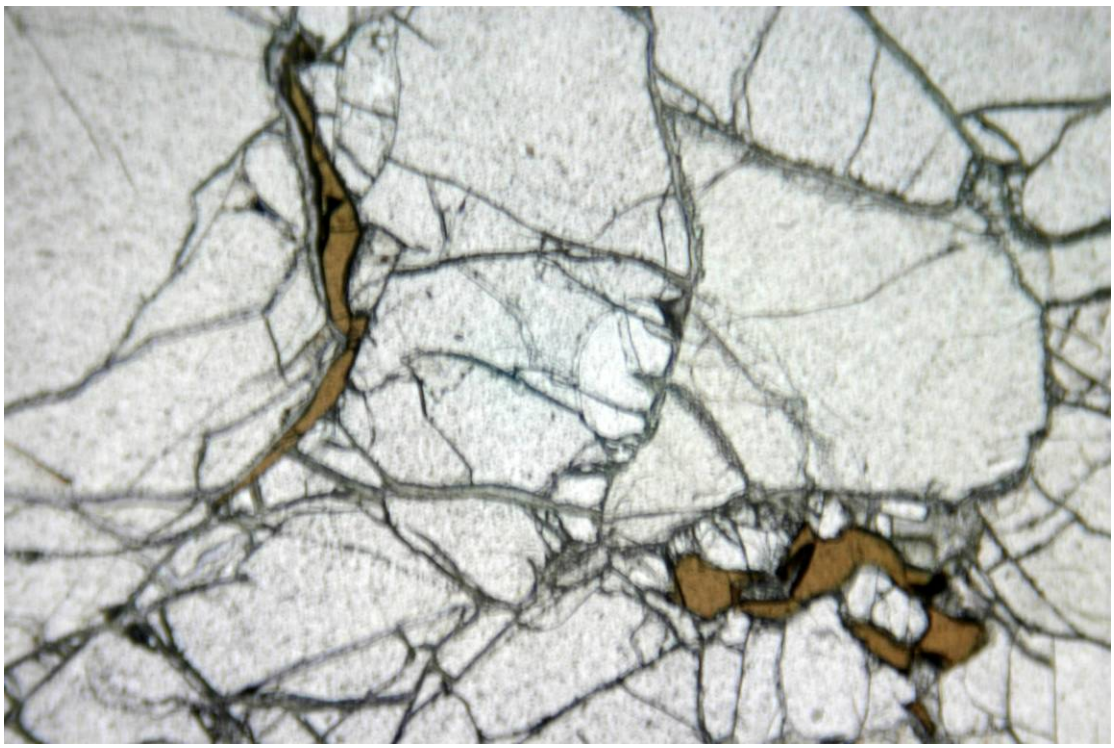

Fig. 4.3 - Texture of xenolith PSS11: sp adjacent to cpx

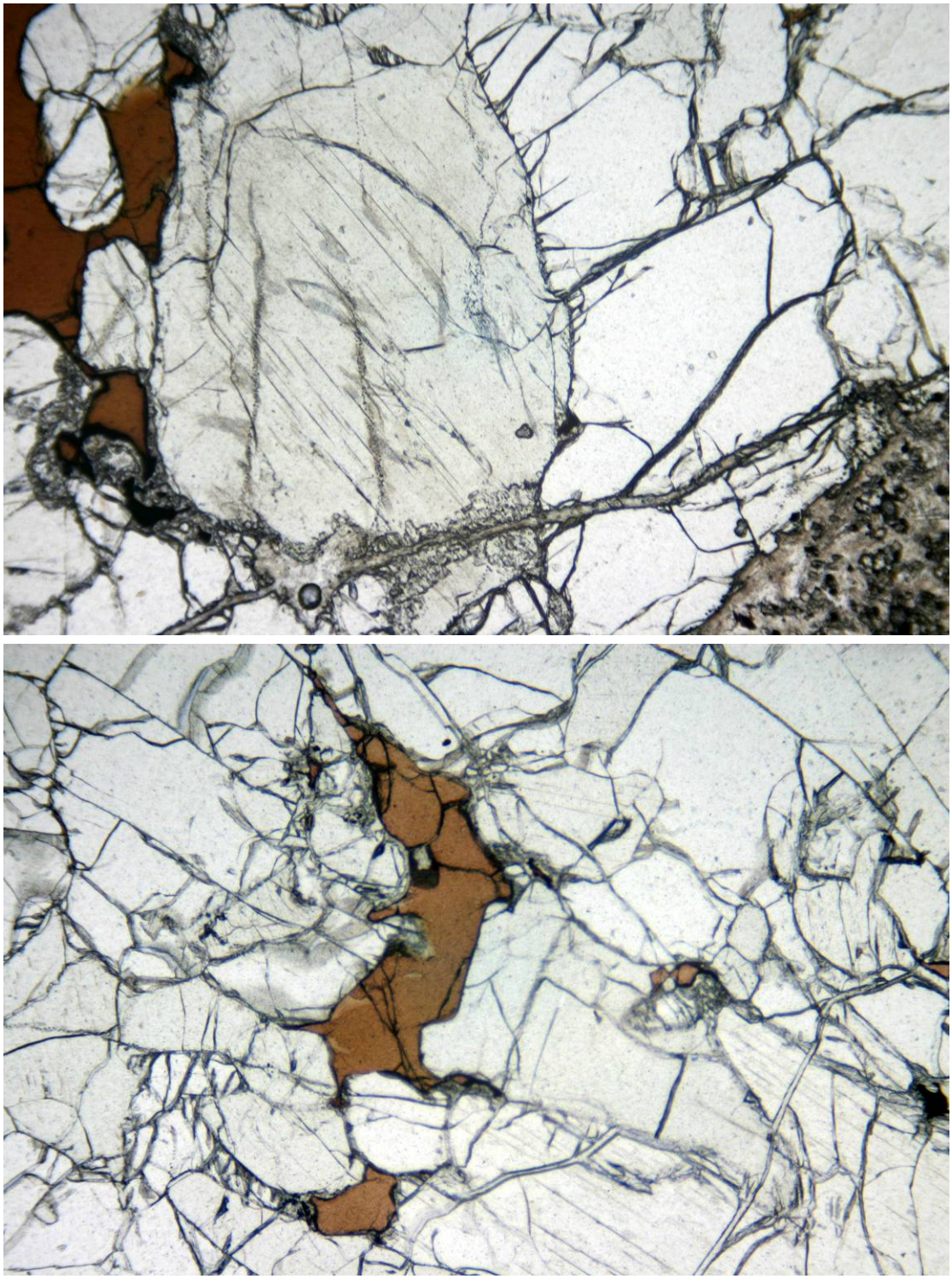

Fig. 4.3 - Texture of xenolith PSS20: cpx exsolution lamella in opx

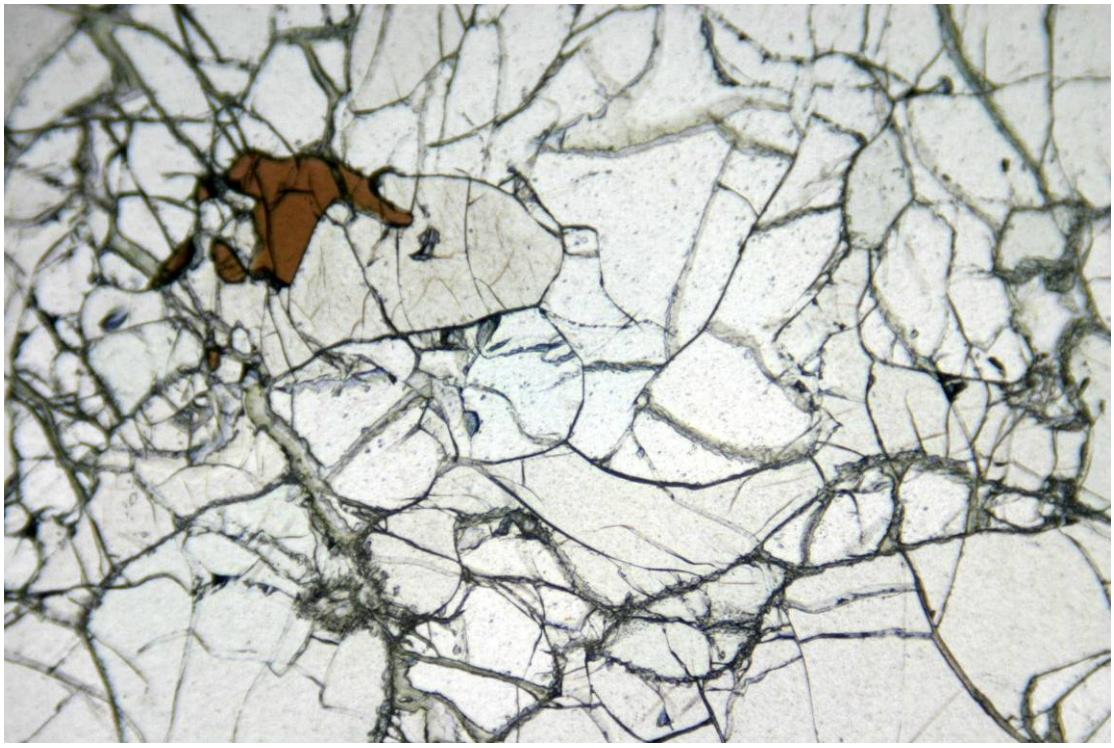

Fig. 4.3 - Texture of xenolith LS01

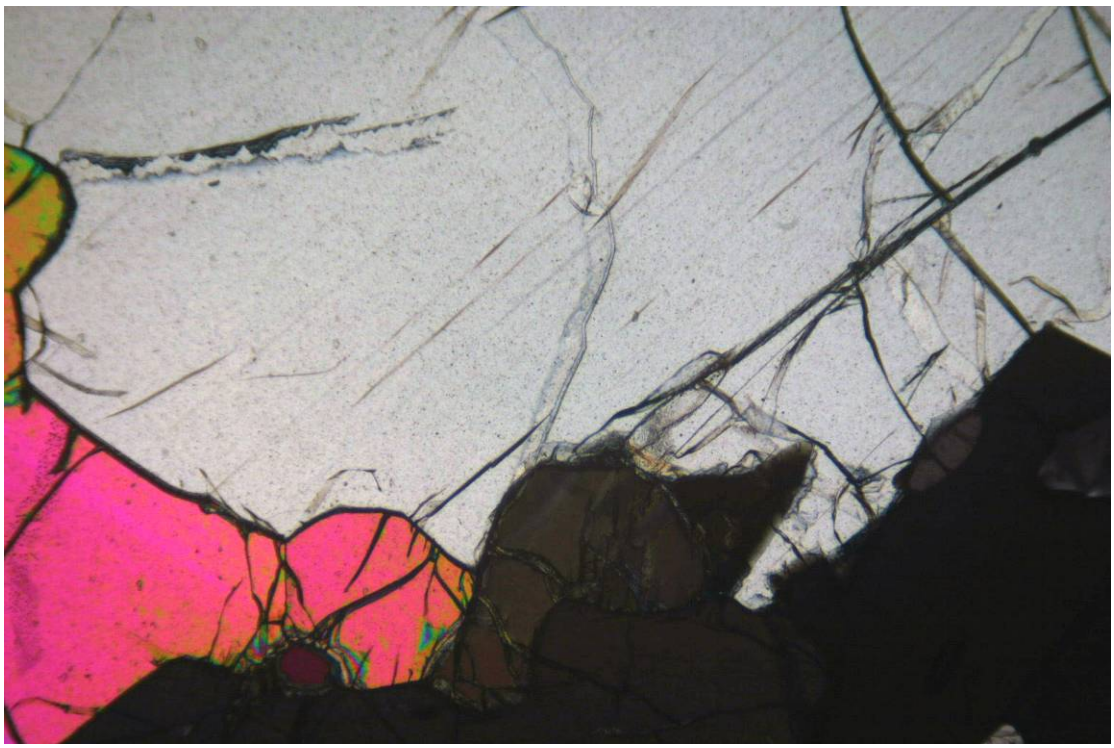

Fig. 4.3 - Texture of xenolith LS01 in crossed light

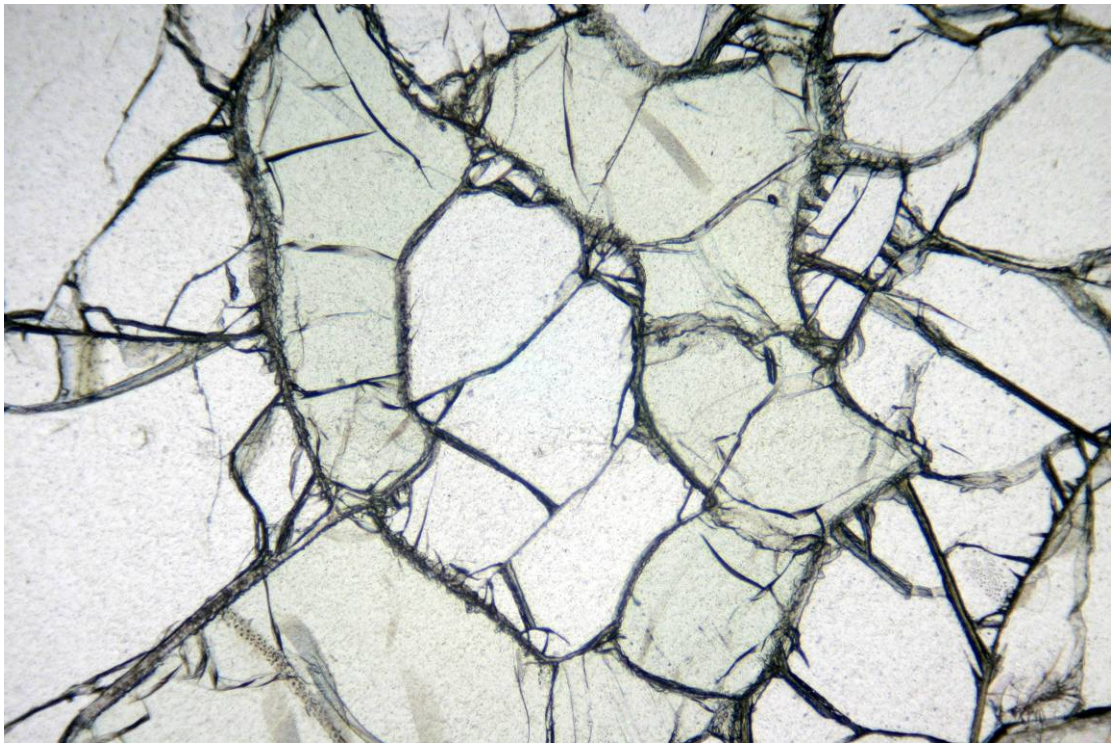

Fig. 4.3 - Texture of xenolith LS03

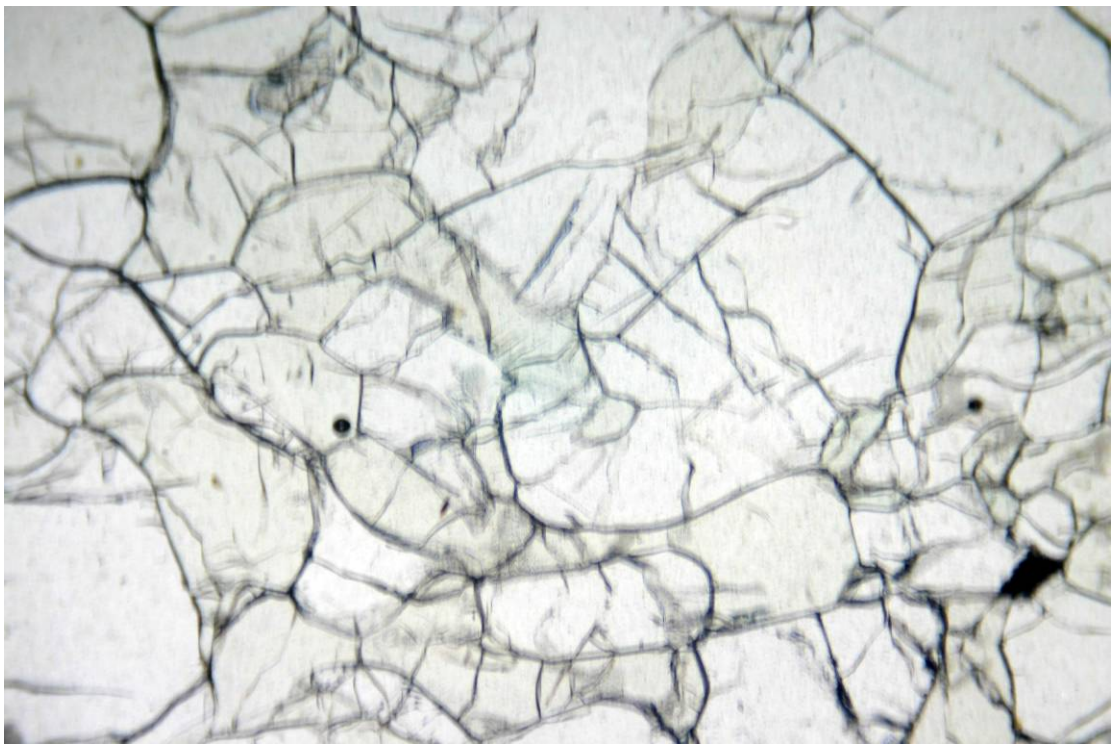

Fig. 4.3 - Texture of xenolith FS02

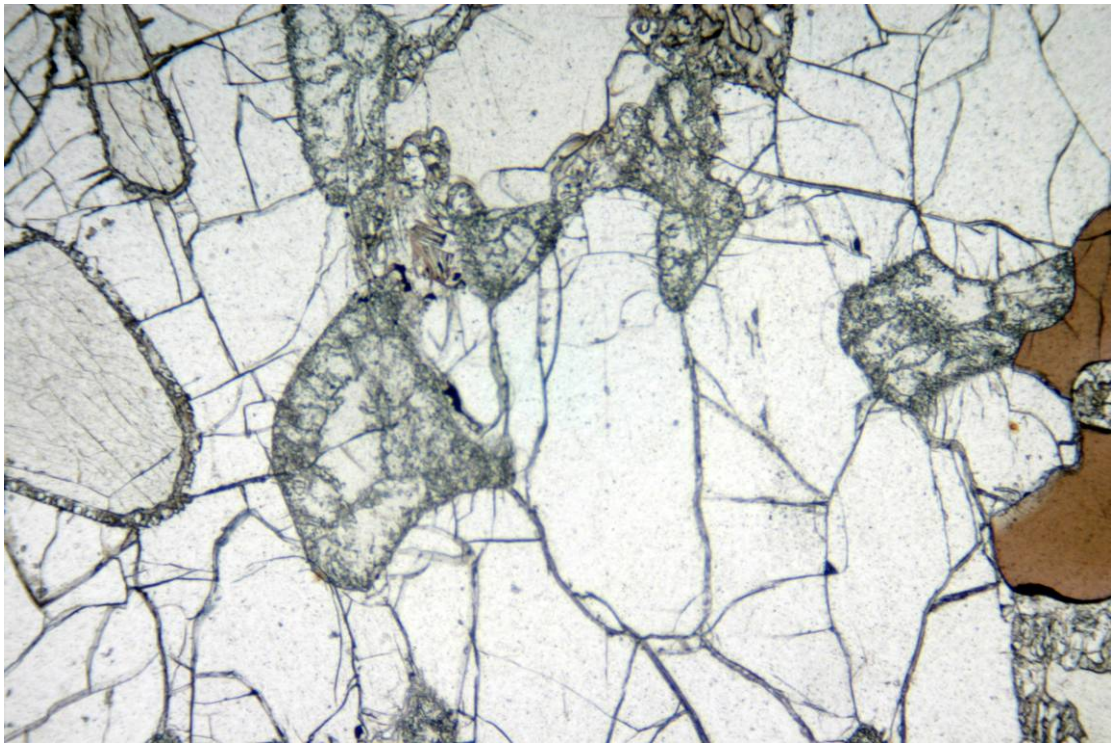

Fig. 4.3 - Texture of xenolith FS18 with a possible basalt infiltration

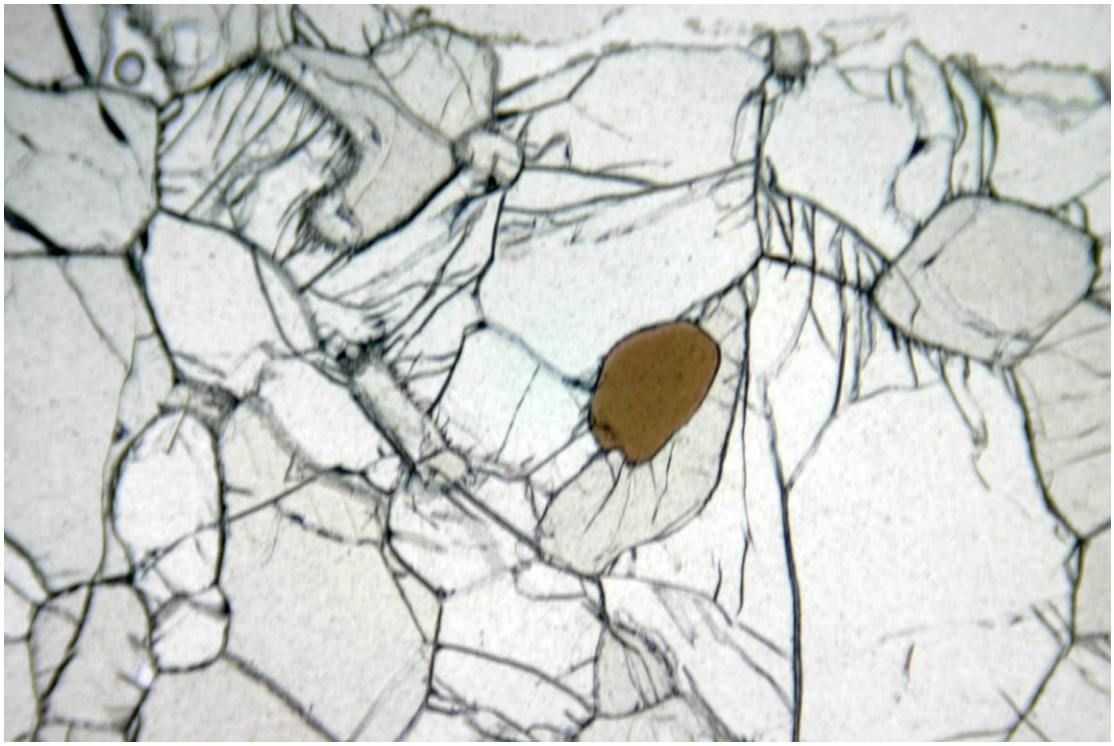

Fig. 4.3 - Texture of xenolith FS19: spinel in opx

**Mineral mode estimates by point counting**

The polished thin sections are scanned into digital picture, then enlarged and marked with a 40 by 40 grid and counted based on the different color of minerals (transparent for ol, dark green to brown for opx, green for cpx and totally black or dark brown for sp). The point counting resulting in the modal percentage of minerals is reported in Table 4.1. As the thin section represents just a small part of the xenoliths, it may not perfectly comparable with modal estimates obtained by mass balance betwwn whole rock and mineral analyses. A petrographic classification diagram was used (Fig. 4.4) for the Subei basin xenoliths. The samples which have cpx modal content less or equal to 5% are classified as harzburgite, those with cpx modal content from 6 to 9% are named cpx-poor lherzolite. Xenoliths with ol mode content < 40% are named olivine websterite while those with ol mode content >90% are named dunite. Most of the xenoliths are lherzolites (Table 4.1, Fig. 4.1), rarely, harzburgites. Olivine websterites and pyroxenites are rare. Among 14 Panshishan xenoliths, just PSS17 falls within harzburgite field with cpx mode content of 5% and PSS01, PSS10 and PSS20 are cpx-poor lherzolite. Among 22 xenoliths from Lianshan, LS 26 is harzburgite while samples LS04 and LS24 are olivine websterite (ol content about 40%). LS16 has olivine mode content up to 92%, and classifies as dunite, having 3% modal content of cpx, so LS16 is referring as cpx-bearing dunite. Six samples (LS03, LS12, LS15, LS17, LS19 and LS21), with cpx content range from 6 to 9 are named cpx-poor lherzolites. The rest are lherzolites. Xenoliths from Fangshan seems more depleted in cpx mode content, three samples FS06, FS25 and FS30 are harzburgites, FS11, FS13, FS16, FS24 and FS 26 are cpx-poor lherzolites. All the samples from the three localities encompass the compositions ascribed to upper mantle peridotite, from fertile

lherzolite with cpx mode content up to 23% to cpx-poor lherzolite with cpx mode contents about 6-9% and rarer harzburgite with cpx mode content as low as 3%.

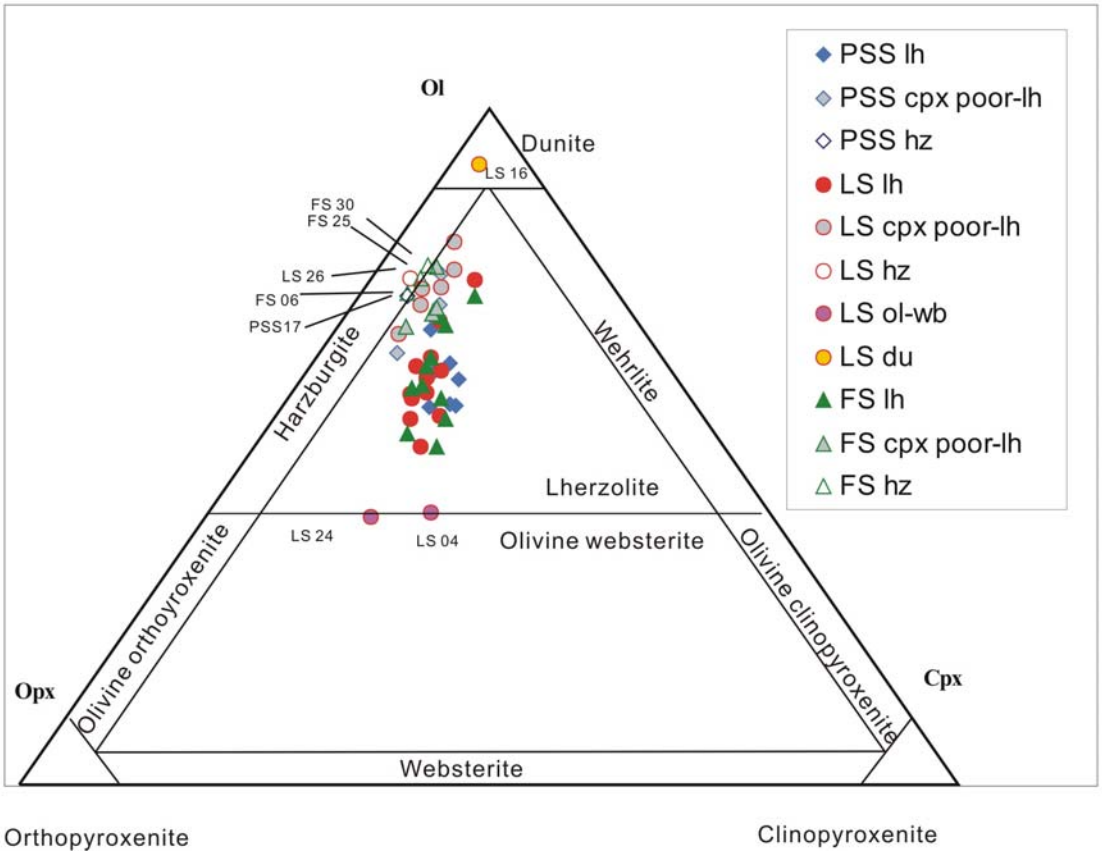


Fig. 4.4 - Petrographic classification for peridotite xenoliths from Subei basin.
PSS: Panshishan, LS: Lianshan, FS: Fangshan; lh: Lherzolite, cpx poor-lh: with cpx modal content in the range of 6-9%; hz: Harzburgite, ol-wb: Olivine Websterite, Du: Dunite. Light blue diamond, Panshishan lherzolite; light blue filled grey diamond, Panshishan cpx-poor lherzolite; blue open diamond, Panshishan harzburgite; red dot, Lianshan lherzolite; red filled grey dot, Lianshan cpx-poor lherzolite; red open dot, Lianshan harzburgite; red filled pink dot, Lianshan olivine websterites; red filled golden dot, Lianshan dunite; green triangle, Fangshan lherzolite, green filled grey triangle, Fangshan cpx-poor lherzolite; green open triangle. Fangshan harzburgite)

# Chapter 5 - Geochemistry

This chapter compiles all the geochemical data, including whole rock composition, major and trace element analyses of minerals, oxygen isotope data determinations of xenoliths minerals. These data are treated separately in the following sections. The acquisition of this large data set needs totally different sample preparations (see Chapter3 Analytical Methods for details). Whole rock major element compositions were obtained with XRF analyses of pressed powder disc; in–situ mineral major element measurements were performed on polished thin section (30-40μm in thickness) with electron microprobe (EMP), whereas mineral trace elements were obtained with LA-ICPMS on selected minerals grains (recovered by FTIR sample preparation) and mounted in polished epoxy pellets; oxygen isotopic ratios have been determined using a laser fluorination on separated mineral grains; finally, in situ water contents of peridotitic minerals have been obtained with FTIR instrument on ad-hoc prepared double polished thin section (200 μm in thickness). Despite the carefulness in limiting the amount of material necessarily for the cited analytical work, not all of the xenoliths are big enough to sustain the entire analytical protocol. So it is a pity that the analytical results reported below do not include all samples originally selected to investigate Subei basin lithospheric mantle.

In order to check the modal percentage, estimated by point counting, a mass balance calculation (12 samples), based on the whole rock major elements content and minerals major element content (Table 5.1 to Table 5.5) are made. No hydrous phases, as well as glassy patches are observed in all samples (see chapter 4) and all the xenoliths of three populations investigated are four phase

peridotites (ol, opx, cpx and sp). All the main oxides ($SiO_2$, $TiO_2$, $Al_2O_3$, $Cr_2O_3$, $Fe_2O_3$, MnO, MgO, CaO, $Na_2O$ and $K_2O$) were thus used for the regression calculation. The result of the calculations (oxides are recalculate to 100%), and the confidence level of regression is 95%. The results are reported in Table 5.1. Compared with the mineral modal percentages obtained on the basis of point counting estimates, the mass balance method gives the comparable results. The difference between the two methods is, as expected, evident just for olivine estimation (since olivine is the most abundant phase in peridotite) (e.g. PSS15, PSS17, LS06 and LS20). The discrepancy of 5% in olivine modal evaluation does not contradict the classification obtained with point counting method, applied to the entire sample collection used for this study. I am thus confident in considering the modal estimates obtained by counting point reliable to classify the entire sample collection.

**Whole-Rock**

Four samples of Panshishan, seven samples of Lianshan and one sample of Fangshan were selected for XRF analyses. Among these samples PSS17 is the only harzburgite, PSS01, LS03, LS17 and FS11 are cpx-poor lherzolithes, all the others are lherzolites. Major and minor elements analyses of the Subei basin mantle xenoliths of Panshishan, Lianshan and Fangshan are reported in Table 5.1.

The twelve Subei basin mantle samples show Mg# [(MgO/40.3)/((MgO/40.3) + (FeO/70.85)) ×100 %mol] encompassing the entire upper mantle peridotitic residual trend, from the most fertile LS22 lherzolite (Mg#=90.17) to most residual (Mg#=93.22) LS17 cpx-poor lherzolite (Fig. 5.1). Among the Subei basin samples, the highest Mg# values, theoretically well beyond the complete

consumption of the clinopyroxenes, are represented by the cpx-poor lherzolite LS17 and the lherzolite LS20 of Lianshan population with estimated cpx modal 5% and 8% contents respectively.

The lherzolites of the three localities have $SiO_2$ contents (in weight %) ranging from 44.2 to 45.6%; the harzburgite of Panshishan PSS17 has a $SiO_2$ content of 44.3. The $TiO_2$ contents in all the xenoliths are less than 0.15 wt%. $TiO_2$ contents in Lianshan lherzolites range from 0.01 wt% (LS17) to 0.14 wt% (LS22). and the two Lianshan cpx-poor lherzolites are 0.01 wt% (LS17) and 0.05 wt% (LS03). Among the four samples of Panshishan, the two lherzolites have highest $TiO_2$ contents of 0.11 wt% for PSS11 and 0.17 wt % for PSS15. and the cpx-poor lherzolite PSS01 has a middle value of (0.08 wt %) $TiO_2$ contents. The harzburgite PSS17, as expected, present the lowest $TiO_2$ (0.02 wt %) among the samples. The only one Fangshan sample (FS11 cpx-poor lherzolite) has $TiO_2$ content of 0.07 wt%.

The entire Subei xenolith population has whole rock $Al_2O_3$ contents which vary in range from 1.2 (LS17) up to 3.18 wt% (PSS11). On the whole, $Al_2O_3$ is negatively correlated with Mg# (Fig. 5.1). Panshishan samples seem to align along a residual trend from the most fertile lherzolite (PSS11) towards the most residual harzburgite (PSS17). The only one Fangshan sample perfectly fit this possible residual trend. Lherzolite LS17 and cpx-poor lherzolite LS20 may be included in this trend to form the lowermost limit of this alignment. Three Lianshan samples LS03, LS05 and LS22 are out from this alignment, showing low Mg# compared with the aluminum contents.

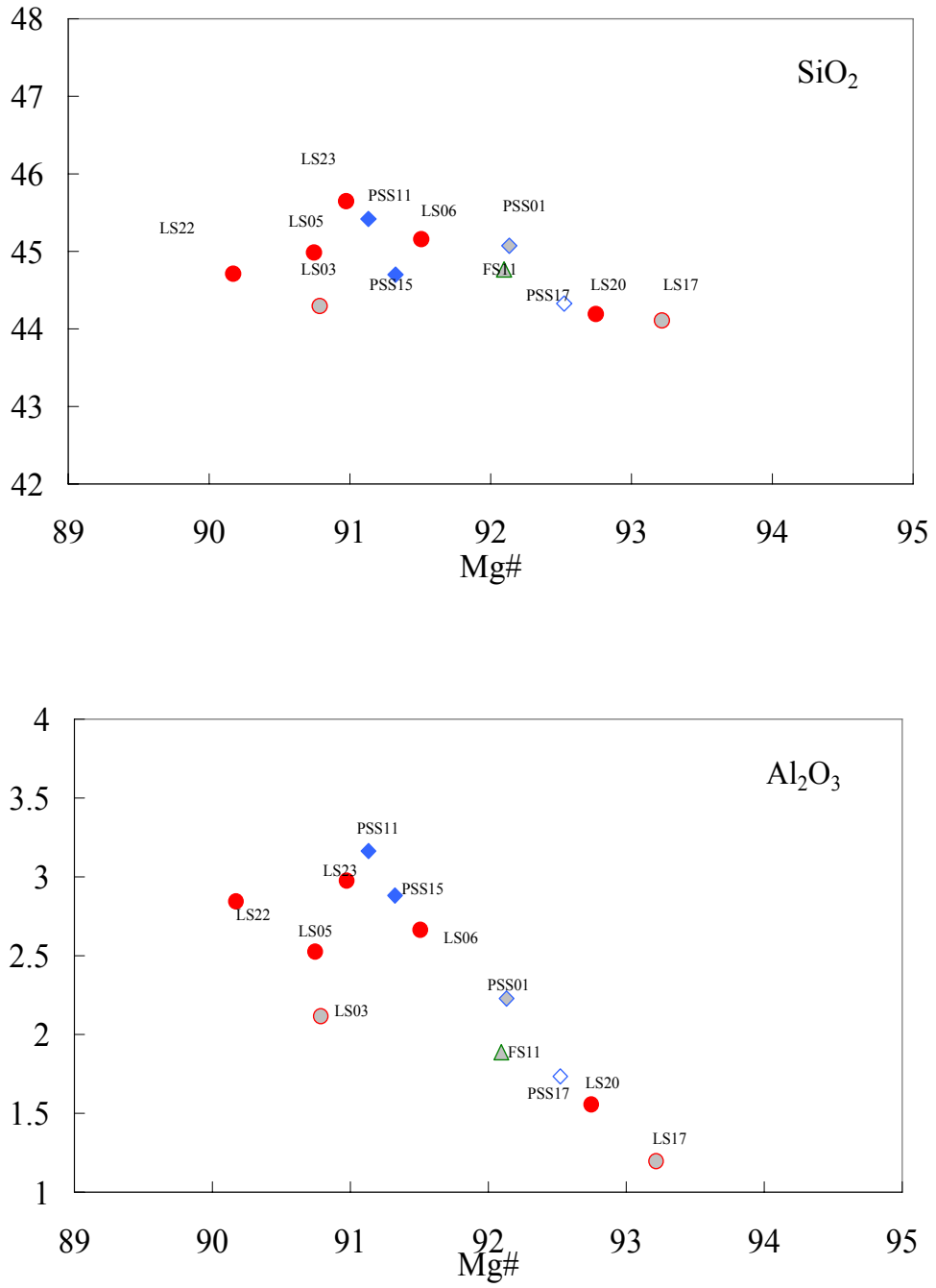


Fig. 5.1 - Whole-rock major element: $SiO_2$ and $Al_2O_3$ contents vs Mg# (symbols are as in Fig. 4.4. Panshishan lherzolite, light blue diamond; Panshishan cpx-poor lherzolite, light blue filled grey diamond; Panshishan harzburgite, blue open diamond; Lianshan lherzolite, red dot; Lianshan cpx-poor lherzolite, red filled grey dot; Fangshan cpx-poor lherzolite, green filled grey triangle.)

The $FeO_T$ contents vary between 6.01 wt% (sample LS17) and 7.92 wt% (sample LS22). On the whole, Subei basin mantle xenoliths show $FeO_T$ contents in the range of values (6.8-8.5 wt %) of worldwide spinel-bearing peridotites (Griffin et al., 2008). LS17, LS20 lherzolites are excluded by this consideration since the they present low to very low FeOt contents, comparable to the most restitic cratonic mantle.

The CaO contents in the xenoliths of the three localities range from 0.89 to 2.96 wt%. Panshishan lherzolites have CaO contents range from 1.91 to 2.58 wt%; PSS01 cpx-poor lherzolite has CaO content of 1.90; as expected for theoretical residual composition, PSS17 harzburgite show the lowest CaO contents. However Ca is anomalously low in this harzburgite, if compared with other fusible elements (such us Al, Ti). Fangshan lherzolite FS11 has CaO contents (2.11 wt %) in the range of Subei basin lherzolites.

The $Na_2O$ content is very low, for all the analyzed xenoliths from Subei basin varied range from 0.03 to 0.13 wt%. The $Na_2O$ contents of Lianshan lherzolites covered a large range, from 0.03 to 0.13, with cpx-poor lherzolites range from 0.03 to 0.07, whereas Panshishan lherzolites have a narrower range (0.11 to 0.13 wt %). As occurred for CaO contents also $Na_2O$ in harzburgite PSS17 (0.03 wt %) is coherent with a residual composition. Fangshan cpx-poor lherzolite FS11 has $Na_2O$ value (0.09 wt %), is in the range of all the lherzolites.

Among the analyzed xenoliths, LS17 lherzolite from Lianshan, has the highest Mg# value up to 93.22, and always has the highest or lowest value of oxides except for CaO and $Na_2O$, which the harzburgite PSS17 having the lowest values.

**Whole rock trace elements**

In analyzed Subei basin mantle xenoliths Cr contents vary from 1423 to 3103 ppm and show a broad negative correlation with Mg# (Fig. 5.2a). Cr contents for Lianshan lherzolites range from 1423 ppm to 2756 ppm, two cpx-poor lherzolite LS03 and LS17 have Cr content 2425 and 1563 ppm. Panshishan lherzolites have Cr contents from 2463 ppm to 3103 ppm. The cpx-poor lherzolite PSS01 has Cr content 1561ppm and he harzburgite PSS17 has Cr content 2171 ppm). The Fangshan cpx-poor lherzolite FS11 has 1731 ppm of Cr.

In mantle xenoliths Ni is primary retained in olivine. In Subei mantle xenoliths Ni varies from 1870 to 2247 ppm and it is positively correlated with Mg# (Fig. 5.2b). Ni contents of Lianshan lherzolites range from 1870 to 2168 ppm, two cpx-poor lherzolite LS03 and LS17 have Ni content 2226 and 2226 ppm. Panshishan lherzolites have Ni contents from 1955 to 2055 ppm. The cpx-poor lherzolite PSS01 has Ni content 2021ppm. The harzburgite PSS17 has the highest value of Ni. Fangshan cpx-poor lherzolite FS11 has 2122 ppm of Ni

In Subei peridotites, V, compatible minor element easily accommodated in spinel, range from 26.8 to 78.9 ppm, with lherzolites almost encompassing the entire range. On the whole, V has good negative correlation with Mg#, at given Mg#, lherzolite of Panshishan have V contents higher than those of Lianshan and Fangshan. (Fig. 5.2c)

Sr is an incompatible element in peridotite/basaltic system. In Subei xenoliths it varies from 1.8 to 11.7 ppm, with Lianshan and Panshishan lherzolites showing with values varying from 1.8 to 11.3 ppm and from 4.3 to 11.7 ppm respectively. The cpx-poor lherzolites have a narrow rang of 8.3 ppm

to 9.3 ppm for Sr content. The harzburgite PSS17 shows relatively high Sr content (9.3 ppm), whereas Fangshan cpx-poor lherzolite record lower Sr content (6.1 ppm). Sr contents do not show correlation with relative Mg# among lherzolite, cpx-poor lherzolite and harzburgite. (Fig. 5.2d).

Y contents in most of xenoliths vary from 7 to 10 ppm except for harzburgite PSS 17 which reach 4.8 ppm. Cpx-poor lherzolite LS17 has the lowest Y contents (4.9 ppm). A negative correlation is observed in Y vs Mg# (Fig. 5.2e); at given Mg#, lherzolites from Panshishan have higher Y contents than those from Lianshan and Fangshan.

Considering this group of selected minor and trace element, lherzolite PSS15 have the highest Cr, Sr and Y contents and harzburgite PSS17 the highest and lowest Ni and Y contents respectively.

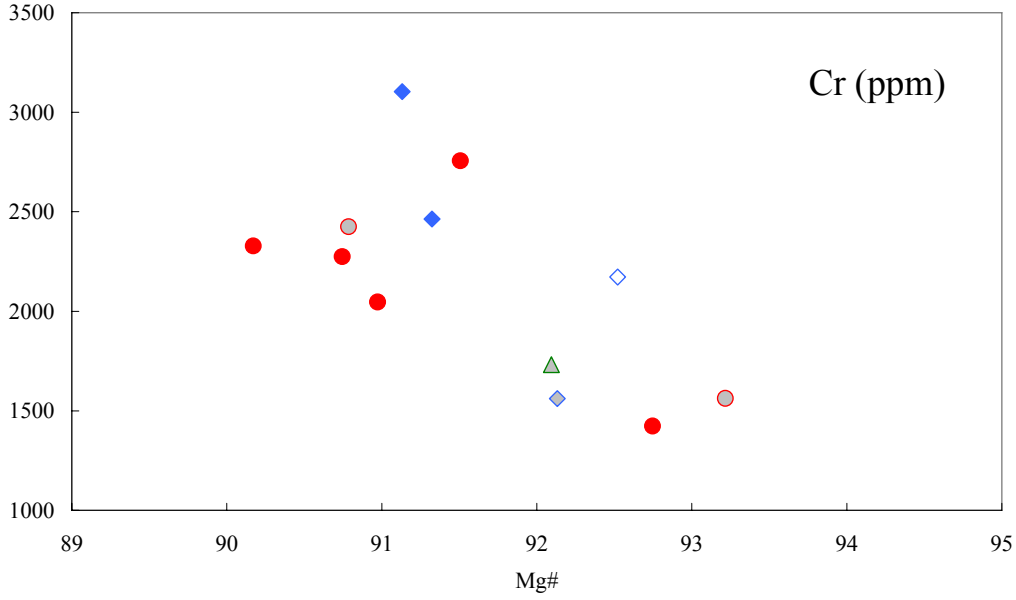

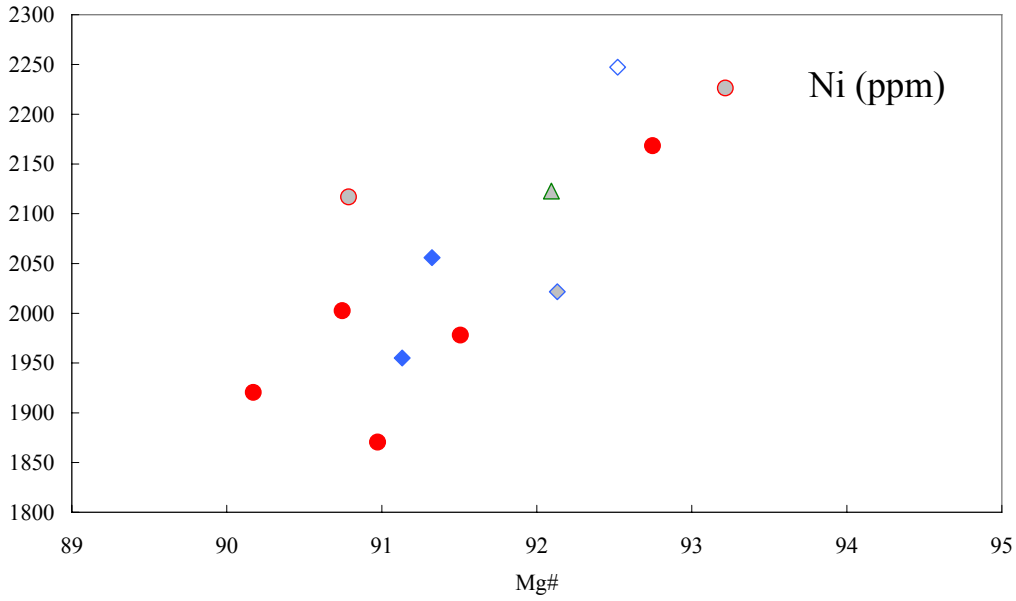
Ni (ppm)
2300
2250
2200
2150
2100
2050
2000
1950
1900
1850
1800
89
90
91
92
93
94
95
Mg#

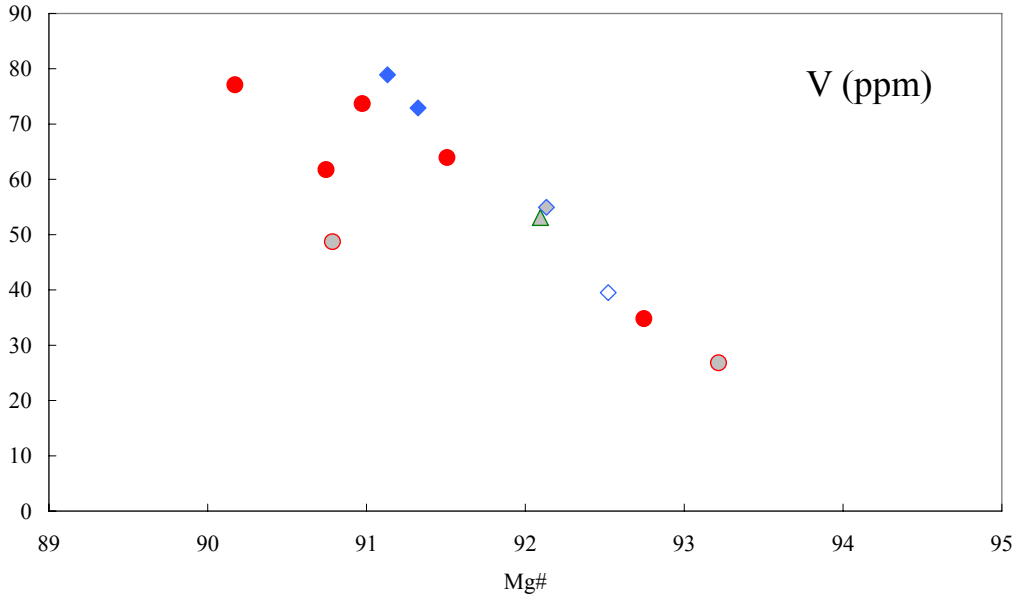
V (ppm)
90
80
70
60
50
40
30
20
10
0
89
90
91
92
93
94
95
Mg#

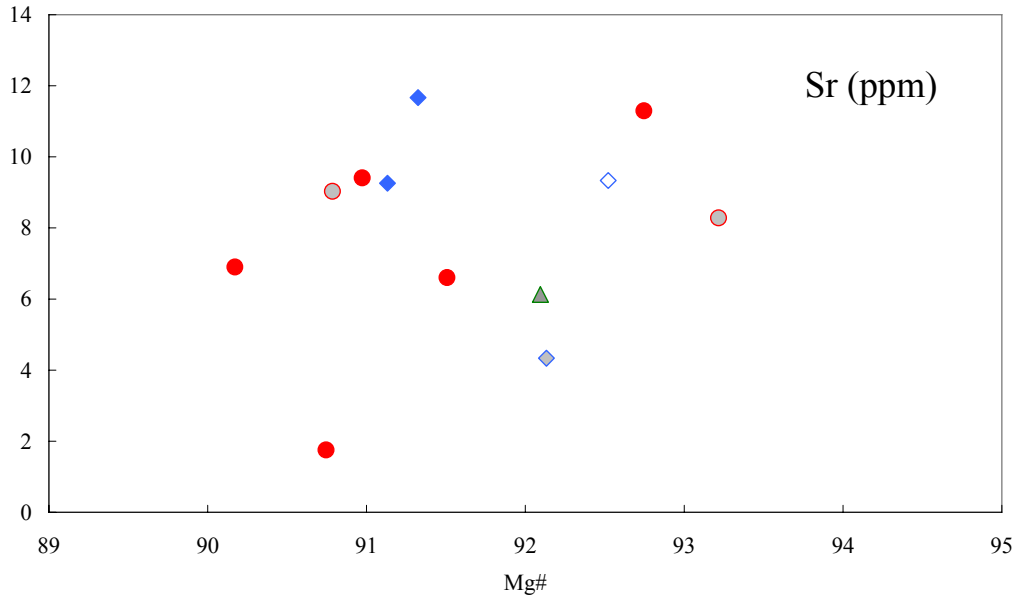


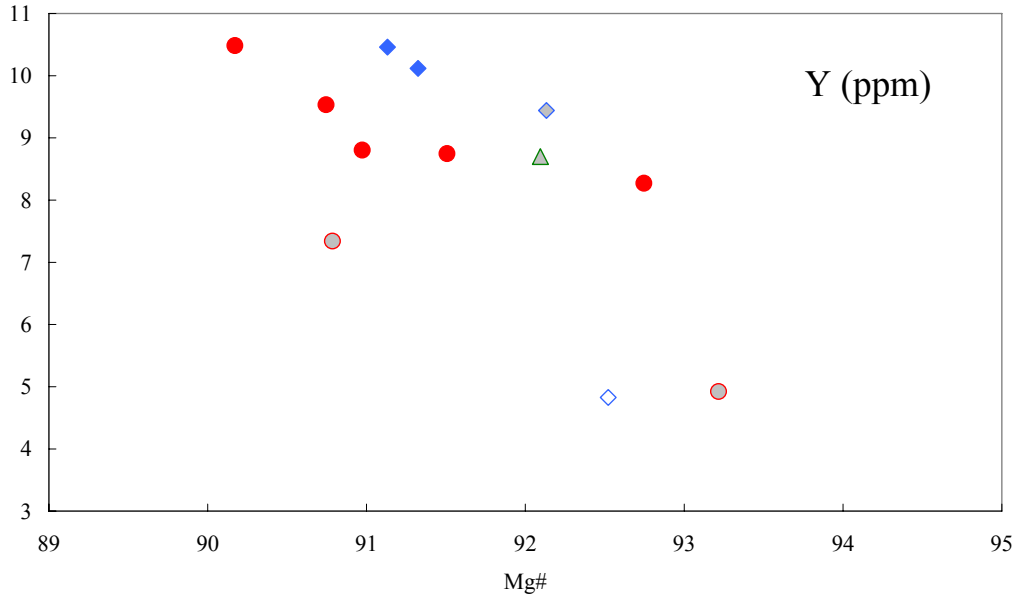


Fig. 5.2 Whole-rock trace element: Cr, Ni, V, Sr and Y (ppm) vs Mg# (symbols are as in Fig. 5.1)

## Major element melting modeling

The major element relationships identified for the Subei basin xenolith groups suggest that these elements are largely governed by stoichiometry and phase equilibrium both under subsolidus conditions and during melting (e.g. Niu, 1997). Niu (1997) model starts from an initial composition and iteratively calculates the major element compositions of successive residua applying different melting degrees. The results are represented as melting (residua) curves with the major oxides ($SiO_2$, $Al_2O_3$, TiO, $FeO_T$, CaO and $Na_2O$) plotted against MgO, as melting index. Curves for isobaric batch melting at pressure of P=2 GPa (dashed line in Fig. 5.3) and polybaric near fractional melting (1% melt porosity) at P=1.5-2.5 GPa (continuous line in Fig. 5.3) are also plotted on these diagrams. Two fertile mantle compositions were chosen as starting points: the preferred source (PS) proposed by Niu (1997) with $SiO_2$ wt%=45.5, $TiO_2$ wt%=0.18, $Al_2O_3$ wt%=4.20, FeO wt%=7.70, MgO wt%=38.33, CaO wt%=3.40 and $Na_2O$ wt%=0.30 and the primitive mantle value (PM) proposed by McDonough (1995) with $SiO_2$ wt%=45.0, $TiO_2$ wt%=0.20, $Al_2O_3$ wt%=4.45, FeO wt%=8.05, MgO wt%=37.80, CaO wt%=3.55 and $Na_2O$ wt%=0.36. As usually observed in progressive mantle depletion by extraction of basaltic components, $SiO_2$, $TiO_2$ $Al_2O_3$ and CaO wt% decrease as MgO wt% increase. (Fig. 5.3).

Peridotite samples of Panshishan, Lianshan and Fangshan are plotted in these grids and shown in Fig. 5.3. As theoretically expected, the near fractional melting are more efficient to enrich or deplete major elements at certain MgO contents, in comparison with batch melting. Cpx-poor lherzolite LS17 has MgO content of 44.1 wt%, outside the limit of the theoretical depletion curves

starting from both PS and PM sources, which implies unrealistic partial melting degrees > 25% for a lherzolite with 9% of cpx modal contents.

In Fig 5.3a, $SiO_2$ content vs MgO content. Lherzolites LS23 and PSS11 have $SiO_2$ content higher than both PS and PM starting point values and above the melting curve. Lherzolites LS20, cpx-poor lherzolite LS17 and harzburgite PSS17 have highest MgO contents, and, on the whole, all the samples do not fit any residual trends, showing higher $SiO_2$ with respect modeled MgO.

Most samples including harzburgite PSS17 overlap the $TiO_2$ theoretical partial melting curves (Fig. 5.3b), except for the Panshishan lherzolite PSS15, having $TiO_2$ value (0.18 wt %) close to PS starting point. Excluding the lherzolites LS20, cpx-poor lherzolite LS17 and harzburgite PSS17, the rest of the samples in $TiO_2$-MgO plot, indicate melting degrees from 6% to 8%.

The $Al_2O_3$ content of the xenoliths, except LS17, LS20 and PSS17, define a clear melting trend with MgO, but at higher $Al_2O_3$ values, with respect to those modeled by the Niu (1997) curves.

Peridotite melting in sp-bearing system does not impoverish FeO content even at highest melting degree (Niu, 1997; Herzberg, 2004). Most all Subei xenoliths have FeO contents less than 7 wt%, and negatively correlated with MgO; however the trend to not follow the theoretical melting curve.

Most lherzolites perfectly fit the CaO theoretical partial melting curves, except for three high MgO content samples, lherzolites LS20, cpx-poor lherzolite LS17 and harzburgite PSS17. By contrast, Fangshan cpx-poor lherzolite FS11 plots out from the theoretical trends, having high CaO, with respect the MgO contents.

The melting model suggests that $Na_2O$ rapidly decreases, even at very low degree of partial melting. In Subei xenoliths $Na_2O$ seems to be unaffected by

partial melting events, showing almost constant values (0.12 wt %) independently by MgO contents.

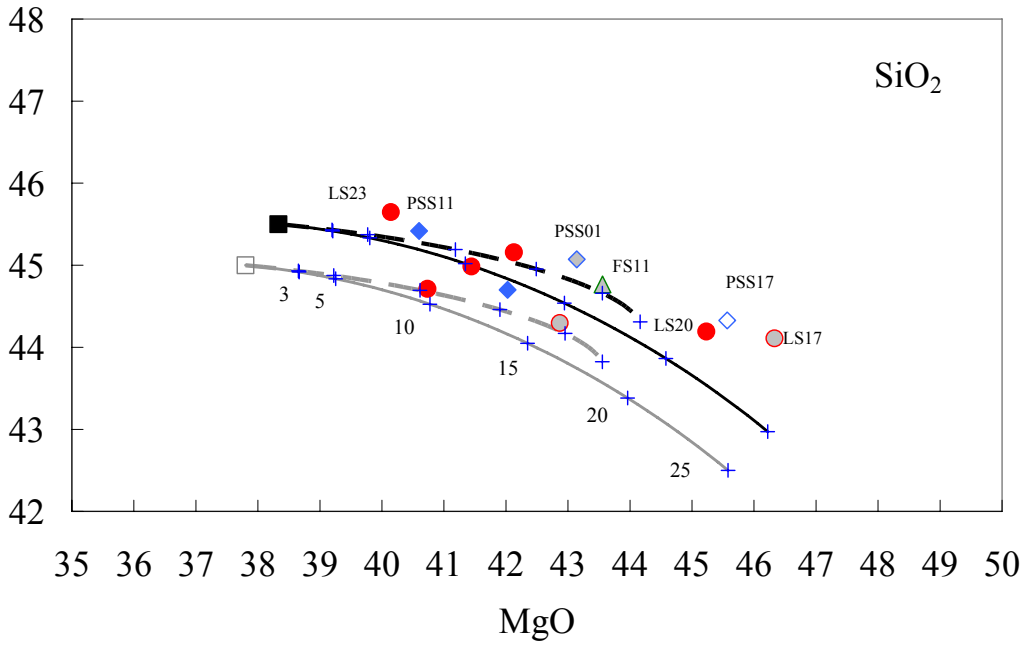


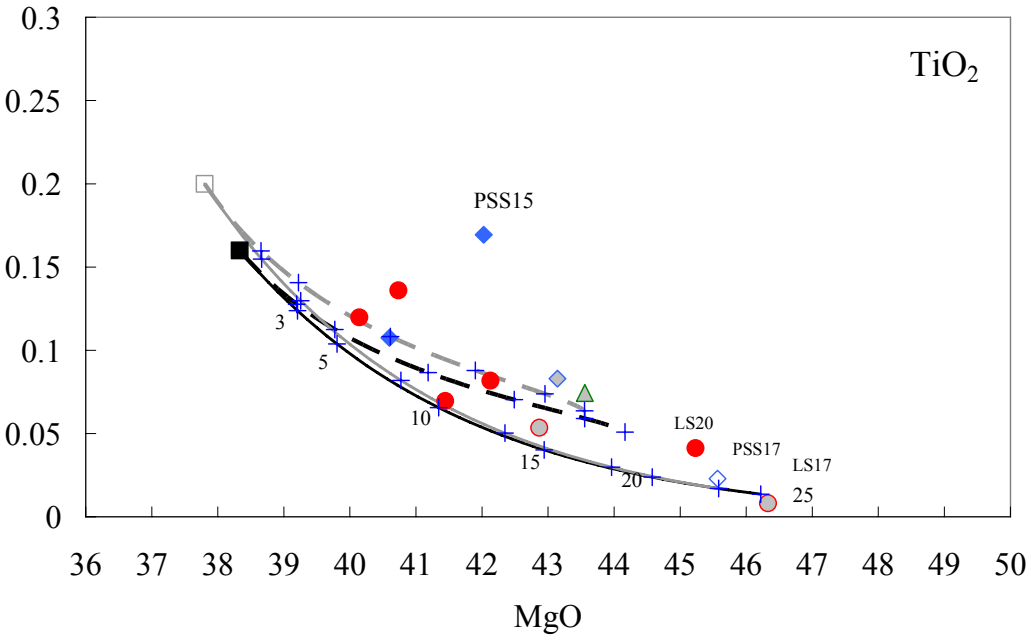

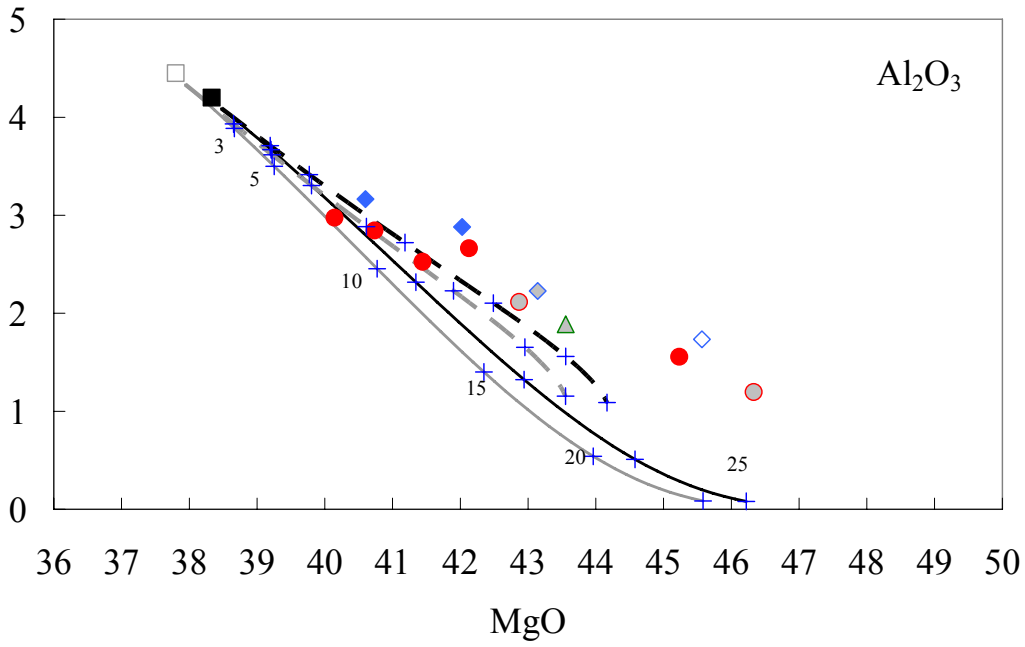
Al2O3
3
5
10
15
20
25
0
1
2
3
4
5
36 37 38 39 40 41 42 43 44 45 46 47 48 49 50
MgO

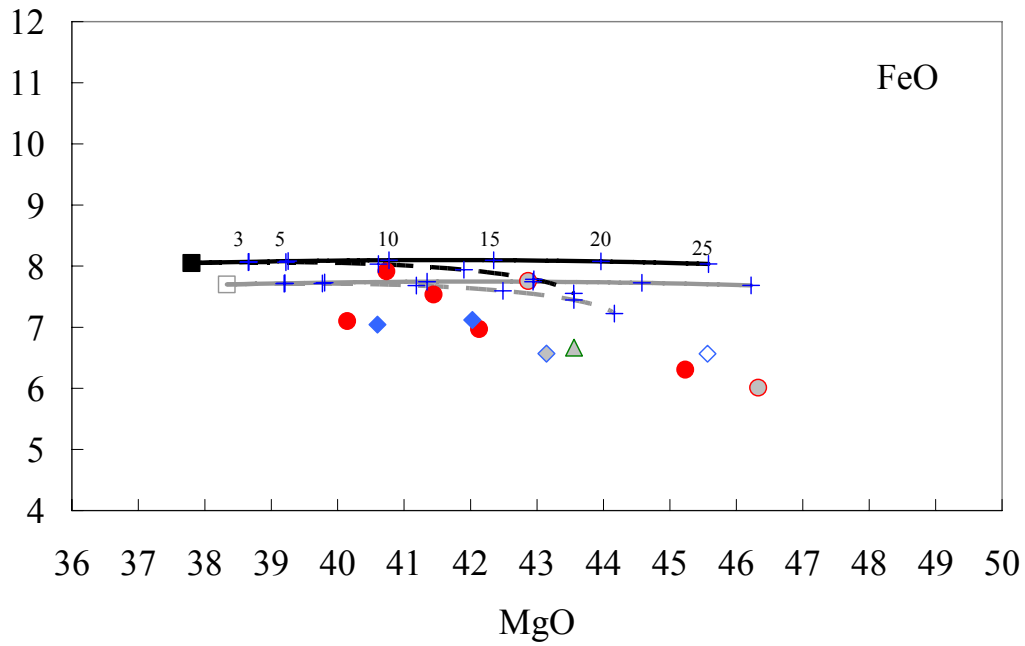
FeO
3
5
10
15
20
25
4
5
6
7
8
9
10
11
12
36 37 38 39 40 41 42 43 44 45 46 47 48 49 50
MgO

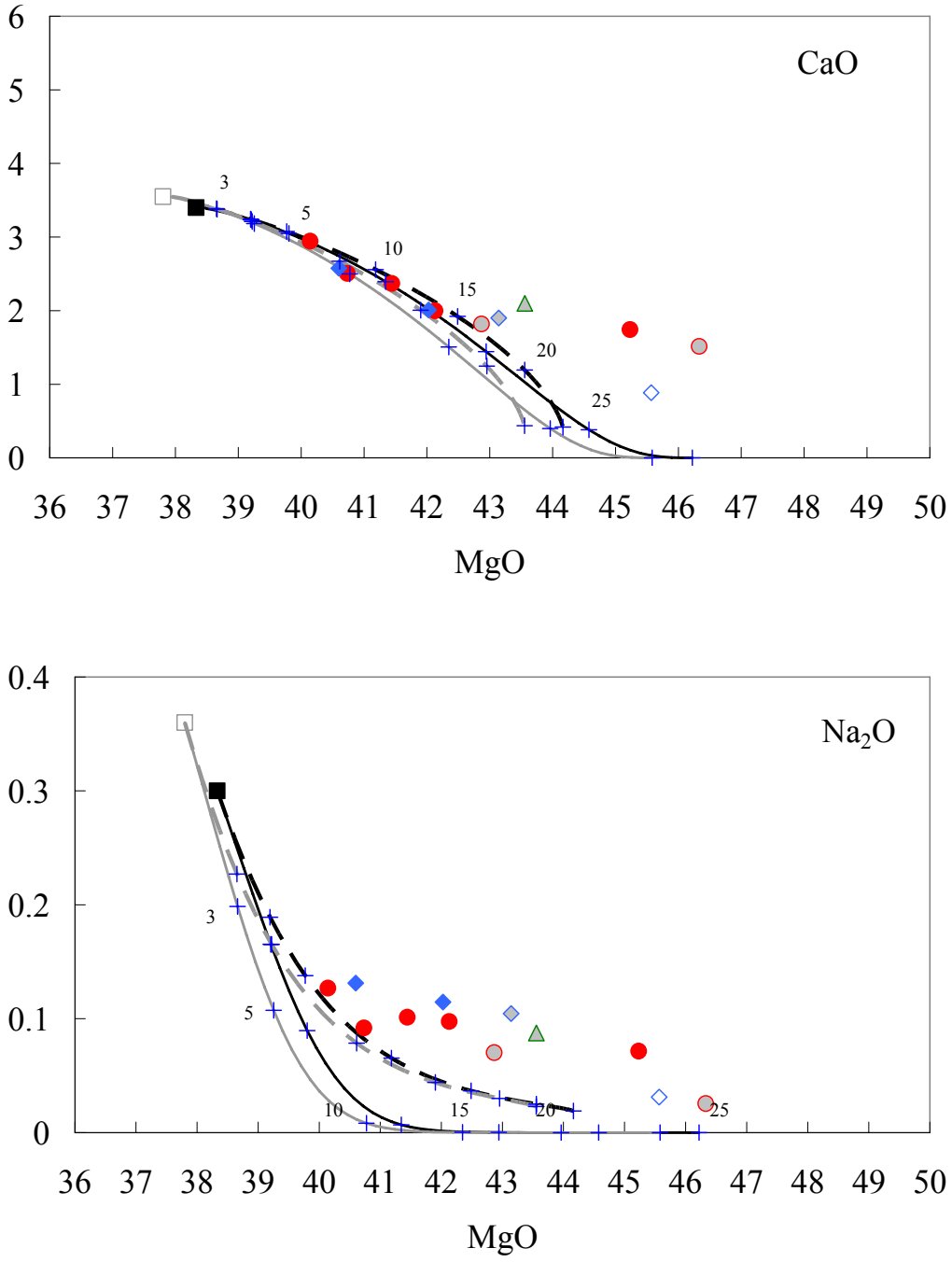


Fig. 5.3 Whole-rock major element compositions (wt %) for the eastern China xenolith suite plotted in the Niu (1997) diagram (symbols as in Fig 5.1. Dashed and continuous lines represent batch (P= 2 GPa; F < 0.25) and fractional (P =2–0.8 GPa; F < 0.25) melting models, respectively, starting from a Primitive Mantle source (large open square; McDonough and Sun, 1995) and from the 'preferred source' (PS) (large black square) proposed by Niu (1997).

As it has been previously described, not all the major elements of Subei mantle xenoliths fit well with the theoretical partial melting curves of spinel-peridotite. This may be caused by the choice of the stating point mantle composition, for example $SiO_2$ is richer than the chosen starting point and, although $Al_2O_3$ have a good negative correlation with MgO, does not fit the curves. Post-melting processes may have masqueraded the original melting trend, as it seems the case for sample PSS15 which has high $TiO_2$ content at certain MgO content.

Al and Ca element are strongly influenced by partial melting in mantle xenoliths when melt extraction occur. In CaO vs $Al_2O_3$ content diagram (Fig. 5.4, Griffin et al., 2008), a general trend from primitive mantle to a depleted cratonic peridotite xenoliths can be envisaged for the Subei basin lherzolites. The harzburgite PSS17 is little away from this trend.

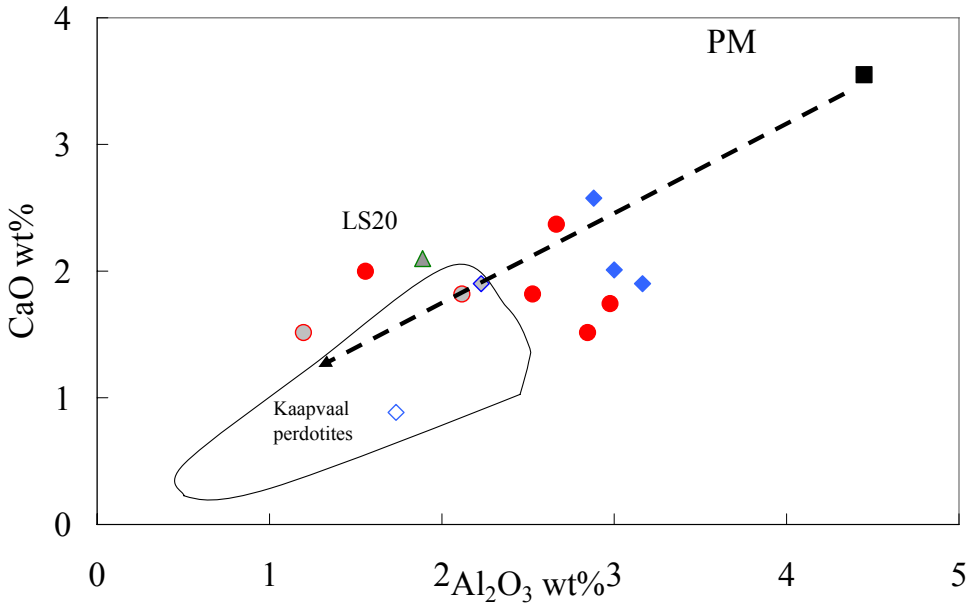


Fig. 5.4 - Whole-rock CaO vs $Al_2O_3$ (wt %) daigram. PM: primitive mantle, McDonough and Sun (1995) (symbols as in Fig 5.1)

## Major elements of minerals

Totally 52 xenoliths from Subei basin from the three localities Panshishan, Lianshan and Fangshan are chosen for major elements analysis in minerals. 14 xenoliths from Panshishan: 10 lherzolites, 3 cpx-poor lherzolites and 1 harzburgite (PSS17). 22 xenoliths from Lianshan: 12 lherzolites, 6 cpx-poor lherzolites, 1 harzburgite LS26, 2 olivine websterite LS04 and LS24 and 1(dunite LS16). 16 xenoliths from Fangshan: 11 lherzolites, 4 cpx-poor lherzolites and 1 harzburgite FS06. Most xenoliths have well equilibrated protogranular textures with large mineral grain size (see Chapter 4). Major element contents have been acquired in both core and rim of single mineral. In general all the peridotitic phases, including spinel, result very homogeneous in compositions in each sample. This allows to consider the average compositions of the mineral phases, as representative of the composition of that phase in that sample. The average data for ol, cpx, opx and sp are reported in Tables 5.2, 5.3, 5.4, and 5.5. Each single analyses for all samples can be found in appendix folder EMPA.

### Olivine

Olivine Fo [100×Mg/ (Mg+Fetotal), mol%] ranges from 89.23 to 91.83; the lowest and highest value are represented by Lianshan lherzolite LS22 and dunite LS16 respectively. Fo values for Panshishan lherzolites range from 89.45 to 90.55; Panshishan cpx-poor lherzolites range from 89.94 to 90.36. The harzburgite PSS17 has a Fo value of 90.58, higher than the Panshishan lherzolites and cpx-poor lherzolite. Fo values for lherzolites from Lianshan range from 89.23 to 90.38, Lianshan lherzolites have Fo values ranging from 90.52 to 91.76, with cpx-poor lherzolite group showing the highest values. The

harzburgite samples LS26 has Fo = value of 90.93. Olivine websterites LS04 and LS24 have Fo values (89.56 and 89.89 respectively) in the range of lherzolites. The dunite LS16 has the highest Fo value among all xenoliths (91.83). Fo value for lherzolites from Fangshan range from 89.72 to 91.09, the harzburgite sample FS16 has Fo value of 91.00. Lherzolites and cpx-poor lherzolites from Lianshan have a broad range of Fo composition than those from Panshishan and Fangshan. Lherzolites from Panshishan have Fo value limited to 90.55, while 6 of the 14 Fangshan lherzolites have Fo value higher than 90.5.

CaO content in olivines of studied samples range from 0.01 to 0.13, with the lowest and highest values represented by olivines of Panshishan lherzolite PSS19 and Fangshan lherzolite FS03. CaO content olivines in lherzolites from Panshishan range from 0.01 to 0.05 wt%; the three cpx-poor lherzolites from Panshishan have olivines with nearly the same CaO contents of about 0.03. CaO content for the harzburgite PSS17 is 0.04 wt%. CaO contents for olivines in Lianshan lherzolites and cpx-poor lherzolites have similar range from 0.02 to 0.05 wt%, the harzburgite sample LS26 has olivine CaO content 0.03 wt%. Olivine-websterites LS04 and LS24 show olivines with almost the same CaO values (0.04 wt %). CaO content for the dunite LS16 is 0.03. Among the three populations, olivines in lherzolites, cpx-poor lherzolites and harzburgites from Fangshan show the highest CaO contents (from 0.04 to 0.13 wt %)( Fig. 5.5a).
NiO contents in olivine for all xenoliths from Subei basin range from 0.21 to 0.47, which the lowest and highest values represented by the olivines of Fangshan lherzolite FS14 and Panshishan lherzolite PSS02. NiO contents for Panshishan lherzolites and cpx-poor lherzolites range from 0.21 to 0.47 wt%, and from 0.32 to 0.37 wt% respectively. NiO content for olivine in harzburgite

PSS17 is 0.43 wt%, which is higher than most of the lherzolites from Panshishan. NiO content for olivines in Lianshan lherzolites and cpx-poor lherzolites range from 0.29 to 0.38 wt% and from 0.29 to 0.42 wt% respectively. The harzburgite LS26 has NiO content of 0.34 wt%, nearly the same content recorded in the olivines of the olivine-websterites LS04 and LS24, and lower than those from most Lianshan lherzolites. NiO content of olivines in dunite LS16 is 0.36 wt%. Most Fangshan olivines in lherzolites present lower NiO contents with respect to those of Panshishan and Lianshan xenoliths, ranging from 0.20 to 0.25 wt% except olivine one FS18 which has higher content 0.36 wt%. NiO content for olivines in cpx-poor lherzolites and harzburgite FS06 ranges from 0.23 to 0.43 wt%, with the lowest value recorded for the harzburgite.

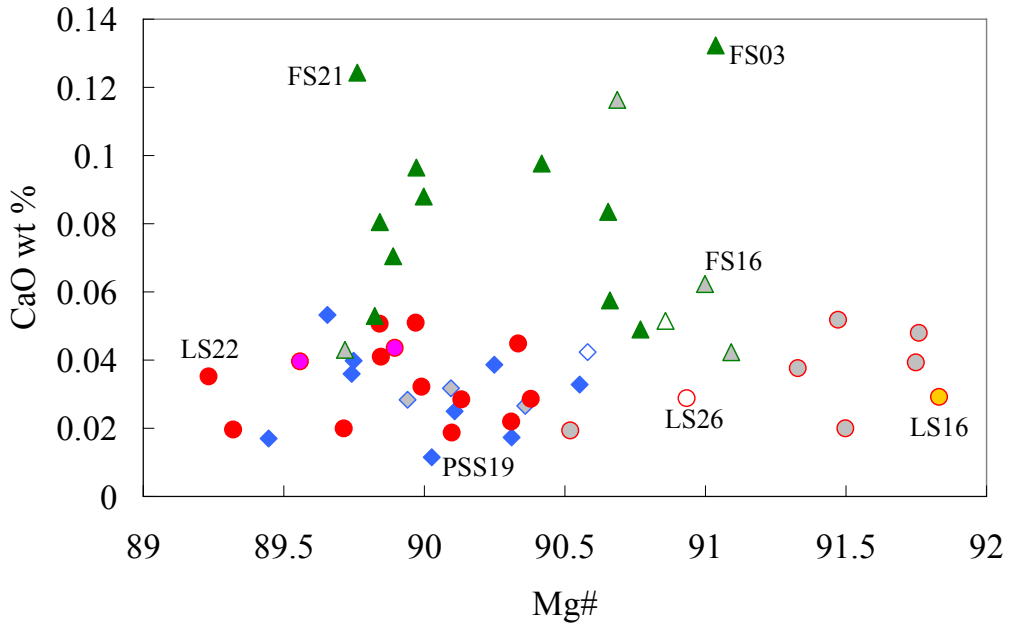

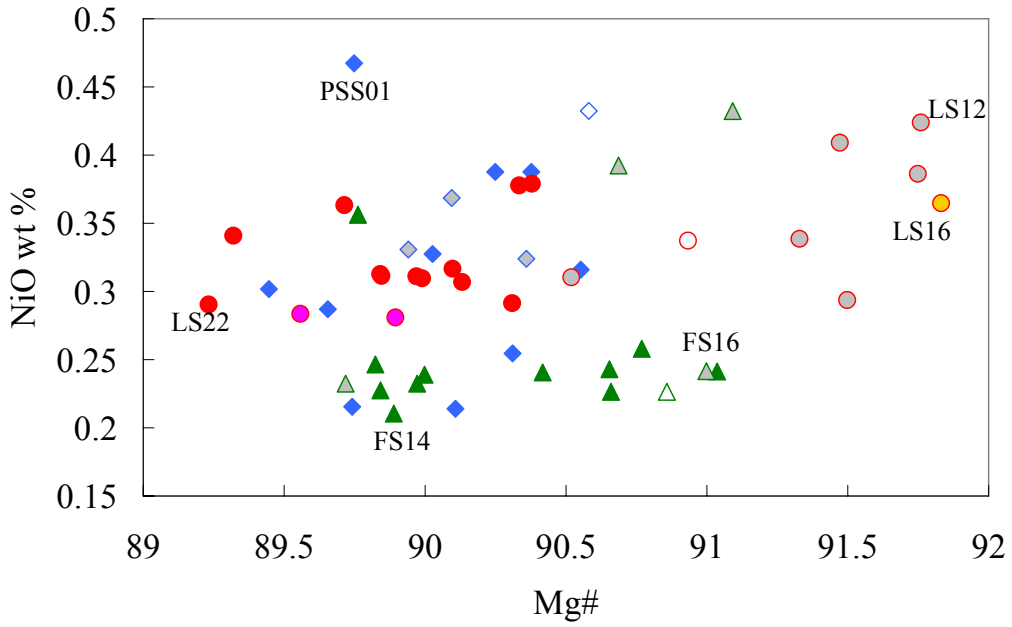


Fig. 5.5 - CaO and NiO in olivines vs Mg# Light blue diamond, Panshishan lherzolite; light blue filled grey diamond, Panshishan cpx-poor lherzolite; blue open diamond, Panshishan harzburgite; red dot, Lianshan lherzolite; red filled grey dot, Lianshan cpx-poor lherzolite; red open dot, Lianshan harzburgite; red filled pink dot, Lianshan olivine websterites; red filled golden dot, Lianshan dunite; green triangle, Fangshan lherzolite, green filled grey triangle, Fangshan cpx-poor lherzolite; green open triangle. Fangshan harzburgite)

**Spinel**

Al, Cr, Fe and Mg are the major component for spinel. Mg# [100×Mg/(Mg+$Fe_{total}$), mol%] and Cr # [100×Cr/(Cr+Al) mol%] can give us important information of the spinel evolution and, on the whole, on the nature of the mantle.

Cr# in sp for all xenoliths have large range, from the lowest value of Panshishan lherzolite PSS19 (7.95), to the highest value of Lianshan cpx-poor lherzolite LS21 (48.35). Sp Cr# values for Panshishan lherzolites range from 7.95 to 16.01; Cr# value for cpx-poor lherzolites from 12.01 to 22.45; whereas spinel in harzburgite PSS17 has the highest Cr# value than in Panshishan

lherzolites (23.78); Sp-Cr# values of Lianshan lherzolites and cpx-poor lherzolites range from 8.63 to 22.81; from Lianshan it ranges from 24.35 to 48.25. Harzburgite LS26, olivine websterites LS04 and LS24 08 and dunite LS16 have Sp-Cr# 40.71, 9.83-9.08 and 47.28 respectively. Cr# values for Fangshan lherzolites and cpx-poor lherzolites range from 9.6 to 19.58 and from 18.09 to 34.08, respectively. Harzburgite FS06 has Sp-Cr# value of 37.38. On the whole, spinels of harzburgites and most cpx-poor lherzolite have higher Cr# values compared with those of lherzolites.

Mg# values in spinels of Panshishan lherzolites range from 75.21 to 78.91, Mg# value in spinels of Panshishan cpx-poor lherzolites range from 74.64 to 77.94 whereas spinels of harzburgite PSS17 have on average Mg# value of 74.32, lower than those of Panshishan lherzolites and cpx-poor lherzolites. Sp-Mg# values for lherzolites and cpx-poor lherzolites from Lianshan range from 73.33 to 77.84 and from 65.97 to 74.24 respectively. The harzburgites LS26 has spinel with Mg# value of 66.00. The Mg# values of the olivine websterites LS04 and LS24 are 77.02 and 77.52 respectively and for the dunite LS16 Sp-Mg# is 66.96. Sp-Mg# value for Fangshan lherzolites most range from 75.94 to 78.70 except FS23 has a low value of 69.17, Sp-Mg# value for Fangshan cpx-poor lherzolites range from 73.64 to 76.42. The harzburgite FS06 has spinel at Mg# value of 69.24. Lherzolites in the three xenolith populations have always spinels with higher Mg# values with respect to the cpx-poor lherzolites and harzburgite. The sole exceptions are for the lherzolite FS23.

In Subei mantle xenoliths Sp-Cr# is positively correlated with Sp-Mg# as expected for a residual trend (Fig. 5.6). Most lherzolites and the olivine websterites have high Sp-Mg# and low Sp-Cr# values; in contrast cpx-poor

lherzolites, harzburgites and dunite have low Sp-Mg# and high Sp-Cr# values.

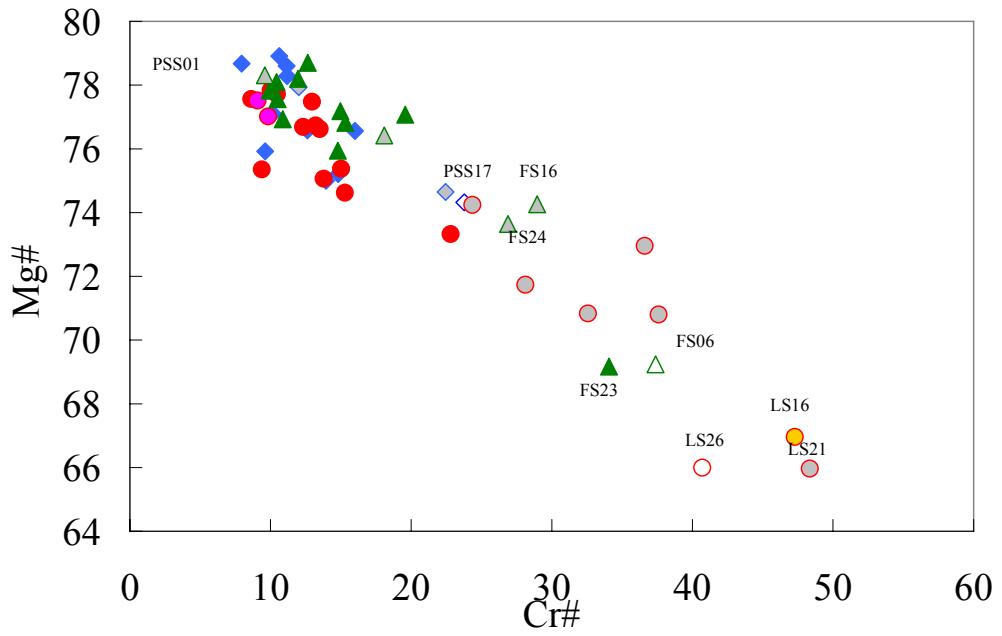


Fig. 5.6 - Diagram of Mg# vs Cr# in spinels. Symbols are as Fig. 5.5

**Orthopyroxene**

Orthopyroxenes in all xenoliths have Mg# compositions ranging from 89.73 to 92.30, which the lowest and highest value represented by Lianshan lherzolite LS31 and Lianshan dunite LS16 respectively. Mg# value for opx in Panshishan lherzolites range from 89.98 to 90.81, Mg# value for opx in Panshishan cpx-poor lherzolites range from 90.45 to 90.63, the harzburgite PSS17 has opx with Mg# value of 91.34, higher than those of the Panshishan lherzolites and cpx-poor lherzolites. Mg# value in opx from Lianshan lherzolites and cpx-poor lherzolites range from 89.73 to 90.99 and. from 90.93 to 92.05 respectively. Harzburgite LS26 has opx with Mg# value of 91.58, and for the olivine websterites LS04 and LS24 are 90.18 and 90.30. Opx of dunite LS16 shows the highest value (92.30) among the three xenolith populations. Mg# values for

lherzolites from Fangshan range from 89.90 to 91.43. Mg# value for cpx-poor lherzolite from Fangshan range from 90.52 to 92.16, the harzburgite FS06 has Mg# values of 91.64. On the whole, Lherzolites from Panshishan, Lianshan and Fangshan have Mg# values less than 91.5 and always have lower value compared with harzburgites from the same locality. Cpx-poor lherzolites from Lianshan have a higher Mg# value than lherzolites.

$SiO_2$ contents of the opx in all xenoliths range from 53.70 to 57.72 wt%, with the lowest and highest values of the Lianshan cpx-poor lherzolite LS19 and Panshishan lherzolite PSS16 respectively. $SiO_2$ contents of opx in lherzolites from Panshishan range from 54.96 to 57.72 wt%, the harzburgite PSS17 has an opx-$SiO_2$ content of 56.84 wt%. Opx-$SiO_2$ content in lherzolites and cpx-poor lherzolites from Lianshan range from 54.61 to 56.74 wt% and from 53.70 to 57.27 wt% respectively. The harzburgite LS26 have Opx-$SiO_2$ content of 56.01 wt% and for the olivine websterites LS04 and LS24 54.93 and 54.97 wt% respectively. Opx-$SiO_2$ content for the dunite LS16 is 57.13 wt%. $SiO_2$ content of opx in Fangshan lherzolites range from 53.78 to 55.72 wt%, $SiO_2$ content of opx in Fangshan cpx-poor lherzolites range from 54.93 to 56.34, wt%; the opx in harzburgite FS06 have $SiO_2$ contents of 55.93. In Fig.5.7a, the Fangshan lherzolites show relatively low Opx-$SiO_2$ contents compared with Panshishan and Lianshan lherzolites at given Mg#. Lherzolites PSS19 and PSS16 have very high Opx-$SiO_2$ contents compared with xenoliths in of Panshishan.

Orthopyroxenes, on the whole, show $TiO_2$ contents in the range of 0-0.22 wt%, with the lowest and the highest values represent by Lianshan harzburgite LS26 and Fangshan lherzolite FS18. Opx-$TiO_2$ contents for lherzolites from Panshishan range from 0.07 to 0.15 wt%, for cpx-poor lherzolites from

Panshishan range from 0.11 to 0.16 wt%. The harzburgite PSS17 has Opx-$TiO_2$ content of 0.06, lower than the lherzolites. Opx-$TiO_2$ contents for Lianshan lherzolites and cpx-poor lherzolites range from 0.05 to 0.15 wt%. and from 0.02 to 0.05 wt% respectively. Harzburgite sample and LS26 has opx with $TiO_2$ contents very low (close to EMP detection limit) and. Opx in olivine websterites LS04 and LS24 contain 0.13 and 0.10 wt% of $TiO_2$, and opx- $TiO_2$ in dunite LS16 lower content (0.07 wt%). $TiO_2$ contents in lherzolites and the four cpx-poor lherzolites from Fangshan range from 0.07 to 0.22 wt%; and from 0.01 to 0.13 wt%. Opx in harzburgite FS06 has $TiO_2$ content negligible. A negative correlation exists (Fig. 5.7b) between $TiO_2$ content and Mg# in opx for xenoliths which have having Mg# value < 91.5. By contrast, the correlation becomes positive for those samples with Opx-Mg# higher than 91.5.

$Al_2O_3$ contents of opx in all xenoliths range from 1.82 to 6.33 wt% with most samples (46 of 52) having opx with $Al_2O_3$ content less than 5 wt%. The lowest value is from by Lianshan dunite LS16 and highest value is from Fangshan lherzolite FS18. $Al_2O_3$ content in opx of lherzolites from Panshishan range from 3.65 to 4.60 wt%. $Al_2O_3$ content in opx of cpx-poor lherzolites from Panshishan range from 3.58 to 4.31 wt%, the harzburgite PSS17 has an $Al_2O_3$ content of 3.37 wt%, lower than the lherzolites and cpx-poor lherzolites. Opx- $Al_2O_3$ contents lherzolites and cpx-poor lherzolites from Lianshan range from 3.49 to 4.49 wt%; and from 1.88 to 3.37 wt% respectively, lower than the values of lherzolites. HarzburgiteLS26 have opx with $Al_2O_3$ contents of 2.29, the olivine websterites LS04 and LS24 4.50 and 4.39 wt% respectively. Opx-$Al_2O_3$ content for Fangshan lherzolites and cpx-poor lherzolites from range from 3.81 to 6.33 wt% and from 2.84 to 4.61 wt% respectively; the harzburgite FS06 has $Al_2O_3$ content of 3.11 wt%. On the whole, opx of Fangshan

lherzolites show higher $Al_2O_3$ contents, at comparable Mg# with respect to those of Panshishan and Lianshan (Fig. 5.7c).

$Cr_2O_3$ content of opx in all xenoliths range from 0.21 (Panshishan PSS18 lherzolite) to 0.82 (Fangshan FS23 lherzolite) wt%, Opx- $Cr_2O_3$ content for Panshishan lherzolites range from 0.21 to 0.37 wt%, $Cr_2O_3$ content for Panshishan cpx-poor lherzolites range from 0.30 to 0.39 wt% the harzburgite PSS17 has a $Cr_2O_3$ content of 0.45 wt%, higher than opx of Panshishan lherzolites and cpx-poor lherzolites. Opx $Cr_2O_3$ content for Lianshan lherzolites range from 0.21 to 0.51 wt% and for Lianshan cpx-poor lherzolites range from 0.24 to 0.54 wt%. LS26 harzburgite has opx $Cr_2O_3$ content 0.47 wt% whereas, for the olivine websterites LS04 and LS24 are 0.30 and 0.26 wt% respectively. Opx in dunite LS16 has on average $Cr_2O_3$ 0.44 wt% $Cr_2O_3$ contents. Opx- $Cr_2O_3$ contents in Fangshan lherzolites range from 0.37 to 0.82 wt%, whereas in cpx-poor lherzolites range from 0.30 to 0.63 wt%, the harzburgite FS06 has opx with 0.67 wt% $Cr_2O_3$ content. As shown in Fig. 5.7d, opx of Panshishan lherzolites and cpx-poor lherzolites have a narrow range of $Cr_2O_3$ contents, whereas lherzolites and cpx-poor lherzolites from Lianshan and Fangshan are much scatter.(Fig. 5.7d).

Expect opx in PSS18 (where $Na_2O$ content is not detected by the instrument), the rest of xenoliths have opx with $Na_2O$ contents range from 0.01 to 0.19 wt%; the lowest and highest values in Fangshan cpx-poor lherzolite FS24 and lherzolite FS18 respectively. $Na_2O$ content of opx in Panshishan lherzolites range from 0.07 to 0.11 wt%; $Na_2O$ content of opx in Panshishan cpx-poor lherzolites range from 0.03 to 0.11 wt%; the harzburgite PSS17 has opx with 0.03 wt% $Na_2O$ content, lower than those of lherzolites and cpx-poor lherzolites. $Na_2O$ contents of opx from Lianshan lherzolites range from 0.03 to

0.13 wt%. $Na_2O$ contents of opx from Lianshan lherzolites range from 0.04 to 0.07wt% The harzburgite LS26 has opx with $Na_2O$ content 0.01 wt%. The olivine websterites LS04 and LS24 contain opx with 0.11 and 0.09 wt% of $Na_2O$ contents, and is 0.08 wt% for the dunite LS16. $Na_2O$ contents in opx from Fangshan lherzolites range from 0.08 to 0.19 wt%; $Na_2O$ contents in opx from Fangshan lherzolites range from 0.01 to 0.11 wt%; opx in harzburgite FS06 has $Na_2O$ content of 0.08 wt %.( Fig. 5.7e)

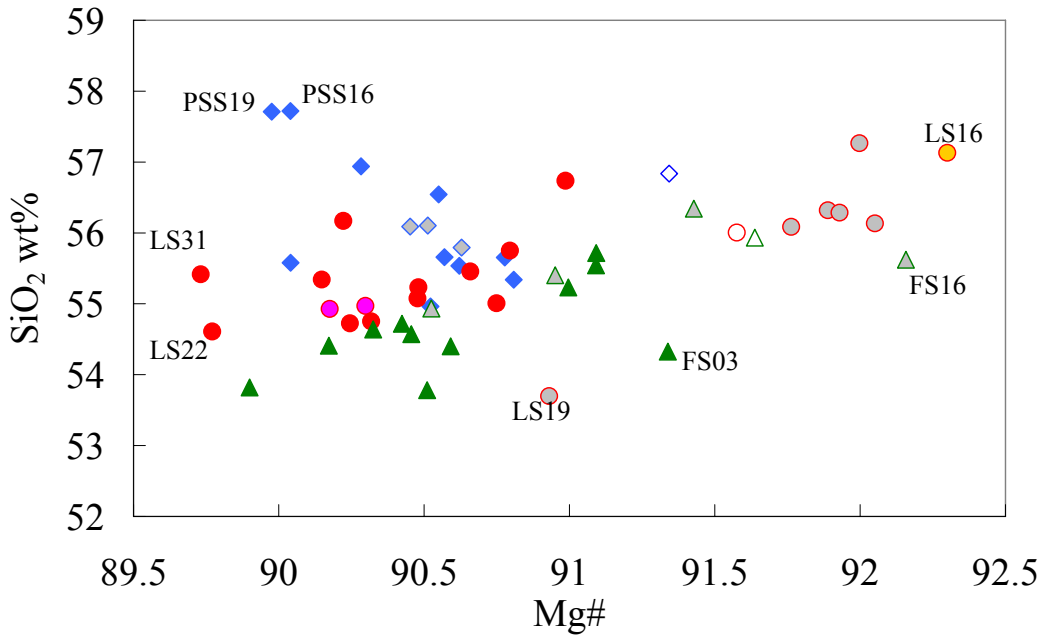

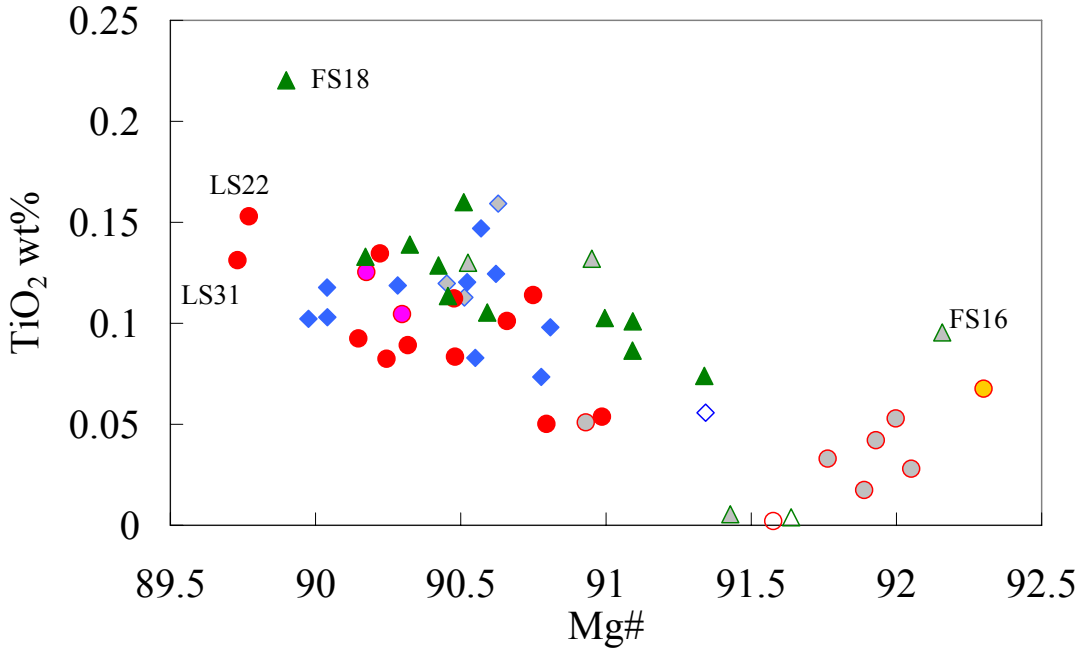
0.25
0.2
0.15
0.1
0.05
0
TiO2 wt%
FS18
LS22
LS31
FS16
89.5
90
90.5
91
91.5
92
92.5
Mg#

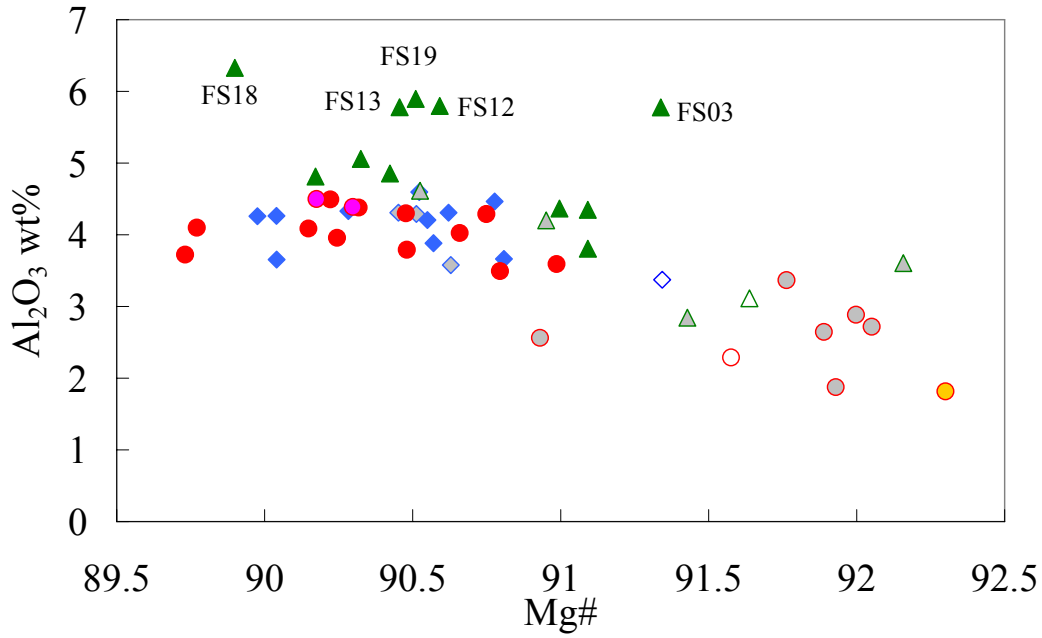
7
6
5
4
3
2
1
0
Al2O3 wt%
FS19
FS18
FS13
FS12
FS03
89.5
90
90.5
91
91.5
92
92.5
Mg#

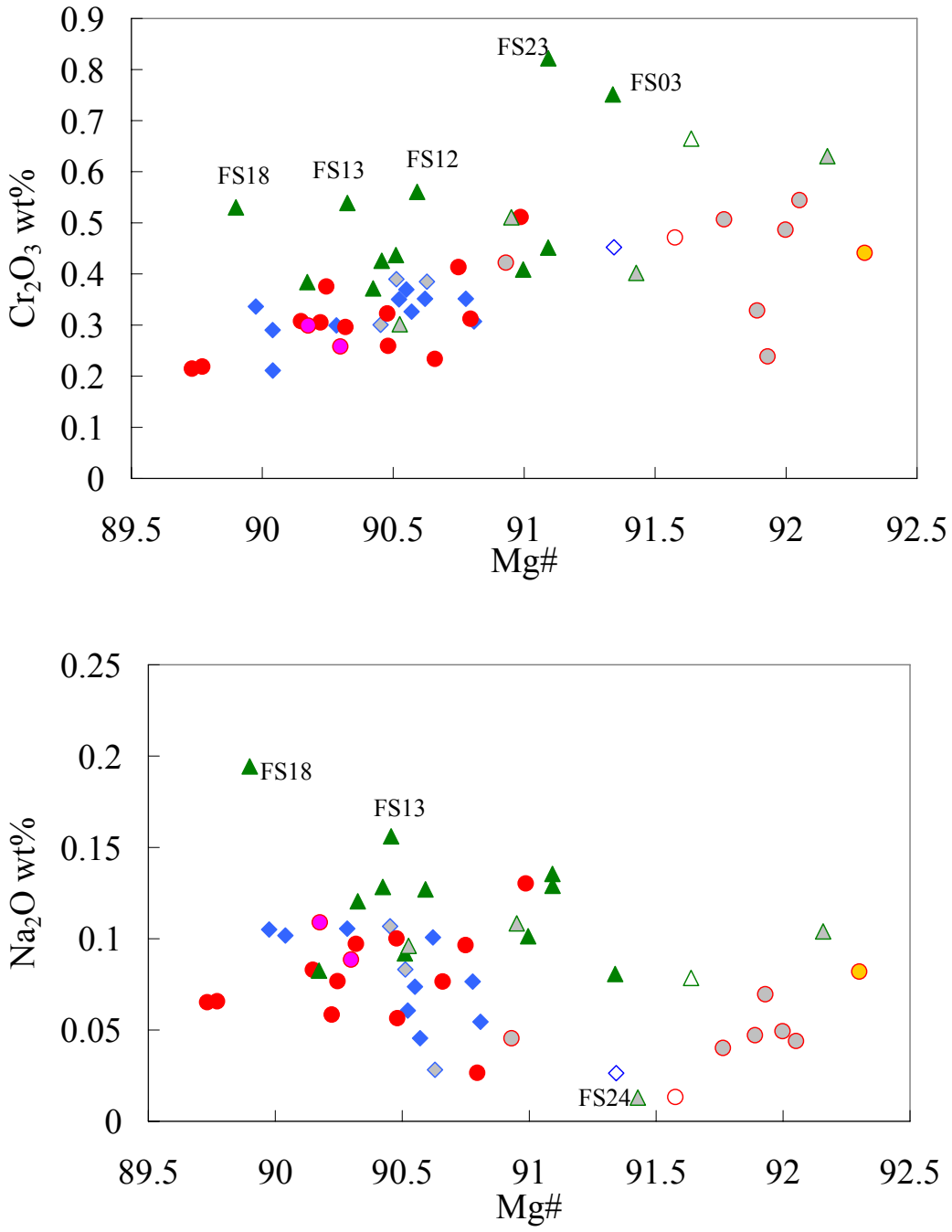


Fig. 5.7 - $SiO_2$, $TiO_2$, $Al_2O_3$, $Cr_2O_3$, and $Na_2O$ in orthopyroxene vs Mg# diagrams. Symbols are as Fig. 5.5

**Clinopyroxene**

Cpx-Mg# compositions in all xenoliths range from 88.64 to 93.81, with the lowest and the highest values from Fangshan lherzolite FS19 and Lianshan dunite LS16. Cpx-Mg# values for Panshishan lherzolites and cpx-poor lherzolites range from 89.17 to 92.46, and from 91.32 to 92.49 respectively; the harzburgite PSS17 has opx-Mg# value of 92.84. Opx-Mg# of cpx in Lianshan lherzolites and cpx-poor lherzolites range from 90.50 to 92.62. and from 92.72 to 93.46 respectively; on the whole higher than those recorded in Lianshan lherzolites. The harzburgite LS26 has cpx with Mg# value of 93.72. Mg# values in the olivine websterites LS04 and LS24 are 90.04 and 90.50 respectively. Cpx Mg# values of Fangshan lherzolites and cpx-poor lherzolites range from 88.64 to 91.40, and from 90.89 to 93.76 respectively; the harzburgites FS06 has cpx with Mg# value of 92.00. Fangshan lherzolites have cpx with Mg# value less than 91.5, and have lower values compared with the opx of the cpx-poor lherzolites and the harzburgite. Cpx of Panshishan lherzolites have a narrow range of Mg# compared with Lianshan lherzolites. The dunite shows cpx which records the highest Mg# values whereas those in olivine websterites record the lowest Mg# value.

Cpx-$TiO_2$ contents in all xenoliths range from 0.01 to 0.72 wt%, with the lowest and highest values in Lianshan harzburgite LS26 and Lianshan lherzolite LS22 respectively. Cpx-$TiO_2$ contents in Panshishan lherzolites range from 0.28 to 0.62 wt%, Cpx $TiO_2$ contents in Panshishan cpx-poor lherzolites range from 0.53 to 0.65 wt%, the harzburgite PSS17 shows cpx with $TiO_2$ contents of 0.21 wt%, lower than those in lherzolites and cpx-poor lherzolites. Cpx of Lianshan lherzolites have large range of $TiO_2$ contents (0.19 to 0.72 wt %), Cpx $TiO_2$ contents in Lianshan cpx-poor lherzolites range from

0.03 to 0.22 wt%. The harzburgite LS26 have cpx with TiO2 content of 0.01 wt%, and for the olivine websteritesLS04 and LS24 is near a same (0.63 wt %). $TiO_2$ content in cpx of the dunite LS16 is 0.25 wt%. $TiO_2$ contents of cpx in Fangshan lherzolites and cpx-poor lherzolites from range from 0.15 to 0.52 wt% and; from 0.03 to 0.56 wt% respectively; the harzburgite FS06 has cpx $TiO_2$ content of 0.03 wt%. A negative correlation can be observed between TiO2 and Mg# in cpx of Lianshan xenoliths (Fig. 5.8a); this correlation is not clear for Panshishan and Fangshan samples.

Cpx $Al_2O_3$ contents in all xenoliths range from 2.11 to 7.94 wt%. The lowest value is representing by Lianshan harzburgite LS26 and highest value is represent by Fangshan lherzolite FS18. $Al_2O_3$ content for cpx in Panshishan lherzolites and cpx-poor lherzolites from range from 4.91 to 7.48 wt%, and from 4.55 to 6.53 wt% respectively. Cpx in the harzburgite PSS17 has an $Al_2O_3$ content of 4.23 wt%, lower than those the lherzolites and cpx-poor lherzolites. Cpx Al2O3 contents for lherzolites from Lianshan range from 4.99 to 7.05 wt%. Cpx $Al_2O_3$ contents for cpx-poor lherzolites from Lianshan range from 2.99 to 4.36 wt%. The harzburgite LS26 has $Al_2O_3$ content of 2.01 wt%, cpx in the olivine websterites LS04 and LS24 7.01 wt% and 6.79 wt%. $Al_2O_3$ content in cpx of Fangshan lherzolites range from 5.39 to 7.94 wt%; $Al_2O_3$ content in cpx of Fangshan cpx-poor lherzolites range from 2.50 to 6.88 wt%; the harzburgite FS06 has cpx containing $Al_2O_3$ 4.18. In the Fig, 5.8b, except for three lherzolites from Panshishan (PSS02, PSS12 and PSS19) and one from Fangshan (FS23), the other xenoliths show cpx with a good correlation between $Al_2O_3$ and Mg#. FS24 has very low $Al_2O_3$ content compare to other Fangshan xenoliths.

Cpx $Cr_2O_3$ content in all xenoliths range from 0.41 to 1.60 wt%, the lowest and highest values in Panshishan lherzolite PSS18 and Fangshan lherzolite FS23 cpx. $Cr_2O_3$ contents of cpx from Panshishan lherzolites and cpx-poor lherzolites range from 0.41 to 0.91 and from 0.85 to 0.89 respectively, the harzburgite PSS17 has a $Cr_2O_3$ content of 1.05, higher than the Panshishan lherzolites and cpx-poor lherzolites. $Cr_2O_3$ contents for lherzolites from Lianshan range from 0.59 to 1.28. $Cr_2O_3$ contents for lherzolites from Lianshan range from 0.54 to 1.29. The harzburgite LS26 has $Cr_2O_3$ content of 0.63 wt%, for the olivine websterites LS04 and LS24 are 0.76 and 0.50 respectively. $Cr_2O_3$ content for the dunite LS16 is 1.48, the highest value among Lianshan xenoliths. $Cr_2O_33$ content for lherzolites from Fangshan range from 0.75 to 1.60, $Cr_2O_3$ content for lherzolites from Fangshan range from 0.60 to 1.28, the harzburgite sample FS06 has $Cr_2O_3$ content of 1.38. No correlation is observed between $Cr_2O_3$ content and Mg# value (Fig. 5.8c).

Cpx CaO content in all xenoliths range from 17.63 to 24.12 wt%, whit the lowest value in Fangshan lherzolite FS18 and the highest value in cpx-poor lherzolite FS24. Cpx-CaO contents in Panshishan lherzolites and cpx-poor lherzolites range from 19.59 to 22.45 wt%. and from 20.37 to 22.63 wt%. respectively. The harzburgite PSS17 has a cpx-CaO content of 22.30 wt%. CaO contents for lherzolites from Lianshan range from 20.22 to 22.32 wt%., whereas in cpx-poor lherzolites range from 20.89 to 22.42 wt%. The harzburgite LS26 has cpx-CaO content of 23.85 wt%, and the olivine websterites LS04 and LS24 have 20.03 and 20.41 wt%. and the dunite LS16 has 21.08 wt%. CaO contents in cpx of Fangshan lherzolites and cpx-poor lherzolites range from 17.63 to 20.14 wt% and from 20.16 to 24.12 wt%. The harzburgite FS06 has cpx-CaO content of 20.53 wt%. A good correlation

between CaO content and Mg# value is shown in Fig. 5.8d. Fangshan lherzolites show lower cpx-CaO content and Mg# values compared to lherzolites from the other two localities.

Cpx $Na_2O$ contents in all xenoliths range from 0.16 to 2.19 wt%: which the lowest and highest value are represent by Lianshan harzburgite LS26 and Panshishan lherzolite PSS19 respectively. Cpx-$Na_2O$ contents for from Panshishan lherzolites and Cpx $Na_2O$ content for cpx-poor lherzolites range from 0.89 to 2.19 wt%, and from 1.07 to 1.57 wt% respectively; the harzburgite PSS17 has cpx-$Na_2O$ content in cpx of 0.85 wt%, lower than lherzolites and cpx-poor lherzolites of Panshishan. $Na_2O$ contents in cpx for from Lianshan lherzolites and from cpx-poor lherzolites are in the range of 1.16 -1.96 wt% and 0.94 to 1.65 wt% respectively. The harzburgite sample LS26 has $Na_2O$ contents in cpx of 0.16 wt%, and for the olivine websterites LS04 and LS24 are 1.76 and 1.65 wt%. $Na_2O$ contents in cpx of dunite LS16 is 1.93 wt%. $Na_2O$ contents in cpx for lherzolites from Fangshan are in the range of from 0.80-1.92 wt%., for lherzolites are 0.26 to 1.62 wt% and in the harzburgite FS06 are 0.99 wt %.( Fig. 5.8e).

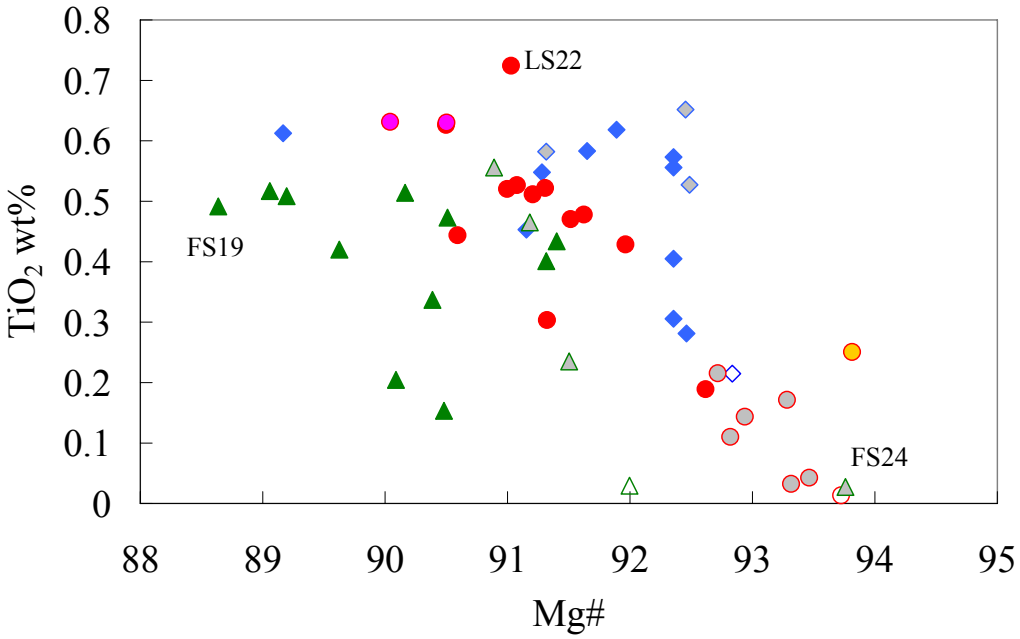
0.8
0.7
0.6
0.5
0.4
0.3
0.2
0.1
0
TiO2 wt%
LS22
FS19
FS24
88
89
90
91
92
93
94
95
Mg#

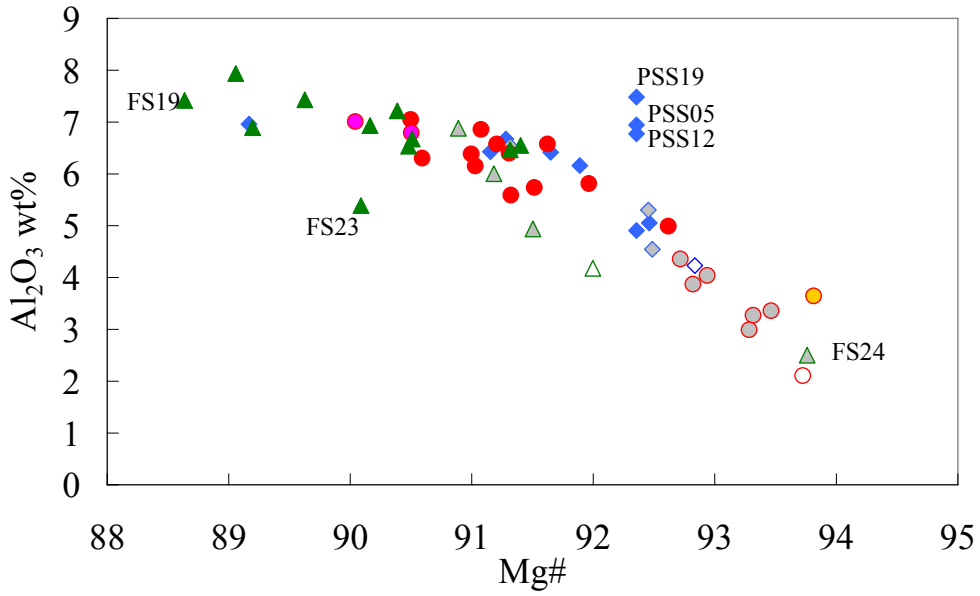
9
8
7
6
5
4
3
2
1
0
Al2O3 wt%
FS19
PSS19
PSS05
PSS12
FS23
FS24
88
89
90
91
92
93
94
95
Mg#

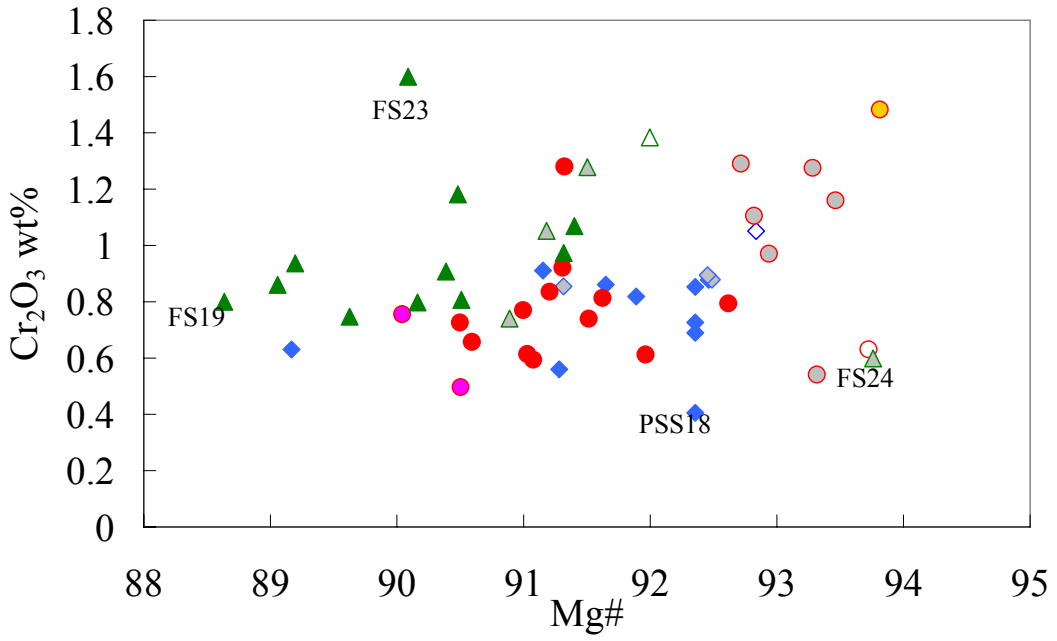
1.8
1.6
1.4
1.2
1
0.8
0.6
0.4
0.2
0
Cr2O3 wt%
FS23
FS19
FS24
PSS18
88
89
90
91
92
93
94
95
Mg#

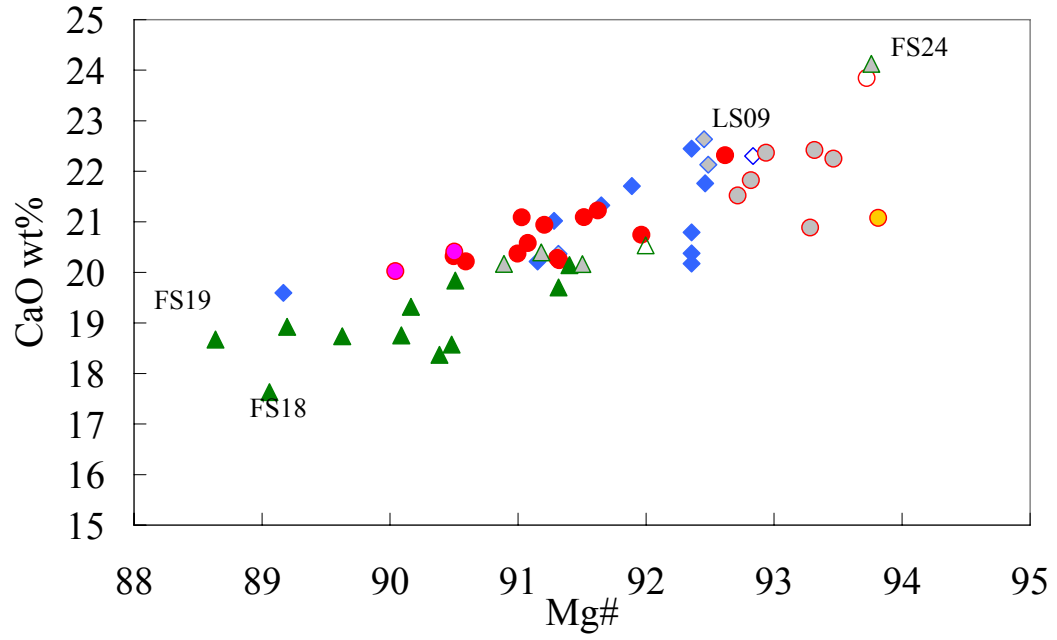
25
24
23
22
21
20
19
18
17
16
15
CaO wt%
FS24
LS09
FS19
FS18
88
89
90
91
92
93
94
95
Mg#

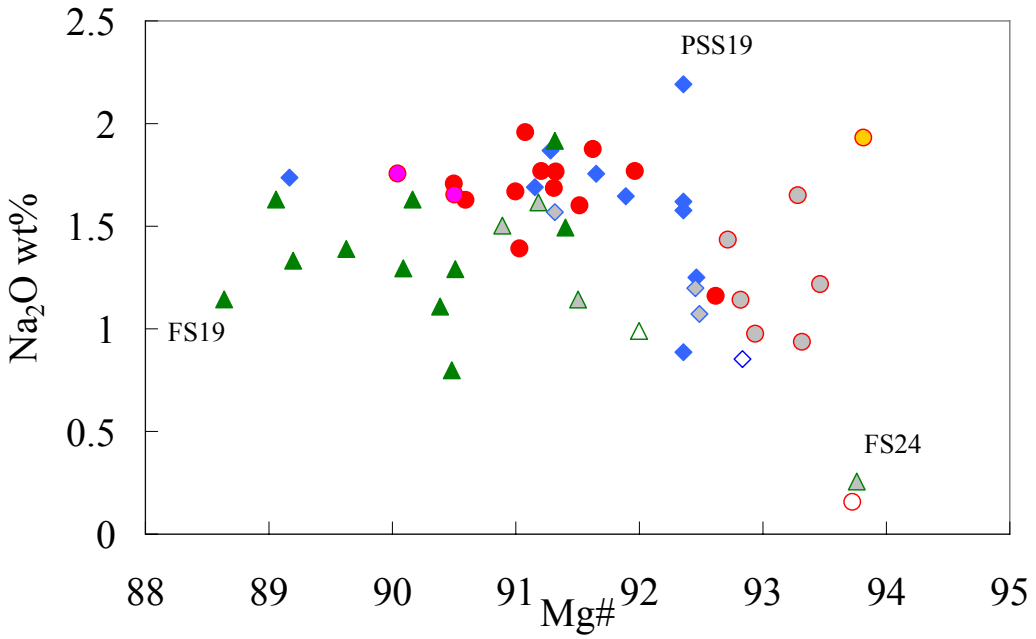


Fig. 5.8 - $TiO_2$, $Al_2O_3$, $Cr_2O_3$, CaO and $Na_2O$ in clinopyroxene vs Mg# diagrams. Symbols are as Fig. 5.5 Light blue diamond, Panshishan lherzolite; light blue filled grey diamond, Panshishan cpx-poor lherzolite; blue open diamond, Panshishan harzburgite; red dot, Lianshan lherzolite; red filled grey dot, Lianshan cpx-poor lherzolite; red open dot, Lianshan harzburgite; red filled pink dot, Lianshan olivine websterites; red filled golden dot, Lianshan dunite; green triangle, Fangshan lherzolite, green filled grey triangle, Fangshan cpx-poor lherzolite; green open triangle. Fangshan harzburgite

**Trace elements**

Cpx is the most important phase that controls the incompatible trace element whole rock budget in anydhrous spinel peridotite. Trace element compositions of cpx and one opx are carried out by LA-ICP-MS. Totally 47 samples from Subei basin for cpx are chosen for trace elements analysis. 12 xenoliths from Panshishan: 9 lherzolites, 2 cpx-poor lherzolite and 1 harzburgite PSS17. 22 xenoliths from Lianshan: 12 lherzolites, 6 cpx-poor lherzolites, 1 harzburgite LS26, 2 olivine websterites LS04 and LS24 and 1 dunite LS16. 13 xenoliths from Fangshan: 8 lherzolites, 4 cpx-poor lherzolites and 1 harzburgite FS06. Some opx from FS16 are also measured. Differences between individual analyses of the same minerals were all within analytical precision, except for high variable element such as Pb, Zr, Nb, Hf. Average trace element abundances of Panshishan, Lianshan and Fangshan mantle xenolith minerals are thus reported in Table 5.7. A C1 chondrite values (Sun and McDonough, 1989) are used to normalization for the REE (Rear Earth Element), and primitive mantle values (McDonough and Sun 1995) are used to normalization for trace elements (Fig. 5.9, 5.10, 5.11).

All the xenoliths from Subei basin have cpx with very variable trace elements contents (La from 0.1 to 80 X C1 chondrite and Yb from 2.3 to 12 X C1 chondrite). Based on the REE pattern (LREE, Light Rare Earth Element; MREE, Middle Rare Earth Element; HREE Heavy Rare Earth Element) and $(La/Sm)_N$ (N indicate C1 Chondrite normalization) and $(Sm/Yb)_N$, the cpx are subdivided into five different groups.

**Group I,** with LREE-depleted pattern;

**Group II**, with upward convex pattern;

**Group III**, with flat REE pattern;

**Group IV,** with LREE-enriched pattern;

**Group V,** with spoon-shaped pattern.

**Panshishan**

**Group I - LREE-depleted pattern**

Among the Panshishan cpx, those of lherzolites PSS01, PSS07, SS12, PSS13 and PSS19 are included in this group (Fig. 5.9). Panshishan cpx of this group, are characterized by strong depleted LREE (compared with MREE and HREE) pattern, accompanying with high Mg#, $Al_2O_3$ contents, and low $Cr_2O_3$ contents. The $(La/Sm)_N$ ratios are low, ranging from 0.13 to 0.88. MREE and HREE were distributed in a near flat pattern with $(Sm/Yb)_N$ from 0.63 to 1.03 (Fig. 5.11), associated with a weak Zr ($Zr^*=Zr_N/((Nd+Sm)_N/2)$), 0.61 to 0.93) and strong Ti ($Ti^*=Ti_N/((Eu+Gd)_N)/2$) 0.38 to 0.61) negative anomalies (Fig. 5.11). Cpx of lherzolite PSS19 has a strong Eu positive anomaly (Eu*=Eu/(Sm+Gd)/2=1.61) associated with remarkable Sr positive anomaly. Strong Zr (and Hf) negative anomaly also occurs (Zr*=0.29) and weak Nd and Ti anomalies are also observed.

**Group II - Upward convex pattern**

Lherzolites PSS05, PSS11, PSS15 and ol-websterite PSS16 cpx are referred to this group. Group II Panshishan cpx are characterized by a flat distribution of Tm, Yb, Lu (HREE), MREE convex upward and slightly LREE distributions (Fig. 5.9). Most samples of this group have $(La/Sm)_N$ less than 0.9 and $(Sm/Yb)_N$ 1.05 - 1.35, except PSS05 which has the convex upward profile

smother than the other PSS Group II cpx. In this group strong Nb, Ti and weak Zr (and Hf) negative anomalies are also observed. Sample PSS05 shows strong Th and U and Th enrichments (10 times PM).

**Group III - Flat REE pattern**

Among Panshishan samples just the harzburgite PSS17 cpx are referring to this group. They are characterized by low REE contents (about 5 X C1 values, HREE compatible with residual cpx expected to find in a harzburgite), a flat distribution in REE pattern with $(La/Sm)_N$ and $(Sm/Yb)_N$ near 1. PSS17 show a weak Zr (and Hf) and Ti negative anomalies.

**Group IV - LREE-enriched pattern**

Lherzolite PSS02 is the only sample of the Panshishan xenoliths suite having LREE enriched cpx (Fig. 5.9). They are characterized by LREE strong enrichment; but also MREE and HREE reflect a slight enrichment (Fig. 5.11). The lherzolite PSS02 shows $(La/Sm)_N$ and $(Sm/Yb)_N$ 3.31 and 1.34 respectively. PSS02 cpx has remarkable Ti (Ti* = 0.30) and less pronounced Zr (and Hf) negative anomalies, as well as strong Th and U enrichments (10 X PM) (Fig. 5.9).

**Group V - Spoon-shaped pattern**

Lherzolite PSS10 cpx are referred to this group. They are characterized by a LREE spoon-shaped pattern. La and Ce are enriched, whereas other LREE depleted. Cpx PSS10 have $(La/Sm)_N$ and $(Sm/Yb)_N$ 1.27 and 3.35 respectively. Zr and Ti negative anomalies are also observed.

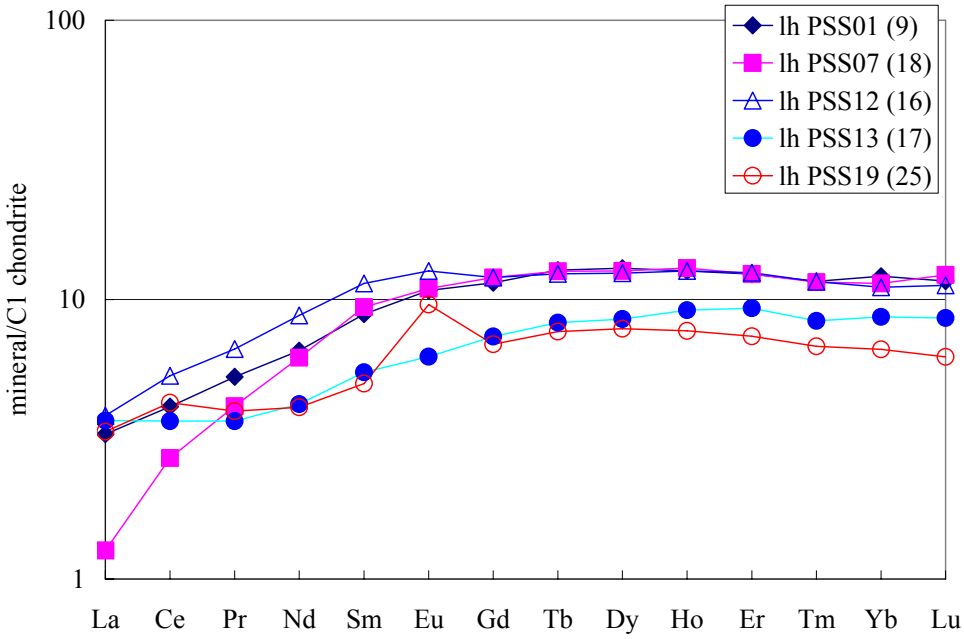
100
10
1
mineral/C1 chondrite
lh PSS01 (9)
lh PSS07 (18)
lh PSS12 (16)
lh PSS13 (17)
lh PSS19 (25)
La Ce Pr Nd Sm Eu Gd Tb Dy Ho Er Tm Yb Lu

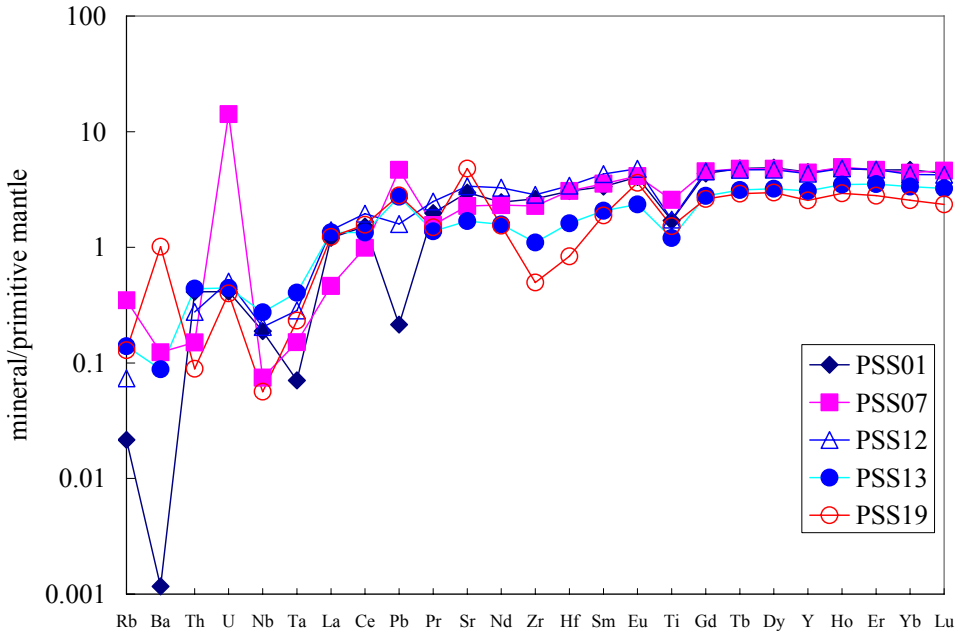
100
10
1
0.1
0.01
0.001
mineral/primitive mantle
PSS01
PSS07
PSS12
PSS13
PSS19
Rb Ba Th U Nb Ta La Ce Pb Pr Sr Nd Zr Hf Sm Eu Ti Gd Tb Dy Y Ho Er Yb Lu

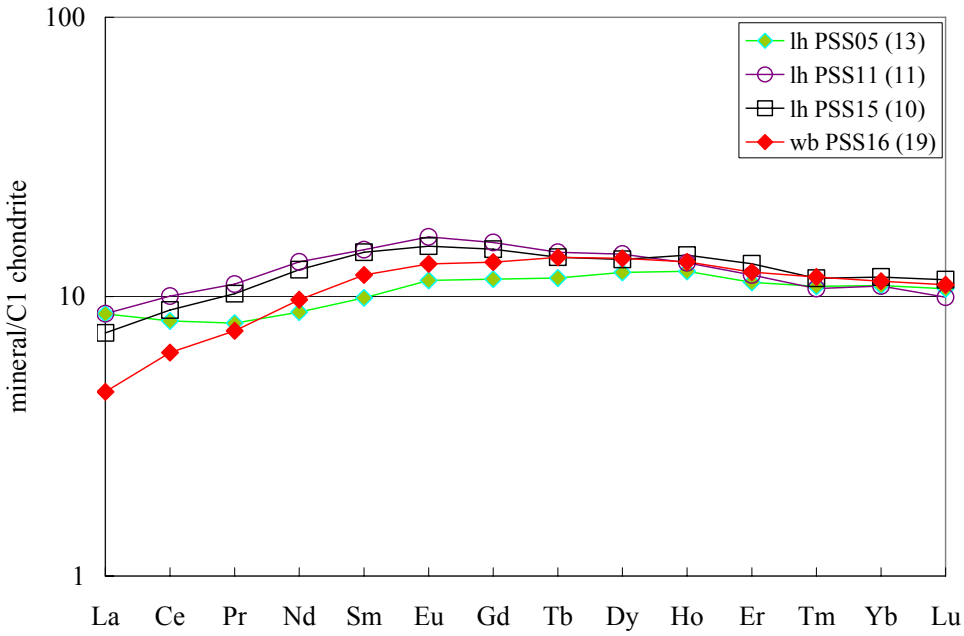
100
10
1
mineral/C1 chondrite
lh PSS05 (13)
lh PSS11 (11)
lh PSS15 (10)
wb PSS16 (19)
La Ce Pr Nd Sm Eu Gd Tb Dy Ho Er Tm Yb Lu

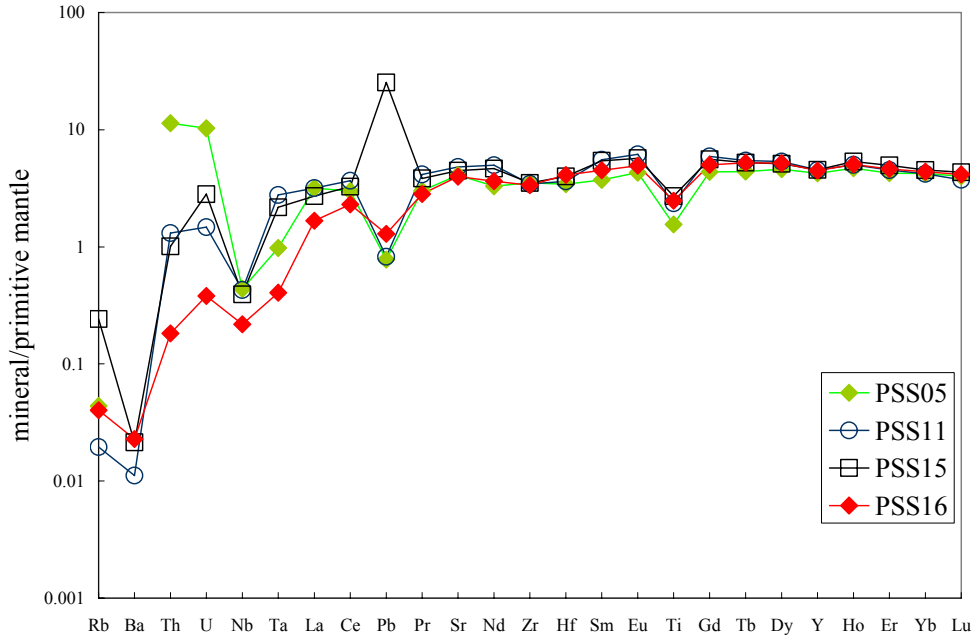
100
10
1
0.1
0.01
0.001
mineral/primitive mantle
PSS05
PSS11
PSS15
PSS16
Rb Ba Th U Nb Ta La Ce Pb Pr Sr Nd Zr Hf Sm Eu Ti Gd Tb Dy Y Ho Er Yb Lu

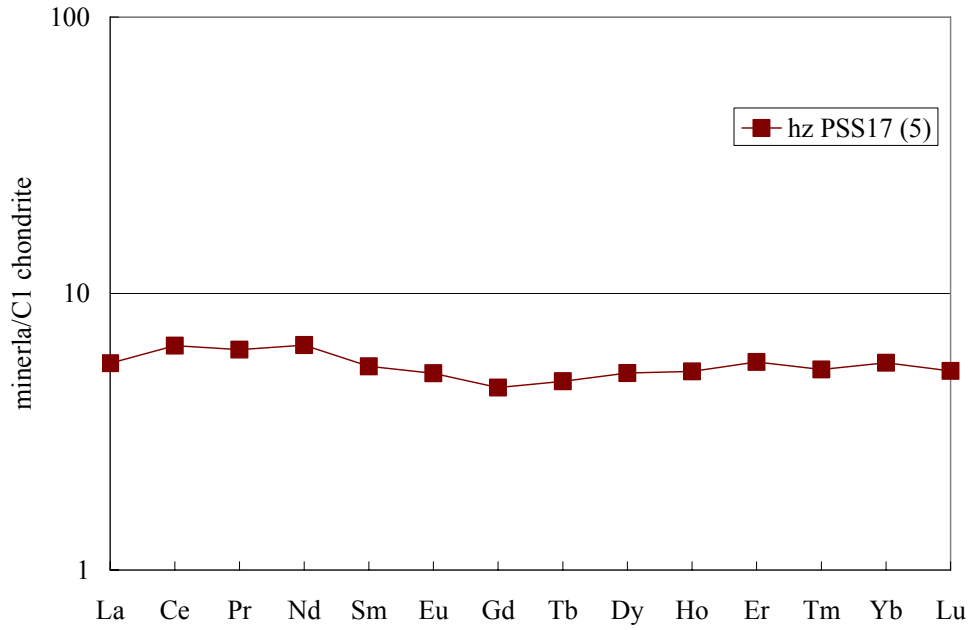
100
10
1
minerla/C1 chondrite
hz PSS17 (5)
La Ce Pr Nd Sm Eu Gd Tb Dy Ho Er Tm Yb Lu

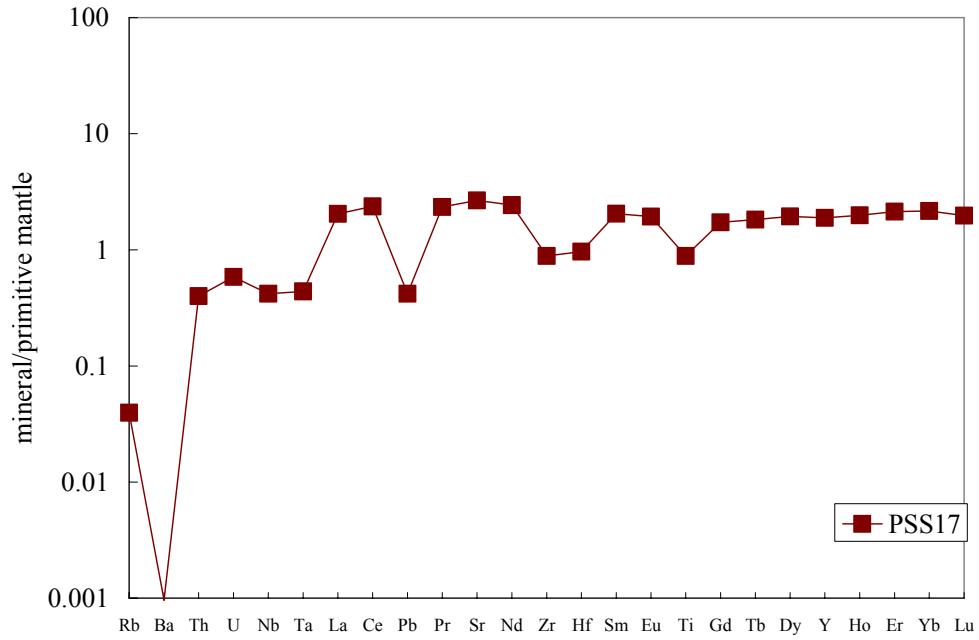
100
10
1
0.1
0.01
0.001
mineral/primitive mantle
PSS17
Rb Ba Th U Nb Ta La Ce Pb Pr Sr Nd Zr Hf Sm Eu Ti Gd Tb Dy Y Ho Er Yb Lu

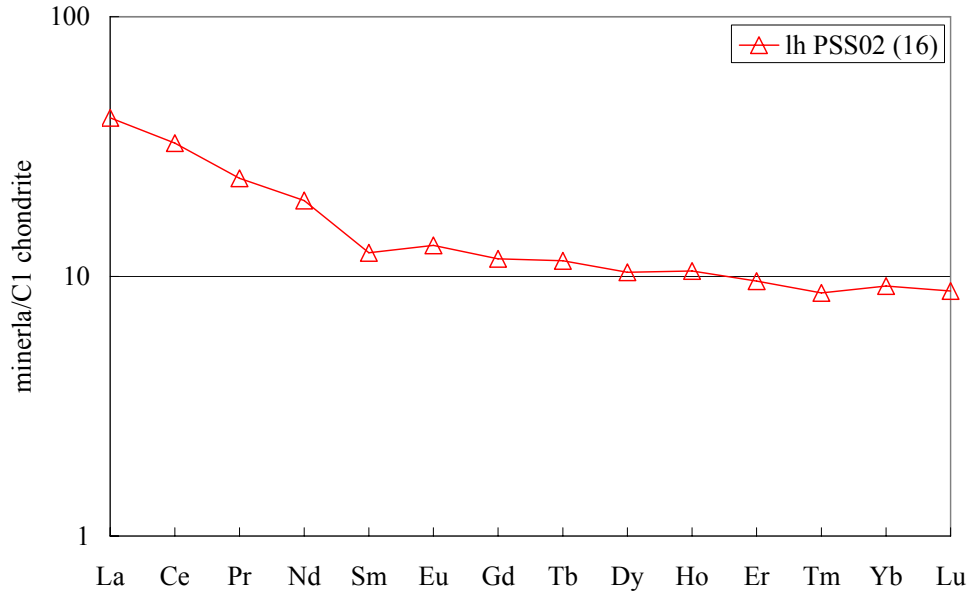
100
10
1
minerla/C1 chondrite
lh PSS02 (16)
La Ce Pr Nd Sm Eu Gd Tb Dy Ho Er Tm Yb Lu

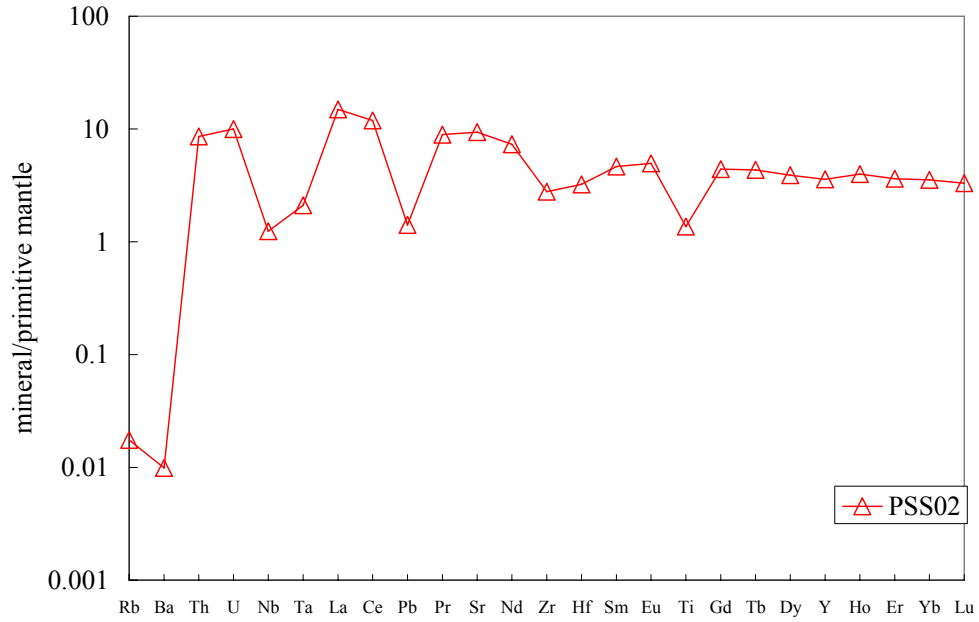
100
10
1
0.1
0.01
0.001
mineral/primitive mantle
PSS02
Rb Ba Th U Nb Ta La Ce Pb Pr Sr Nd Zr Hf Sm Eu Ti Gd Tb Dy Y Ho Er Yb Lu

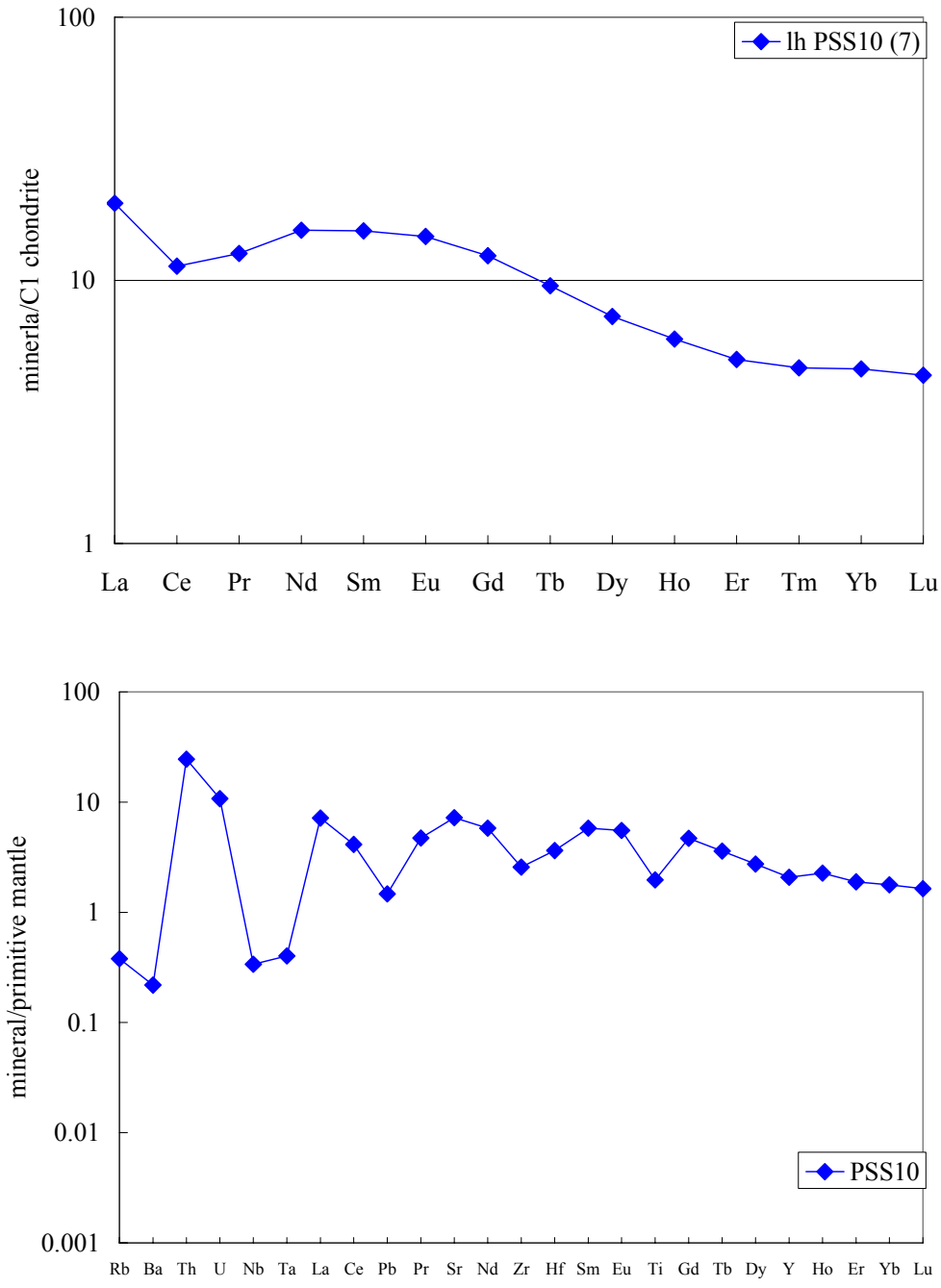


Fig. 5.9 - REE and trace element patterns of clinopyroxenes from peridotite xenoliths from Panshishan. From Group I to group V.

**LianShan**

**Group I - LREE-depleted pattern**

Cpx of lherzolites LS01, LS05, LS06, LS07, LS09, LS12, LS23, LS31 and ol-websterites LS04, LS24 are referred to this group.

They show $(La/Sm)_N$ ranging from 0.06 to 0.42 and $(Sm/Yb)_N$ from 0.3 to 1.05 respectively(Fig. 5.10). All LianShan cpx of group I show $Yb_N$ around 10, except LS09 and LS12 cpx that have Yb contents proximal to values theoretically assigned to cpx in residual lherzolites (and cpx bearing harzburgite). Depleted LS12 lherzolite with 8% modal cpx, is coherent with Yb contents of its clinopyroxenes ($Yb_N$=5.67), conversely the fertile LS 09 lherzolite, having 22% modal cpx, is difficult to account cpx with $Yb_N$=7.92.

Ti negative and weaker (almost absent) Zr (and Hf) anomalies are observed in PM incompatible trace element diagram. LS09 and LS12cpx show more pronounced Zr negative anomalies (Ti*=0.25 -0.2) than other cpx of this group.

**Group II - Upward convex**

Only cpx of LS22 lherzolite among the 22 Lianshan xenoliths analyzed, presents this profile. It is characterized by a slight LREE-depleted [$(La/Sm)_N$=0.72] and MREE- [$(Sm/Yb)_N$ =1.64] enriched pattern (Fig. 5.10). Sr, Ti and Zr (Hf) negative anomalies are observed, in PM normalized incompatible trace element pattern (Fig. 5.12).

**Group III - Flat REE pattern**

Only cpx from the harzburgite LS26 (cpx< 5%) represents the group III for the Lianshan xenolith suite. It is strongly depleted in all REEs (Fig. 5-12) as

well as other incompatible trace elements (Fig. 5.10). The REE contents (mainly MREE and HREE) and distribution recall opx REE profile rather than cpx REE profile ($(Yb)_N$=1.56) as expected from the residual (close to the complete cpx consumption) harzburgite.

**Group IV - LREE-enriched pattern**

Cpx of LS02, LS15, LS17, LS20 lherzolites, LS21 harzburgite and LS16 dunite, are referred to this group. They are characterized by strong enrichment in both LREE and MREE, and low to very low HREE contents (La, 20-60 XC1 chondrite; $(La/Sm)_N$ =1.97-10 and $(Sm/Yb)_N$=1.57-4.24). LS21 harzburgite (modal cpx 6%), LS 15 cpx-poor lherzolite (modal cpx 6%) and LS16 cpx-bearing dunite (modal cpx 3%) have (almost) coherently low to very low Yb contents ($Yb_N$=2.91,4.23 and 4.05 respectively). By contrast the fertile LS02 lherzolite (modal cpx 23%), contains cpx with the lowest Yb contents of this group ($Yb_N$ =2.65).A strong Th and U enrichments and prominent Ti and Nb negative anomalies are observed in all the cpx of this group.

**Group V - Spoon-shaped pattern**

Four Lianshan lherzolites (LS03, LS08, LS19 and LS30) belong to this group. Cpx of this group are characterized by a slight enriched in LREE, and a near flat to flat MREE-HREE pattern [$(La/Sm)_N$ ratios 0.68-4.69, and $(Sm/Yb)_N$ ratios 0.69-0.95] (Fig. 5.10). Only weak Ti negative anomaly is observed in the entire group V Lianshan cpx with the exception of LS03 cpx, which are richer in La (and Ce) and show a remarkable Zr (and Hf ) negative anomaly, together with evident Sr positive anomaly (Fig. 5.10).

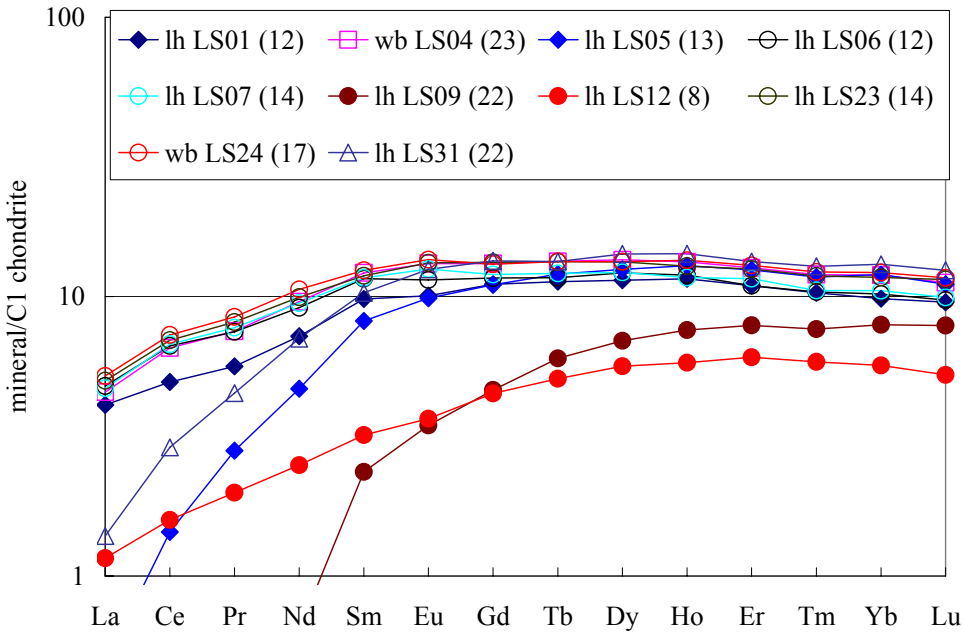
100
10
1
mineral/C1 chondrite
lh LS01 (12)
wb LS04 (23)
lh LS05 (13)
lh LS06 (12)
lh LS07 (14)
lh LS09 (22)
lh LS12 (8)
lh LS23 (14)
wb LS24 (17)
lh LS31 (22)
La Ce Pr Nd Sm Eu Gd Tb Dy Ho Er Tm Yb Lu

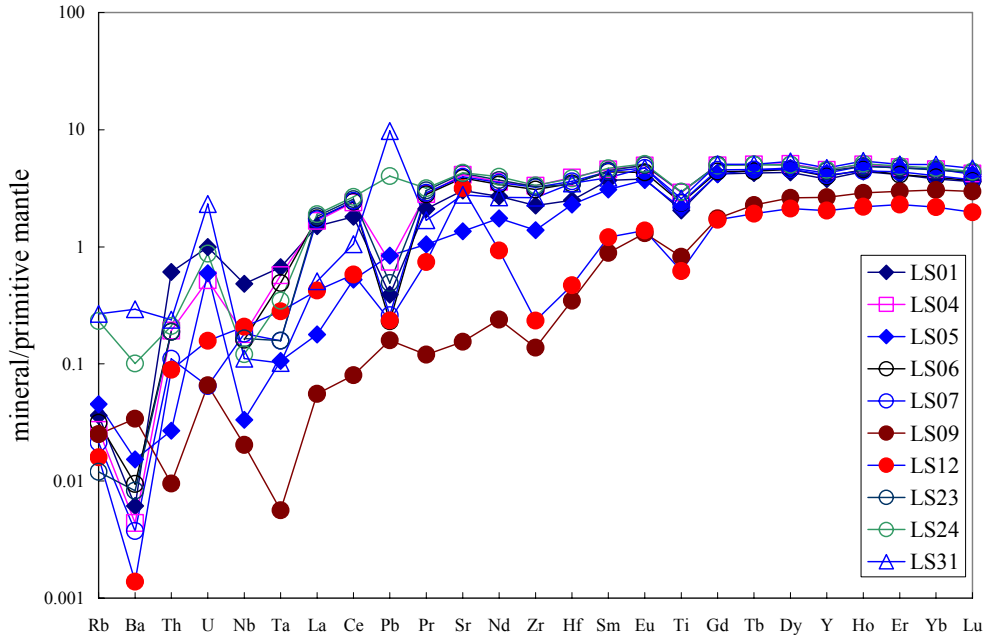
100
10
1
0.1
0.01
0.001
mineral/primitive mantle
LS01
LS04
LS05
LS06
LS07
LS09
LS12
LS23
LS24
LS31
Rb Ba Th U Nb Ta La Ce Pb Pr Sr Nd Zr Hf Sm Eu Ti Gd Tb Dy Y Ho Er Yb Lu

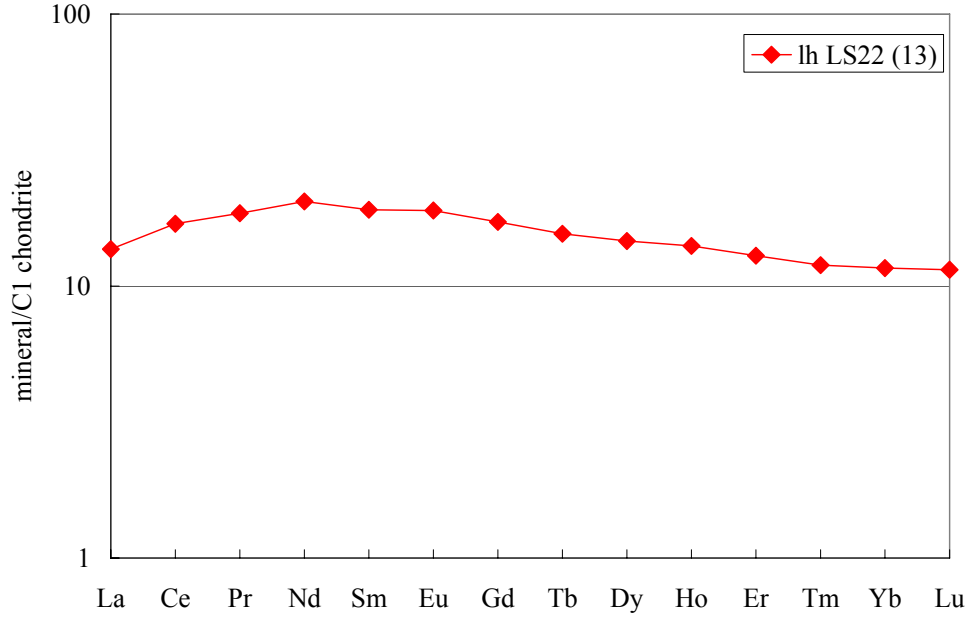
100
10
1
mineral/C1 chondrite
lh LS22 (13)
La Ce Pr Nd Sm Eu Gd Tb Dy Ho Er Tm Yb Lu

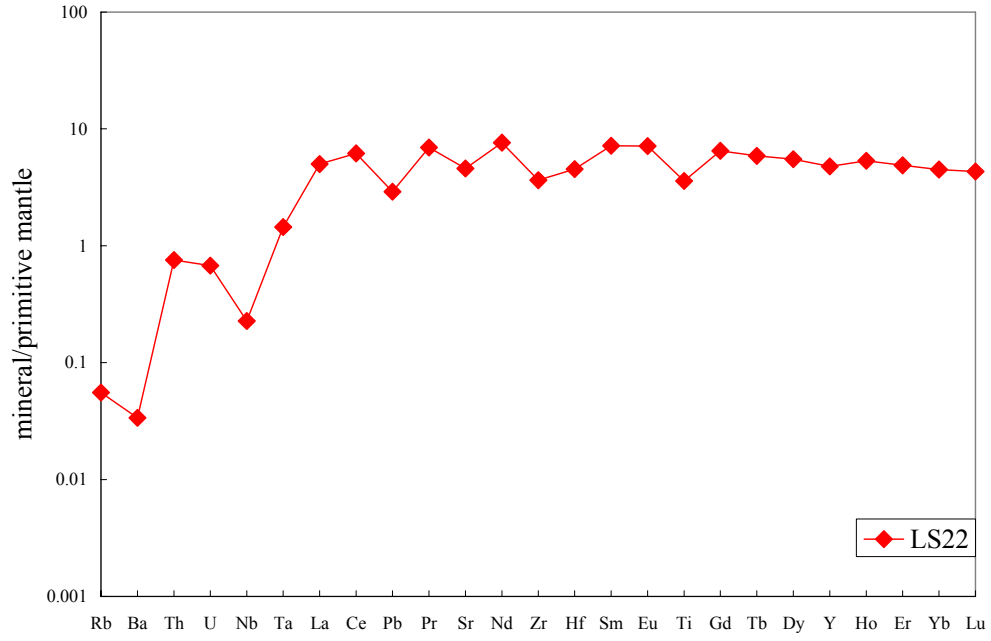
100
10
1
0.1
0.01
0.001
mineral/primitive mantle
LS22
Rb Ba Th U Nb Ta La Ce Pb Pr Sr Nd Zr Hf Sm Eu Ti Gd Tb Dy Y Ho Er Yb Lu

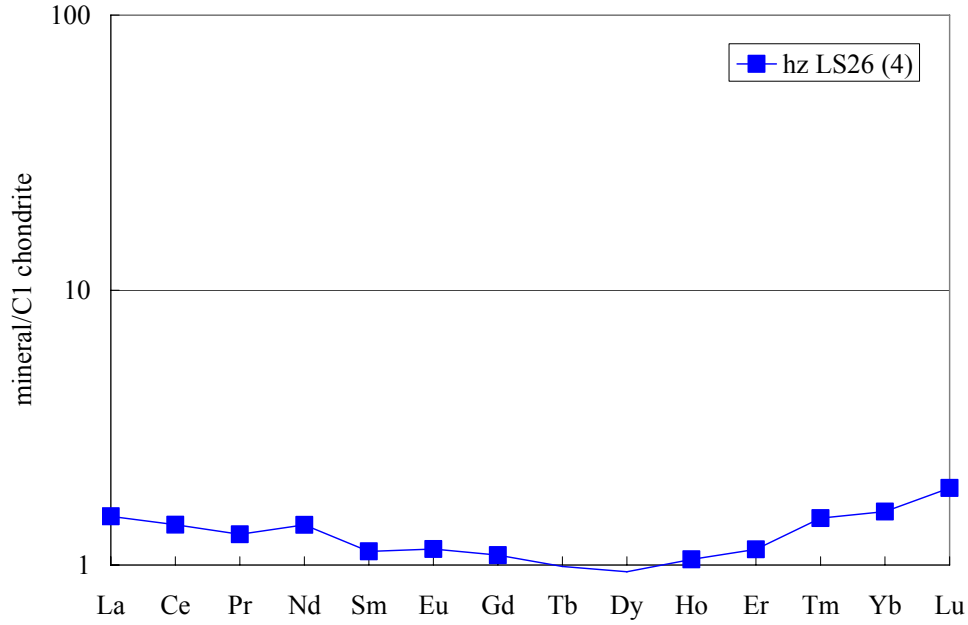
100
10
1
mineral/C1 chondrite
hz LS26 (4)
La Ce Pr Nd Sm Eu Gd Tb Dy Ho Er Tm Yb Lu

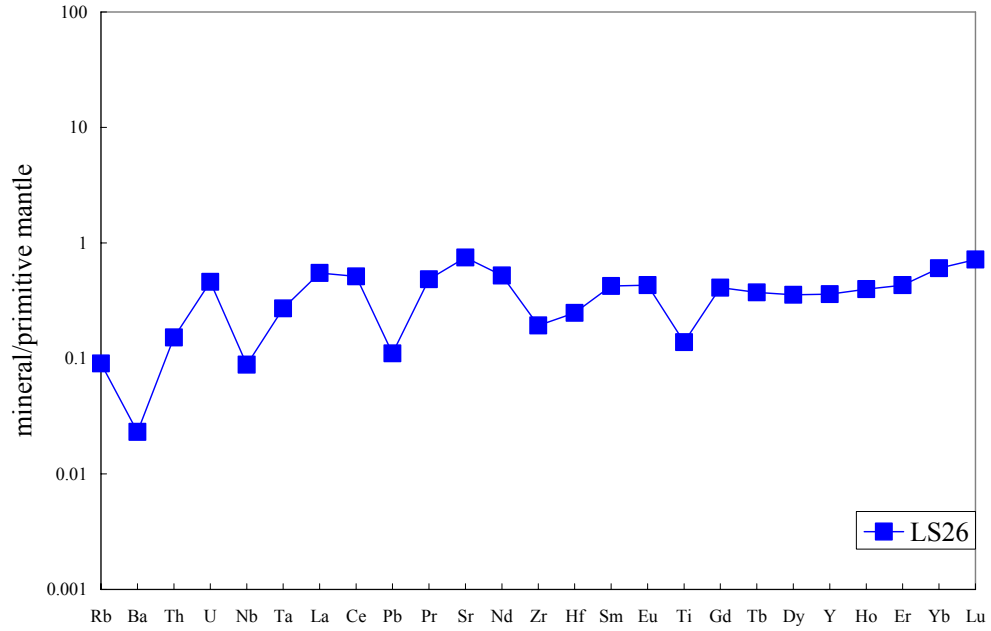
100
10
1
0.1
0.01
0.001
mineral/primitive mantle
LS26
Rb Ba Th U Nb Ta La Ce Pb Pr Sr Nd Zr Hf Sm Eu Ti Gd Tb Dy Y Ho Er Yb Lu

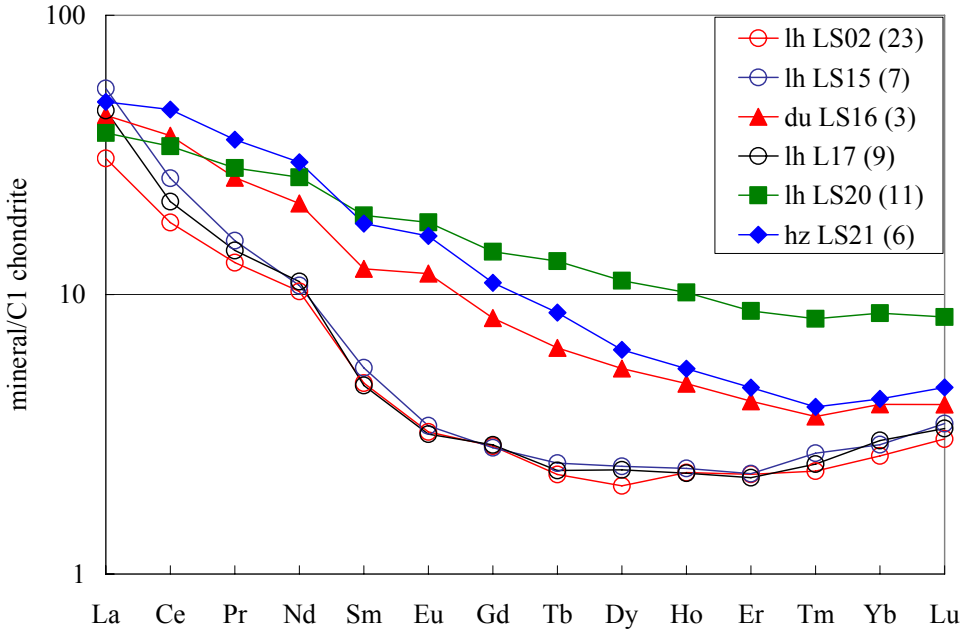
100
10
1
mineral/C1 chondrite
lh LS02 (23)
lh LS15 (7)
du LS16 (3)
lh L17 (9)
lh LS20 (11)
hz LS21 (6)
La Ce Pr Nd Sm Eu Gd Tb Dy Ho Er Tm Yb Lu

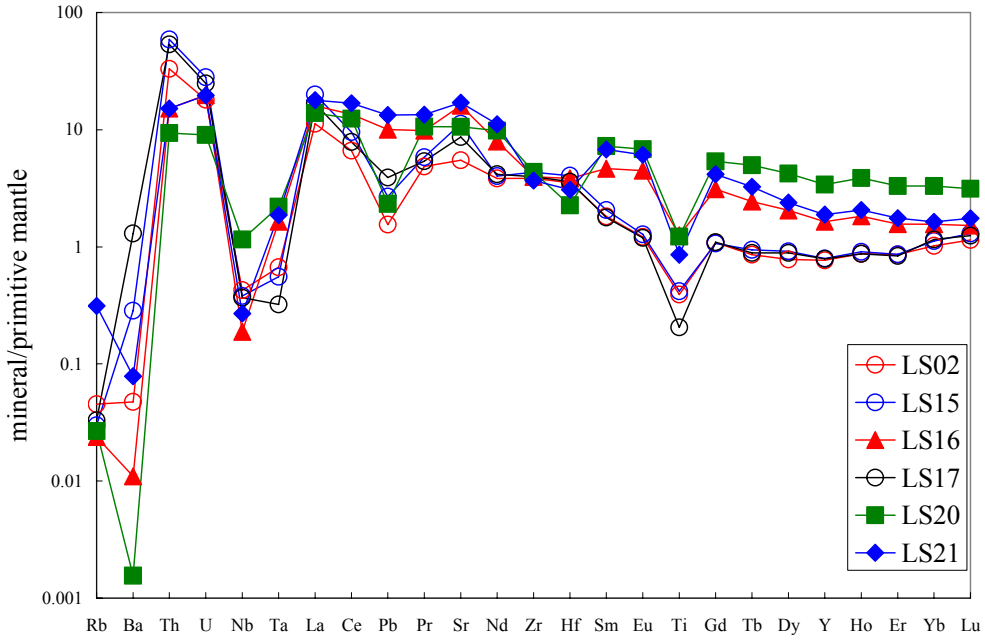
100
10
1
0.1
0.01
0.001
mineral/primitive mantle
LS02
LS15
LS16
LS17
LS20
LS21
Rb Ba Th U Nb Ta La Ce Pb Pr Sr Nd Zr Hf Sm Eu Ti Gd Tb Dy Y Ho Er Yb Lu

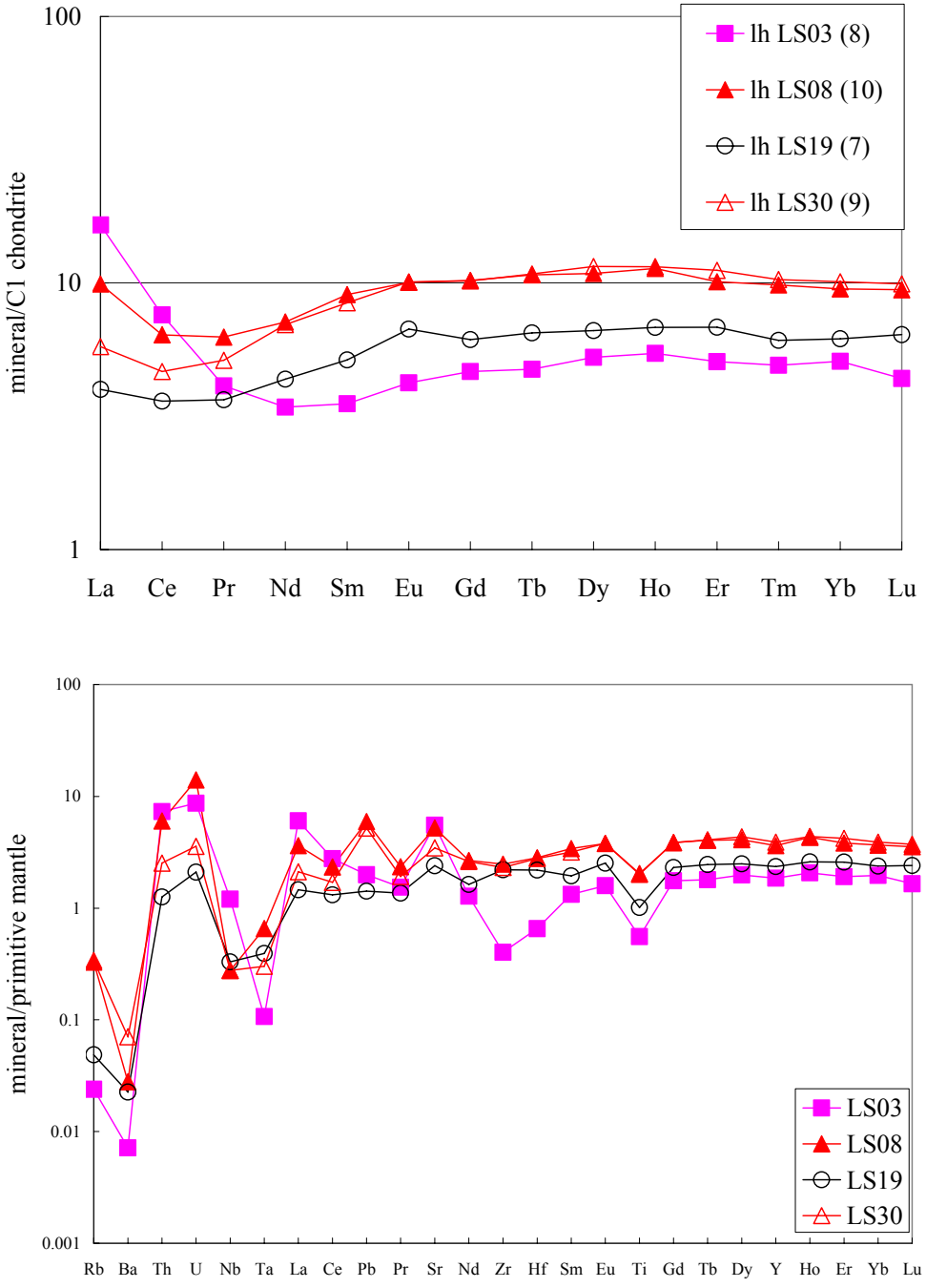


Fig. 5.10 - REE and trace element patterns of clinopyroxenes from peridotite xenoliths from Lianshan

**FangShan**

Just three cpx groups have been recognized in Fangshan xenoliths. Group II and group III are missing.

**Group I - LREE-depleted pattern**

Cpx of lherzolites FS03, FS07, FS12 and FS26 referred to this group. They are characterized by strongly LREE depleted and flat MREE – HREE pattern: $(La/Sm)_N$ 0.61-0.81 and $(Sm/Yb)_N$ 0.75-1.03 (Fig.5.11), associated with ubiquitous strong Ti negative anomalies, and feeble to absent Zr (and Hf) negative anomaly. Interesting to note the most fertile lherzolite of this group (FS03, modal cpx 13%) show the lowest HREE contents ($Yb_N$=6.55)

**Group IV - LREE-enriched pattern**

Only FS06 and FS16 harzburgites show cpx belonging to group IV. Both are enriched in LREE (La, 70 X C1 chondrite) with respect to MREE and HREE, but they differ in term of MREE and HREE distribution [$(La/Sm)_N$, 0.70-1.42 and $(Sm/Yb)_N$, 4.38-2.26] (Fig. 5.11). FS06 and FS16 cpx have almost the same U-Th contents (U, 20 X PM). Both harzburgites show cpx with strongly negative anomalies in Nb, Zr (Hf) and Ti, more pronounced in sample FS16.

**Group V - Spoon-shaped pattern**

A large number of FangShan samples (all lherzolites: FS01, FS11, FS14, FS17, FS19, FS21 and FS23) have cpx referring to this group. They present a slight LREE and flat to feeble convex upward MREE- HREE distribution [(MREE-HREE ~ 10 times C1 chondrite; $(La/Sm)_N$ and $(Sm/Yb)_N$, 1.42-4.04 and 0.96-1.71 respectively]. All samples show Th and U enrichment (amplified

in FS14 and FS21 cpx) associated with remarkable Ti, and weak to absent Zr (Hf) negative anomalies.

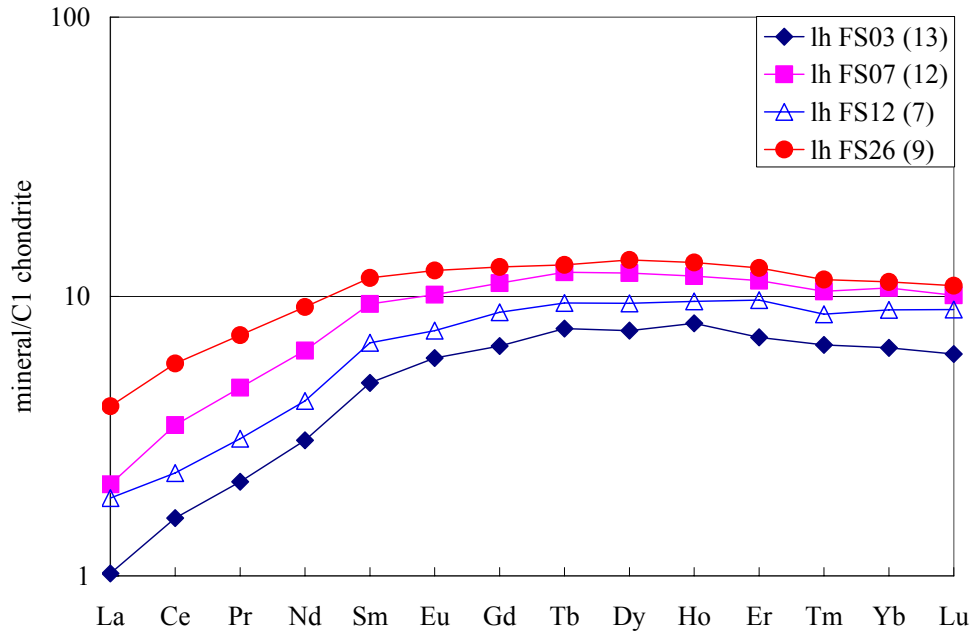


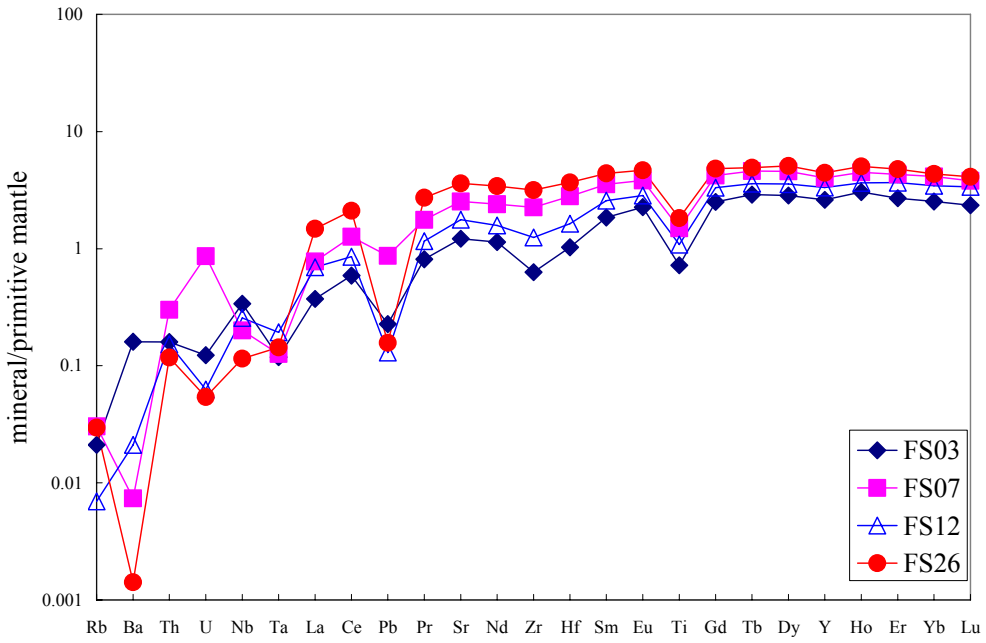

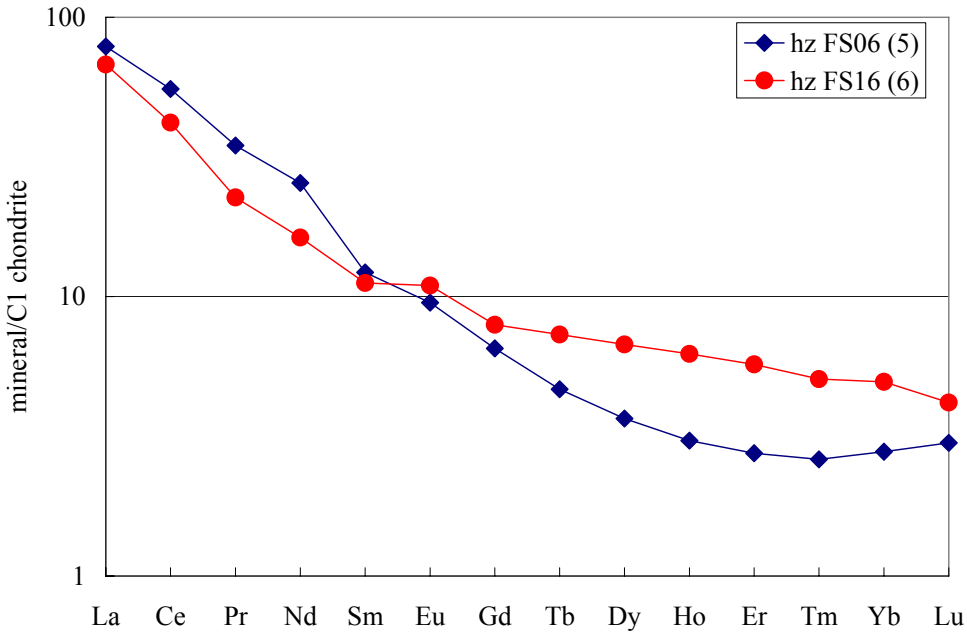
100
10
1
mineral/C1 chondrite
hz FS06 (5)
hz FS16 (6)
La Ce Pr Nd Sm Eu Gd Tb Dy Ho Er Tm Yb Lu

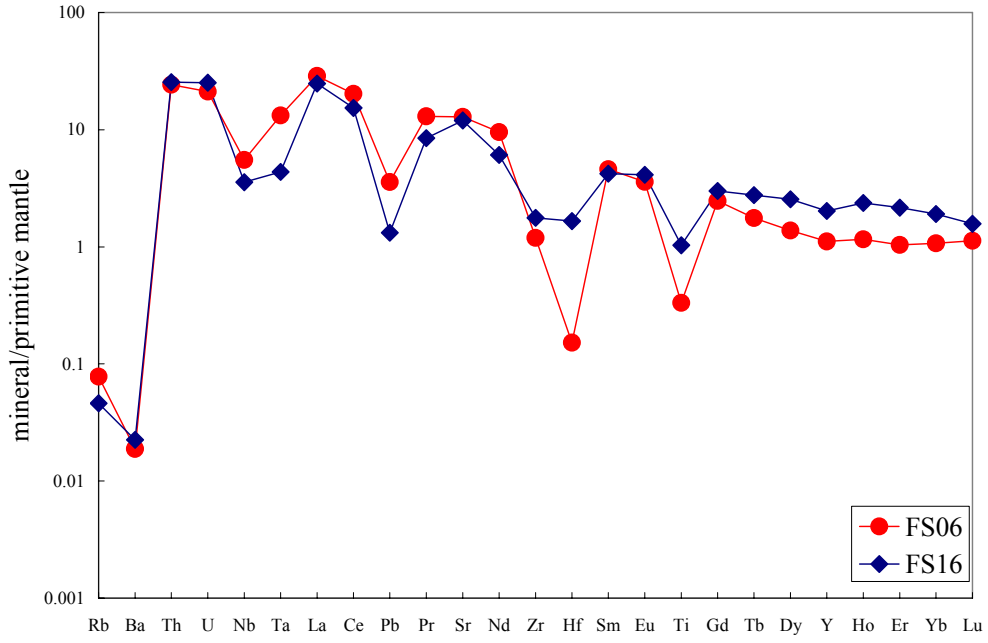
100
10
1
0.1
0.01
0.001
mineral/primitive mantle
FS06
FS16
Rb Ba Th U Nb Ta La Ce Pb Pr Sr Nd Zr Hf Sm Eu Ti Gd Tb Dy Y Ho Er Yb Lu

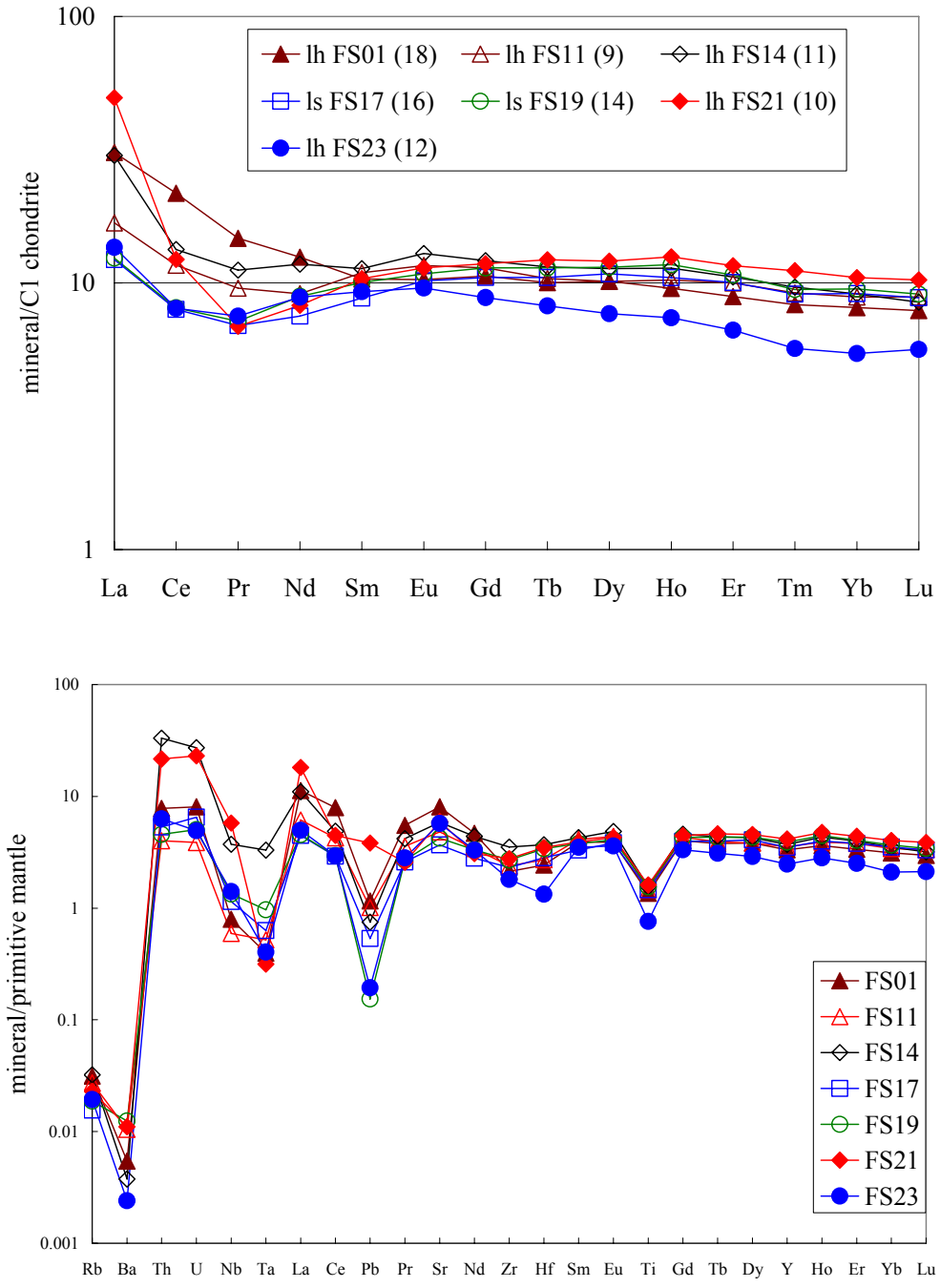


Fig. 5-13 REE and trace element patterns of clinopyroxenes from peridotite xenoliths from Fangshan

Regardless the localities, in the simplified REE diagram with $(La/Sm)_N$ versus $(Sm/Yb)_N$ ratios (Fig. 5.12) the five cpx groups are plotted. Most of samples of LREE-depleted group I fall in the third quadrant, whereas samples of LREE-enriched group IV are in the opposite first quadrant. The upward convex group II show a little differences among them, three samples are in second quadrant, and the other two samples are in the third quadrant having $(Sm/Yb)_N$ less than 1. The flat REE pattern Group III are clustered around the one-one coordinates, and the spoon-shaped pattern group V are distributed along the x-axis in the first and the fourth quadrant.

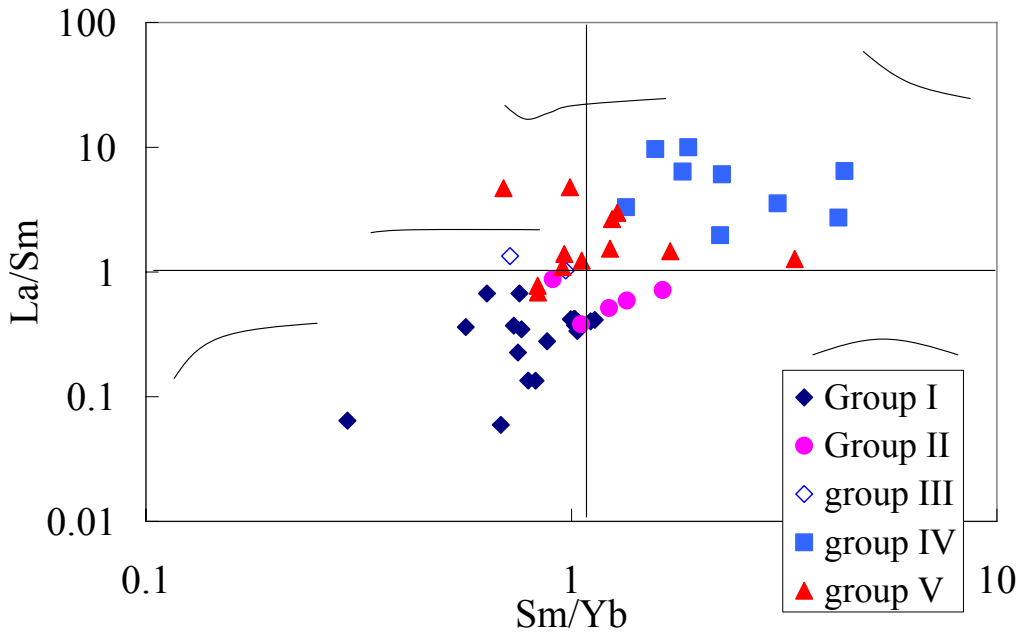


Fig. 5.12 - Simplified REE pattern with $(La/Sm)_N$ vs $(Sm/Yb)_N$ of Subei basin clinopyroxenes

The cpx HREE abundances suggest that the samples have experienced various degree of melting, for example $Yb_N$ varied from 4.60 to 12.12 for Panshishan

xenoliths, 1.56 to 13.04 for Lianshan xenoliths and 2.78 to 11.27 for Fangshan xenoliths. The modelling of melting process is discussed below (see Chapter 8).

**Mineral Oxygen isotopes**

The isotope composition of oxygen in peridotite xenoliths can provide important information on mantle region.

Oxygen isotope ratios are reported as permil deviations from SMOW (standard mean ocean water) according to the conventional δ-notation:

$\delta^{18}O=[(({}^{18}O/{}^{16}O)_{sample} - ({}^{18}O/{}^{16}O)_{ref})/ ({}^{18}O/{}^{16}O)_{ref})] \times 10^3$.

The fractionation factor between two phases A and B is defined as "$\alpha_{A-B}$", where $\alpha_{A-B}=R_A/R_B$ , and R is the ${}^{18}O/{}^{16}O$ ratio. The O-isotope fractionation between two phases is reported as $\Delta_{A-B}=10^3$ ln $\alpha_{A-B}$, often approximated to $\Delta_{A-B}=\delta_A - \delta_B$.

Mattey et al. (1994) reported oxygen isotopic composition of 76 samples of olivine in spinel-, garnet- and diamond-facies peridotites, and as sin-genetic inclusions within diamond. The laser fluorination method of $O_2$ extraction was used to obtain quantitative extraction, otherwise hardly achieved with conventional fluorination. Accordingly, the $\delta^{18}O$ values of olivine are almost invariant: they average 5.18±0.28‰ (2σ), with an overall variation from 4.8 to 5.5‰. The $\delta^{18}O$ values of opx range from 5.48 to 6.1‰, and coexisting clino-pyroxenes from 5.28 to 5.9‰. The $\Delta^{18}O_{cpx-ol}$ values are positive and always close to 0.4‰, consistent with isotopic equilibrium at typical mantle temperatures (>1100 °C). The bulk compositions of spinel-, garnet- and diamond-facies mantle peridotites are similar, with a calculated bulk mantle $\delta^{18}O$ of +5.5‰.

Ionov et al. (1994) studied spinel and garnet–bearing peridotites from the Vitim Volcanic Field in Siberia. These rocks define a suite of fertile mantle xenoliths that are LREE-depleted and have strongly depleted strontium and neodymium isotopic compositions. Determination of ${}^{18}O/{}^{16}O$ ratios by

conventional and laser-assisted fluorination techniques yield a very narrow range of whole-rock $\delta^{18}O$ values for both spinel peridotites (+5.4 to +5.8‰) and garnet lherzolites (+5.5 to +5.8‰ ). Mineral $\delta^{18}O$ values for the xenoliths are: ol =5.1 to 5.8‰, opx= 5.7 to 6.0‰, cpx =5.5 to 6.2‰, grt=5.5 to 6.0‰, and sp=4.9 to 5.5‰. Similarly, $\delta^{18}O$ ranges for silicate mineral pairs vary from only 0.5 to 0.7‰. The sixteen peridotite xenoliths analysed exhibit equilibrium O-isotope fractionations between minerals of a magnitude expected from theoretical and experimental considerations, which may be possibly ascribed to temperature-controlled $^{18}O$ distribution between olivine and pyroxenes in spinel-bearing peridotites. On chemical bases they also define a possible source rock for MORB-like melts with $\delta^{18}O$ values varying from ca. + 5.7 to + 6.1‰.

Chazot et al. (1997) determined oxygen isotope ratios of minerals from anhydrous and hydrous (amphibole-bearing) spinel lherzolites from Yemen, as well as from hydrous spinel lherzolites and amphibole megacrysts from Nunivak Island, Alaska, using the laser fluorination technique. Oxygen isotopic compositions of olivine vary from 5.1 to 5.4‰ and $\delta^{18}O$ values of opx, cpx and sp range from 5.68 to 5.98‰, from 5.53 to 5.77‰, and from 4.0 to 4.75‰, respectively.

Harmon and Hoefs (1995) measured the O-isotope composition of 743 Neogene volcanic rocks worldwide in order to define possible systematic variations in the $\delta^{18}O$ values of basalts (historic lavas, submarine glasses, and lavas with < 0.75 wt% $H_2O$) from different geodynamic settings. They find that Mid-ocean-ridge basalts (MORB) have uniform O-isotope composition, with $\delta^{18}O$=+5.7±0.2‰. Basalts erupted in different tectonic settings show $^{18}O/^{16}O$ ratios that are both lower and higher than MORB, with continental basalts enriched in $^{18}O$ by ca. 1‰ over oceanic basalts.

Totally 32 samples from Subei basin for cpx are chosen for oxygen isotopic analyses.10 xenoliths from Panshishan: 8 lherzolites, 1 harzburgite PSS17 and 1 olivine websterite PSS16. 10 xenoliths from Lianshan, all are lherzolites. 12 xenoliths from Fangshan: 10 lherzolites, and 2 harzburgite FS06 and FS16. The stable oxygen isotope composition of minerals from mantle xenoliths studied in this thesis, are reported in Table 5.6 and shown in Fig. 5.13. The mineral are olivine, orthopyroxene, clinopyroxene and spinel of peridotite xenoliths from Panshishan, Lianshan and Fangshan. Analyses were duplicated for each mineral, and some samples with no consistent $\delta^{18}O$ values were measured several times. The oxygen isotope shows no relationship with the different rock types (lherzolite, harzburgite, olivine websterite and dunite). In Panshishan xenoliths, the $\delta^{18}O$ values range 5.28 to 5.78 ‰ for olivine, from 5.87 to 6.53 ‰ for opx, from 5.18 to 6.15 ‰ for cpx, and 4.11 to 5.37 ‰ for sp. The results are similar to those reported by Yu et al. (2005), although these authors refer a broader range of $\delta^{18}O$ values for for ol, opx and cpx. In Lianshan xenoliths, the $\delta^{18}O$ values range from 5.42 to 5.96 ‰ for olivine, from 6.01 to 6.67 ‰ for opx, from 5.77 to 6.34 ‰ for cpx, and 4.52 to 5.58 ‰ for sp. In xenoliths from Fangshan area, the $\delta^{18}O$ values range from 5.12 to 6.32 ‰ for olivine, from 5.79 to 6.57 ‰ for opx, from 5.33 to 6.31 ‰ for cpx, and from 4.37 to 5.39 ‰ for sp. Most of the samples have $\delta^{18}O$ values within the range of the worldwide mantle xenoliths. Fractionation between opx and ol are always positive in Panshishan and Lianshan xenoliths, as expected for mantle phases in O-isotope equilibrium. Also most xenoliths from Fangshan area have opx $\delta^{18}O$ values higher than ol, with the exception of samples FS12 and FS13, showing clear disequilibrium fractionation. The observed positive fractionation between pyroxene and olivine satisfies the theoretical calculations of Zheng (1993),

who modeled the oxygen isotope fractionation among anhydrous silicate minerals by means of the modified incremental method, and described the following order of $^{18}O$-enrichment: quartz > albite $\geqslant$ K-feldspar > sillimanite $\geqslant$leucite > andalusite > Jadeite > kyanite > anorthite $\geqslant$ cordierite > diopside > wollastonite > zircon $\approx$ garnet > olivine. Because the equilibrium constant is temperature-dependent, we can express the general formula of this relation for geological conditions as:

$$1000 \ln \alpha_{(xy)} = a_{(xy)} \times 10^6 / T^2 + c_{(xy)}$$

Where *a* and *c* are temperature coefficients for minerals x and y.

As a function of δ, the equation above becomes:

$$1000\ln[(1000 + \delta_x)/(1000 + \delta_y)] = a_{(xy)} \times 10^6 / T^2 + c_{(xy)}.$$

For O-isotope exchange between anhydrous phases, the value of $b = 0$ (Bottinga and Javoy, 1973).As for the latter case, the graphical expression of this equation is a straight line passing for the origin: (y = mx + 0), with $\Delta^{18}O_{x-y}$ = y; a = x; $10^6/T^2$ = m (angular coefficient), the so-called “pseudo-isotherm”.

Accordingly, we can draw δ–δ diagrams where the O-isotope composition of one phase is plotted vs. the O-isotope composition of another phase, assuming the system is bi-mineralic. Although several minerals may contribute to the paragenesis of a rock, the δ–δ plots can be conveniently used to infer the behavior of a mineral, likely the phase with the lowest diffusivity and/or highest modal abundance vs. the behavior of another phase, which is modally subordinate and has higher diffusivity. In the case of mantle peridotites, it is convenient to plot the $\delta^{18}O$ values of olivine ($\geq$ 50% volume) vs. those of the other phases, which are modally subordinate and have slightly higher diffusivities at mantle conditions.

In the $\delta^{18}O_{olivine}$ vs. $\delta^{18}O_{orthopyroxene}$ plot, samples from Panshishan and Lianshan lie along two pseudo-isotherms, defined by the $\Delta_{ol\text{-}opx}$ = 0.5 and $\Delta_{ol\text{-}opx}$ = 0.9 ‰ fractionation. O-isotope equilibrium at temperatures of *900* and *1200*°C have been calculated on the basis of these fractionation values (Chiba et al., 1989; Zheng, 1993; Fig. 5.13). Olivine and opx are the most abundant and "refractory" phases of the studied xenoliths and more likely preserve the primary O-isotope record at mantle conditions. The data of FangShan are more scattered and likely reflect a disturbed O-isotope equilibrium condition. Similarly, the $\delta^{18}O_{ol}$ vs. $\delta^{18}O_{cpx}$ plot shows very large variations in sample distribution. This may be due to the occurrence of cpx with possible re-crystallized cpx crystal

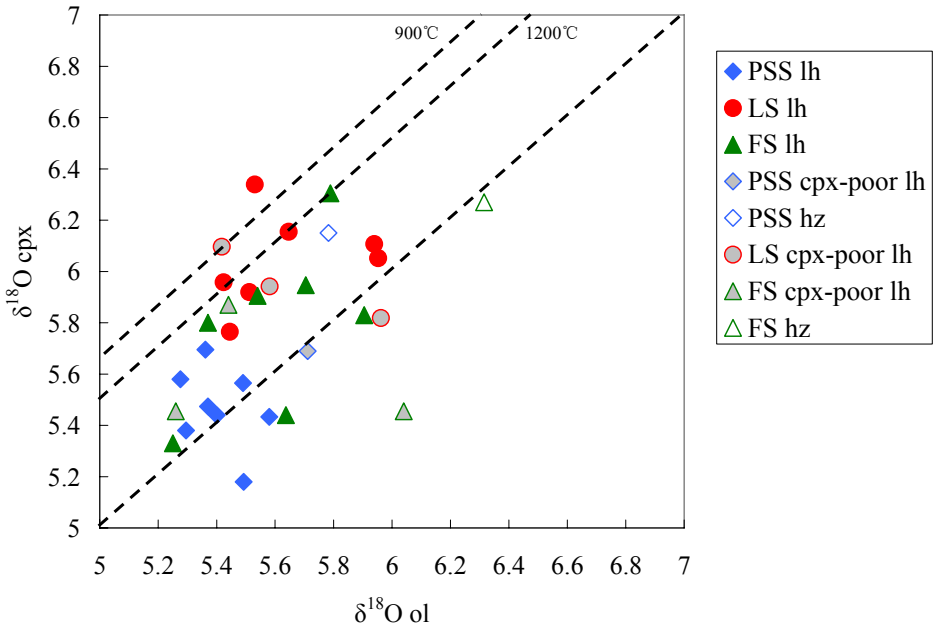

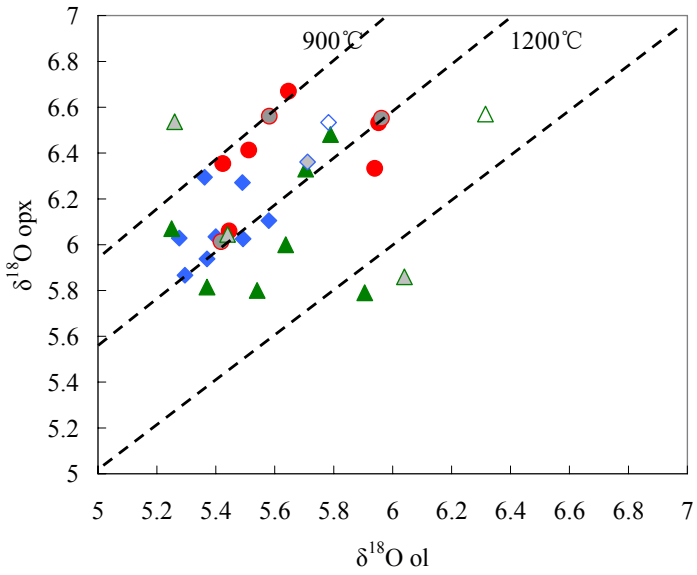


Fig. 5.13 - Oxygen isotope composition for olivine, orthopyroxene and clinopyroxene in xenoliths from Subei basin. $\Delta$=0 are also shown. Light blue diamond, Panshishan lherzolite; light blue filled grey diamond, Panshishan cpx-poor lherzolite; blue open diamond, Panshishan harzburgite; red dot, Lianshan lherzolite; red filled grey dot, Lianshan cpx-poor lherzolite; red open dot, Lianshan harzburgite; red filled pink dot, Lianshan olivine websterites; red filled golden dot, Lianshan dunite; green triangle, Fangshan lherzolite, green filled grey triangle, Fangshan cpx-poor lherzolite; green open triangle. Fangshan harzburgite)

# Chapter 6 – P-T and Oxygen fugacity estimates

## Temperature and Pressure estimates

Since all xenolith investigated in this thesis show none evidence of textural intra-mineral disequilibrium, they represent good examples for thermo-barometric evaluation. Within individual sample both opx and cpx have homogeneous major element compositions, particularly regarding mg-number, and, together with ol, they show mutual equilibrium relationships, as indicated by the Fe/Mg exchange equilibrium of Brey and Köhler (1990)(Fe/Mg opx/cpx=1.08, Fe/Mg ol/cpx=1.22 and Fe/Mg ol/opx=1.09). To reinforce the validity of such estimates, temperatures were calculated using only cpx and opx cores. The obtained temperatures when plotted against Fe/Mg opx/cpx follow a general trend included between the 10 and 50kbar of Brey and Köhler experimental curves.

Nominal equilibration temperatures (for a pressure arbitrarily assumed to be 15 Kbar, see below), for PSS, LS and FS xenoliths are reported in Table 6.1.

The Panshishan and Lianshan lherzolites record very similar range of temperatures varying on average from 816°C to 1014°C and from 823°C to 1001°C respectively (Table 6.1, Fig. 6.1). The harzburgite PSS17 from Panshishan show a temperature of 922°C and the olivine websterite PSS16 has a temperature of 1033°C. The harzburgite LS21 and LS26 from Lianshan show a temperature of 855 °C and 821°C and the olivine websterite LS04 and LS24 985°C and 961°C. Among each sample only calculated temperatures with values differing maximum 70°C are considered for geothermal considerations and for the subsequent pressure calculation. This limit has been determinated

considering the propagating errors combining EMP data, nature of the sample together with the error of the thermometer formula itself. Despite the textural and (apparent) geochemical equilibrium of both Panshishan and Lianshan xenoliths, in a few samples the calculated temperatures may differ up to 126°C (PSS13) and 141°C (LS05), with Panshishan mantle population showing the largest number of disequilibria samples. I consider disequilibrium evident in samples with differences in temperatures > 70 °C. Fangshan lherzolites record temperatures ranging from 1002°C to 1208°C, with just one sample (FS24) recording much lower values (811°C; Table 6.1, Fig. 6.1). Fangshan harzburgites FS06 and FS16 record temperatures of 1057°C and 1073°C. Fangshan xenoliths result thermally well equilibrated (in all samples T values differ less then 41°) with the highest temperatures among the three xenolith populations.

Pressures were estimated based on the Ca distribution between olivine and clinopyroxene (Kohler and Brey, 1990). Considering that Ca contents in olivine is proximal to detection limit in EMP analyses, as well as the high diffusion rate of Ca in olivine compared with that in pyroxenes the reliability of this barometer is strongly dependent on the state of equilibrium for each ol–cpx pair (Witt-Eickschen and Kramm, 1997). For this reason pressure estimates were calculated for the ol cores, combined with the opx–cpx BandK thermometer, to yield realistic pressures for ‘equilibrated’ parageneses. In addition, since spinel is the only aluminous phase, it is reasonable to consider the range of 12–18 Kbar as the barometric conditions at the time of the xenolith entrainment.

Pressure estimates range between 12 to 25, 11 to 23 and 11 to 33 Kbar for Panshishan, Lianshan and Fangshan lherzolites, respectively. The harzburgite

PSS17 from Panshishan has a pressure of 25Kbar. Harzburgite LS21 and LS26 from Lianshan have a pressure of 17 and 16Kbar, and olivine websterite LS04 and LS24 has a pressure of 21 and 21.5 Kbar. Harzburgite FS06 and FS16 from Fangshan have a pressure of 24 and 32kbar. There is no significant pressure difference between rock types. The results are shown in Table 6.1. Most of the calculate pressures for Panshishan, Lianshan and Fangshan exceed the sp stability field. This could be due to the weakness of the thermo-barometric method applied, that however have been taken into account in estimating the errors, reported in the P-T diagrams as error bars (Fig. 6.1). Notwithstanding the calculated errors, we are confident in consider that xenoliths sampling the mantle beneath Subei basin record high deep lithospheric mantle condition. In P-T diagram, only Lianshan xenolith population seems to trace a trend, which recalls a possible geotherm. The few (and heterogeneous) P-T data of Panshishan, seem to recall the Lianshan geothermometric condition. On the other hand, Fangshan xenoliths seem to reflect a mantle domain well constrained between 17 and 23 Kbar, and hotter with respect to Lianshan and Panshishan.

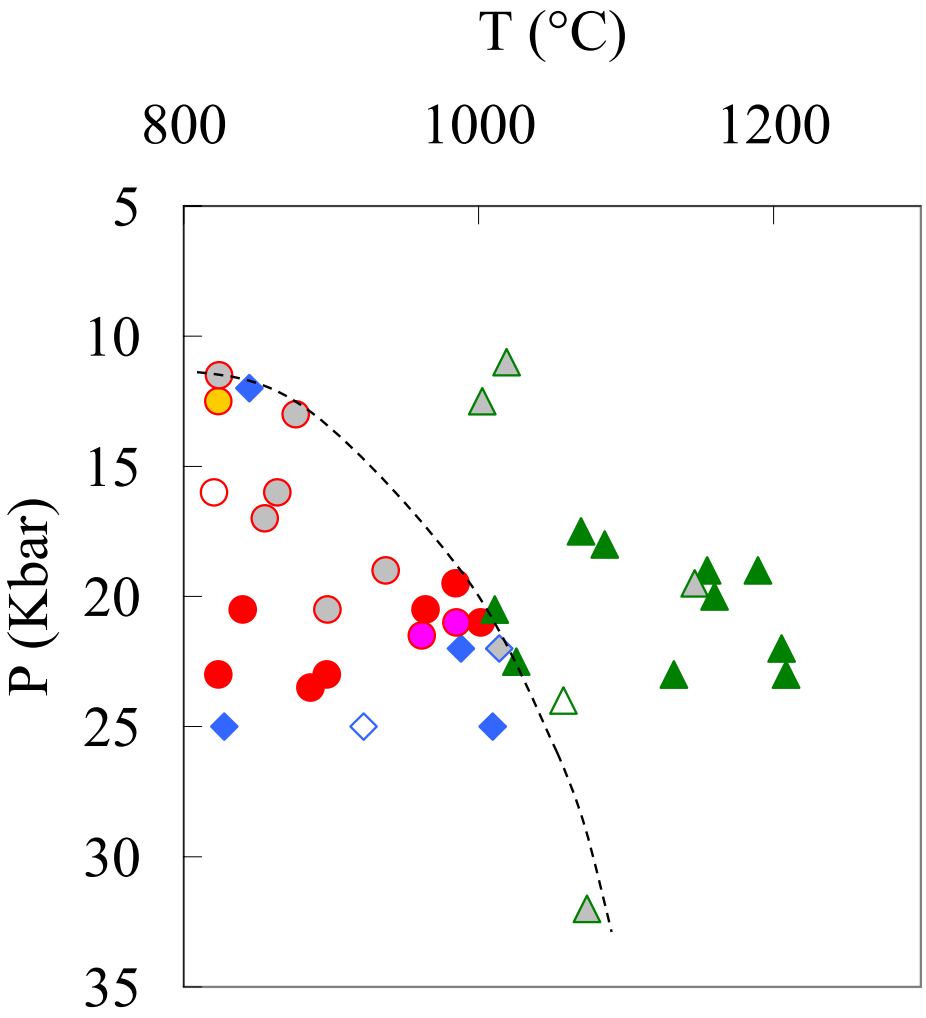


Fig. 6.1 - Pressure vs equilibrium temperature of Subei basin xenoliths. Light blue diamond, Panshishan lherzolite; light blue filled grey diamond, Panshishan cpx-poor lherzolite; blue open diamond, Panshishan harzburgite; red dot, Lianshan lherzolite; red filled grey dot, Lianshan cpx-poor lherzolite; red open dot, Lianshan harzburgite; red filled pink dot, Lianshan olivine websterites; red filled golden dot, Lianshan dunite; green triangle, Fangshan lherzolite, green filled grey triangle, Fangshan cpx-poor lherzolite; green open triangle. Fangshan harzburgite

**Oxygen fugacity**

Oxygen fugacity ($f_{O2}$) values, reported in Table 6.1, were obtained from the equilibrium:

$$6Fe_2SiO_4 + O_2 = 2Fe_3O_4 + 6FeSiO_3$$

$$\log (fO_2)P,T = - 6\log aOL_{Fe2SiO2} + 3\log aOPX_{Fe2Si2O6} + 2\log aSP_{Fe3O4}$$

Calculated following the protocol of Woodland et al. (1992).

A crucial point for $f_{O2}$ estimates is the determination of the $Fe^{3+}/Fe^{2+}$ ratios of the various phases. The $Fe^{3+}$ content of the orthopyroxenes and spinels has been calculated using the Carswell and Gibbs (1987) and O'Neill and Navrotsky (1983) methods respectively, assuming all the iron in olivine to be $Fe^{2+}$. The amount of $Fe^{3+}$ in the spinel solid-solution is difficult to evaluate, considering the high dilution of $Fe_3O_4$ component in the upper mantle spinels. The $Fe_3O_4$ activity has been calculated using experimental data from Nell and Wood (1991).

P–T differences have a significant effect on the calculated oxygen fugacity expressed relative to the fayalite-magnetite-quartz buffer [FMQ] ($\log f_{O2}$). A difference of 100°C in the calculated temperature produces a variation in the ($\log f_{O2}$) of 0.15-0.2; pressure has a larger effect, producing differences of 0.3-0.5 log bar units for an assumed error of 5 Kbar in pressure calculation.

However, $Fe^{3+}$ content of spinel contributes to the greatest uncertainty in $f_{O2}$. Propagating counting errors yield an uncertainty in $Fe^{3+}/Fe$ of 0.025. For the calculated [FMQ] $\log f_{O2}$ the uncertainty in $f_{O2}$ is 0.3-0.4 log units. At very low $Fe^{3+}$ contents, the uncertainty can become a significant proportion of the total concentration and the corresponding uncertainty in $f_{O2}$ is greater. For example, a [FMQ] $\log f_{O2}$ of -2.5 will have an associated uncertainty of about 0.8 log units.

The $f_{O2}$ conditions of the xenoliths have no correlation with the rock type (dunite, harzburgite, lherzolite and olivine websterite). Based on the obtained results the $f_{O2}$ conditions calculated for Panshishan and Fangshan samples range over four orders of magnitude from log $f_{O2}$~ 0.25 to -4.12 FMQ and from 2.26 to -2.13 FMQ, respectively (Table 6.1); Lianshan samples present a more restricted range, with log $f_{O2}$ from 0.55 to -2.4 FMQ.

As shown in Fig. 6.2, no correlation between equilibrium temperature and oxygen fugacity is observed. A general negative correlation between oxygen fugacity and pressure exist (Fig. 6.3). Interesting to note the Panshishan mantle domain, which record the lower pressure estimates, present also $f_{O2}$ values which extend the range of log $f_{O2}$ (FMQ), calculated for garnet-bearing peridotite xenoliths in many cratons, to both more oxidized and more reduced values (Creighton et al., 2009 and reference therein)

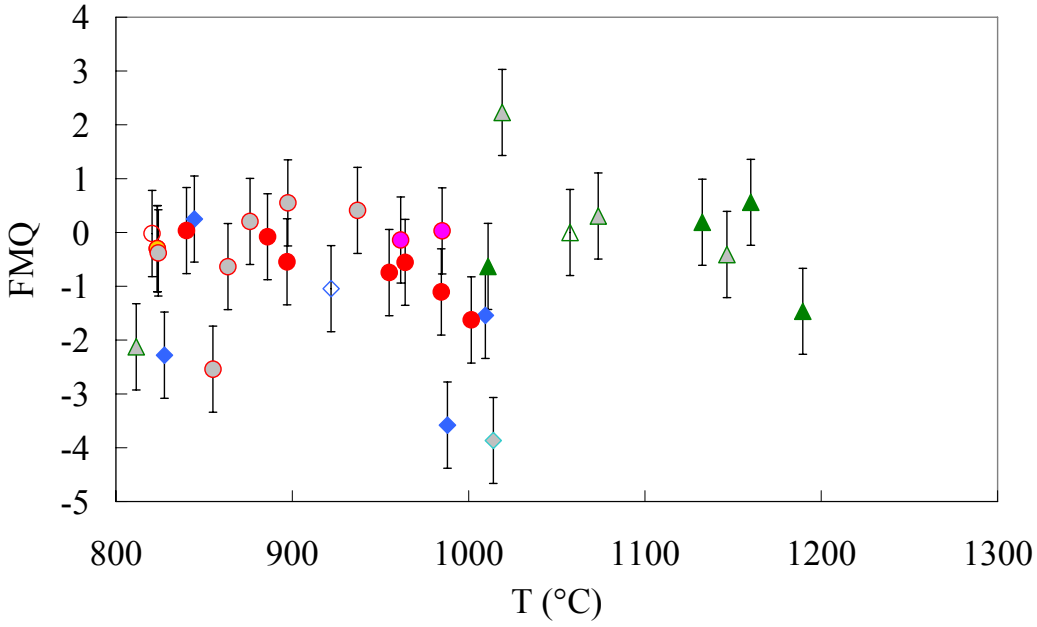


Fig. 6.2 - Oxygen fugacity vs equilibrium temperature of Subei basin xenoliths. (Symbols are as Fig. 6.1)

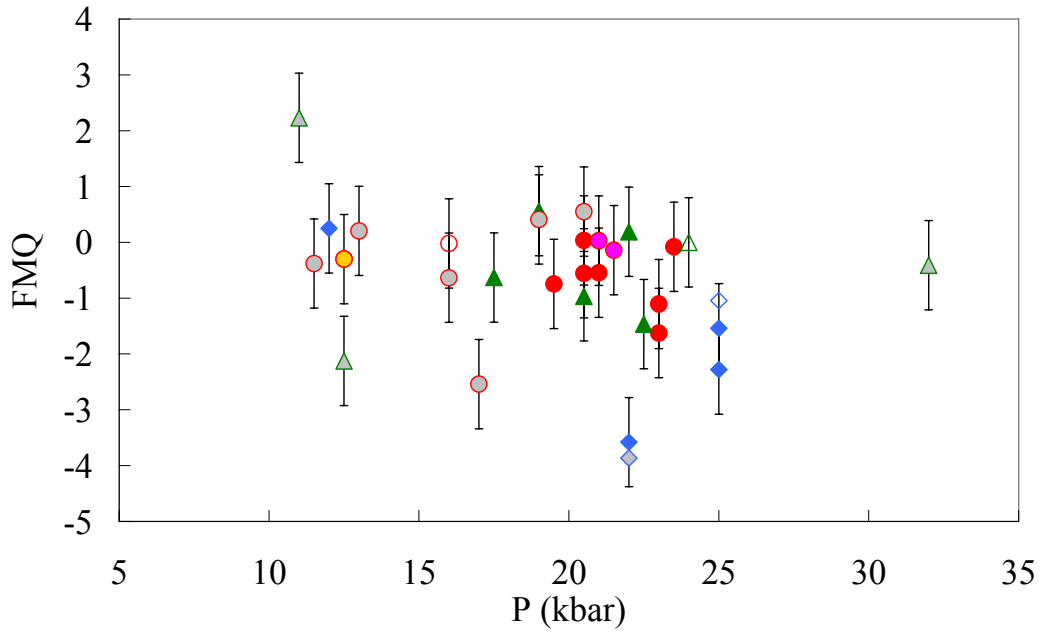


Fig. 6.3 - Oxygen fugacity vs Pressure of Subei basin xenoliths. (Symbols are as Fig. 6.1)

# Chapter 7 - Water content in opx and cpx

Hydrogen is one of the most pervasive elements in the lithosphere. It is a mobile, reactive component which can cause major changes in the chemical and physical properties of the Earth's crust and mantle, thus strongly affecting their rheological behavior (Hirth and Kohlstedt, 2003; Yang et al., 2008; van der Lee et al., 2008; Hirschmann et al., 2005). The evolution of this element along with its distribution with respect to tectonic settings is far from being fully understood. Most of the mantle petrologists' interest in hydrous components has, so far, been focused on the volatile reservoirs in the upper mantle and on the role these components may play in understanding and characterizing mantle processes, such as melting and metasomatism.

Hydrogen, in the chemical form of OH and $H_2O$, enters the structure of major minerals which are usually formulated as anhydrous. Initial studies were focused on water in quartz because of its weakening effect upon the mechanical strength of this mineral (e.g. Paterson, 1982). Hydroxide groups have subsequently been found in other nominally anhydrous minerals, such as feldspars, nepheline, garnets, sillimanite (and other aluminosilicates), rutile and zircon. These molecules and ions are structurally bounded in definite sites with distinct orientations and often persist in the minerals even at temperatures as high as 1200° C. Numerous studies were developed on the $H_2O$ storage capacity of peridotitic minerals, namely olivines, orthopyroxenes, clinopyroxenes and garnet. Measurements of OH concentrations in these nominally anhydrous minerals (NAMs) indicate that a large quantity of "water", amounting to about a third of the water in the oceans, is stored within the upper

mantle (Ingrin and Skogby, 2000). In this respect the upper mantle may represent the most important "water" reservoir on Earth. These mantle minerals can be brought up to the Earth's surface as xenoliths or xenocrysts in volcanics, probably not in chemical equilibrium with the surrounding melt (Nazzareni et al., 2008; Wade et al, 2008). Geochemical evidences support the retention of primary hydrogen concentrations in mantle minerals (Bell and Rossmann, 1992b), and these concentrations may also be modified during eruption, especially by reduction-oxidation reactions in iron-rich mantle minerals (Skogby and Rossman, 1989; Ingrin and Skogby, 2000).

Olivine is definitely the most abundant phase within the upper mantle, thus in order to model the Earth's mantle $H_2O$ budget, measurements of water contents in mantle olivines would be essential. However, diffusion profiles of hydrogen across olivine grains in mantle xenoliths suggest that olivine can loose significant portions of its water during transportation to the surface (Peslier and Luhr, 2006). This fact, together with the crystallographic inability to incorporate those key trace elements (i.e. alkalis, HFSE, REE) relevant for the comprehension of mantle melting and magma differentiation processes, strongly limit the use of this mineral. On the other hand, calculations of water content of melts in equilibrium with mantle pyroxenes (i.e. Bell et al., 2004), and initial calculations of the total amount of hydrous species stored in the mantle (200 to 550 ppm $H_2O$; Bell and Rossman, 1992) leads to the assumption that the OH in pyroxenes from mantle xenoliths is not incorporated or removed during the journey to the surface (Peslier et al., 2002). Pyroxenes, particularly clinopyroxenes, are also the most suitable and abundant upper mantle phase that can incorporate trace elements from the environment, thus marking the petrological processes. Besides T-P-X, many factors, such as water and oxygen

fugacity, crystallographic charge-coupled substitutions and diffusive properties of hydrogen within the mineral structures, play an important role in determining the concentration of hydrous species preserved in a mineral. Petrologists are gathering an increasing number of data from pyroxenes in intraplate (cratonic and off-cratonic) and suprasubduction settings in order to evaluate if water content in NAMs may be related to the geological evolution, thus somehow representing a fingerprint of the various processes which affect the lithosphere with time.

**Hydrogen species and water content**

All analyzed pyroxene grains in these peridotite xenoliths exhibit several absorption bands in the typical OH-stretching vibration region (3000-3800 $cm^{-1}$); the representative infrared spectra are shown in Fig. 7.1a, Fig. 7.1b, Fig. 7.2a, Fig. 7.2b, Fig 7.3a, and Fig. 7.3b for Panshishan, Lianshan and Fangshan xenoliths. By contrast, the coexisting olivine in these samples generally displays very weak, if any, H absorption (Fig. 7.4). The relative absorbance of these bands are highly variable for different grains even within the same sample, which is attributed to different orientations of different grains with respect to the infrared beam direction. The position and shape of these absorption bands are mostly similar to available results for the corresponding minerals (Skogby and Rossman, 1989; Skogby et al., 1990; Peslier et al., 2002; Stalder and Skogby, 2002, 2003; Grant et al., 2007b; Yang et al., 2008; Li et al., 2008; Bonadiman et al., 2009), while slight differences for some spectra may be associated with the chemical composition and crystal structure of the hosted phases. Correspondingly, it is suggested that these absorption bands are mainly related with the stretching vibration of structural hydroxyl.

Base on the position, the IR absorption bands of pyroxenes can be divided into different groups for each mineral: 1) clinopyroxene: 3600-3635 $cm^{-1}$, 3510-3550 $cm^{-1}$, 3445-3470 $cm^{-1}$; 2) orthopyroxene: 3570-3595 $cm^{-1}$, 3500-3525 $cm^{-1}$, 3390-3415 $cm^{-1}$, 3300-3315 $cm^{-1}$. The last one is very rare. This hypothesis is further supported by the polarized analysis of some oriented grains: the absorption intensity of each peak varied according to the polarizing direction. Hydrogen profile measurements performed on many pyroxene grains in each suite of samples along various crystallographic directions show no obvious variations between core and rim regions (Fig. 7.5), indicating that diffusion loss of H in clinopyroxene and orthopyroxene during their ascent is insignificant. For olivine grains with weak OH absorption bands (Fig. 7.4), the main peaks are at 3572 $cm^{-1}$ and 3525 $cm^{-1}$ which are typical for mantle olivine (Bell and Rossman, 1992a; Berry et al., 2005; Demouchy et al., 2006; Peslier and Luhr, 2006; Grant et al., 2007b).

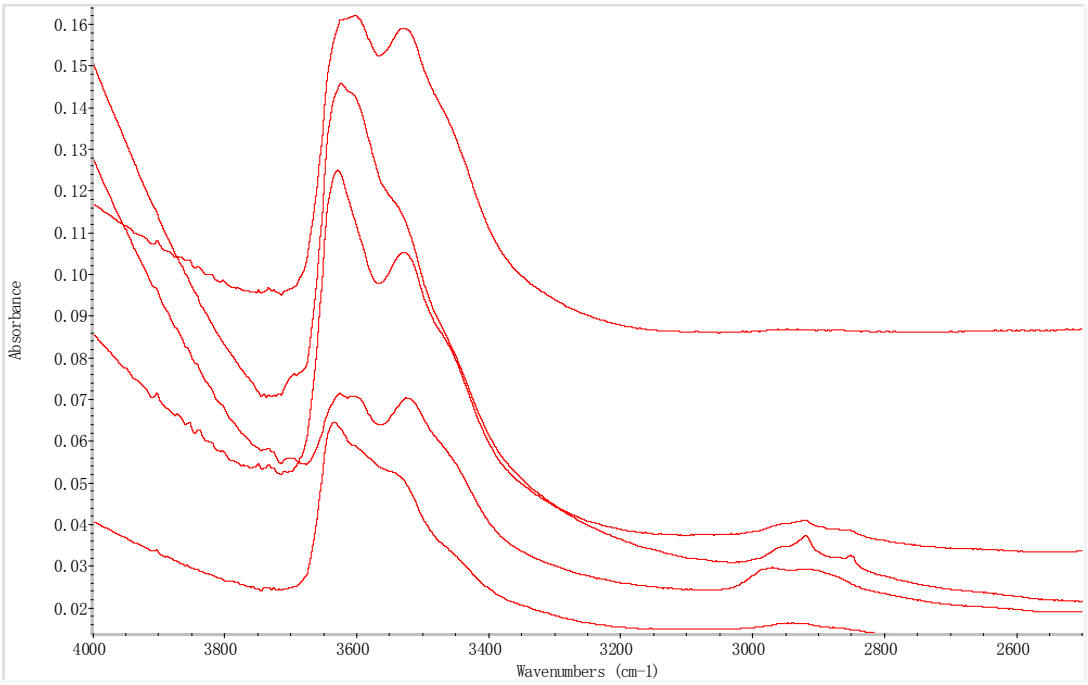


Fig. 7.1a - Representative IR spectra for cpx in Panshishan peridotite xenolith (The spectra are shown in a full scale)

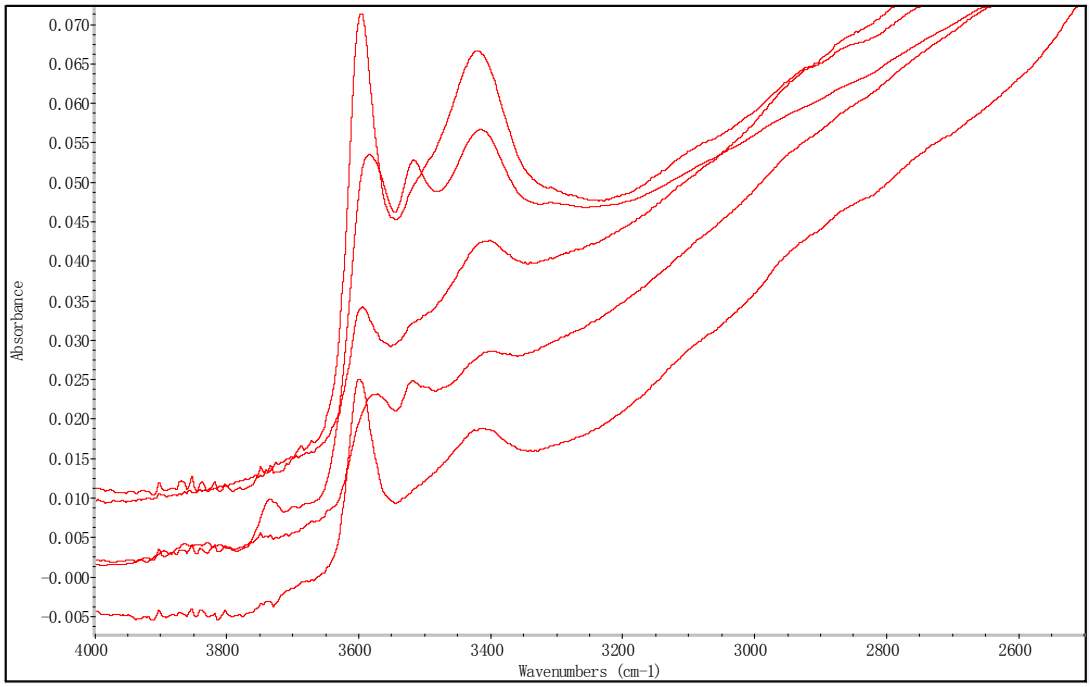


Fig. 7.1b - Representative IR spectra for opx in Panshishan peridotite xenolith.

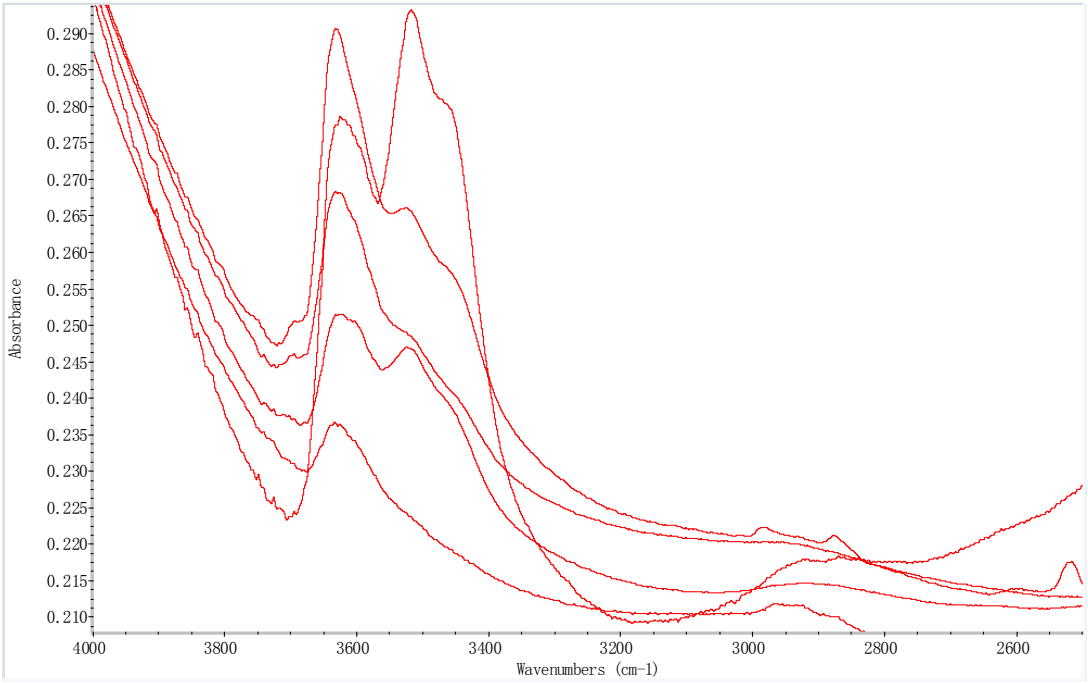


Fig. 7.2a - Representative IR spectra for cpx in Lianshan peridotite xenolith.

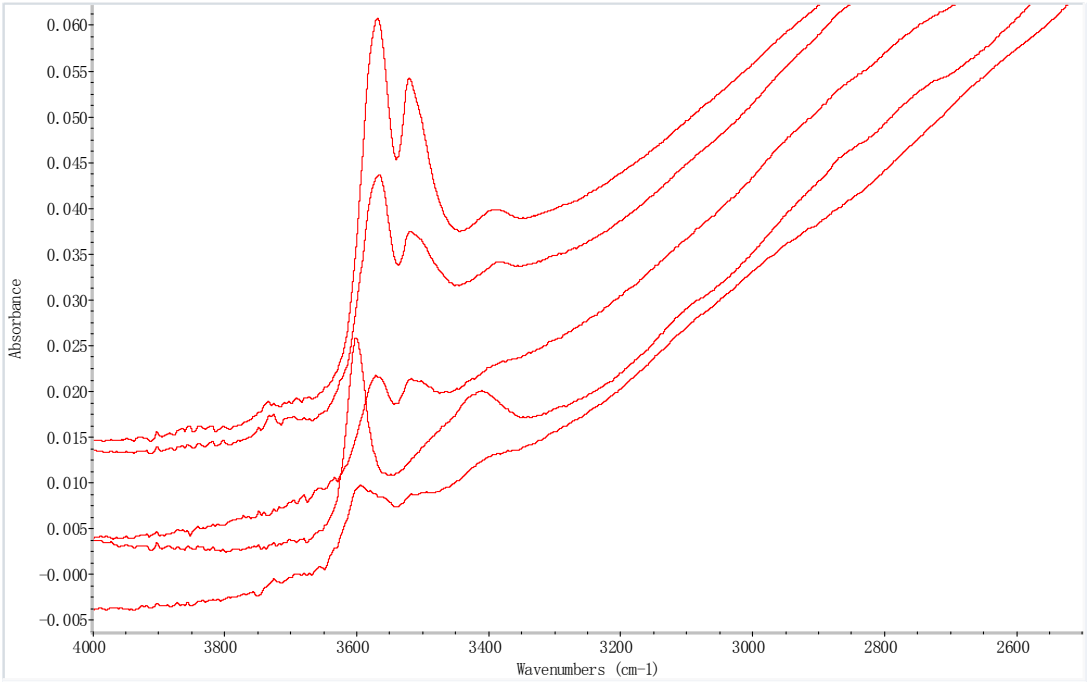


Fig. 7.2b - Representative IR spectra for opx in Lianshan peridotite xenolith

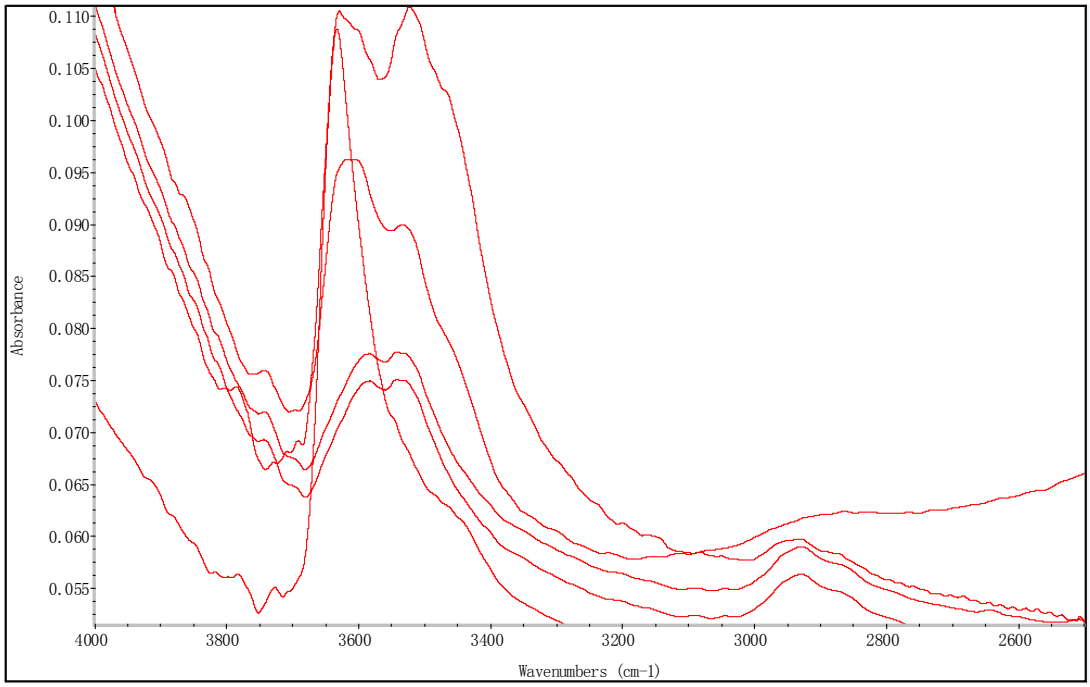


Fig. 7.3a - Representative IR spectra for cpx in Fangshan peridotite xenolith

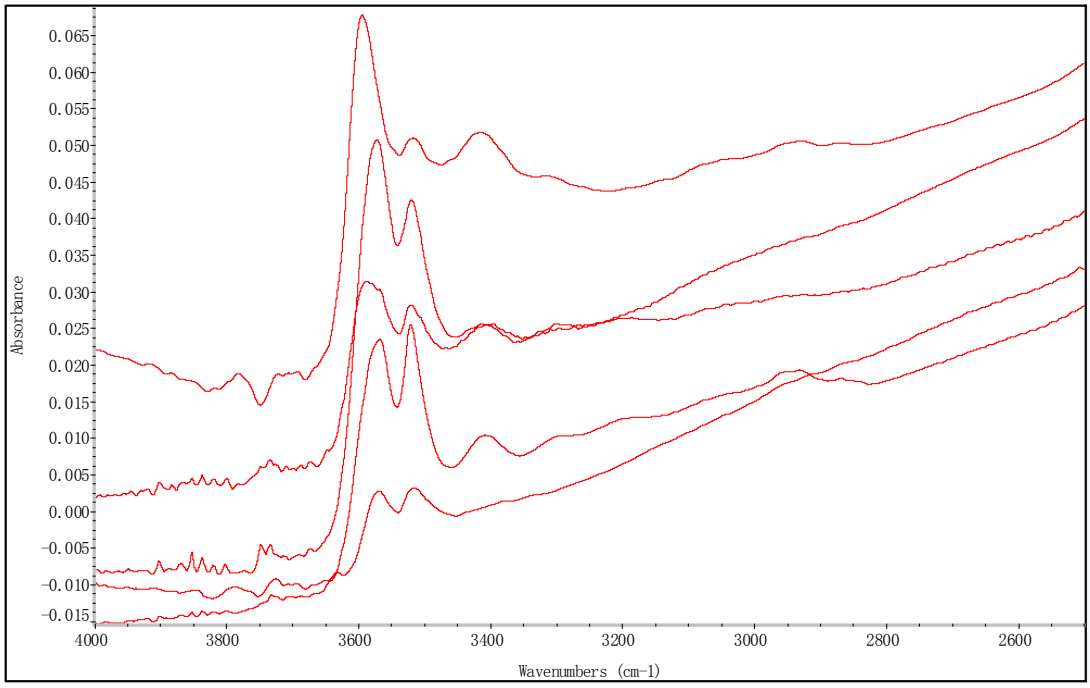


Fig. 7.3b - Representative IR spectra for opx in Fangshan peridotite xenolith

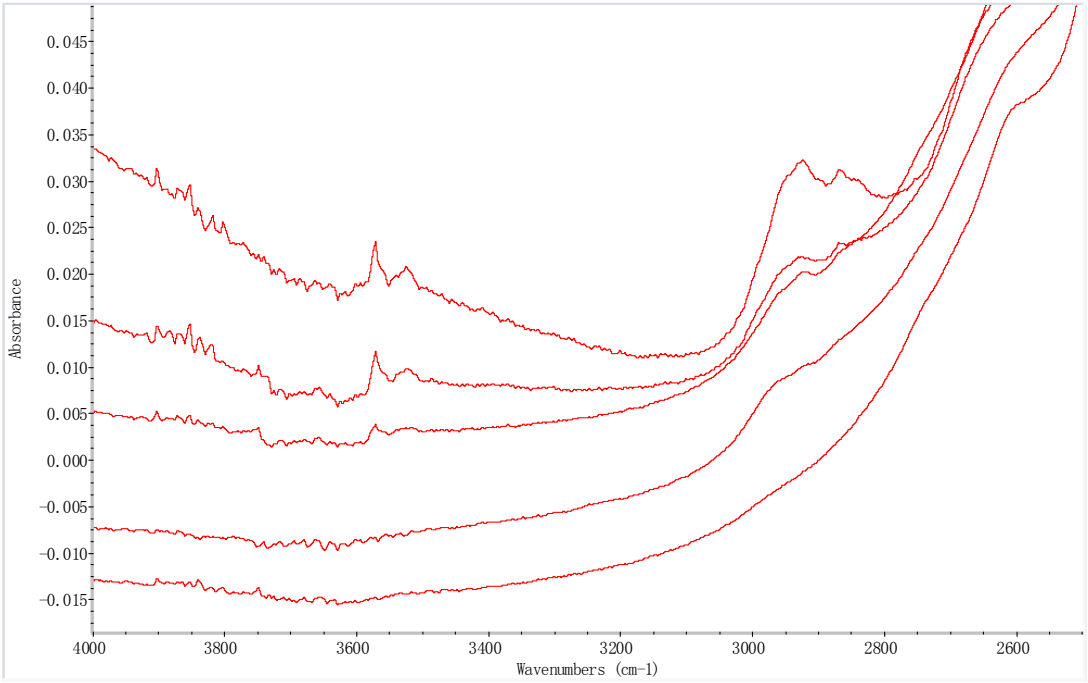


Fig. 7.4 - Representative IR spectra for ol in Panshishan peridotite xenolith

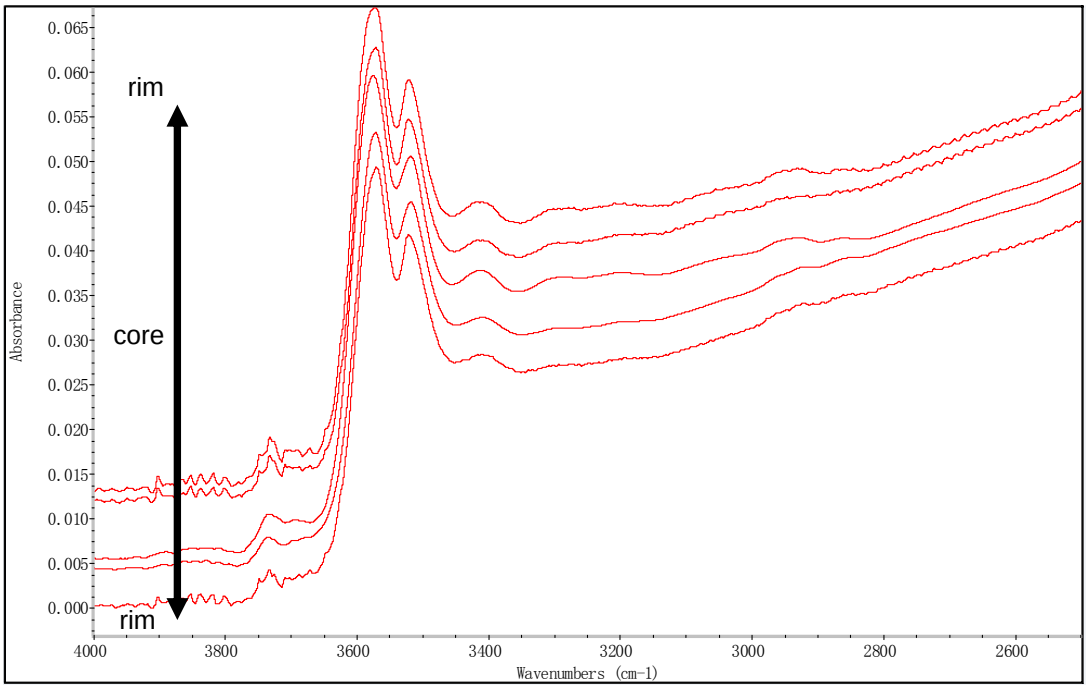


Fig. 7.5 - Profile analyses of H absorption in Lianshan opx

**Water content in minerals**

The determined water content for cpx and opx of Subei basin peridotite are reported in Table 7.1. Water content varies from 37 to 183 ppm for cpx and 13 to 74 ppm for opx in these peridotite xenoliths. Water contents range from 64 to 183 ppm for cpx and from 16 to 61 ppm for opx in Panshishan peridotites; from 37 to 102 ppm for cpx and from 13 to 45 ppm for opx in Lianshan peridotites; from 41 to 177 ppm for cpx and from 21 to 74 ppm for opx in Fangshan peridotites. As shown in Fig. 7.6a, as more than 50% of the sampled xenoliths are lherzolites, they cover the whole range of water content in opx and cpx. Compare to lherzolites, the cpx-poor lherzolites have a lower up limited water content with less than 100ppm for cpx and less than 50ppm for opx. Two harzburgites PSS17 and FS06 have high water content and harzburgite LS26 have low water content of 57 ppm for cpx and 19 ppm for opx. The two Lianshan olivine websterite have water content of 56 to 80 ppm for cpx and 28 to 34 ppm for opx. The water content of cpx correlates with opx ($R^2$=0.58) with a ratio cpx/opx of 2.34 (Fig. 7.6a), cpx/opx ratio is 2.01 and $R^2$=0.63 for Panshishan, cpx/opx ratio is 1.97 and $R^2$=0.77 for Lianshan and cpx/opx ratio is 2.79 and $R^2$=0.95 for Fangshan. Taking into account all the peridotites from the NCC (Aubaud et al., 2007; Yang et al., 2008; Bonadiman et al., 2009; this study), this ratio is 1.97 ($R^2$=0.77, Fig. 7.6b). These values agree well with the reported H-partition coefficient between cpx and opx from both experimental and natural mantle samples (Bell and Rossman, 1992a; Peslier et al., 2002; Koga et al., 2003; Aubaud et al., 2004, 2007; Bell et al., 2004; Grant et al., 2007b; Tenner et al., 2009). The pyroxenes from Subei basin peridotites thus achieved equilibrium for hydrogen in the mantle and preserved

their initial water content. The latter is confirmed by the homogeneous distribution of water within individual pyroxene grains revealed by core-rim profile analyses (Fig. 7.5).

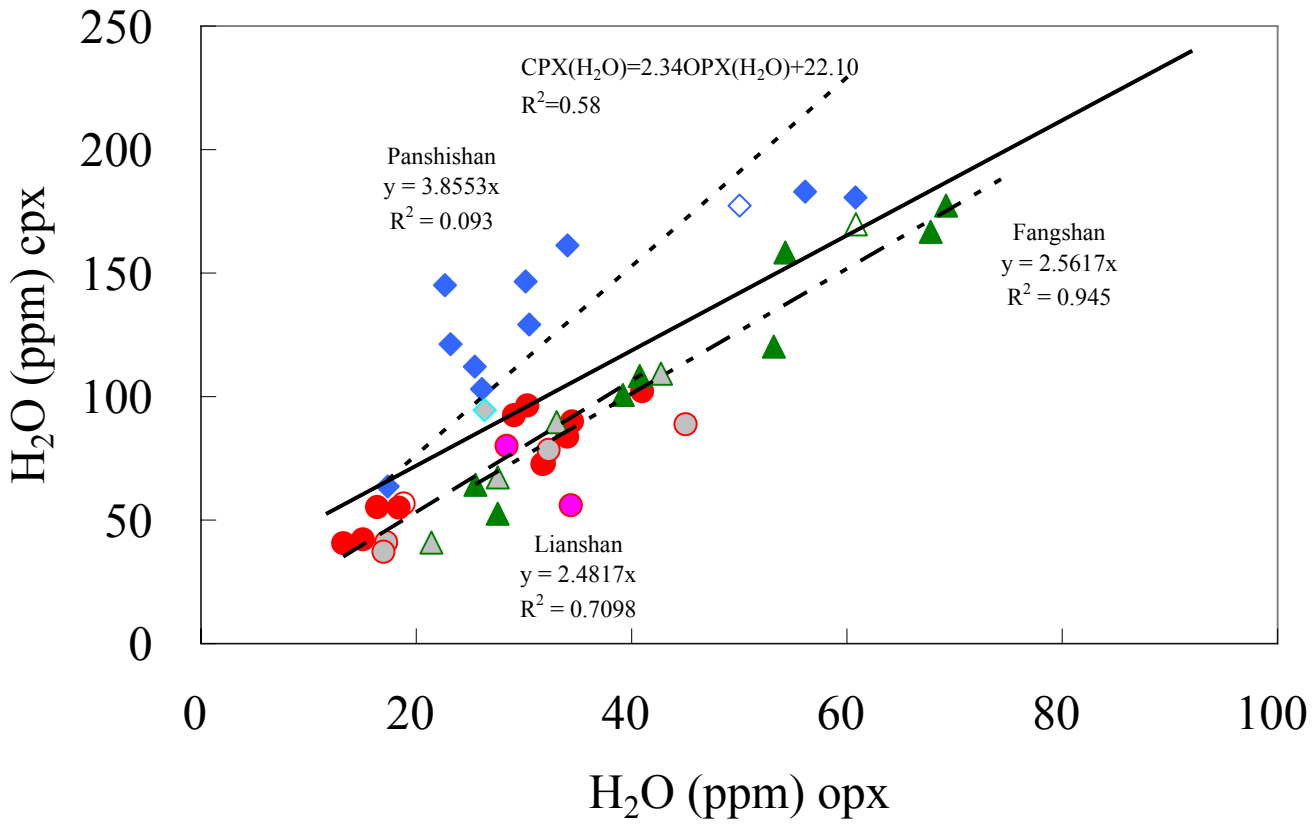


Fig. 7.6a - Water content of cpx and opx in Panshishan, Lianshan and Fangshan xenoliths. (Symbols are as Fig. 4.4. Light blue diamond, Panshishan lherzolite; light blue filled grey diamond, Panshishan cpx-poor lherzolite; blue open diamond, Panshishan harzburgite; red dot, Lianshan lherzolite; red filled grey dot, Lianshan cpx-poor lherzolite; red open dot, Lianshan harzburgite; red filled pink dot, Lianshan olivine websterites; red filled golden dot, Lianshan dunite; green triangle, Fangshan lherzolite, green filled grey triangle, Fangshan cpx-poor lherzolite; green open triangle. Fangshan harzburgite)

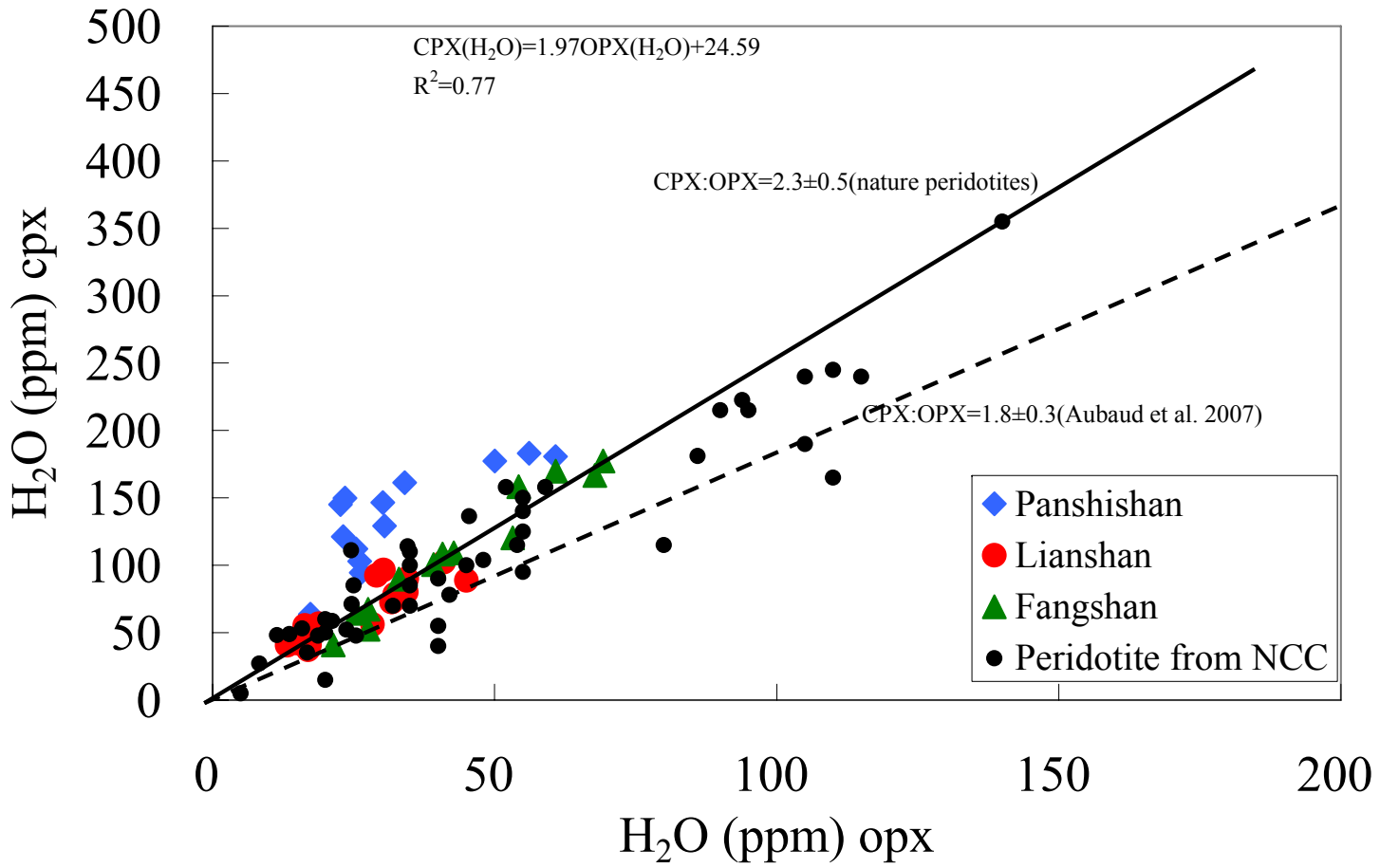


Fig. 7.6b - Water content of cpx and opx in Panshishan, Lianshan, Fangshan and NCC peridotites (Yang et al., 2008; Xia et al., 2010; Bonadiman et al., 2009)

**Whole rock water content**

Generally, water content of olivine from peridotite xenoliths hosted by alkaline basalts is very low (mostly <10 ppm, Bell and Rossman, 1992a; Peslier and Luhr, 2006; Grant et al., 2007b). In addition to their initial low water contents, this could partly be caused by loss of H in olivine during ascent due to its very fast velocity (e.g. Demouchy et al., 2006; Peslier and Luhr, 2006). By contrast, the coexisting pyroxenes usually preserve their initial H-information (Peslier et al., 2002; Bell et al., 2004; Grant et al., 2007a; Yang et al., 2008; Bonadiman et al., 2009; this study), which are possibly related with their slower H diffusion rates (H may diffuses 1-3 orders of magnitude faster in olivine than in pyroxenes: Wade et al., 2008). In our case, the OH contents measured in ol (~ 0 ppm) cannot represent their source value. Instead, an initial $H_2O$ content can be calculated for ol by considering equilibrium partitioning between pyroxenes and ol. The $H_2O$ partition coefficients between pyroxene and olivine determined by experiments are highly variable. The values obtained at low pressure (<3 GPa) are much higher than those at high pressure (>8GPa): At low pressures, Koga et al. (2003) obtained a value of 12±2 for Dopx/ol from a single experiment at P=1.8 GPa; Aubaud et al. (2004) (revised according to the new calibration of Aubaud et al. 2007) determined Dcpx/ol and Dopx/ol of 28±2 (n=2) and 14±2 (n=4) respectively at P=1-1.5 GPa; Hauri et al. (2006) reported Dcpx/ol and Dopx/ol of 15±5 (n=5) and 10±3 (n=8) respectively at P=0.5-1.6 GPa; Grant et al. (2007a) determined Dopx/ol=25±1 (n=2) at 289 P=1.5 GPa; Tenner et al. (2009) obtained Dcpx/ol of 27 (n=1) at P=3 GPa. In contrast, at higher pressures, Withers and Hirschmann (2007) reported Dopx/ol of 1.3±0.2 (n=4) at P=8.0-12 GPa; Withers and Hirschmann (2008) obtained Dopx/ol of 1.5±0.2 (n=3) at P=8.0 GPa. The difference between low-pressure and high-pressure experiments is probably related to reduced pyroxene Al content at P>3 GPa, it has been confirmed by experiments 294 that Al could enhance water solubility in pyroxene. Grant et al. (2007a) have shown that ol, opx and cpx from 8 peridotite xenoliths preserved the $H_2O$ contents of their mantle source and had Dcpx/ol values of 88±48 and 22±24 for spinel peridotites (P=1.1-2.8 GPa) and garnet peridotites

298 (P=3.7-7.4 GPa) respectively. The Subei basin xenoliths hosted by Cenozoic basalts are from relatively thin 300 lithospheric mantle (<80-100 km; Menzies et al. 2007), and the partition coefficient of $H_2O$ between pyroxene and olivine should be similar to those determined by low-pressure experiments (i.e. Dcpx/ol>10; Koga et al. 2003; Hauri et al. 2006; Aubaud et al. 2007, 2009; Grant et al. 2007a; Tenner et al. 2009). In the following, we use a Dcpx/ol = 10 to calculate the $H_2O$ content of coexisting ol; the calculated values should therefore represent maximum estimates. The recalculated whole-rock $H_2O$ contents based on mineral modes should also represent maximum estimates. The calculated $H_2O$ content of whole rocks (table 7.1) are between 8-58 ppm and mostly less than 40 ppm.

# Chapter 8 - Discussion and conclusions

## Depletion event/s

In spinel-bearing peridotites clinopyroxene is the major host for most trace elements and commonly its incompatible-element pattern control that of the peridotite with the exception of Ba, Nb, and Ti (Chalot-Prat and Boullier, 1997; Zangana et al., 1999; Gregoire et al., 2000). Melting and enrichment processes have been modelled using major element whole rock and mineral geochemistry, as well as REE patterns (e.g. Johnson et al, 1990; Norman, 1998; Gregoire et al., 2000; Xu et al., 2000; Wang and Gasparik, 2001; Neumann et al., 2004)(Fig. 5.9, 5.10, 5.11).

The group I xenoliths from Panshishan, Lianshan and Fangshan can be considered as residues from partial melting processes. The ubiquitous presesence of these LREE-depleted cpx in the three populations indicate that partial melting played an important role in the history of Subei basin lithospheric mantle. Trace element abundances can be used to illustrate the extent of the partial melting process. To assess the extent of partial melting, we applied the trace element non-modal partial melting equations of Johnson et al. (1990).

Three melting models, based on batch, fractional and incremental melting equations, have been formulized (Johnson et al., 1990; Norman, 1998; Yang et al., 1998; Xu et al., 2000). In batch melting, solid and liquid fractions remain together throughout the entire melting interval, while in fractional melting infinitesimal increments of melting occur, accompanied by instantaneous segregation (and separation) of the melt from the solid residue. Incremental melting is intermediate to these two theoretical end-members, in which small, but finite, increments of melting and segregation occur, with a new starting composition applied after each segregation event. Equilibrium partitioning of elements is maintained in all models. Fractional melting depletes the residue in the most incompatible elements (i.e LREE) far more effectively than batch melting and the two processes are easily distinguished in REE and incompatible element diagrams (Johnson et al., 1990; Norman, 1998). Although infinitesimal melt

fractions produced by fractional melting are quite different from large melt portions produced by batch melting, liquids produced by the two melting models are virtually indistinguishable if fractional melts are integrated or aggregated following segregation from source (Johnson et al., 1990). Cpx REE melting models are subsebently compared with GroupI cpx, in order to evaluate the degree of melting for the Subei Basin mantle domain.

In general, minerals do not enter the melt in their modal proportions, thus non-modal partial melting is necessary to model the pattern. The important input parameters in the models are starting bulk composition, partition coefficients, proportions of minerals in the bulk solid, and those contributing to the liquid, and melting equations. The proportions of minerals in the bulk solid were assumed to be 55 vol% olivine, 25 vol% orthopyroxene, 18 vol% clinopyroxene and 2 vol% spinel for spinel-bearing peridotite and 55 vol% olivine, 20 vol% orthopyroxene, 15 vol% clinopyroxene and 10 vol% garnet for garnet-bearing peridotites at the beginning of the melting processes. The proportions of minerals contributing to the liquid were 10 vol% olivine, 20 vol% orthopyroxene, 68 vol% clinopyroxene and 2 vol% spinel in spinel facies phase and 13 vol% olivine, 12 vol% orthopyroxene, 25 vol% clinopyroxene and 50 vol% garnet in garnet facies (Table 8.1). The cpx is rapidly consumed when melting process occurs in both spinel and garnet facies.

The partition coefficients between mineral and melt for REE and other trace element are chosen from literature (Database of Geochemical Earth Reference Model GERM, http://earthref.org/GERM, Fujimaki et al., 1984; McKenzie and O'Nions, 1991; Nielsen et al., 1992; Hart and Dunn., 1993; Dunn and Sen, 1994; Zack et al., 1997; Johnson 1994,1998; Takazawa et al., 2000; Adam et al., 1994,2006; Elkins et al., 2008), which were obtained in both experimental and natural samples. In the former, two phases are equilibrated at the temperature and pressure of interest and the concentration of the element is subsequently measured in both. In the latter, the concentration of element is simply measured in two natural phases thought to be in equilibrium. The range of partition coefficient for element changes, thus we choose a set of data which give a smooth REE pattern (Table 8.2). The starting bulk

composition was a primitive mantle value (McDonough and Sun, 1995), and using the mineral/melt partition coefficient for each element, we calculate the element distribution in cpx in spinel and garnet facies (Table 8.3).

The equations are those given by Johnson et al. (1990) :

$$C^i=C^0\times[D^0/(D^0+F\times(1-P))$$

for non-modal batch melting, and

$$C^i=C^0\times[1-P\times F/D^0]^{(1/P-1)}$$

For nor-modal fractional melting, in which $C^0$ and $C^i$ are the concentrations of REE elements (such as La, Ce, ……Lu) in cpx in the initial source and residue, respectively; $D^0$ is the bulk partition coefficient of element for all the phase in the initial source; P is the sum of the partition coefficient of phases in the proportions they enter the melt; and F is the extent of depletion (incremental melting, each increment of melt was produced by 1% batch melting. Because melt presumably would segregate from its source after 1% batch melting, resulting residue from each increment becomes the source for the next 1% batch melt).

Use the parameter set and equation above, we model the melting process in both spinel and garnet facies for batch melting and fractional melting (Fig. 8.1, 8.2).

In both spinel and garnet peridotites, fractional melting are much more efficient to decrease the LREE content in cpx than batch melting at comparable degree of melting. I compare the data from the Subei basin peridotites with the calculated model of melting, the batch melting fails to produce the REE exhibited by the highly depleted cpx in peridotite, both the petrography and REE abundances of this xenolith are inconsistent with it being a residue of batch melting. The fractional melting model fits the data better than batch melting.

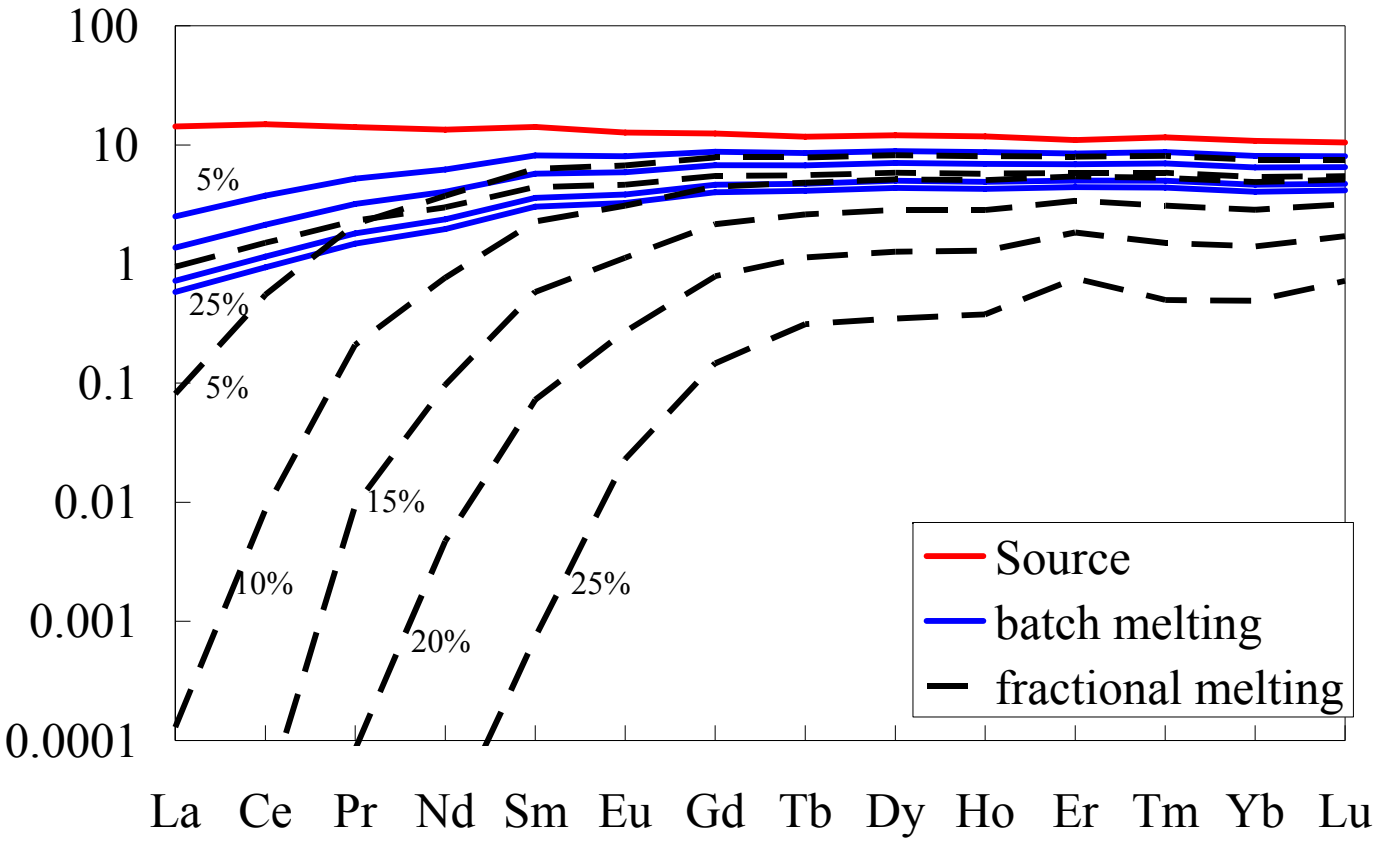


Fig. 8.1 - Melting modelling using both batch and fractional melting in spinel facies. The extent of melting F is from 0 to 25%. Red line is the REE distribution in a primitive mantle cpx (McDonough and Sun, 1995). Blue continuous line are batch melting and black dashed line are fractional melting.

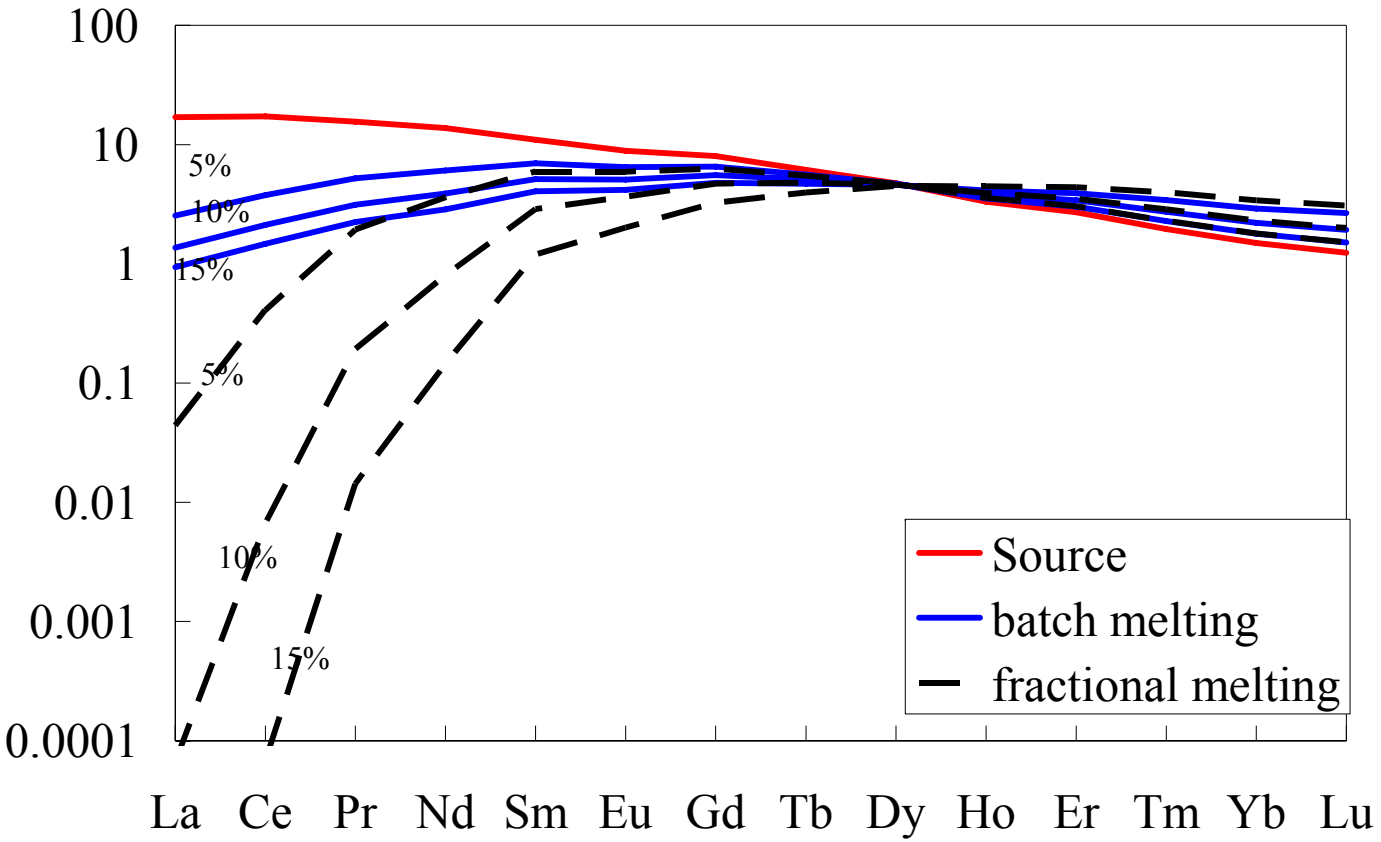


Fig. 8.2 - Melting modelling using both batch and fractional melting in garnet facies. The extent of melting F is from 0 to 15%. Red line is the REE distribution in a primitive mantle cpx (Bonadiman et al., 2005). Blue continuous line is batch melting and black dashed line is fractional melting.

Samples of group I from each localities show depleted LREE pattern, other groups show either LREE or MREE enrichment, which can not produced by melting, so only group I REE pattern in fractional melting model are shown below (Fig. 8.3). In each locality, we chose the samples which have the lowest and the highest value of REE to represent the REE ranges in the samples of this group. For Lianshan cpx in group I, LS09 is also shown in the plot as it has depleted LREE compare to LS24.

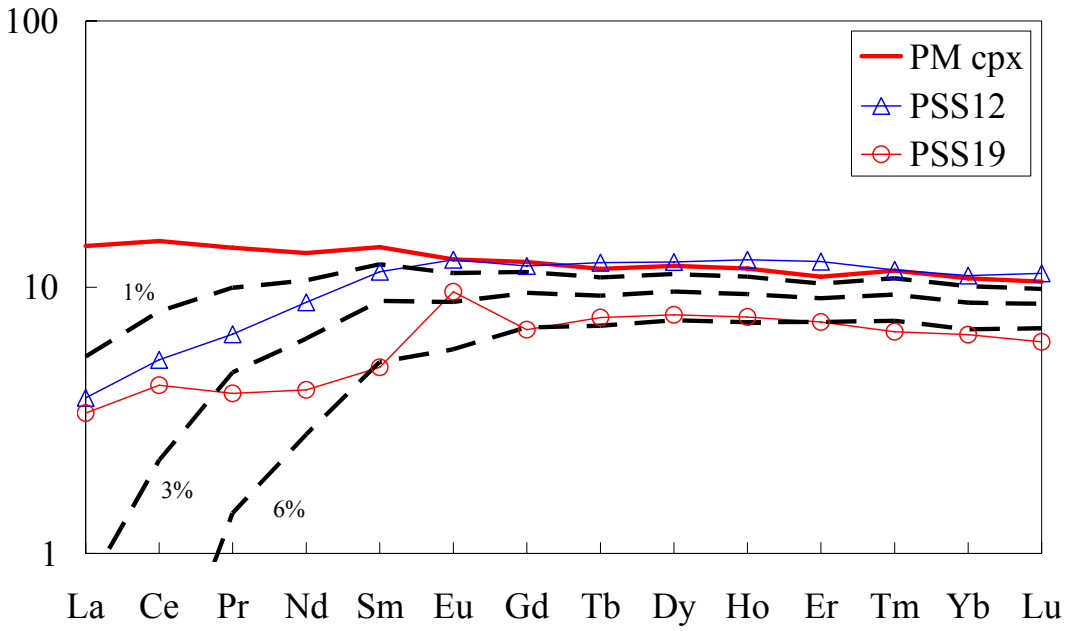

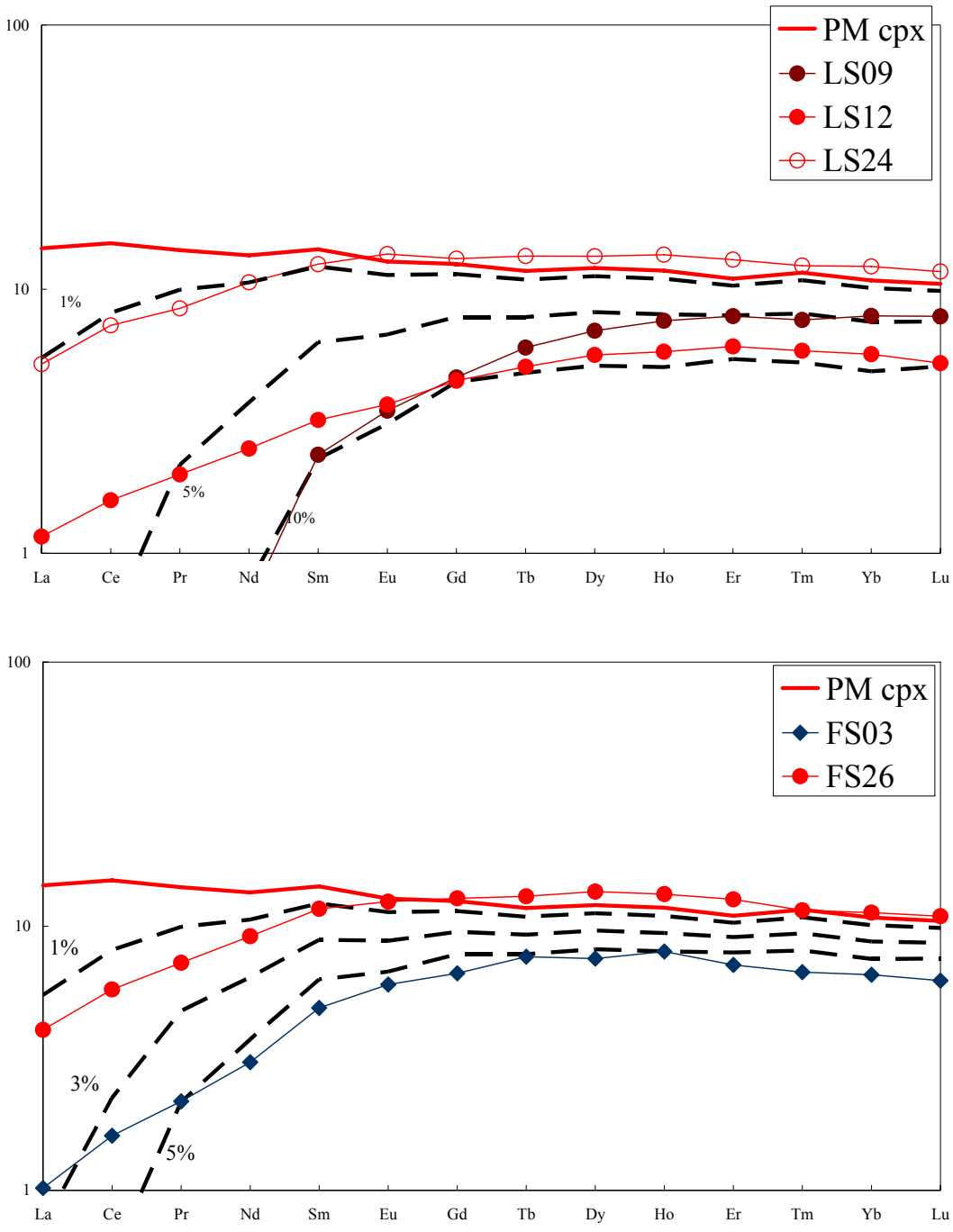


Fig. 8.3 - Modelling of REE patterns in spinel facies for clinopyroxenes from Subei basin xenoliths.

For Group I cpx from Panshishan, Fractional melting produces a matching REE pattern for the depleted lherzolite at 6% melting, although some samples (e.g. PSS13 and PSS19) have LREE which do not match the melt curve possibly due to later enrichment process.

For group I cpx from Lianshan, 1% melting of PM cpx can produce the most fertile sample LS24, 5% melting of PM cpx can produce the same HREE pattern of LS09, but not match for the LREE pattern. and the most depleted sample LS12 require a near 10% fractional melting to produce the HREE pattern, while the LREE are more enriched compare to the melting curve. For Fangshan group I samples, to match the patterns for REE, an extent F about 1-5% fractional melting can cover the sample REE pattern.

As shown in chapter 5 (Fig. 5.9, 5.10), the group II xenoliths have an upward convex REE pattern. Melting modeling in garnet facies can raise the MREE and HREE content, which may possibly produce the REE pattern in group II (Fig. 8.4). Since there are no sample in Fangshan and only one sample for Lianshan within this group, we put all the samples including PSS05, PSS11, PSS15, PSS16 and LS22 in one figure. Sample PSS10 in group V from Panshishan is also plot in the melting grids, as it has MREE upward convex. Despite element La, which may be affected by later host magma interaction, the cpx in PSS10 have the same M-HREE pattern as the PM cpx melting at 3% , but near 2 times higher.

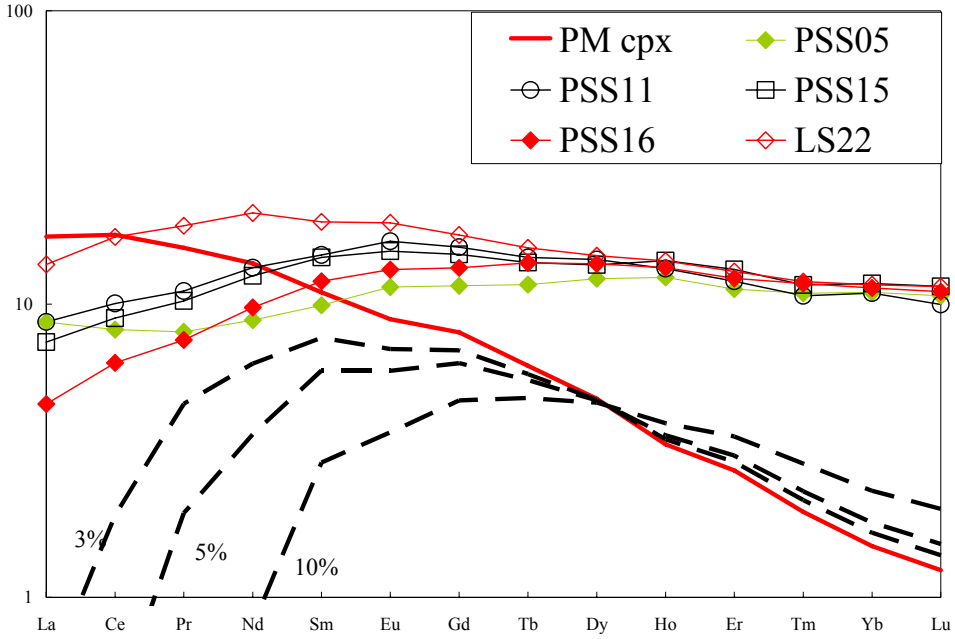


Fig. 8.4a - Modelling of REE patterns in garnet phase for clinopyroxenes from Subei basin xenoliths

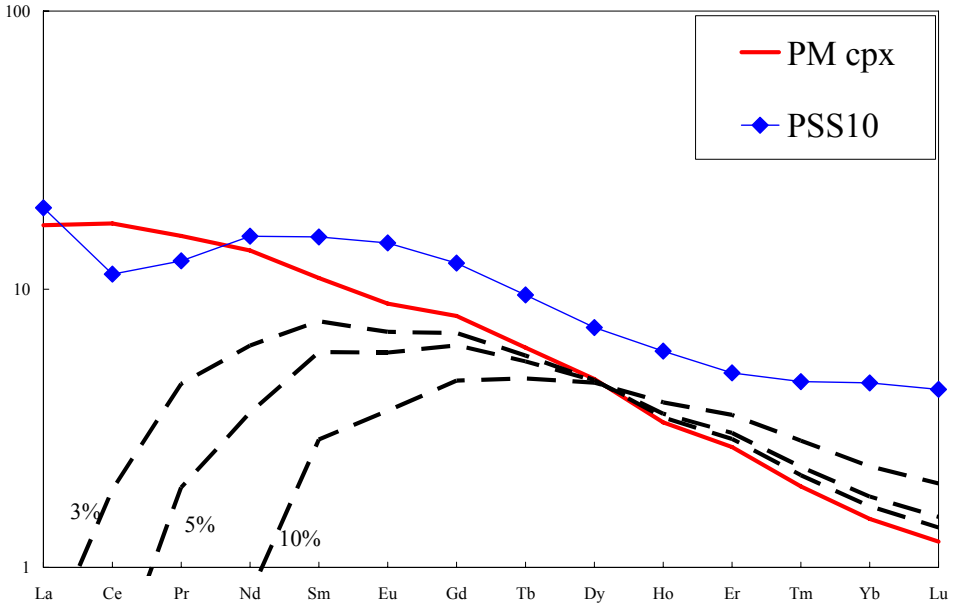


Fig. 8.4b - Modelling of REE patterns in garnet phase for PSS10 clinopyroxenes

The simple melting model applied to sp-bearing system is not able to re-produce the observed group II cpx upward convex trace element pattern; therefore I tested the hypothesis that Group II trace element profile could be consistent with a prior partial melting in the garnet stability field. Subsequently, the xenoliths would be re-mobilized towards shallower lithospheric domains (sp-stability field) and the residual garnet would break up, and subsolidus reactions take places. The starting mineral proportions are 55 vol% ol, 20 vol% opx, 15 vol% cpx and 10 vol% grt (the same set as previous calculation) at the initial stage of melting. The proportions of minerals contributing to the liquid were 13 vol% ol, 12 vol% opx, 25 vol% cpx and 50 vol% grt for garnet phase. For melting occurred in the range of degree (F) of 1%-20%, the residue will have a proportion of minerals of 0.55-0.13F, 0.2-0.12F, 0.15-0.25F and 0.1-0.5F % for ol, opx, cpx and sp, respectively. Subsequently I model the passage of this theoretical grt-peridotite in sp-stability field. I apply the fellow reaction:

0.261 ol+grt=0.765 opx+0.222 cpx+0.264 sp (Takazawa et al., 1996)

As the spinel appear, the original grt trace element contents will be distributed among the other peridotite minerals and until grt disappears. Fig. 8.5 shows REE patterns at F of 1, 3, 5, 10, 15, and 20 %. 20% of melting is ideally the maximum degree of melting for the complete consumption of the grt. The results show an almost flat constant MREE-HREE pattern, and slight depleted in LREE applied the batch melting equation; a large LREE fractionation is modelled with the fractional melting equation.(Fig. 8.5)

I compare REE pattern of group II cpx, including PSS05, PSS11, PSS15, PSS16 and LS22, with the calculated model of melting. The grt/sp transfer

model is able to accont for the profiles of GROUP II cpx, with the exception of lherzoliteLS22. (Fig. 8.6)

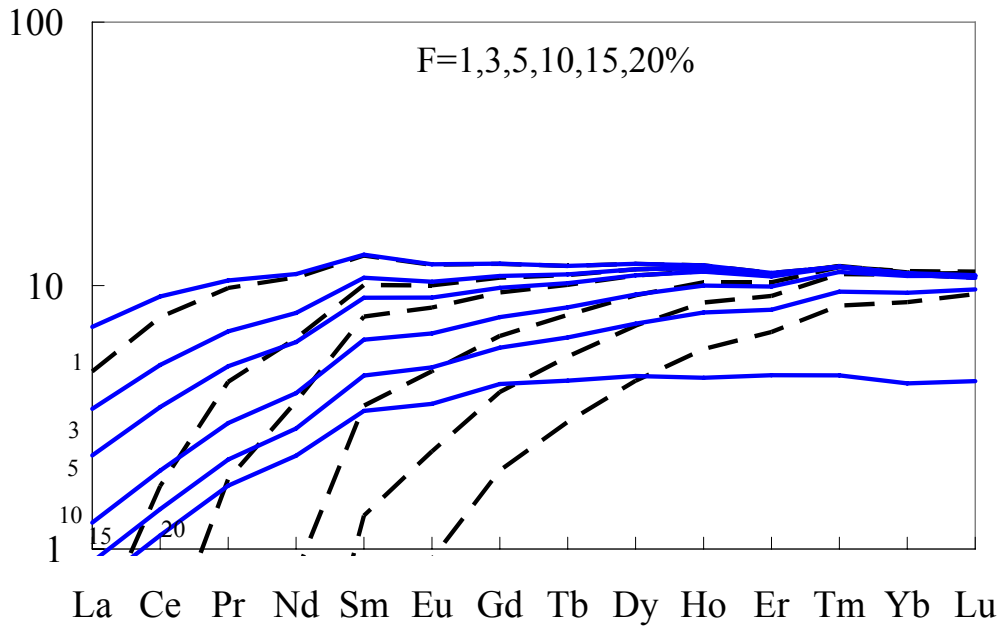


Fig. 8.5 - Melting modelling in garnet facies and re-equilibration in spinel facies. Batch melting: Continued line. Fractional melting: dashed line.

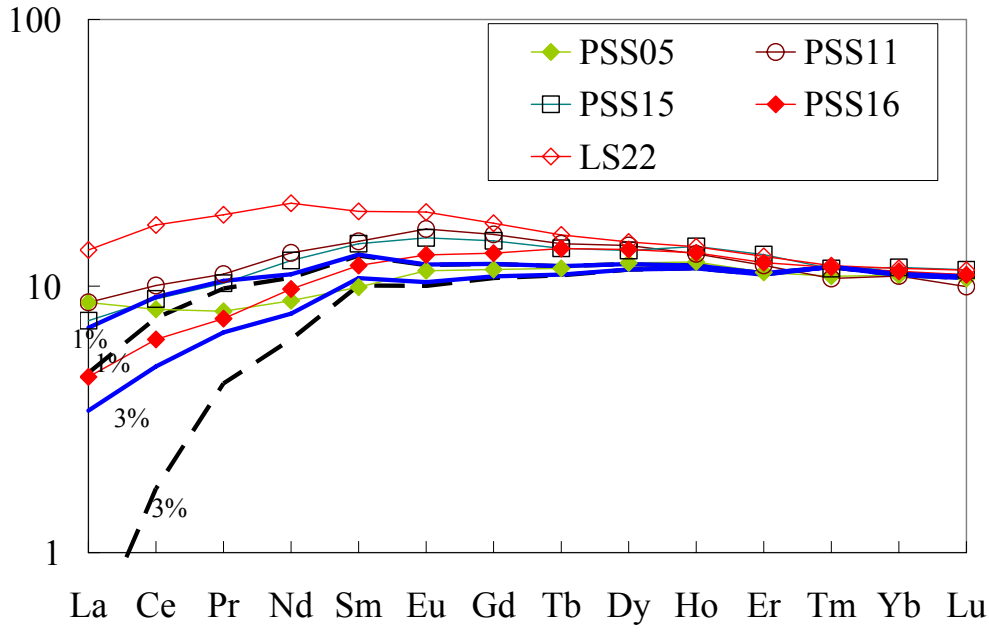

Fig. 8.6 - Modelling of REE patterns in garnet facies for Group II cpx

**Zr and Sr modeling**

Zr and Sr concentrations of clinopyroxenes were used by Yang et al. (1998) to model melting processes, because they may more effectively distinguish batch melting from fractional melting models. However, Sr is affected easily by metasomatism, so possible metasomatic effects must be ruled out before modelling. The Zr–Sr plots of cpx from Subei basin peridotites (Fig. 8.7) show that depleted and slightly metasomatized clinopyroxenes result in a consistent correlation whereas more strongly metasomatized samples, such as samples in group II and group III in each localities, deviate significantly and are more enriched in Sr at given Zr levels. Melting trends based upon batch melting and fractional melting are shown in Fig. 8.7. The compositional variations for Zr and Sr in the cpx from Subei basin peridotites can be successfully modelled using a Sr content of 108 ppm and Zr content of 47 ppm for the source, rather than Sr content of 38.1 ppm and Zr content of 39.4ppm used in the modelling of Yang et al. (1998). Although both batch melting and fractional melting models reproduce the natural trends in Sr and Zr of the cpx, different melting degrees are required for each melting style. To reproduce Zr and Sr contents of the most depleted sample LS09, which have the lowest Zr and Sr values, more than 25% batch melting would be required, which is unrealistic (Fig. 8.7). In contrast, fractional melting produce residual peridotite with the Sr and Zr values of LS09 with reasonable degrees of melting of about 9%.

The xenoliths we studied undergo a melt extracting event to have the HREE pattern we observed. I did not have our date to constrain the time this event happen, use Reisberg et al. (2005) Re-Os isotope data, an age of 1.8Ga can be aspect.

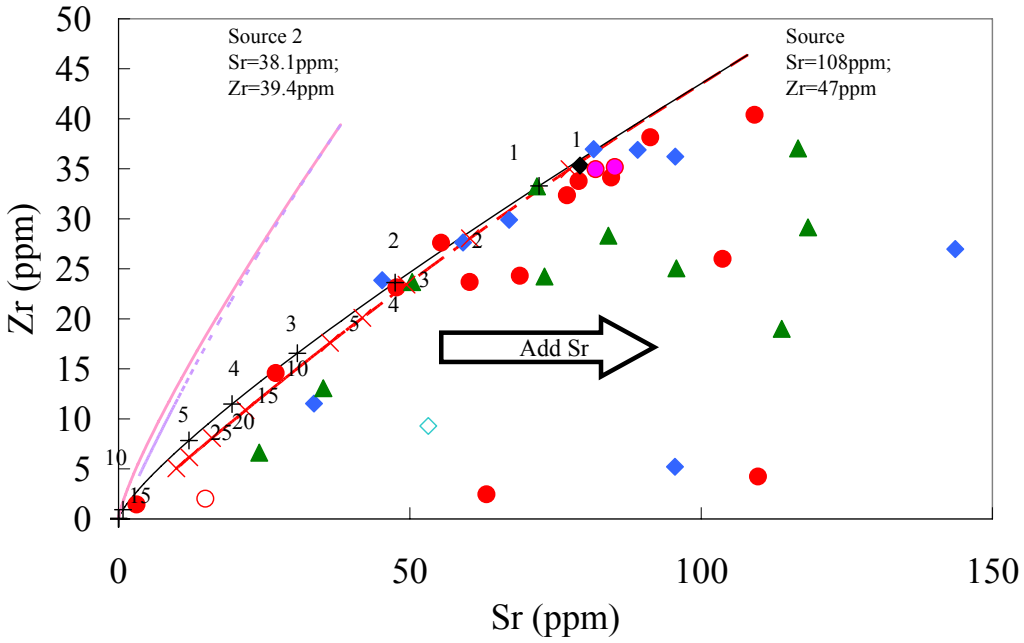


Fig. 8.7 - Batch and fractional melting models for Zr and Sr contents in clinopyroxenes from Subei basin. Samples with Sr content more than 150ppm are not shown. Batch melting, Dashed line; Fractional melting, continued line. Soure Zr, Sr conents are best fitting the data. Source2 Zr, Sr contents are from Yang et al., 1998. Symbols are as Fig. 4.4. Light blue diamond, Panshishan lherzolite; light blue filled grey diamond, Panshishan cpx-poor lherzolite; blue open diamond, Panshishan harzburgite; red dot, Lianshan lherzolite; red filled grey dot, Lianshan cpx-poor lherzolite; red open dot, Lianshan harzburgite; red filled pink dot, Lianshan olivine websterites; red filled golden dot, Lianshan dunite; green triangle, Fangshan lherzolite, green filled grey triangle, Fangshan cpx-poor lherzolite; green open triangle. Fangshan harzburgite

**Enrichment process (metasomatism)**

Using the trace element composition of depleted peridotites, the partial melting style and degree of melting occurring in mantle peridotites have been modelled. In this paragraph the composition of the metasomatized peridotites has been used to reveal the nature of enrichment processes and the geochemical signature of the metasomatic agent/s (O'Reilly and Griffin, 1988; Gorring and Kay, 2000; Wang and Gasparik, 2001). In fact, many lithospheric mantle regions record several episodes of both partial melting and metasomatic overprints (Zangana et al., 1999; Xu et al., 2000). In addition, highly depleted peridotites record generally stronger metasomatism in their clinopyroxene (e.g. Frey and Green, 1974; O'Reilly and Griffin, 1988; Gregoire et al., 2000). For the samples from Subei basin, the entire cpx group IV have Mg# large than 91 coupled with $Yb_N$ less than 8 (down to 2.6 for LS02). In such cases, modelling partial melting processes using these elements without consideration of metasomatic effects may lead to false conclusions, so we should treat this carefully.

The melting calculations detailed above explain REE pattern of depleted-REE group xenoliths as due to different degrees of depletion (Fig. 8.7). However, all the enriched xenoliths in group IV have geochemical signatures (Fig. 5.9, 5.10, 5.11) that cannot be interpreted by melt depletion processes and reflect subsequent metasomatic events. In xenoliths from Subei basin, although no hydrous minerals occurred and metasomatized texture are very rare, the large range of $(La/Ce)_N$ (0.34-4.04) indicate that metasomatic processes have affected the three xenolith populations. Highly depleted (indices of melt extraction such as $Yb_N$ or $Al_2O_3$ content, Mg# in mineral major element content) samples have a strong enrichment in the LREE pattern.

**Nature of metasomatic agents**

Differences in clinopyroxene compositions between enriched discrete lherzolite and composite lherzolite document distinct metasomatic agents and variations in the degree of metasomatism. Previous studies have demonstrated various metasomatic agents occurring in mantle peridotites, including carbonatitic melts (e.g. Yaxley et al., 1998; Gorring and Kay, 2000; Wang and Gasparik, 2001), siliceous melts (e.g. Vannucci et al., 1998; Zangana et al., 1999; Gregoire et al., 2000), adakitic (Kepezhinskas et al., 1995, 1996; Schiano et al., 1995; Coltorti et al., 2007), melilitic or melanephelinitic melts (Chalot-Prat and Boullier, 1997) and fluids ($CO_2$-, $H_2O$-, halogen- or P-rich) (Gorring and Kay, 2000; Larsen et al., 2003; Frezzotti et al., 2010). These metasomatic agents may give rise to distinct chemical variations within the mantle minerals. Using the partition coefficients between mineral and melt (see detail in appendix), the nature of the metasomatism agent/s can be rebuilt. Fig. 8.8 show the equilibrium melts for group IV cpx in Subei basin xenoliths. For these samples, except FS06, the equilibrium metasomatic melt has a strong negative anomaly of Ti and positive anomaly of Zr. The equilibrium metasomatism melt of FS06 do not has positive anomaly of Zr. In Fig. 8.9 $(La/Yb)_N$ vs Ti/Eu plot (Coltorti et al., 1999), FS06 fall in the carbonatitic metasomatism field. Samples of PSS02 and LS20 fall in the silicate metasomatism field. For group IV cpx, the metasomatism agent is a mixture of carbonatitic metasomatism and silicate metasomatism

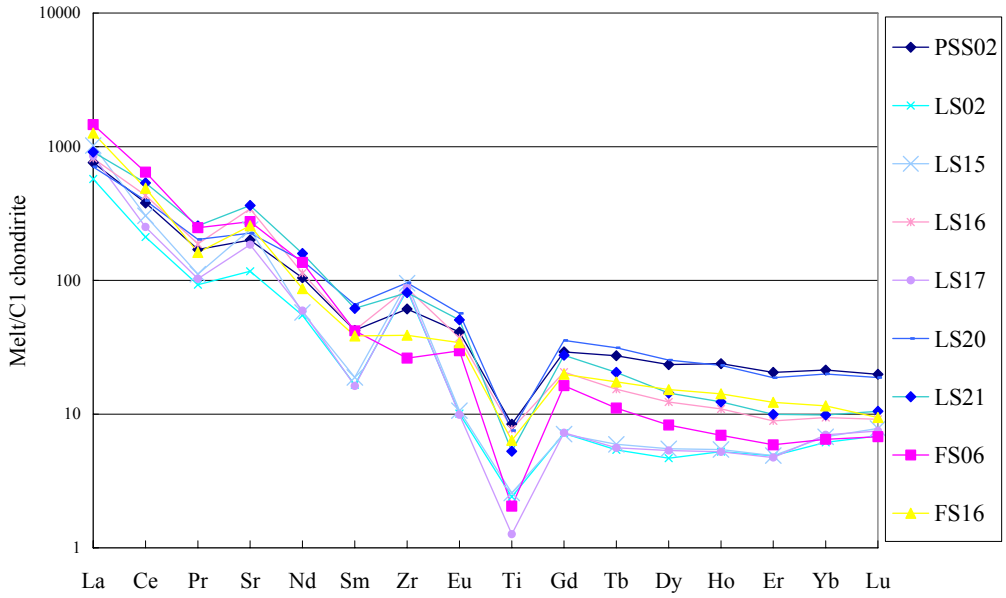


Fig. 8.8 – Inferred metasomatic melts in equilibrium with Group IV cpx.

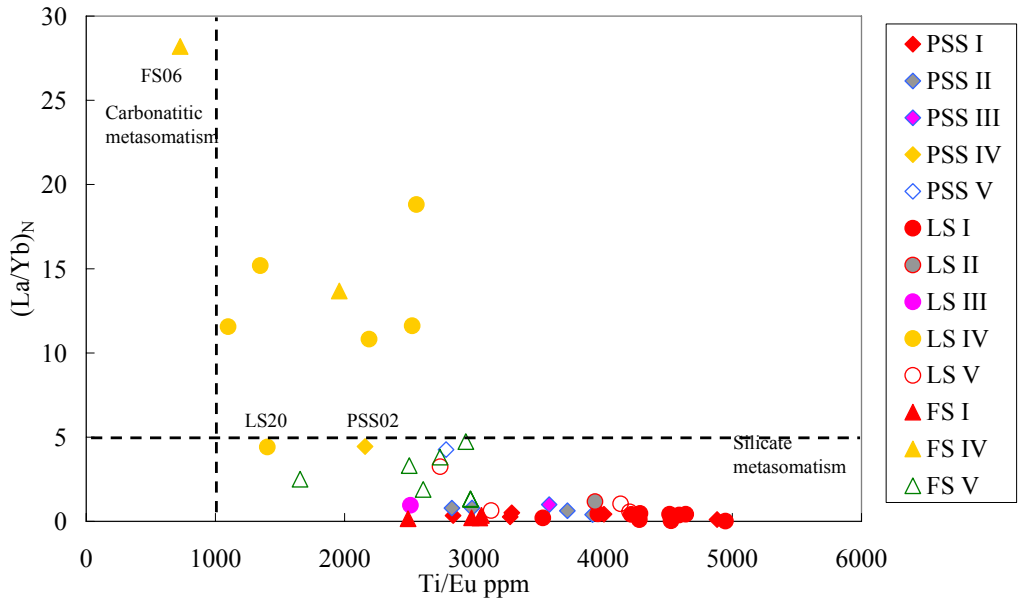


Fig. 8.9 - (La/Yb)N vs Ti/Eu ratios of clinopyroxene from Subei basin xenoliths

## Hydration/dehydration processes

*Preservation of initial water content of the mantle source*

The premise to investigate the possible relationship between water content in mantle minerals with other geochemistry parameters is whether the water content I measured is the initial water content of the mantle source. The solubility of hydrogen in nominally anhydrous minerals (NAMs) increases with increasing pressure (Keppler and Bolfan-Casanova, 2006, and references therein); thus, when peridotite xenoliths are transported to the surface by their host magmas, hydrogen can potentially diffuse escaping from the NAMs as the pressure abruptly decreases. Hydrogen diffusion experiments predict that at 1000ºC hydrogen undergone towards a complete resetting (in a millimeter scale), in individual grains of olivine and pyroxene in a few tens of hours (Kohlstedt and Mackwell, 1998; Hercule and Ingrin, 1999; Carpenter et al., 2000; Stadler and Skogby, 2003). In contrast, studies on natural samples suggest that pyroxenes preserve their mantle-derived equilibrium OH contents, but olivines do not (Bell and Rossman, 1992a; Bell et al., 2004; Peslier et al., 2002; Grant et al., 2007a; Gose et al., 2009). Possible explanations for the discrepancy may be related to the facts that (1) the diffusion loss of hydrogen depends on the H-content of co-existing minerals and melt, as well as water and oxygen fugacities of the system; (2) the incorporation of hydrogen into minerals does not only depend on diffusion rate of hydrogen, but also on diffusion rate in point defects, slower of at least several orders of magnitude with respect to other mineral lattice regions (Kohlstedt and Mackwell, 1998). (3) Experiments are usually made at $H_2O$-saturation conditions, which probably do not prevail in natural systems.

The following evidences suggest that the pyroxenes of Subei basin peridotite samples have largely preserved their initial water content in the mantle source:

(1) All the samples are chemically homogeneous for individual phases, and no major element compositional zoning was observed for each studied grain (EMPA).

(2) The FTIR analyses were usually performed in the core region of clean, crack- and inclusion-free grains of relatively large size. It is thus inferred that the loss of hydrogen caused by diffusion during the quick ascent would be very small (Peslier and Luhr, 2006).

(3) Homogeneous distribution of $H_2O$ in pyroxenes demonstrate by core-rim profile analysis for cpx and opx grains of the NCC peridotites (Fig. 6.5) have not revealed significant heterogeneities in $H_2O$ distribution within single grains, the latter normally being ascribed to diffusion. The H-related IR absorption is usually homogeneous between their core and rim region, indicating negligible depletion or enrichment of H from diffusion or exchange.

(4) The studied samples are usually very fresh, and all the spectra show no signal of any evident hydrous phases, which would produce sharp bonds in the region of >3660 $cm^{-1}$. In this case, there is no evident interference from other H-bearing phases, neither any exchange of H between them.

(5) $H_2O$ correlations between cpx and opx. As shown in Fig. 6.6, $H_2O$ content of cpx and opx shows good positive correlation. The partition coefficient between cpx and opx (Dcpx/opx) of 2.34 has been calculated for the cpx/opx pairs of Subei basin samples. If we include in the $H_2O$ opx *vs* $H_2O$ cpx space all published data NCC peridotite (Panshishan, Lianshan, Fangshan, Nushan and Hannuoba from Yang et al., 2008; Penglai, Qixia, Changle, and Hebi from Xia et al., 2010) the positive correlation remains, but the calculated partition

coefficient becomes 1.97 (Fig. 6.6b) This values is proximal to the range of values reported in literatures for natural peridotite xenoliths: Dcpx/opx =2.3±0.5 (n=38, Bell and Rossman, 1992a; Peslier et al., 2002; Grant et al., 2007b; Li et al., 2008). The range of partition coefficients between cpx and opx for $H_2O$ measured in natural peridotites is also close to that experimentally determined by low-blank SIMS method: Aubaud et al. (2004) report Dcpx/opx =1.8±0.3 (n=1, the value is revised according to new calibration of Aubaud et al. 2007); Hauri et al. (2006) obtain Dcpx/opx =0.9-1.4 (n=6); finally Tenner et al. (2009) report Dcpx/opx =1.2-2.0 (n=3).

The relationships between $Al_2O_3$ (%) and $H_2O$ (ppm) as evidence in opx of Subei basin xenoliths (Fig. 8.10), are also found in sub-arc mantle wedge samples (Peslier et al., 2002; Grant et al., 2007a), as well as in off-craton intraplate mantle (Grant et al., 2007a; Yang et al., 2008), with different slopes due to the higher values of water contents in the mantle wedge with respect to the intraplate setting. This correlation is also supported by experimental results of Rauch and Keppler (2002) which show that water solubility increases with increasing of $Al_2O_3$ contents (up to 1 wt%) in synthetic enstatite. This implies that the hydrogen dissolution in these minerals is combined with that of $Al^{3+}$, because the $Al_2O_3$ diffusion coefficient is so low that significant loss is unlikely. Preservation of cpx and opx equilibrium also implies that pyroxenes from the Subei basin peridotites have comparable geochemical behavior of other localities and have not undergone significant change of hydrogen during the ascent of the xenolith.

Based on heterogeneous distribution of $H_2O$ within olivine single grain (higher content in the core and lower content in the rim), several studies suggested significant loss of hydrogen in olivines caused by H diffusion in this phase

during xenolith ascent to the surface (Demouchy et al., 2006; Peslier and Luhr, 2006); however, other studies did not observe any water heterogeneity in olivines (Bell et al., 2004; Grant et al., 2007b). I can not unravel this issue on the basis of olivine measurements of Subei basin peridotite xenoliths because their water content is too low to be detected.

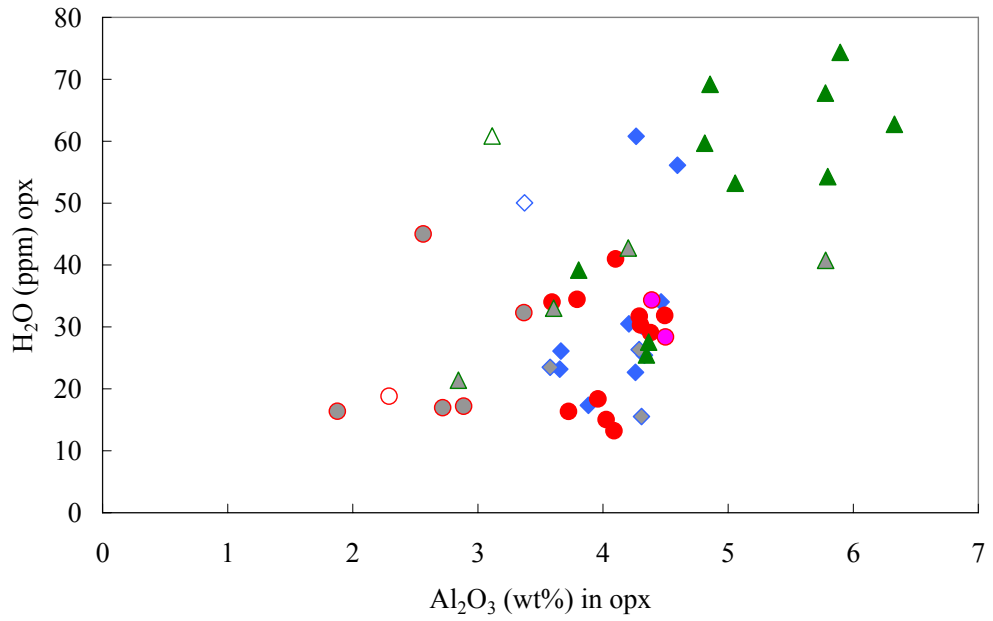


Fig. 8.10 - Correlation between $H_2O$ (ppm) and $Al_2O_3$ (%) in peridotite opx Symbols are as Fig. 7.6. Light blue diamond, Panshishan lherzolite; light blue filled grey diamond, Panshishan cpx-poor lherzolite; blue open diamond, Panshishan harzburgite; red dot, Lianshan lherzolite; red filled grey dot, Lianshan cpx-poor lherzolite; red open dot, Lianshan harzburgite; red filled pink dot, Lianshan olivine websterites; red filled golden dot, Lianshan dunite; green triangle, Fangshan lherzolite, green filled grey triangle, Fangshan cpx-poor lherzolite; green open triangle. Fangshan harzburgite

**Possible role on water content**

Besides T-P-X, many other factors, such as water and oxygen fugacities, crystallographic charge-coupled substitutions and diffusive properties of hydrogen within the mineral structures play an important role in determining the concentration of hydrous species preserved in a mineral (Johnson et al., 2002; Johnson and Rossmann, 2003). I investigate the relationship between different geochemical parameters and water content in minerals in order to better constrain the effects and controls of $H_2O$ distribution in mantle peridotites. As shown in Fig. 7.6a, water content has no clear differences among the rocktype, regardless of lherzolites, cpx-poor lherzolites, harzburgites and olivine websterites.

In this section we discuss and compare pyroxene water contents with the geochemical parameters that are commonly used to characterize mantle processes such as melting and enrichment related to recent metasomatism. In particular we focused our attention on the MgO and $Al_2O_3$ contents in pyroxene and REE abundances of clinopyroxenes. I preferred to use the MgO content of pyroxenes instead of the most popular geochemical parameter Mg# to represent the mantle depletion degree, because MgO is a better indicator of the degree of melt extraction with respect to chemical-physical components (e.g., Lee et al., 2003; Niu, 2004). There is no correlation between water content with major element oxides such as $SiO_2$, $TiO_2$, FeO, CaO, NiO and $Na_2O$ (not shown in the Figs). Because of water behaves incompatibly during mantle processes (e.g., Dixon et al., 1988; Michael, 1988; Michael, 1995.), we can expect the water content to decrease with increasing MgO. In this respect we could explore the processes which enrich or deplete the lithospheric mantle in hydrous species with time. Among each population of Panshishan, Lianshan

and Fangshan, no clear correlation with the MgO content in a single mineral apparently exists (Fig. 8.11a, b). The same if we consider different group of cpx REE pattern, there is no clear correlation between water content with MgO content in the group or between the groups.

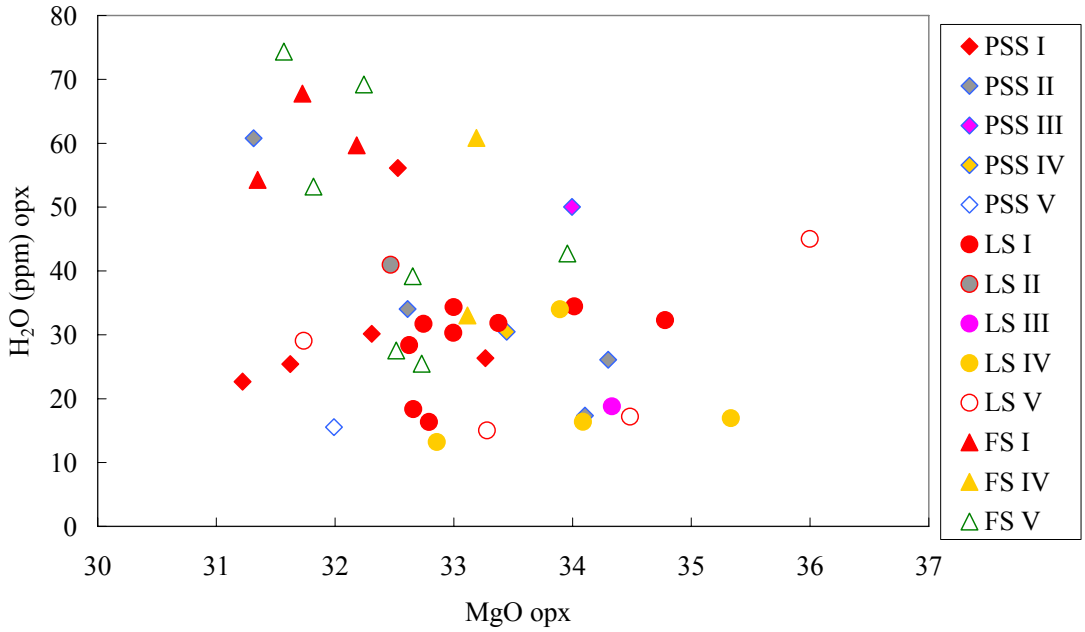


Group I, with LREE-depleted pattern;

Group II, with upward convex pattern;

Group III, with flat REE pattern;

Group IV, with LREE-enriched pattern;

Group V, with spoon-shaped pattern.

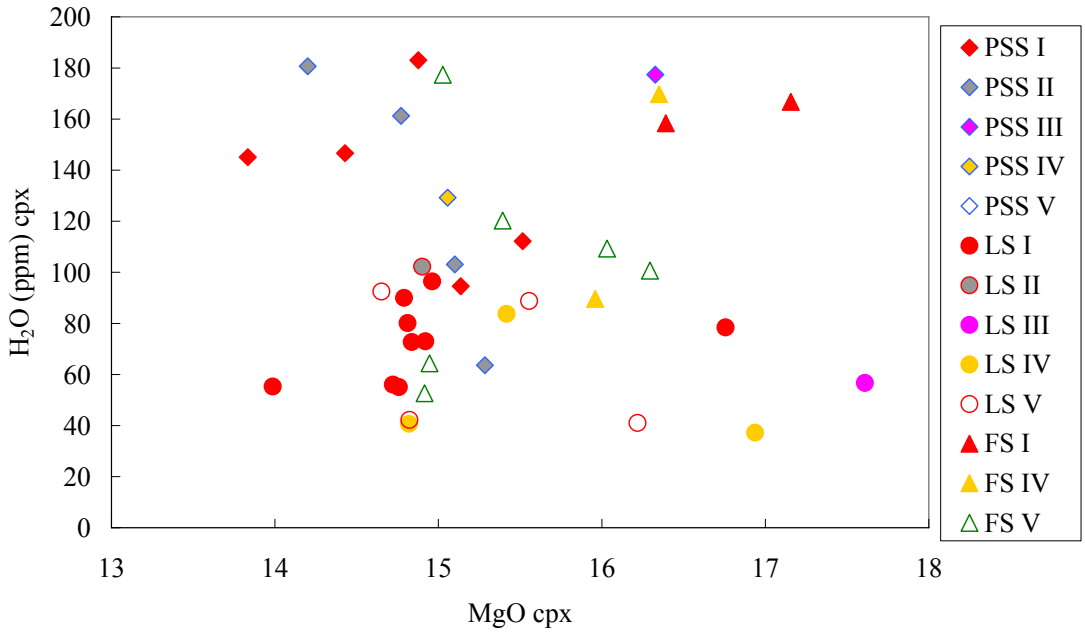


Fig. 8.11 - MgO (wt%) versus (a) orthopyroxene $H_2O$ and (b) clinopyroxene $H_2O$ content.

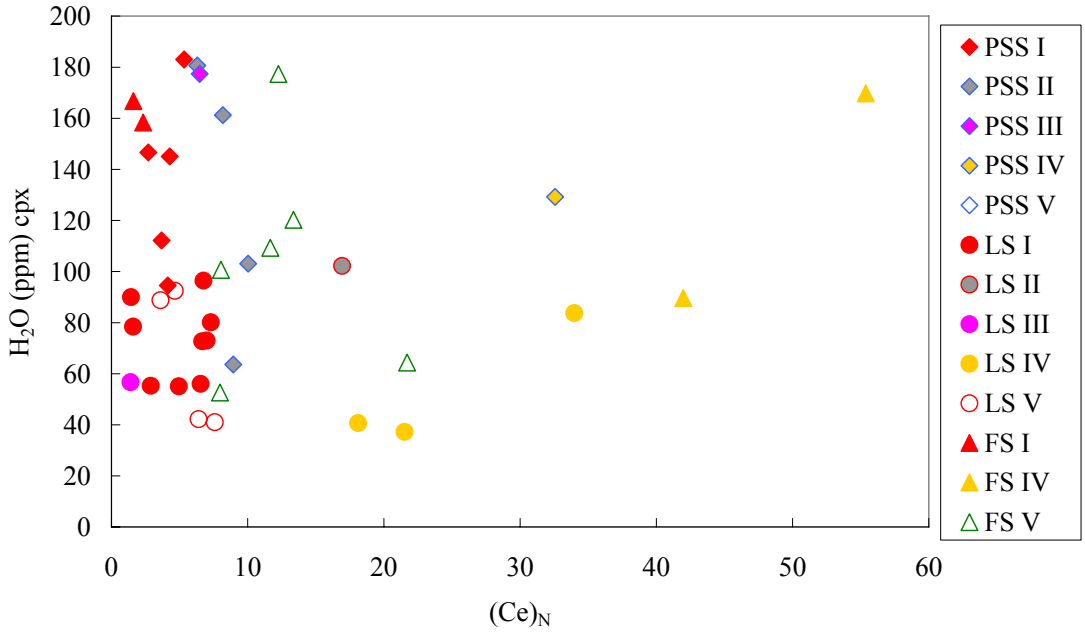

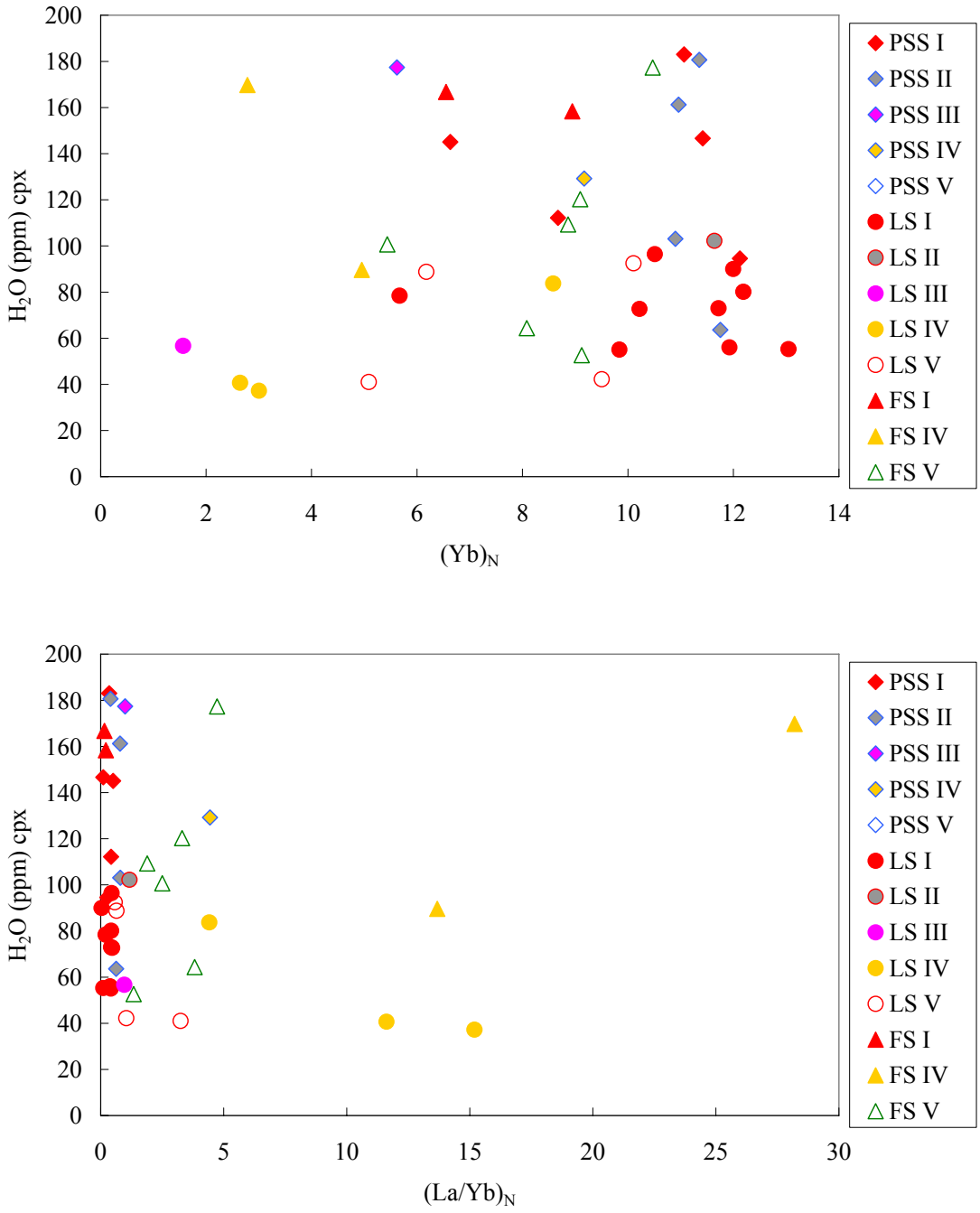


Fig. 8-12 $Ce_N$ (a), $Yb_N$ (b) and $(La/Yb)_N$ (c) versus clinopyroxene $H_2O$ content

To further explore possible relationships between water contents and different geochemical parameters, we looked at pyroxene trace element contents. I limited the comparison to the REE (in clinopyroxenes), since they are commonly used to investigate melting (HREE) and/or enrichment processes (LREE) (see discussion above). Element Ce is chosen as a representative of incompatible LREE and element Yb is chosen as a representative of compatible HREE, to exam possible relationship with water contents in Fig. 8.12a,b and the $(La/Yb)_N$ represent LREE/HREE ratio with water content in cpx are also shown in Fig. 8.12c. As shown in last two discuss sections, the group I LREE depleted samples are the production of mantle melting process and not undergone metasomatism event and in the contrast group IV LREE enriched samples are strongly affect in metasomatism event. If the water content of the minerals is controlled by melting event, a correlation of MgO with water content, and $Ce_N$ and $Yb_N$ with water content for samples in group should be observed. If the water content of the minerals is affected by later metasomatism event, a correlation of $(La/Yb)_N$ ratio and $Ce_N$ with water content for samples in group IV should be observed. In my study more than 80 samples from Subei basin, no such expected correlation are shown, the water content of the minerals are neither only controlled by melting event nor metasomatism event.

Based on the negative correlation between water content of pyroxenes and oxygen fugacity observed in Mexican and Simcoe (WA, USA) spinel peridotite xenoliths, Peslier et al (2002) suggested that pyroxene water contents are mainly controlled by the redox state of peridotites. In order to test this model in the Subei basin xenoliths, I compare the $H_2O$ contents of both cpx and opx

with the calculated $f_{O2}$ values. As already stated in Chapter 6, the majority of the sample are not characterized by oxidized signature ($\Delta$FMQ>0) and no correlation between pyroxene $H_2O$ content and peridotite $\Delta$FMQ values can be observed (Fig. 8.13). Therefore, the water content of the Subei basin samples is not related to high oxygen fugacity as has been argued in the case of some subduction zone peridotites (Simcoe, Peslier et al., 2002).

The possible correlation between water content with oxygen isotopic compositions is also check, shown in Fig. 8.14. There are no clear correlation regard localities or REE group.

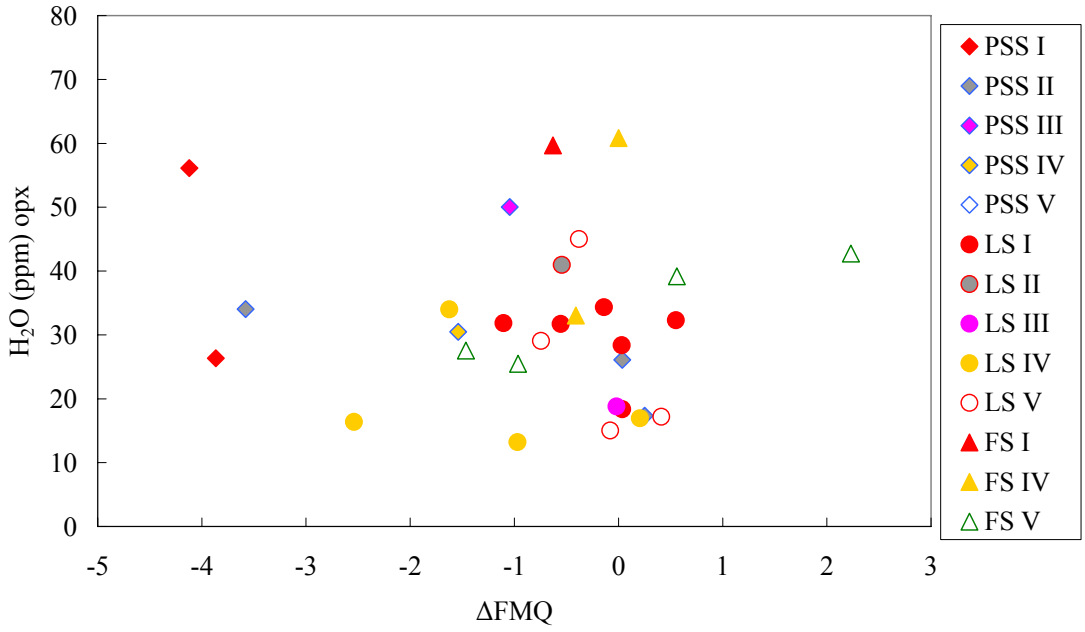

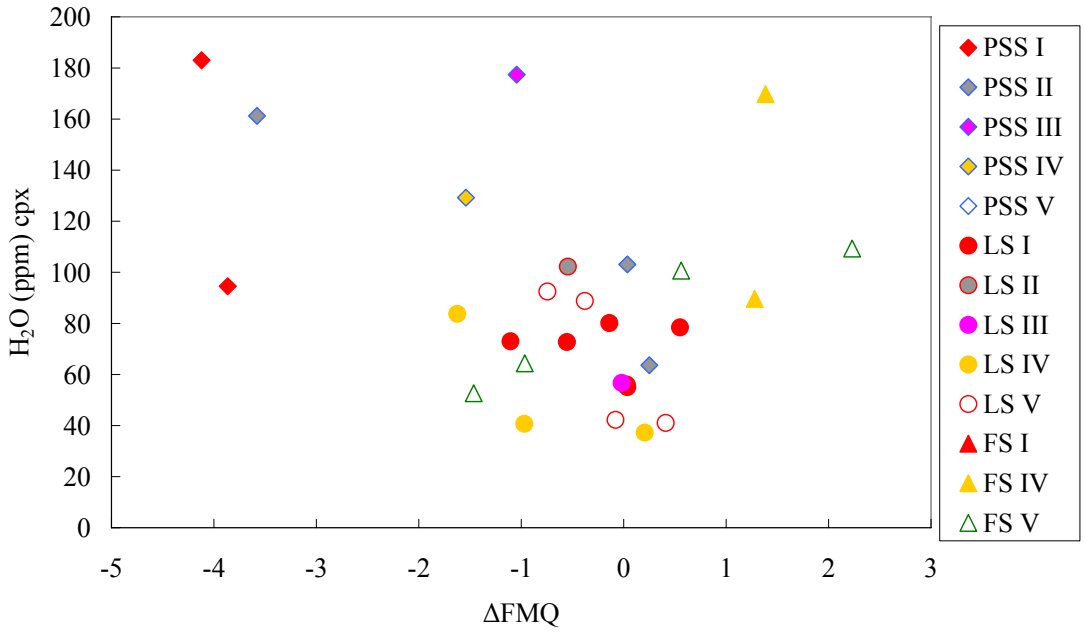


Fig. 8.13 - Opx $H_2O$ content (a) and cpx $H_2O$ content (b) versus ΔFMQ

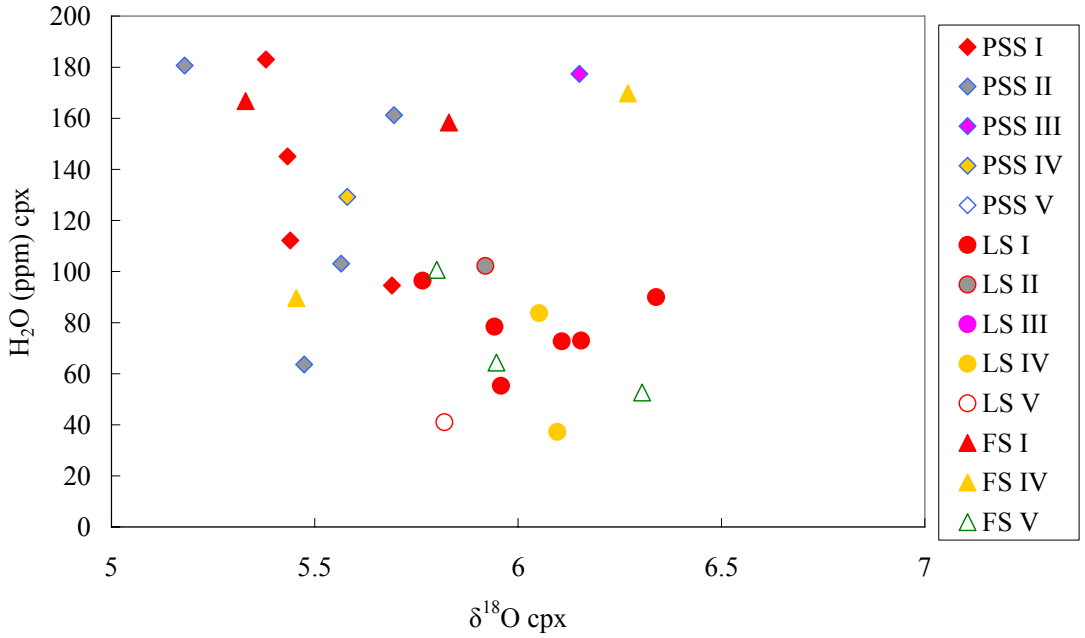


Fig. 8.14 - Cpx $H_2O$ content versus $\delta^{18}O$

## 8.4 Low water content of Subei basin xenoliths and Comparison with continental lithospheric and oceanic mantle

Yang et al. (2008) noticed that the Nushan and Hannuoba peridotites have much lower water contents compared with peridotites from worldwide craton and off-craton areas. I based my study on the water contents in NCC lithospheric mantle on the original results obtained from NAM $H_2O$ measurements of three xenoliths localities, main objects of this thesis, combined with those reported in the previously published data (Aubaud et al., 2007; Yang et al., 2008;). The interpretation is based on a total of 105 peridotites hosted by Cenozoic basalts from 9 localities (Panshishan, Lianshan, Fangshan, Nushan, Hannuoba, Penglai, Qixia, Changle, and Hebi) of the eastern part of the NCC. As described below, the Cenozoic lithospheric mantle of the NCC (at least the eastern part of it) appears to have lower water content compared to the continental craton and off-craton lithospheric mantle worldwide as well as the oceanic mantle.

### Comparison with the continental craton and off-craton lithospheric mantle

Water contents of peridotites from the NCC (Aubaud et al., 2007; Yang et al., 2008; Bonadiman et al., 2009; this study) and other continental regions worldwide (Bell and Rossman, 1992a; Peslier et al., 2002; Demouchy et al., 2006; Grant et al., 2007b; Li et al., 2008; Bonadiman et al., 2009) are compiled in Fig. 8.11. Tectonically, continental mantle peridotite can be classified as: on craton peridotites, such as samples from South Africa and Colorado Plateau (Bell and Rossman, 1992a; Grant et al., 2007b; Li et al., 2008) and off-craton peridotite, such as samples from Basin and Range (USA), Massif Central

(France), Patagonia (Chile) and Antarctic samples (Bell and Rossman, 1992a; Peslier et al., 2002; Demouchy et al., 2006; Grant et al., 2007b; Li et al., 2008; Bonadiman et al., 2009).

Water contents of cpx of the NCC peridotites range between 5 and 355 ppm; 85 of the 92 analyzed samples contain less than 200 ppm, and the average value is 108±61 ppm. In contrast, $H_2O$ contents of cpx of the craton peridotites data set range between 370 and 950 ppm with the average value of 577±209 ppm (397±61 ppm if slab-influenced Colorado Plateau samples (Li et al., 2008) are excluded). On the whole, the cpx of the off-craton peridotites range between 5 and 528 ppm with the average value of 316±151 ppm (Fig. 8.15a). $H_2O$ content of opx of the NCC peridotites range between 5 and 140 ppm, 96 of the 106 analyzed samples contain less than 80 ppm and the average value is 42±27 ppm. Differently, $H_2O$ content of opx of the on-craton peridotites range between 180 and 400 ppm and the average value is 297±94 ppm (244±107 ppm if slab-influenced Colorado Plateau samples (Li et al., 2008) are excluded); that of the off-craton peridotites range between 9 and 300 ppm and the average value is 125±77 ppm (Fig. 8.15b).

The estimated whole rock water content (calculated $H_2O$ contents of ol by assuming Dcpx/ol=10 for all the samples) of the NCC peridotite xenoliths range between 6 and 85 ppm with the average value of 25±18 ppm. In contrast, with that recorded in on- craton peridotites is more than 60 ppm (except one dunite from Colorado with 27 ppm) and the average values is 119±54 ppm (124±62 ppm if slab-influenced Colorado Plateau samples (Li et al., 2008) are excluded); that of off-craton peridotites is between 10 and 154 ppm, and the average value is 78±45 ppm (Fig. 8.15c). The comparison of the water contents in the NCC pyroxenes listed above and tghose from the two different tectonic

setting, show consistent differences. Among the off-craton" peridotites only a few have water contents similar to those of NCC mantle xenoliths (Fig. 8.15c). These are harzburgite and dunite samples which have experienced high degrees of partial melting (Peslier et al., 2006; Li et al., 2008; Bonadiman et al., 2009): as $H_2O$ behaves as a highly incompatible element during partial melting of a mantle source (in solid/liquid system $H_2O$ has the almost the same geochemical behavior of La; Hauri et al., 2006; Tenner et al., 2009), the peridotite residues undergoing higher degrees of partial melting are expected to be more depleted in water. Moreover, lherzolites from San Carlos Cenozoic basalts have a similar low water contents (171 to 178 ppm for cpx, 53 to 82 ppm for opx, and 2 to 4 ppm for ol, Li et al., 2008) to those of the NCC lherzolites. The low water contents of these rocks have been interpreted as the result of water loss during partial melting (Li et al., 2008).

**Comparison with the oceanic mantle**

The available data for oceanic peridotites are very scarce; they are limited to three abyssal peridotites from Gakkel ridge, Arctic Ocean (Peslier et al. (2007) ) and Cape Verde mantle xenoliths, Atlantic Ocean (Bonadiman et al., 2009) the $H_2O$ content are <1-5 ppm for ol 25-60 ppm for opx and 130-200 for cpx. The low water content of these samples is likely the consequence of water loss during the slow adiabatic decompression; thus they do not necessarily represent the mid-oceanic basalt (MORB). Gose et al. (2009) investigated a suit of abyssal peridotites from the Mid-Atlantic Ridge; the measured $H_2O$ contents of opx range between 160 and 270 ppm and suggest to reflect the original mantle contents. This range is much higher than that of opx of the

NCC peridotites (between 5 and 140 ppm, with 96 out of 106 samples being <80 ppm; Fig. 7.7).

In contrast to oceanic peridotites and xenoliths, the $H_2O$ content of MORB and OIB have been well constrained from melt inclusion and glass (Dixon et al., 1988, 1997, 2002; Michael, 1988, 1995; Stolper and Newmann, 1994; Sobolev and Chaussidon, 1996; Danyushevsky et al., 2000; Nichols et al., 2002; Saal et al., 2002; Simons et al., 2002; Wallace, 2002; Asimow et al., 2004; Seamon et al., 2004; Workman et al., 2006). Based on these data, the $H_2O$ content of the source of MORB and OIB is calculated to be about between 50 to 250 ppm and between 300 to 1000 ppm respectively. Consequently, the $H_2O$ contents of the NCC peridotites are lower than the oceanic mantle represented by the source of MORB and OIB.

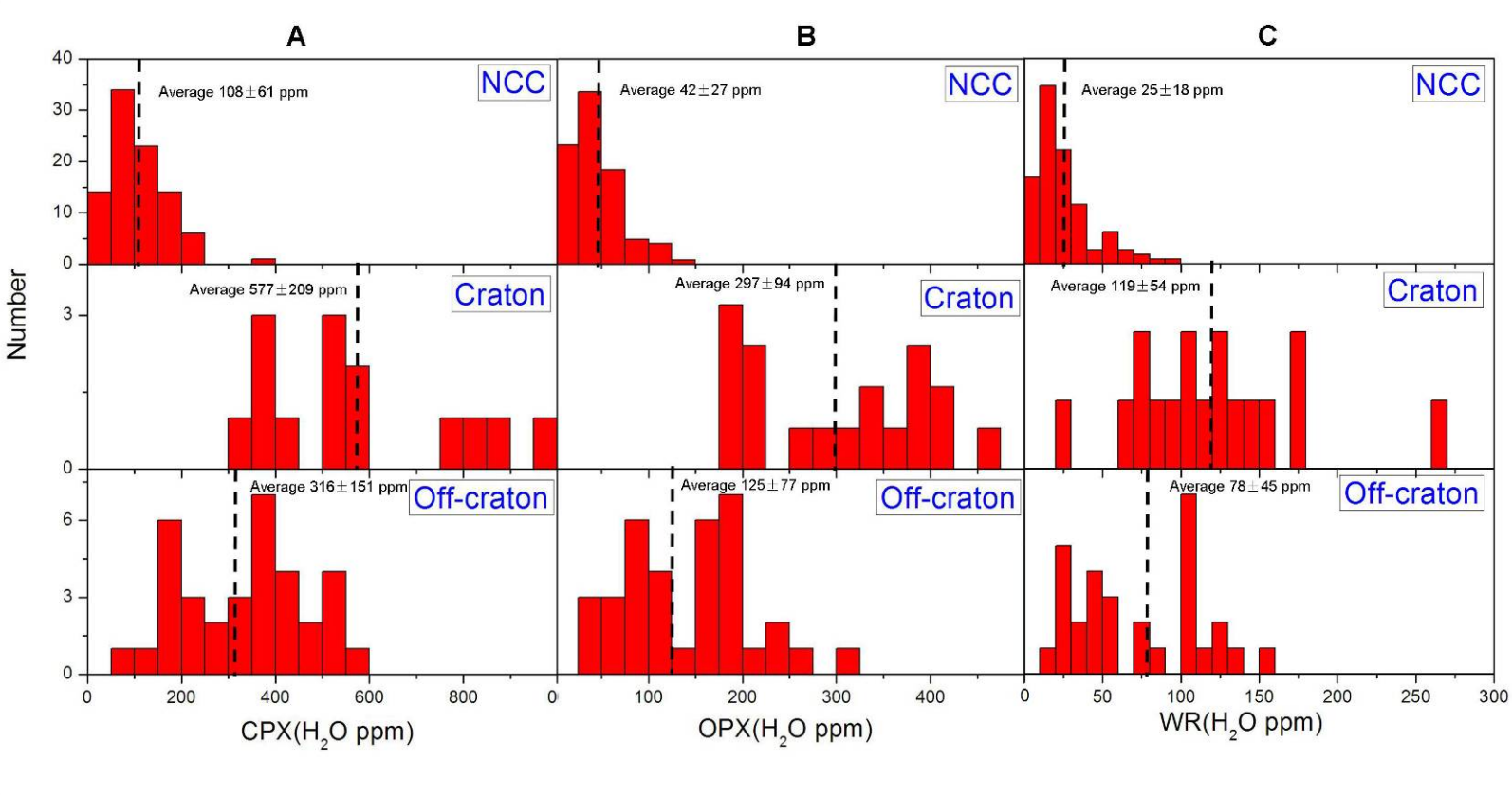


Fig. 8.15 - Comparison of $H_2O$ content of cpx, opx and whole rock of the NCC peridotite xenoliths with that of craton and off-craton peridotites

**Implications from the low water content of the eastern NCC**

As I mentioned in Chapter 2, the mechanisms responsible for lithospheric thinning of the NCC have been extensively debated (Menzies and Xu, 1998; Griffin et al., 1998; Zheng et al., 1998, 2001, 2006; Xu et al., 2001, 2008b; Gao et al., 2002, 2004, 2008; Zhang et al., 2002, 2008, 2009; Zhang, 2005; Wu et al., 2003, 2006; Niu, 2005; Menzies et al., 2007). Several models have been proposed, that can be grouped into two end-members: "top-down" rapid (<10 Ma) delamination model versus "bottom-up" protracted (possibly up to 100Ma) thermo-mechanical-chemical erosion model. Delamination would have produced the removal of the entire lithospheric mantle and probably part of the lower crust (Wu et al., 2003, 2005; Gao et al., 2004, 2008); thus the resulting (present) lithospheric mantle beneath the NCC would be asthenospheric mantle newly accreted and cooled during the late Mesozoic-Early Cenozoic thinning. On the other hand, thermal erosion models predict that most of the present lithospheric mantle should be relict of Archean-Protorozoic mantle after the thinning (Griffin et al., 1998; Menzies and Xu, 1998; Xu et al., 2001).

According to the delamination model, the newly formed lithospheric mantle should be directly cooled asthenosphere because there was no significant asthenosphere-derived basaltic magmatism accompanied by the NCC lithospheric thinning (Menzies et al., 2007 and references therein). If the delamination model is accepted, the water content of the present lithospheric mantle should be similar to that of the source of MORB (50-250 ppm), which is not the case for the majority of the eastern NCC peridotites. Moreover, the fact that the NCC peridotites display much lower water content than the

oceanic peridotites from Mid-Atlantic Ridge (Gose et al., 2009) also argues against the asthenosphere source.

Therefore, we suggest that the low water contents of the eastern NCC samples result from the reheating from below by an upwelling asthenosphere flow that occurred in concert with lithospheric thinning. If so, most of the Cenozoic lithospheric mantle of the eastern NCC should be considered the relict mantle after lithospheric thinning during late Mesozoic-Early Cenozoic. A few peridotite xenoliths from Nushan and Changle (Yang et al., 2008; Xia et al., 2010) having $H_2O$ content more than 50 ppm (up to 85 ppm) may actually represent newly accreted lithospheric materials from upwelling asthenosphere. This scenario is in agreement with the available age constraints from Re-Os isotopic data on the peridotite xenoliths hosted by Cenozoic basalts from the eastern NCC (including whole rock and sulfides) (Meisel et al., 2001; Gao et al., 2002; Xia et al., 2004; Reisberg et al., 2005; Wu et al., 2005; Zhi et al., 2007; Xu et al., 2008a; Xu et al., 2008b; Zhang et al., 2009). Using the Os proxy isochron ($^{187}Os/^{188}Os$ vs. $Al_2O_3$ or Yb etc), the melting age of the eastern NCC lithospheric mantle is early Proterozoic to Mesoproterozoic. Calculate the Re depleted model age ($T_{RD}$) and considering the maximum $T_{RD}$ in a suite of peridotite xenoliths as the minimum lithospheric mantle formation age of that area, we also obtain a Proterozoic age. Even if we consider $T_{RD}$ of each sample (or individual sulfide), Phanerozoic age are still rare and only a few Mesozoic ages exist.

## Conclusion

The main purpose of my thesis was to investigate the water content at mantle condition and possible relationship with mantle processes. More than 50 xenoliths are sampled in three localities from Subei basin, Panshishan, Lianshan and Fangshan, within North China Craton. A series of experiment are performed, including whole rock major and trace element analysies by XRF, minerals major elements analyses by EMP, cpx trace elements analyses by LA-ICP-MS, water content in ol, cpx and opx by FTIR and oxygen isotopic composition in ol, opx, cpx and sp by LF-MS.

Based on the REE pattern in cpx, they were subdivided into five different groups. Group I, with LREE-depleted patterns; Group II, with upward convex patterns, Group III, with flat REE patterns; Group IV, with LREE-enriched patterns; and Group V, with spoon-shape patterns.

The xenoliths underwent a major melt extraction event. Group I samples in fact can be produced by mantle melting <10%. On the other hand Group IV samples have been strong modified during mantle metasomatism event. The water content in all the three localities together with other peridotites hosted by Cenozoic basalts from 9 localities in the eastern part of the NCC show low levels compared to other craton and off-craton xenoliths in continental and oceanic settings. The comparison of water content with the main geochemical parameters, including major element composition of minerals, melting index of MgO content and Mg# for minerals, temperature, pressure and oxygen fugacity of the xenoliths, REE in cpx and oxygen isotope composition do not show any significative correlations. There is no correlation among localities, different REE group and water content. At least for my data, water contents in

the NAMs are not related to main mantle depletion/enrichment process. The indication, although needs to be confirmed by further studies, is that water content may represent a pristine feature of different mantle domains even within similar tectonic settings.

# References

Adam, J. and Green, T.H., 1994. The effects of pressure and temperature on the partitioning of Ti, Sr and REE between amphibole, clinopyroxene and basanitic melts. Chemical Geology 117, 219-233. doi: 10.1016/0009-2541(94)90129-5.

Adam, J. and Green, T.H., 2006. Trace element partitioning between mica- and amphibole-bearing garnet lherzolite and hydrous basanitic melt: 1. Experimental results and the investigation of controls on partitioning behavior. Contrib. Mineral. Petrol., 152, 1-17.

Ackermann, L., Cemic, L., Langer, K., 1983. Hydrogarnet substitution in pyrope: a possible location for water in the mantle. Earth Planet. Sci. Lett., 62, 208–214.

Arndt, N.T., Ginibre, C., Chauvel, C., Albarede, F., Cheadle, M., 1998. Were komatiites wet? Geology, 26, 739-742.

Asimow, P. D., Dixon, J. E., Langmuir, C.H., 2004, A hydrous melting and fractionation model for mid-ocean ridge basalts: Application to the Mid-Atlantic Ridge near the Azores, Geochem. Geophy. Geosys., doi:10.1029/2003GC000568

Asimow, P.D., Stein, L.C., Mosenfelder, J.L., Rossman, G.R., 2006. Quantitative polarized infrared analysis of trace OH in populations of randomly oriented mineral grains. Am. Mineral.,91, 278-284.

Aubaud, C., Hauri, E.H., Hirschmann, M.M., 2004. Hydrogen partition coefficients between nominally anhydrous minerals and basaltic melts. Geophys. Res. Lett., 31(20), L20611

Aubaud, C., Withers, A.C., Hirschmann, M.M., Guan, Y., Leshin, L.A., Mackwell, S., Bell, D.R., 2007, Intercalibration of FTIR and SIMS for hydrogen measurements in glasses and nominally anhydrous minerals, Am. Mineral., 92, 811-828.

Aubaud, C., Hirschmann, M.M., Withers, A.C., Hervig, R. L., 2009. Hydrogen partitioning between melt, clinopyroxene, and garnet at 3 GPa in a hydrous MORB with 6% H2O, Contrib. Mineral. Petrol., 156, 607-625.

Basu, A., Wang, J.W., Huang, W.K., Xie, G.H., Tatsumoto, M., 1991. Major element, REE and Pb, Nd and Sr isotopic geochemistry of Cenozoic volcanic rocks of eastern china: implications for origin from suboceanic-type mantle reservoirs. Earth Planet. Sci. Lett.105, 149–169.

Bell, D.R., Ihinger, P.D., Rossman, G.R., 1995. Quantitative analysis of trace OH in garnet and pyroxenes. Am. Mineral., 80(5-6), 465-474.

Bell, D.R., Rossman, G.R., 1992a. The distribution of hydroxyl in garnets from the subcontinental mantle of Southern Africa. Contrib. Mineral. Petrol., 111, 161-178.

Bell, D.R., Rossman, G.R., 1992b. Water in Earth's mantle: The role of nominally anhydrous minerals. Science, 255, 1391-1397.

Bell, D.R., Rossman, G.R., Moore, R.O., 2004. Abundance and partitioning of OH in a high-pressure magmatic system: Megacrysts from the Monastery kimberlite, South Africa. J. Petrol., 45(8), 1539-1564.

Bolfan-Casanova, N., 2005. Water in the Earth's mantle. Mineral. Mag., 69, 229-257.

Bonadiman, C., Beccaluva, L., Coltorti, M., Siena, F., 2005. Kimberlite-like metasomatism and “garnet signature” in spinel-peridotite xenoliths from Sal, Cape Verd archipelago: relics of a subcontinental mantle domain within the Atlantic ocean lithosphere? J. Petrol., 46(12), 2465-2493

Bonadiman, C., Hao, Y.T., Coltorti, M., Dallai, L., Faccini, B., Huang, Y., Xia, Q.K., 2009, Water content of pyroxenes in intraplate lithospheric mantle. European Journal of Mineralogy, 21, 637-647

Bottinga, Y. and Javoy, M., 1973. Comments on oxygen isotope geothermometry. Earth Plant. Sci. Lett., 20(2), 250-265

Brey, G.P. and Kohler, T.P., 1990. Geothermobarometry in four-phase lherzolites II. new thermobarometers, and practical assessment of existing thermobarometers. J. Petrol., 31(6), 1353–1378.

Carpenter, W. S., Mackwell, S., Dyar, D., 2000. Hydrogen in diopside: Diffusion profiles, Am. Mineral., 85, 480-487.

Carswell, D.A. and Gibb, F.G., 1987. Evaluation of mineral thermometers and barometers applicable to garnet lherzolite assemblages. Contri. Mineral. Petrol., 95, 499-511

Chalot-Prat, F. and Boullier, A.M., 1997. Metasomatism in the subcontinental mantle beneath the Eastern Carpathians( Romania): new evidence from trace element geochemistry. Contrib. Mineral. Petril., 129(4), 284-307

Chen, D.G. and Peng, Z.C. 1988. K–Ar ages and Pb, Sr isotopic characteristics of some Cenozoic volcanic rocks from Anhui and Jiangsu Provinces China, Acta Pet. Sin. 2 12-16 (in Chinese with English abstract).

Chen, D.G. and Wang, Y.X., 1994. Nd, Sr, Pb isotope characters of mantle lherzolite xenoliths from Panshishan, JiangSu. Geochemistry, 23(3), 245-253

Chiba, H., Chacho, T., Clayton, R. N., Goldsmith, J.R., 1989. Oxygen isotope fractionation involving diopside, magnetite, and calcite: application to geothemmetry. Geochi. Cosmochim. Acta, 53, 2985-2995

Choi, S.H., Kwon, S.-T., Mukasa, S.B., Sagong, H., 2005. Sr–Nd–Pb isotope and trace element systematic of mantle xenoliths from late Cenozoic alkaline lavas, South Korea. Chem. Geol. 221, 40–64.

Chough, S.K., Kwon, S.T., Ree, J.H., Choi, D.K., 2000. Tectonic and sedimentary evolution of the Korean peninsula: a review and new view. Earth Sci. Rev. 52, 175–235.

Chung, S.L., 1999. Trace Element and Isotope Characteristics of Cenozoic Basalts around the Tanlu Fault with Implications for the Eastern Plate Boundary between North and South China. Geology, 107, 301-312

Creighton, S., Stachel, T., Matveev, S., Hofer, H., McCammon, C., Luth, R.W., 2009. Oxidation of the Kaapvaal lithospheric mantle driven by metasomatism. Contri. Min. Petro., 157, 491-504

Coltorti, M., Bonadiman, C., Hinton, R.W., Siena, F., Upton, B.G.J., 1999. Carbonatite Metasomatism of the Oceanic Upper Mantle: Evidence from Clinopyroxenes and Glasses in Ultramafic Xenoliths of Grande Comore, Indian Ocean. J. Petrol. 40(1), 133-165

Coltorti, M., Bonadiman, C.m Faccini, B., Ntafilos, T., Seina, F., 2007. Slab melt and intraplate metasomatism in Kapfenstein mantle xenoliths (Styrian Basin, Austria). Lithos, 94, 66-89

Davis, G., 1994. Thermomechanical erosion of the lithosphere by mantle plume. J. Geophys. Res., 99, 15709-15722.

Demouchy, S., Jacobsen, S.D., Gaillard, F., Stern, C.R., 2006. Rapid magma ascent recorded by water diffusion profiles in mantle olivine. Geology, 34(6), 429-432.

Dixon, J.E., Stolper, E., Delaney J.R., 1988. Infrared spectroscopic measurements of $CO_2$ and $H_2O$ in Juan de Fuca basaltic glasses, Earth Planet. Sci. Lett., 90, 87-104

Dunn, T. and Sen, C., 1994. Mineral/Matrix Partition-Coefficients for Ortho-Pyroxene, Plagioclase, and Olivine in Basaltic to Andesitic Systems - a Combined Analytical and Experimental-Study. Geochimica et Cosmochimica Acta, 58, 717-733.

Elkins, L., Gaetani, G., Sims, K., 2008. Partitioning of U and Th during garnet pyroxenite partial melting: Constraints on the source of alkaline ocean island basalts. Earth Planet. Sci. Lett. 265, 270-286

Elphick, S.C., Graham, C.M., Dennis, P., 1988. An ion-microprobe study of anhydrous O diffusion in anorthite: a comparison with hydrothermal data and some geological implications. Contrib. Mineral. Petrol., 76, 440-454.

Fan, Q.C., Hooper, P.R., 1989, The mineral chemistry of ultramafic xenoliths of Eastern China: implications for upper mantle composition and the paleogeoterms. J. Petrol., 30, 1117-1158

Fan, W.M., Menzies, M.A., 1992. Distribution of aged lower lithosphere and accretion of asthenosphere mantle beneath eastern China. Geotectonic et Metallogenia, 16(3-4), 171-180.

Fan, W.M., Zhang, H.F., Baker, J., Jarvis, K.E., Mason, P.R.D., Menzies, M.A., 2000. On and off the North China craton: where is the Archean keel? J. Petrol., 41, 933-950.

Fujimaki, H., Tatsumoto, M. Aoki, K.i., 1984. Partition coefficients of Hf, Zr, and REE between phenocrysts and groundmasses. Journal of Geophysical Research 89: 662-672.

Frezzotti, M.L., Ferrando, S., Peccerillo, A., Petrelli, M., Tecce, F., Perucchi, A., 2010, Chlorinerich metasomatic $H_2O$-$CO_2$ fluids in amphibole-bearing peridotites from Injibara (Lake Tana region, Ethiopian plateau): nature and evolution of volatiles in the mantle of a region of continental flood basalts, Geochim. Cosmochim. Acta,

Frey, F.A. and Green, D.H., 1974. The mineralogy, geochemistry and origin of lherzolite inclusions in Victorian basanites. Geochim. Cosmochim. Acta. 38(7), 1023-1059

Fyfe, W.S.,1970. Lattice energies, phase transformations and volatiles in the Earth's mantle. Phys. Earth Planet. Inter., 3, 196–200.

Gao, S., Rudnick, R., Carlson, R.W., McDonough, W.F., Liu, Y.S., 2002. Re-Os evidence for the replacement of ancient mantle lithosphere beneath the North China craton. Earth Planet. Sci. Lett., 198, 307-322.

Gao, S., Rudnick, R.L., Yuan, H.L., Liu, X.M., Liu, Y.S., Xu, W.L., Ling, W.L., Ayers, J., Wang, X.C., Wang, Q.H., 2004. Recycling lower continental crust in the North China craton. Nature, 432(7019), 892-897.

Gao, S., Rudnick, R.L., Xu, W.L., Yuan, H.L., Liu, Y.S., Walker, R.J., Puchtel, I., Liu, X., Huang, H., Wang, X.R., Yang, J., 2008. Recycling deep cratonic lithosphere and generation of intraplate mahmatism in the North China Craton, Earth Planet. Sci. Lett., 270, 41-53

Goldsmith, J.R., 1987. Al/Si inter-diffusion in albite: effect of pressure and the role of hydrogen. Contrib. Mineral. Petrol., 95, 311-321.

Gorring, M.L., and Kay, S.M., 2000. Carbonatite metasomatized peridotite xenoliths from southern Patagonia: implications fro lithospheric processes and Neogene plateau magmatism. Contrib. Mineral. Petrol., 140(1), 55-72

Gose, J., Schmädicke, E., Beran, A., 2009. Water in enstatite from Mid-Atlantic Ridge peridotite: Evidence for the water content of suboceanic mantle? Geology, 37, 543-546.

Grant, K.J., Ingrin, J., Lorand, J.P., Dumas, P., 2007a. Water partitioning between mantle minerals from peridotite xenoliths. Contrib. Mineral. Petrol., doi: 10.1007/s00410-006-0177-1.

Grant, K.J., Kohn, S.C., Brooker, R.A., 2007b. The partitioning of water between olivine, orthopyroxene and melt synthesized in the system albite-forsterite-$H_2O$. Earth Planet. Sci. Lett., 260, 227-241.

Green, T., Blundy, J., Adam, J., Yaxley, G., 2000. SIMS determination of trace element partition coefficients between garnet, clinopyroxene and hydrous basaltic liquids at 2-7.5 GPa and 1080-1200C. Lithos 53: 165-187

Gregoire, M., Moine, B.N., O'Reilly, S.U., Cottin, J.Y.m Giret, A., 2000. Trace element residence and partitioning in mantle xenoliths metasomatized by highly alkaline, silicate- and carbonate-rich melts (Kerguelen Islands, Indian ocean). J. Petrol., 41(4), 477-509

Griffin, W.L., O'Reilly, S.Y., Afonso, J.C., Begg, G.C., 2008. The composition and evolution of lithospheric mantle: a re-evaluation and its tectionic implications. J. Petrol., Doi:10.1093/petrology/egn033.

Griffin, W.L., Zhang, A.D., O'Reilly, S.Y., Ryan, C.G., 1998. Phanerozoic evolution of the lithosphere beneath the Sino-Korean craton. In: Flower, M., Chung, S.L., Lo,

C.H., Lee, T.Y. (Ed.), Mantle Dynamics and Plate Interactions in East Asia. American Geophysical Union, Washington, DC, pp. 107-126.

Griggs, D.T., 1967. Hydrolytic weakening of quartz and other silicates. Geophys. J. Int., 14, 19-31.

Griggs, D.T., Blacic, J.D., 1965. Quartz: anomalous weakness of synthetic crystals. Science, 147, 292-295.

Hacker, B.R., Ratschbacher, L., Webb, L., Ireland, T., Walker, D., Dong, S.W., 1998. U/Pb zircon ages constrain the architecture of the ultrahigh-pressure Qinling-Dabie Orogen, China. Earth Planet. Sci. Lett., 161, 215-230.

Harmon, R.S. and Hoefs, J., 1995. Oxygen isotope heterogeneity of the mantle deduced from global 18O systematic of basalts from different geotectonic settings. Contrib. Mineral. Petrol., 120, 95-114.

Hart, S.R. and Dunn, T., 1993. Experimental cpx/melt partitioning of 24 trace elements. Contributions to Mineralogy and Petrology 113: 1-8

Hauri, E.H., Gaetani, G.A., Green, T.H., 2006. Partitioning of water during melting of the Earth's upper mantle at $H_2O$-undersaturated conditions. Earth Planet. Sci. Lett., 248, 715-734

He, L.J., Hu, S.B., Wang, J.Y., 2001. Thermal structure of the continental lithosphere beneath east China. Prog. Nat. Sci., 11, 966-969.

Hercule, S. and Ingrin, J., 1999. Hydrogen in diopside: diffusion, kinetics of extraction-incorporation, and solubility. Am. Mineral., 84, 1577-1587.

Herzberg, C., 2004. Geodynamic Information in Peridotite Petrology. J. Petrol., 45(12), 2507-2530

Hirschmann, M.M., Aubaud, C., Withers, A., 2005. Storage capacity of $H_2O$ in nominally anhydrous minerals in the upper mantle Earth Planet. Sci. Lett., 236(1-2), 167-181.

Hirth, G., Kohlstedt, D.L., 1996. Water in the oceanic upper mantle: implications for rheology, melt extraction and the evolution of the lithosphere. Earth Planet. Sci. Lett., 144, 93-108.

Hirth, G., Kohlstedt, D.L., 2003. Rheology of the upper mantle and the mantle wedge: A view from the experimentalists. In: Eiler, J. (Ed.), Inside the Subduction Factory. Geophysical Monograph, American Geophysical Union, 83-105.

Hoang, N., Flower, M., Carlson, R.W., 1996. Major, trace, and isotopic compositions of Vietnamese basalts: interaction of hydrous EM1-rich asthenosphere with thinned Eurasian lithosphere. Geochim. Cosmochim. Acta 60, 4329–4351.

Hu, S., He, L., Wang, J., 2000. Heat flow in the continental area of China: a new data set. Earth Planet. Sci. Lett., 179, 407-419.

Huang, J.L. and Zhao, D.P., 2006. High-resolution mantle tomography of China and surrounding regions. J. Geophys. Res., 111, doi: 2005JB004066.

Ingrin, J. and Skogby, H., 2000. Hydrogen in nominally anhydrous upper-mantle minerals: concentration levels and implications. Eur. J. Mineral., 12(3), 543-570.

Ionov, D.A., Harmon, R.S., France-Lanord, C., Greenwood, P.B., Ashchepkov. I.V., 1994, Oxygen isotope composition of garnet and spinel peridotites in the continental mantle: Evidence from the Vitim xenolith suite, southern Siberia Geochimica et Cosmochimica Acta, vol. 58, Issue 5, pp.1463-1470

Jaupart, C.and Mareschal, J.C., 2003. Constraints on crustal heat production from heat flow data. In: Rudnick, R.L. (Ed.), Treatise on Geochemistry: The Crust. Elsevier, Amsterdam, pp. 65-84.

Johnson, E.A., Rossman, G.R., 2003. The concentration and speciation of hydrogen in feldspars using FTIR and H-1 MAS NMR spectroscopy. Am. Mineral., 88(5-6), 901-911.

Johnson, E.A., Rossman, G.R., 2004. A survey of hydrous species and concentrations in igneous feldspars. Am. Mineral., 89(4), 586-600.

Johnson, E.A., Rossman, G.R., Dyar, M.D., Valley, J.W., 2002. Correlation between OH concentration and oxygen isotope diffusion rate in diopsides from the Adirondack Mountains, New York. Am. Mineral., 87(7), 899-908.

Johnson, K.T.M., 1994. Experimental cpx/ and garnet/melt partitioning of REE and other trace elements at high pressures: petrogenetic implications. Mineralogical Magazine 58, 454-455.

Johnson, K.T.M., 1998. Experimental determination of partition coefficients for rare earth and high-field-strength elements between clinopyroxene, garnet, and basaltic melt at high pressures. Contributions to Mineralogy and Petrology, 133, 60-68.

Johnson, K.T.M., Dick, H.J.B., Shimizu, N., 1990. Melting in the oceanic upper mantle: an ion microprobe study of diopsides in abyssal peridotites. Journal of Geophysical Research 95, 2661–2678.

Karato, S., 1990. The role of hydrogen in the electrical conductivity of the upper mantle. Nature, 347(6290), 272-273.

Kepezhinskas, P.K., Defant, M.J., Drummond, M.S., 1995. Na metasomatism in the island-are mantle by slab melt-peridotite interaction: ecidence from mantle xenolths in the north Kamchatka Ace. J. Petrol., 36(6), 1505-1527

Kepezhinskas, P.K., Defant, M.J., Drummond, M.S., 1996. Progressive enrichment of island arc mantle by melt-peridotite interaction inferred from Kamchatka xenoliths. Geochim. Cosmochem. Acta, 60(7), 1217-1229

Keppler, H.and Bolfan-Casanova, N., 2006. Thermodynamics of water solubility and partitioning. In: Keppler, H., Smyth, J.R. (Ed.), Water in Nominally Anhydrous Minerals. Mineralogical Society of America, Washington D C, pp. 193-230.

Keppler, H. and Smyth, J.R., 2006. Water in Nominally Anhydrous Minerals. Washington D C, Mineralogical Society of America.

Koga, K., Hauri, E., Hirschmann, M., Bell, D., 2003. Hydrogen concentration analyses using SIMS and FTIR: Comparison and calibration for nominally anhydrous minerals. Geoch. Geophy. Geosys., 4(2), 1019.

Kohlstedt, D.L. and Mackwell, S.J., 1998. Diffusion of hydrogen and intrinsic point defects in olivine. Z. Phys. Chem., 207, 147-162.

Kohler, T.P. and Brey, G.P., 1990. Calcium exchange between olivine and clinopyroxene calibrated as a geothermobarometer for natural peridotites from 2 to 60 kb with applications. Geochim. Cosmochim. Acta, 54, 2375-2388

Kronenberg, A.K., 1994. Hydrogen speciation and chemical weakening of quartz. In: Heaney, P.J., Prewitt, C.T., Gibbs, G.V. (Ed.), Silica: physical behavior, geochemistry and materials applications. Mineralogical Society of American, Washington D C, pp. 123-176.

Kronenberg, A.K., Kirby, S.H., Aines, R.D., Rossman, G.R., 1986. Solubility and diffusional uptake of hydrogen in quartz at high water pressures: implications for hydrolytic weakending. J. Geophys. Res., 91, 12723-12744.

Kushiro, I., 1972. Effect of water on the composition of magmas formed at high pressures. J. Petrol., 13, 311-334

Kusky, T.M., Li, J.H., Tucker, R.D., 2001. The Archean Dongwanzi ophiolite complex, North China Craton 2.505-billion-year-old oceanic crust and mantle. Science, 292, 1142-1145.

Larsen, L.M., Pedersen, A.K., Sundvoll, B., Frei, R., 2003. Alkali picrites formaed by melting of old metasomatized lithospheric mantle: manitdlat member, vaigat formation, Palaeocene of west Greenland. J. Petrol., 44(1), 3-38

Lee, C.T., Brandon, A.D., Norman, M., 2003. Vanadium in peridotites as a proxy for paleo-fO2 during partial melting prospects, limitations, and implications. Geochim. Cosmochim. Acta, 67, 3045–3064.

Li, J.H., Hou, G.T., Huang, X.N., Zhang, Z.Q., Qian, X.L., 2001. Constraints on the super continental cycles: evidence from Precambrian geology of North China Craton. Acta Petrolei Sinica, 17, 177-186.

Li, J.H., Qian, X.L., Huang, X.N., Liu, S.W., 2000. Tectonic framework of the North China Craton and its cratonization in the early Precambrian. Acta Petrolei Sinica, 16, 1-10.

Li, Y.L., Uwe, W., Zheng, Y.F. and Zhi, X.C., 1999. Laser probe oxygen isotope analysis of minerals from mantle-derived rocks in eastern China. Chinese Science Bulletin 44, 740-744

Li, Z.X., 1994. Collision between the North and South China blocks: a crustal detachment model for suturing in the region east of the Tanlu fault, Geology, 22 , 739–742.

Li, Z.X., Lee, C.T., Peslier, A.H., Lenardic, A., Mackwell, S.J., 2008. Water contents in mantle xenoliths from the Colorado Plateau and vicinity: implications for the mantle rheology and hydration-induced thinning of continental lithosphere. J. Geophys. Res., 113, B09210.

Liu, D.Y., Nutman, A.P., Compston, W., Wu, J.S., Shen, Q.H., 1992. Remnants of >3800 Ma crust in the Chinese part of the Sino-Korean craton. Geology, 20, 339-342.

Ma, X.Y., 1989. Lithospheric Dynamics Map of China and Adjacent Seas (1:4,000,000) and Explanatory Notes. Beijing, Geological Publishing House.

McDonough, W.F. and Sun, S.S., 1995. The composition of Earth. Chemical Geology 120, 223–253.

McKenzie, D. and O'Nions, R.K., 1991. Partial melt distributions from inversion of rare Earth element concentrations. Journal of Petrology 32: 1,021-1,091.

Martin, R.F. and Donnay, G., 1972. Hydroxyl in the mantle. Am. Mineral., 57, 554-570.

Mattey, D., Lowry, D., Macpherson, C., 1994. Oxygen isotope composition of mantle peridotite. Earth Planet. Sci. Lett., 128, 231-241.

Meade, C. and Jeanloz, R., 1991. Deep-focus earthquakes and recycling of water into the Earth. Science, 252, 68-72.

Menzies, M.A., Xu, Y., 1998. Geodynamics of the North China Craton. In: Flower, M., Chung, S.L., Lo, C.H., Lee, T.Y. (Eds.), Mantle Dynamics and plate interactions in East Asia. American Geophysical Union Monograph, vol. 27, pp. 155–165.

Menzies, M.A., Weiming, F., Zhang, M., 1993. Palaeozoic and Cenozoic lithoprobes and the loss of N120 km of Archaean lithosphere, Sino-Korean craton, China. Geological Society of London Special Publication, vol. 76, pp. 71–81.

Menzies, M., Xu, Y.G., Zhang, H.F., Fan, W.M., 2007. Integration of geology, geophysics and geochemistry A key to understanding the North China Craton. Lithos, 96, 1-21

Michael, P.J. 1995. Regionally distinctive sources of depleted MORB: evidence from trace elements and $H_2O$. Earth Planet. Sci. Lett., 131, 301-320.

Michael, P.J. 1988. The concentration, behaviour and storage of $H_2O$ in the suboceanic upper mantle: Implications for mantle metasomatism. Geochim. Cosmochim. Acta, 52, 555-566

Nazzareni, S., Skogby, H., Pompilio, M., Zanazzi, P.F., 2008. Water content of pyroxenes from Etna and Aeolian volcanoes: implications for the hazard of active Italian volcanoes. Abstr. Vol. SIMPAIC General Assembley, Sestri Levante 7–12 September 2008.

Neumann, E-R., Griffin, W.L., Pearson, N., O'Reilly, S.Y., 2004. The Evolution of the Upper Mantle beneath the Canary Islands: Information from Trace Elements and Sr isotope Ratios in Minerals in Mantle Xenoliths. J. Petrol., 45(12), 2573-2612

Nielsen, R.L., Gallahan, W.E., Newberger, F., 1992. Experimentally determined mineral-melt partition coefficients for Sc, Y and REE for olivine, orthopyroxene, pigeonite, magnetite and ilmenite. Contributions to Mineralogy and Petrology 110, 488-499

Niu, Y.L., 1997. Mantle Melting and Melt Extraction Processes beneath Ocean Ridges: Evidence from Abyssal Peridotites. J. Petrol. 38(8), 1047-1074

Niu, Y.L., 2004. Bulk-rock major and trace element compositions of abyssal peridotites: implications for mantle melting, melt extraction and post-melting processes beneath mid ocean ridges. J. Petrol., 45, 2423–2458

Niu, Y.L., 2005. Generation and evolution of basaltic magmas: some basic concepts and a new view on the origin of Mesozoic-Cenozoic basaltic volcanism in eastern China. Geol. J. Chi.Uni., 11, 9-46.

Nyblade, A.A., Pollack, H.N., Jones, D.L., Pdomore, F., Mushayandebvu, M., 1990. Terrestrial heat flow in East and Southern Africa. J. Geophys. Res., 95, 17371-17384.

O'Neill, H.C. and Navrotsky, A., 1983. Simple spinels; crystallographic parameters, cation radii, lattice energies, and cation distribution. Am. Mineral., 68(1), 181-194

O'Reilly S.Y. and Griffin, W.L., 1988. Mantle metasomatism beneath western Victoria, Australia: I. Metasomatic processes in Cr-diopside lherzolites. Geochim. Cosmochim. Acta, 52(2), 433-447

O'Reilly, S.Y., Griffin, W.L., Poudjom Djomani, Y.H., Morgan, P., 2001. Are lithospheres forever? Tracking changes in subcontinental lithospheric mantle through time. GSA Today 4–9.

Okay, A.I., Xu, S.T., Sengor, A.M.C., 1989. Coesite from the Dabie Shan eclogites, central China. Eur. J. Mineral., 1, 595-598.

Paterson, M.S., 1982. The determination of hydroxyl by infrared absorption in quartz, silicate glasses and similar materials. Bull. Minéral., 105, 20-29.

Pearson, D.G., Shirey, S.B., Carlson, R.W., Boyd, F.R., Pokhilenko, N.P., Shimizu, N., 1995a. Re–Os, Sm–Nd and Rb–Sr isotope evidence for thick Archean lithospheric mantle beneath the Siberia craton modified by multi-stage metasomatism. Geochim. Cosmochim. Acta 59, 959–977.

Pearson, D.G., Shirey, S.B., Carlson, R.W., Boyd, F.R., Nixon, P.H., 1995b. Stabilisation of Archean lithospheric mantle: a Re–Os isotope study of peridotite xenoliths from the Kaapvaal craton. Earth Planet. Sci. Lett. 134, 341–357.

Peslier, A.H. and Luhr, J.F., 2006. Hydrogen loss from olivines in mantle xenoliths from Simcoe (USA) and Mexico: mafic alkalic magma ascent rates and water budget of the sub-continental lithosphere. Earth Planet. Sci. Lett., 242, 302-319.

Peslier, A.H., Luhr, J.F., Post, J., 2002. Low water contents in pyroxenes from spinel-peridotites of the oxidized, sub-arc mantle wedge. Earth Planet. Sci. Lett., 201, 69-86.

Priestley, K., Debayle, E., McKenzie, D., Pilidou, S., 2006. Upper mantle structure of eastern Asia from multimode surface waveform tomography. J. Geophys. Res., 111, doi: 2005JB004082.

Rauch, M. and Keppler, H., 2002. Water solubility in orthopyroxene. Contrib. Mineral. Petrol., 143, 525-536.

Ree, J.H., Cho, M., Kwon, S.T., Nakamura, E., 1996. Possible eastward extension of Chinese collision belt in South Korea: the Imjingang belt. Geology 24, 1071–1074.

Reisberg, L., Zhi, X.C., Lorand, J-P., Wagner, C., Peng, Z.C., Zimmermann, C., 2005. Re-Os and S systematic of spinel peridotite xenoliths from east central China: evidence for contrasting effects of melt percolation. Earth and Planet. Sci. Lett., 239, 286-308

Rossman, G.R., 1996. Studies of OH in nominally anhydrous minerals. Phys. Chem. Miner., 23(4-5), 299-304.

Rudnick, R.L., Gao, S., Ling, W.L., Liu, Y.S., McDonough, W.F., 2004. Petrology and geochemistry of spinel peridotite xenoliths from Hannuoba and Qixia, North China craton. Lithos, 77, 609-637.

Salters, V.J. and Stracke, A. 2004. Composition of the depleted mantle. Geochem. Geophys. Geosyst., 5, Q05B07, doi:10.1029/2003GC000597.

Schiano, P., Clocchiatti, R., Shimizu, N., Maury, R.C., Jochum, K.P., Hofmann, A.W., 2002. Hydrous, silica-rich melts in the sub-arc mantle and their relationship with erupted arc lavas. Nature, 377, 595-600

Skogby, H. and Rossman, G.R., 1989. OH- in pyroxene: an experimental study of incorporation mechanisms and stability. Am. Mineral., 74, 1059-1069.

Skogby, H., Bell, D.R., Rossman, G.R., 1990. Hydroxide in pyroxene - variations in the natural environment. Am. Mineral., 75(7-8), 764-774.

Song, Y., Frey, F.A., Zhi, X.C., 1990. Isotopic characteristics of Hannuoba basalts, eastern China: implications for their petrogenesis and the composition of subcontinental mantle. Chem. Geol. 85, 35–52.

Stalder, R.and Skogby, H., 2002. Hydrogen incorporation in enstatite. Eur. J. Mineral., 14(6), 1139-1144.

Stalder, R.and Skogby, H., 2003. Hydrogen diffusion in natural and synthetic orthopyroxene. Phys. Chem. Miner., 30(1), 12-19.

Sun, S.S. and McDonough, W.F., 1989. Chemical and isotopic systematics of oceanic basalts: implications for mantle composition and processes

Sun, W.D., Peng, Z.C., Zhi, X.C., Wang, Z.R., Zhou, X.H., 1998, Osmium isotope determination on mantle-derived peridotite xenoliths from Panshishan with N-TIMS. Chinese. Sci. Bull. 43, 573-576

Takazawa, E., Frey, F., Shimizu, N., Obata, M., 1996. Evolution of the Horoman Peridotite (Hokkaido, Japan): implications from pyroxene compositions. Chemical Geology 134, 3–26.

Takazawa, E., Frey, F., Shimizu, N., Obata, M., 2000. Whole rock compositional variations in an upper mantle peridotite (Horoman, Hokkaido, Japan): are they consistent with a partial melting process? Geochimica et Cosmochimica Acta, 64, 695-716

Tenner, T. J., Hirschmann, M. M., Withers, A. C., Hervig, R. L., 2009. Hydrogen partitioning between nominally anhydrous mantle minerals and melt between 3 and 5 GPa and applications to hydrous peridotite partial melting, Chem. Geol., 262, 42-56.

van der Lee, S., Regenauer-Lieb, K., Yuen, D.A., 2008. The role of water in connecting past and future episodes of subduction. Earth Planet. Sci. Lett., 273, 15–27.

Vannucci, R., Bottazzi, P., Wulff-Pedersen, E., Neumann, E.R., 1998. Partitioning of REE, Y, Sr, Zr and Ti between clinopyroxene and silicate melting in the mantle under La Palma (Canary Islands): implications for the nature of the metasomatic agents. Earth Planet. Sci. Lett., 158(1), 39-51

Wade, J., Plank, T., Hauri, E.H., Kelley, K.A., Roggensack, K., Zimmer, M., 2008, Prediction of magmatic water contents via measurement of $H_2O$ in clinopyroxene phenocrysts. Geology, 36, 799–802.

Walker, R.J., Carlson, R.W., Shirey, S.B., Boyd, F.R., 1989. Os, Sr, Nd, and Pb isotope systematic of southern African peridotite xenoliths: implications for the chemical evolution of subcontinental mantle. Geochim. Cosmochim. Acta, 53, 1583–1595.

Wang, W.Y. and Gasparik, T., 2001. Metasomatic clinopyroxene inclusions in dimonds from the Liaoning Province, China. Geochim. Cosmochim. Acta, 65(4), 611-620

Wang, X.M., Liou, J.G., Mao, H.K., 1989. Coesite-bearing eclogites from the Dabie Mountains in central China. Geology, 17, 1085-1088.

Williams, Q. and Hemley, R.J., 2001. Hydrogen in the deep earth. Annu. Rev. Earth Planet. Sci., 29, 365-418.

Withers, A.C. and Hirschmann, M.M., 2007. $H_2O$ storage capacity of $MgSiO_3$ clinoenstatite at 8-13 GPa, 1100-1400ºC, Contrib. Mineral. Petrol., 154, 663-674.

Withers, A.C. and Hirschmann, M.M., 2008. Influence of temperature, composition, silica activity and oxygen fugacity on the $H_2O$ storage capacity of olivine at 8GPa, Contrib. Mineral. Petrol., 156, 595-605.

Witt-Eickschen, G. and Kramm, U., 1997. Mantle upwelling and metasomatism beneath Central Europe: geochemical and isotopic constraints from mantle xenoliths from the Rho¨n (Germany). Journal of Petrology 38, 479–493.

Woodland, A.B, Kornprobst, J., Wood, B.J, 1992, Oxygen Thermobarometry of Orogenic Lherzolite Massifs, Journal of Petrology, 33, 203-230

Workman, R.K. and Hart, S.R., 2005. Major and trace element composition of the depleted MORB mantle (DMM). Earth Planet. Sci. Lett., 231, 53-72.

Workman, R. K., Hauri, E.H., Hart, S.R., Wang, J.H., Blusztajn, J., 2006. Volatile and trace element in basaltic glasses from Samoa: implications for water distribution in the mantle, Earth Planet. Sci. Lett., 241, 932-951.

Wu, F.Y., Lin, J.Q., Wilde, S.A., Zhang, X.O., Yang, J.H., 2005. Nature and significance of the Early Cretaceous giant igneous event in eastern China. Earth Planet. Sci. Lett., 233, 103-119.

Wu, F.Y., Walker, R.J., Ren, X.W., Sun, D.Y., Zhou, X.H., 2003. Osmium isotopic constraints on the age of lithospheric mantle beneath northeastern China. Chem. Geol., 196, 107-129.

Xia, Q.K., Hao, Y.T., Li, P., Deloule, E., Coltorti, M., Dallai, L., Yang, X.Z., Feng, M., 2010. Low water content of the Cenozoic lithospheric mantle beneath the eastern part of the North China Craton. accepted by JGR-Solid Earth

Xu, S.T., Su, W., Liu, Y.C., Jiang, L.L., Ji, S., Okay, A.I., Sengor, A.M.C., 1992. Diamond from the Dabie Shan metamorphic rocks and its implication for tectonic setting. Science, 256, 80-82.

Xu, X.S., Griffin, W. L., O'Reilly, S.Y., Pearson, N. J., Geng, H.Y. and Zheng, J.P. 2008a. Re-Os isotopes of sulfides in mantle xenoliths from eastern China: Progressive modification of lithospheric mantle. Lithos. 102, 43-64

Xu, X.S., O'Reilly, S.Y., Griffin, W.L., Zhou, X.M., Huang, X.L., 1998. The nature of the Cenozoic lithosphere at Nushan, Eastern China. In: Flower, M.F.J., Chung, S.L., Lo, C.H., Lee, T.Y.

Xu, X.S., O'Reilly, S.Y., Griffin, W.L., Zhou, X.M., 2000. Genesis of young lithospheric mantle in southeastern China: an LAM-ICPMS trace element study. J. Petrol., 41(1), 111-148.

Xu, Y.G., 2001. Thermo-tectonic destruction of the Archean lithospheric keel beneath the Sino-Korean craton in China: evidence, timing and mechanism. Phys. Chem. Earth, 26A, 747-757.

Xu, Y.G., 2002. Evidence for crustal components in the mantle and constraints on crustal recycling mechanisms: pyroxenite xenoliths from Hannuoba, North China. Chem. Geol., 182, 301-322

Xu, Y.G., Chung, S.L., Ma, J., Shi, L., 2004. Contrasting Cenozoic lithospheric evolution and architecture in the Western and Eastern Sino-Korean Craton: constraints from geochemistry of basalts and mantle xenoliths. J. Geol., 112, 593-605.

Xu, Y.G., 2007. Diachronous lithospheric thinning of the North China Craton and formation of the Daxin'anling - Taihangshan gravity lineament. Lithos, 96, 281-298.

Xu, Y. G., Blusztajn, J., Ma, J.L., Suzuki, K., Liu, J.F., Hart, S.R., 2008b, Late Archean to Early Proterozoic lithospheric mantle beneath the western North China craton: Sr-Nd-Os isotopes of peridotite xenoliths from Yangyan and Fansi, Lithos, 102, 25-42.

Yang. H.J., Sen, G., Shimizu, N., 1998. Mid-ocean ridge melting: constraints from lithospheric xenoliths at Oahu, Hawaii. J. Pertol. 39(2), 277-295

Yang, J.H., Wu, F.Y., Wilde, S.A., 2003. A review of the geodynamic setting of large-scale late Mesozoic gold mineralization in the North China Craton: an association with lithospheric thinning. Ore Geol. Rev., 23, 125-152

Yang, X. Z., Xia, Q.K., Deloule, E., Dallai, L., Fan, Q.C., Feng, M., 2008. Water in minerals of the continental lithospheric mantle and overlying lower crust: A comparative study of peridotite and granulite xenoliths from the North China Craton, Chem. Geol., 256, 33-45

Yaxley, G.M., Green, D.H., Kamenetsky, V., 1998. Carbonatite Metasomatism in the Southeastern Australian Lithosphere. J. Petrol. 39(11), 1917-1930

Ye, K., Cong, B.L., Ye, D., 2000. The possible subduction of continental material to depths greater than 200 km. Nature, 407, 734-736.

Ying, J. F., Zhang, H. F., Kita, N., Morishita, Y. and Shimoda, G., 2006. Nature and evolution of Late Cretaceous lithospheric mantle beneath the eastern North China Craton: constraints from petrology and geochemistry of peridotitic xenoliths from Junan, Shandong province, China. Earth Planet. Sci. Lett., 244, 622-638.

Yu, H.M., Xia, Q.K., Wang, R.C. and Chen, X.M., 2005. Oxygen isotope and trace element compositions of peridotite xenoliths from Panshishan volcano, SE China. Acta Petrologica Sinica, 21, 1609-1616 (in Chinese with English abstract)

Yui, T.F., Rumble, D., Lo, C.H., 1995. Unusually low $d^{18}O$ ultrahigh-pressure metamorphic rocks from the Sulu terrain, eastern China. Geochim. Cosmochim. Acta, 59, 2859-2864.

Zack, T., Foley, S.F., Jenner, G.A., 1997. A consistent partition coefficient set for clinopyroxene, amphibole and garnet from laser ablation microprobe analysis of garnet pyroxenites from Kakanui, New Zealand. Neues Jahrbuch fur Mineralogie, Abhirchen 172(1): 23-41.

Zangana, N.A., Downes, H., Thirlwall, M.F., Marriner, G.F., Bea, F., 1999. Geochemical variation in peridotite xenoliths and their constituent clinopyroxenes from Ray Pic (French Massif Cental): implications fot the composition of the shallow lithospheric mantle. Chmical Geology, 153, 11-35

Zhang, H.F., Sun, M., Zhou, X.H., Fan, W.M., Zhai, M.G., Yin, J.F., 2002. Mesozoic lithosphere destruction beneath the North China Cration: evidence from Major-, trace-element and Sr-Nd-Pb isotope studies of Fangcheng basalts, Contrib. Mineral. Petrol., 144, 241-253

Zhang, H.F., Sun, M., Zhou, M.F., Fan, W.M., 2004. Highly heterogeneous late Mesozoic lithospheric mantle beneath the North China Craton: evidence from Sr-Nd-Pb isotopic systematics of mafic igneous rocks. Geol. Mag., 141, 55-62.

Zhang, H.F., 2005. Transfromation of lithospheric mantle through peridotite-melt reaction: a case of Sino-Korean craton, Eeath Planet. Sci. Lett., 237,768-780

Zhang, H.F., Goldstein, S.L., Zhou, X.H., Sun, M., Zheng, J.P., et al., 2008. Evolution of subcontinental lithospheric mantle beneath eastern China: Re-Os isotopic evidence from mantle xenoliths in Paleozoic kimberlites and Mesozoic basalts. Contrib. Mineral. Petrol.,155, 271-293 doi: 10.1007/s00410-007-0241-5.

Zhang, H.F., Goldstein, S.L., Zhou, X.H., Sun, M., Cai, Y., 2009. Comprehensive refertilization of lithospheric mantle beneath the North China Craton: further Os-Sr-Nd isotopic constrains, J. Geol. Soc., 166, 249-259

Zhang, M., Menzies, M.A., Suddaby, P., Thirlwall, M.F., 1991. EM1 signature from the post-Archaean subcontinental lithospheric mantle: isotopic evidence from the potassic volcanic rocks in NE China. Geochem. J. 25, 387-298

Zhang, M., Suddaby, P., Thompson, R.N., Thirlwall, M.F., Menzies, M.A., 1995. Potassic volcanic rocks in NE China: geochemical constrains on mantle source and magma genesis. J. Petrol., 36, 1275-1303

Zhao, G.C., Wilde, S.A., Cawood, P.A., Sun, M., 2000. Metamorphism of basement rocks in the Central Zone of the North China craton: implications for Paleoproterozoic tectonic evolution. Precambrian Res., 103, 55-88.

Zhao, G.C., Wilde, S.A., Cawood, P.A., Sun, M., 2001. Archean blocks and their boundaries in the North China Craton: lithological, geochemical, structural and P-T path constraints and tectonic evolution. Precambrian Res., 107, 45-73.

Zheng, J.P., 1999. Mesozoic-Cenozoic Mantle Replacement and Lithospheric Thinning Beneath the Eastern China. Wuhan, Publishing House of China University of Geosciences.

Zheng, J.P., O'Reilly, S.Y., Griffin, W.L., Lu, F.X., Zhang, M., 1998. Nature and evolution of Cenozoic lithospheric mantle beneath Shandong Peninsula, Sino-Korea craton, eastern China, Inter. Geol. Rev., 40, 471-499

Zheng, J.P., O'Reilly, S.Y., Griffin, W.L., Lu, F.X., Zhang, M., Person, N.J., 2001. Relict refractory mantle beneath the eastern North China Block: significance for lithospheric evolution. Lithos, 57, 43-66

Zheng, J.P., Giffin, W.L., O'reilly, S.Y., Yang, J.S., Li, T.F., Zhang, M., Zhang, R.Y., Liou, J.G., 2006. Mineral chemistry of peridotites from Paleozoic, Mesozoic and Cenozoic lithosphere: constraints on mantle evolution beneath eastern China. J. Petrol., 47, 2233-2256

Zheng, Y.F., 1993. Calculation of oxygen isotope fractionation in anhydrous silicate minerals. Geochim. Cosmochim. Acta, 57, 1079-1091.

Zheng, Y.F., Fu, B., Gong, B., Li, L., 2003. Stable isotope geochemistry of ultrahigh pressure metamorphic rocks from the Dabie-Sulu orogen in China: implications for geodynamics and fluid regime. Earth-Sci. Rev., 62, 105-161.

Zheng, Y.F., Fu, B., Gong, B., Li, S.G., 1996. Extreme $^{18}O$ depletion in eclogite from the Su-Lu terrane in East China. Eur. J. Mineral., 8, 317-323.

Zhi, X.C., 1991. Trace element geochemistry of Tertiary continental alkali basalts from Liuhe-Yizheng Jiangsu Province, China, Acta Pet. Sin., 2 30-42 (in Chinese, with English abstract).

Zhi, X.C., Li, Y.L., Zheng, Y.F., 1996, Oxygen isotpe compostion of mantle material from Suwai area (in Chinese with English abstract). Science Bulletin, 41(20),26-31

Zhi, X. C., Reisberg, L., Xu, X.S., 2007. Re-Os geochemistry of mantle peridotite xenoliths from Nushan (in Chinese with English abstract), J. Univ. Sci. Tech. China, 37(8), 945-952.

Zou H.B., Zindler, Alan., Xu, X.S. and Qi, Q., 2000. Major, trace element, and Nd, Sr and Pb isotope studies of Cenozic basalts in SE China: mantle sources, regional variations and tectonic significance. Chemical Geology, 177, 33-47

Zou, H.P., 2001. Continental marginal rifting along the northern South China Sea: the crustal response to the lower lithospheric delamination. Marine Geol. Quaternary Geol., 21, 39-44.

# Appendix

All the tables show in the thesis and the detailed information with respect to the EMPA, LA-ICP-MS and oxygen isotope measurements for xenoliths from Subei basin are compiled and provided below.

Table 2.1 Mineral mode of Panshishan, Lianshan and Fangshan peridotite xenoliths

| Locality | Sample | Rock Type | Mode(%) point counting | | | | Mode(%) mass balance | | | |
|---|---|---|---|---|---|---|---|---|---|---|
| | | | ol | opx | cpx | sp | ol | opx | cpx | sp |
| Panshishan | PSS01 | cpx-poor lh | 69 | 19 | 9 | 3 | 71 | 17 | 10 | 2 |
| | PSS02 | lh | 68 | 21 | 10 | 1 | | | | |
| | PSS05 | lh | 58 | 24 | 13 | 5 | | | | |
| | PSS07 | lh | 60 | 22 | 14 | 4 | | | | |
| | PSS10 | cpx-poor lh | 74 | 17 | 7 | 2 | | | | |
| | PSS11 | lh | 60 | 26 | 11 | 3 | 56 | 30 | 12 | 2 |
| | PSS12 | lh | 57 | 22 | 16 | 5 | | | | |
| | PSS13 | lh | 54 | 25 | 17 | 4 | | | | |
| | PSS15 | lh | 66 | 22 | 10 | 2 | 61 | 27 | 9 | 2 |
| | PSS16 | lh | 55 | 25 | 18 | 2 | | | | |
| | PSS17 | hz | 71 | 22 | 5 | 2 | 76 | 17 | 5 | 2 |
| | PSS18 | lh | 58 | 26 | 13 | 3 | | | | |
| | PSS19 | lh | 53 | 27 | 15 | 5 | | | | |
| | PSS20 | cpx-poor lh | 62 | 27 | 8 | 3 | | | | |
| Lianshan | LS01 | lh | 55 | 28 | 12 | 5 | | | | |
| | LS02 | lh | 52 | 30 | 14 | 4 | | | | |
| | LS03 | cpx-poor lh | 72 | 20 | 6 | 2 | 70 | 20 | 8 | 2 |
| | LS04 | ol-wb | 39 | 35 | 23 | 3 | | | | |
| | LS05 | lh | 56 | 29 | 13 | 2 | 60 | 28 | 11 | 1 |
| | LS06 | lh | 60 | 26 | 11 | 3 | 65 | 24 | 10 | 2 |
| | LS07 | lh | 57 | 27 | 14 | 2 | | | | |
| | LS08 | lh | 66 | 20 | 10 | 4 | | | | |
| | LS09 | lh | 48 | 31 | 17 | 4 | | | | |
| | LS12 | cpx-poor lh | 74 | 15 | 8 | 3 | | | | |
| | LS15 | cpx-poor lh | 69 | 21 | 7 | 3 | | | | |
| | LS16 | du | 90 | 5 | 3 | 2 | | | | |
| | LS17 | cpx-poor lh | 73 | 18 | 8 | 1 | 75 | 16 | 7 | 1 |
| | LS19 | cpx-poor lh | 66 | 26 | 7 | 1 | | | | |
| | LS20 | lh | 74 | 14 | 11 | 1 | 79 | 10 | 10 | 1 |

Lh lherzolite

cpx-poor lh: cpx poor lherzolite with 5<cpx% <10

Hz harzburgite

Ol-wb olivine websterite

Du dunite

Table 2.1 continued

| Locality | Sample | Rock Type | Mode(%) point counting | | | | Mode(%) mass balance | | | |
|---|---|---|---|---|---|---|---|---|---|---|
| | | | ol | opx | cpx | sp | ol | opx | cpx | sp |
| Lianshan | LS21 | cpx-poor lh | 78 | 13 | 6 | 3 | | | | |
| | LS22 | lh | 59 | 26 | 13 | 2 | 63 | 24 | 12 | 2 |
| | LS23 | lh | 60 | 24 | 14 | 2 | 62 | 22 | 15 | 2 |
| | LS24 | ol-wb | 38 | 41 | 17 | 4 | | | | |
| | LS26 | hz | 72 | 20 | 4 | 4 | | | | |
| | LS30 | lh | 62 | 24 | 12 | 2 | | | | |
| | LS31 | lh | 53 | 27 | 17 | 3 | | | | |
| Fangshan | FS01 | lh | 53 | 27 | 18 | 2 | | | | |
| | FS03 | lh | 58 | 27 | 13 | 2 | | | | |
| | FS06 | hz | 72 | 22 | 5 | 1 | | | | |
| | FS07 | lh | 57 | 28 | 12 | 3 | | | | |
| | FS11 | cpx-poor lh | 69 | 21 | 9 | 1 | 68 | 21 | 10 | 1 |
| | FS12 | lh | 51 | 32 | 15 | 2 | | | | |
| | FS13 | lh | 60 | 25 | 12 | 3 | | | | |
| | FS14 | lh | 66 | 20 | 11 | 3 | | | | |
| | FS16 | hz | 76 | 17 | 6 | 1 | | | | |
| | FS17 | lh | 56 | 26 | 16 | 2 | | | | |
| | FS18 | lh | 62 | 24 | 12 | 2 | | | | |
| | FS19 | lh | 49 | 30 | 19 | 2 | | | | |
| | FS21 | lh | 68 | 20 | 10 | 2 | | | | |
| | FS23 | lh | 71 | 15 | 12 | 2 | | | | |
| | FS24 | cpx-poor lh | 65 | 24 | 7 | 4 | | | | |
| | FS25 | hz | 72 | 19 | 5 | 4 | | | | |
| | FS26 | cpx-poor lh | 70 | 20 | 9 | 1 | | | | |
| | FS30 | hz | 77 | 18 | 5 | 0 | | | | |

Table 5.1 - Whole rock composition of peridotite xenoliths from Subei basin

| Sample | PSS01 | PSS11 | PSS15 | PSS17 | LS03 | LS05 | LS06 | LS17 | LS20 | LS22 | LS23 | FS11 |
|---|---|---|---|---|---|---|---|---|---|---|---|---|
| SiO2 | 44.88 | 45.22 | 44.39 | 44.11 | 43.94 | 44.81 | 45.01 | 43.48 | 43.94 | 44.32 | 44.22 | 44.55 |
| TiO2 | 0.08 | 0.11 | 0.17 | 0.02 | 0.05 | 0.07 | 0.08 | 0.01 | 0.04 | 0.13 | 0.12 | 0.07 |
| Al2O3 | 2.22 | 3.15 | 2.86 | 1.73 | 2.10 | 2.52 | 2.66 | 1.18 | 1.55 | 2.82 | 2.88 | 1.88 |
| Fe2O3 | 7.27 | 7.79 | 7.86 | 7.26 | 8.55 | 8.34 | 7.72 | 6.59 | 6.97 | 8.72 | 7.64 | 7.37 |
| MnO | 0.12 | 0.13 | 0.13 | 0.12 | 0.13 | 0.13 | 0.13 | 0.11 | 0.12 | 0.14 | 0.12 | 0.12 |
| MgO | 42.96 | 40.42 | 41.74 | 45.35 | 42.52 | 41.28 | 41.99 | 45.67 | 44.98 | 40.38 | 38.88 | 43.34 |
| CaO | 1.89 | 2.56 | 2.00 | 0.88 | 1.80 | 2.36 | 1.99 | 1.49 | 1.73 | 2.48 | 2.85 | 2.09 |
| Na2O | 0.10 | 0.13 | 0.11 | 0.03 | 0.07 | 0.10 | 0.10 | 0.03 | 0.07 | 0.09 | 0.12 | 0.09 |
| K2O | 0.03 | 0.03 | 0.04 | 0.01 | 0.02 | **nd** | **nd** | 0.01 | 0.02 | 0.03 | 0.02 | **nd** |
| P2O5 | 0.02 | 0.03 | 0.03 | 0.01 | 0.01 | **nd** | **nd** | 0.01 | 0.01 | 0.01 | 0.01 | **nd** |
| LOI | 0.43 | 0.43 | 0.68 | 0.48 | 0.80 | 0.38 | 0.31 | 1.42 | 0.56 | 0.87 | 3.14 | 0.48 |
| TOTALE | 100.00 | 100.00 | 100.00 | 100.00 | 100.00 | 100.00 | 100.00 | 100.00 | 100.00 | 100.00 | 100.00 | 100.00 |
| | | | | | | | | | | | | |
| SiO2 | 45.07 | 45.42 | 44.70 | 44.33 | 44.30 | 44.98 | 45.16 | 44.11 | 44.19 | 44.71 | 45.65 | 44.77 |
| TiO2 | 0.08 | 0.11 | 0.17 | 0.02 | 0.05 | 0.07 | 0.08 | 0.01 | 0.04 | 0.14 | 0.12 | 0.07 |
| Al2O3 | 2.23 | 3.16 | 2.88 | 1.73 | 2.12 | 2.53 | 2.66 | 1.20 | 1.56 | 2.84 | 2.98 | 1.89 |
| Fe2O3 | 7.30 | 7.83 | 7.91 | 7.30 | 8.62 | 8.38 | 7.75 | 6.68 | 7.01 | 8.80 | 7.89 | 7.41 |
| MnO | 0.12 | 0.13 | 0.13 | 0.12 | 0.13 | 0.13 | 0.13 | 0.12 | 0.12 | 0.14 | 0.13 | 0.12 |
| MgO | 43.14 | 40.60 | 42.03 | 45.57 | 42.87 | 41.44 | 42.13 | 46.33 | 45.23 | 40.73 | 40.14 | 43.56 |
| CaO | 1.90 | 2.58 | 2.01 | 0.88 | 1.82 | 2.37 | 2.00 | 1.52 | 1.74 | 2.51 | 2.94 | 2.10 |
| Na2O | 0.10 | 0.13 | 0.11 | 0.03 | 0.07 | 0.10 | 0.10 | 0.03 | 0.07 | 0.09 | 0.13 | 0.09 |
| K2O | 0.03 | 0.03 | 0.04 | 0.01 | 0.02 | **nd** | **nd** | 0.01 | 0.02 | 0.03 | 0.02 | **nd** |
| P2O5 | 0.02 | 0.03 | 0.03 | 0.01 | 0.01 | **nd** | **nd** | 0.01 | 0.02 | 0.01 | 0.01 | **nd** |
| TOTALE | 100.00 | 100.00 | 100.00 | 100.00 | 100.00 | 100.00 | 100.00 | 100.00 | 100.00 | 100.00 | 100.00 | 100.00 |

Table 5.1 continued

| Sample | PSS01 | PSS11 | PSS15 | PSS17 | LS03 | LS05 | LS06 | LS17 | LS20 | LS22 | LS23 | FS11 |
|---|---|---|---|---|---|---|---|---|---|---|---|---|
| Ba | **nd** | **nd** | 1.2 | **nd** | **nd** | **nd** | **nd** | **nd** | **nd** | **nd** | **nd** | **nd** |
| Ce | 4.60 | 5.91 | 4.98 | 4.45 | 3.42 | 5.74 | 5.20 | 1.90 | 4.35 | 3.52 | 2.76 | 4.11 |
| Co | 118 | 110 | 116 | 129 | 119 | 116 | 115 | 125 | 129 | 113 | 107 | 118 |
| Cr | 1562 | 3103 | 2464 | 2172 | 2425 | 2275 | 2756 | 1563 | 1424 | 2328 | 2047 | 1732 |
| La | **nd** | **nd** | **nd** | **nd** | **nd** | **nd** | **nd** | **nd** | **nd** | **nd** | **nd** | **nd** |
| Nb | **nd** | **nd** | 0.2 | 0.1 | **nd** | **nd** | **nd** | **nd** | **nd** | **nd** | **nd** | **nd** |
| Ni | 2022 | 1955 | 2056 | 2247 | 2117 | 2003 | 1978 | 2226 | 2168 | 1921 | 1871 | 2123 |
| Pb | 1.62 | 2.70 | 2.00 | 1.17 | 1.01 | 1.35 | 1.08 | 1.25 | 0.96 | 1.68 | **nd** | 1.11 |
| Rb | 2.67 | 2.84 | 3.48 | 1.58 | 0.93 | 0.65 | 0.26 | 0.93 | 1.27 | 1.23 | 0.78 | 0.85 |
| Sr | 4.34 | 9.26 | 11.67 | 9.34 | 9.03 | 1.76 | 6.60 | 8.28 | 11.30 | 6.90 | 9.41 | 6.13 |
| Th | **nd** | **nd** | 0.20 | **nd** | **nd** | **nd** | **nd** | **nd** | **nd** | 0.14 | 0.23 | **nd** |
| V | 54.9 | 78.9 | 72.9 | 39.5 | 48.7 | 61.8 | 64.0 | 26.8 | 34.8 | 77.1 | 73.7 | 53.1 |
| Y | 9.44 | 10.46 | 10.12 | 4.83 | 7.34 | 9.53 | 8.75 | 4.92 | 8.27 | 10.48 | 8.80 | 8.70 |
| Zn | 45.3 | 64.6 | 60.6 | 51.3 | 53.8 | 47.8 | 55.6 | 46.0 | 48.6 | 53.8 | 50.5 | 42.8 |
| Zr | **nd** | **nd** | 0.6 | **nd** | **nd** | **nd** | **nd** | **nd** | 0.3 | **nd** | **nd** | **nd** |
| Cu | 17.1 | 28.0 | 18.9 | 4.6 | 10.8 | 16.2 | 15.6 | 1.5 | 12.4 | 19.5 | 20.6 | 26.4 |
| Ga | 11.68 | 19.06 | 6.38 | 27.65 | 2.76 | 3.25 | 2.61 | 1.76 | 3.02 | 4.86 | 9.05 | 3.79 |
| Nd | **nd** | **nd** | 1.5 | 0.5 | 0.8 | 1.2 | 1.0 | 0.2 | 0.3 | 0.2 | **nd** | 0.2 |
| S | **nd** | **nd** | **nd** | 166.6 | **nd** | **nd** | **nd** | 177.1 | 140.4 | **nd** | **nd** | **nd** |
| Sc | 5.36 | 8.56 | 6.31 | 2.89 | 4.83 | 8.19 | 5.92 | 2.64 | 3.51 | 7.92 | 6.93 | 6.84 |

nd: not determined

LOI: Lost on ignition

Table 5.2 - Olivine major element composition in peridotite xenoliths from Subei basin

| Location | Sample | $SiO_2$ | $TiO_2$ | $Al_2O_3$ | $Cr_2O_3$ | FeO | MnO | MgO | CaO | $Na_2O$ | $K_2O$ | NiO | TOTAL | Mg# |
|---|---|---|---|---|---|---|---|---|---|---|---|---|---|---|
| Panshishan | PSS01 | 41.98 | 0.03 | 0.00 | 0.01 | 9.99 | 0.16 | 49.58 | 0.04 | 0.00 | 0.00 | 0.28 | 102.08 | 89.85 |
| | PSS02 | 41.31 | 0.03 | 0.00 | 0.04 | 10.00 | 0.14 | 49.59 | 0.06 | 0.00 | 0.00 | 0.50 | 101.67 | 89.84 |
| | PSS05 | 41.07 | 0.00 | 0.02 | 0.01 | 9.55 | 0.13 | 48.82 | 0.03 | 0.01 | 0.00 | 0.21 | 99.85 | 90.11 |
| | PSS07 | 40.89 | 0.00 | 0.00 | 0.00 | 10.38 | 0.14 | 49.40 | 0.02 | 0.01 | 0.01 | 0.31 | 101.16 | 89.46 |
| | PSS10 | 40.75 | 0.00 | 0.00 | 0.01 | 9.43 | 0.13 | 49.58 | 0.03 | 0.01 | 0.00 | 0.32 | 100.28 | 90.36 |
| | PSS11 | 40.77 | 0.00 | 0.01 | 0.01 | 9.54 | 0.16 | 50.24 | 0.03 | 0.00 | 0.01 | 0.39 | 101.15 | 90.38 |
| | PSS12 | 40.97 | 0.01 | 0.00 | 0.02 | 9.95 | 0.18 | 48.80 | 0.04 | 0.00 | 0.00 | 0.22 | 100.18 | 89.74 |
| | PSS13 | 40.97 | 0.00 | 0.00 | 0.00 | 9.24 | 0.13 | 49.69 | 0.03 | 0.01 | 0.01 | 0.32 | 100.40 | 90.55 |
| | PSS15 | 40.54 | 0.01 | 0.01 | 0.01 | 9.64 | 0.16 | 50.04 | 0.04 | 0.00 | 0.00 | 0.39 | 100.82 | 90.25 |
| | PSS16 | 40.47 | 0.00 | 0.03 | 0.02 | 10.04 | 0.16 | 48.72 | 0.05 | 0.00 | 0.00 | 0.29 | 99.78 | 89.64 |
| | PSS17 | 41.91 | 0.02 | 0.00 | 0.04 | 9.38 | 0.12 | 50.18 | 0.04 | 0.00 | 0.01 | 0.42 | 102.11 | 90.51 |
| | PSS18 | 41.03 | 0.00 | 0.00 | 0.02 | 9.37 | 0.16 | 48.99 | 0.02 | 0.00 | 0.00 | 0.25 | 99.85 | 90.31 |
| | PSS19 | 40.93 | 0.01 | 0.01 | 0.01 | 9.80 | 0.13 | 49.63 | 0.01 | 0.01 | 0.01 | 0.25 | 100.78 | 90.03 |
| | PSS20 | 40.74 | 0.00 | 0.00 | 0.02 | 9.81 | 0.14 | 50.05 | 0.03 | 0.01 | 0.00 | 0.37 | 101.18 | 90.09 |
| Lianshan | LS01 | 40.62 | 0.01 | 0.01 | 0.00 | 9.61 | 0.13 | 49.05 | 0.02 | 0.01 | 0.00 | 0.32 | 99.77 | 90.10 |
| | LS02 | 41.16 | 0.01 | 0.01 | 0.00 | 10.05 | 0.13 | 49.59 | 0.02 | 0.01 | 0.00 | 0.33 | 101.31 | 89.79 |
| | LS03 | 42.19 | 0.01 | 0.00 | 0.02 | 8.47 | 0.13 | 50.71 | 0.04 | 0.01 | 0.01 | 0.42 | 102.02 | 91.43 |
| | LS04 | 40.79 | 0.00 | 0.02 | 0.01 | 10.18 | 0.17 | 48.98 | 0.04 | 0.01 | 0.00 | 0.28 | 100.49 | 89.56 |
| | LS05 | 39.86 | 0.01 | 0.01 | 0.01 | 9.48 | 0.14 | 49.93 | 0.03 | 0.02 | 0.00 | 0.38 | 99.85 | 90.38 |
| | LS06 | 40.74 | 0.00 | 0.01 | 0.02 | 9.83 | 0.13 | 48.79 | 0.04 | 0.00 | 0.00 | 0.31 | 99.87 | 89.85 |
| | LS07 | 40.86 | 0.00 | 0.01 | 0.01 | 9.78 | 0.13 | 49.20 | 0.05 | 0.01 | 0.00 | 0.31 | 100.37 | 89.97 |
| | LS08 | 41.04 | 0.00 | 0.00 | 0.00 | 9.68 | 0.14 | 49.57 | 0.03 | 0.01 | 0.01 | 0.31 | 100.79 | 90.13 |
| | LS09 | 40.88 | 0.00 | 0.01 | 0.01 | 9.54 | 0.16 | 49.88 | 0.02 | 0.01 | 0.00 | 0.29 | 100.79 | 90.31 |
| | LS12 | 41.31 | 0.01 | 0.01 | 0.01 | 7.99 | 0.14 | 49.89 | 0.03 | 0.01 | 0.00 | 0.25 | 99.65 | 91.76 |
| | LS15 | 41.27 | 0.00 | 0.00 | 0.01 | 8.54 | 0.13 | 50.43 | 0.04 | 0.01 | 0.00 | 0.34 | 100.76 | 91.33 |
| | LS16 | 40.63 | 0.01 | 0.00 | 0.02 | 8.05 | 0.12 | 50.75 | 0.03 | 0.01 | 0.01 | 0.36 | 99.99 | 91.83 |

Table 5.2 continiued

| Location | Sample | $SiO_2$ | $TiO_2$ | $Al_2O_3$ | $Cr_2O_3$ | FeO | MnO | MgO | CaO | $Na_2O$ | $K_2O$ | NiO | TOTAL | Mg# |
|---|---|---|---|---|---|---|---|---|---|---|---|---|---|---|
| | LS17 | 40.89 | 0.01 | 0.01 | 0.01 | 8.21 | 0.14 | 51.20 | 0.04 | 0.00 | 0.00 | 0.39 | 100.90 | 91.75 |
| | LS19 | 40.67 | 0.01 | 0.01 | 0.00 | 9.32 | 0.12 | 49.89 | 0.02 | 0.00 | 0.00 | 0.31 | 100.36 | 90.52 |
| | LS20 | 41.93 | 0.03 | 0.00 | 0.03 | 9.59 | 0.13 | 49.91 | 0.04 | 0.00 | 0.00 | 0.36 | 102.03 | 90.27 |
| | LS21 | 40.89 | 0.00 | 0.00 | 0.01 | 8.20 | 0.12 | 49.50 | 0.02 | 0.02 | 0.01 | 0.29 | 99.06 | 91.50 |
| | LS22 | 40.52 | 0.01 | 0.01 | 0.01 | 10.44 | 0.14 | 48.51 | 0.04 | 0.01 | 0.01 | 0.29 | 99.99 | 89.23 |
| | LS23 | 41.79 | 0.01 | 0.01 | 0.03 | 10.17 | 0.14 | 49.25 | 0.03 | 0.02 | 0.03 | 0.36 | 101.82 | 89.62 |
| | LS24 | 40.84 | 0.01 | 0.00 | 0.00 | 9.86 | 0.12 | 49.20 | 0.04 | 0.01 | 0.00 | 0.28 | 100.37 | 89.90 |
| | LS26 | 40.89 | 0.01 | 0.01 | 0.02 | 8.96 | 0.12 | 50.38 | 0.03 | 0.01 | 0.00 | 0.34 | 100.76 | 90.93 |
| | LS30 | 40.56 | 0.01 | 0.02 | 0.02 | 9.77 | 0.14 | 48.10 | 0.05 | 0.00 | 0.00 | 0.32 | 99.00 | 89.78 |
| | LS31 | 40.76 | 0.00 | 0.00 | 0.00 | 10.35 | 0.13 | 48.55 | 0.02 | 0.01 | 0.00 | 0.34 | 100.15 | 89.32 |
| Fangshan | FS01 | 41.37 | 0.00 | 0.03 | 0.04 | 9.00 | 0.15 | 49.29 | 0.07 | 0.01 | 0.00 | 0.22 | 100.19 | 90.71 |
| | FS03 | 40.92 | 0.01 | 0.01 | 0.01 | 9.22 | 0.13 | 49.67 | 0.03 | 0.01 | 0.01 | 0.32 | 100.33 | 90.57 |
| | FS06 | 40.89 | 0.01 | 0.01 | 0.01 | 8.84 | 0.14 | 49.26 | 0.05 | 0.01 | 0.01 | 0.23 | 99.45 | 90.86 |
| | FS07 | 40.47 | 0.00 | 0.01 | 0.01 | 9.82 | 0.15 | 48.71 | 0.08 | 0.01 | 0.00 | 0.23 | 99.50 | 89.84 |
| | FS11 | 40.57 | 0.01 | 0.01 | 0.01 | 9.21 | 0.13 | 50.32 | 0.12 | 0.04 | 0.00 | 0.39 | 100.82 | 90.69 |
| | FS12 | 41.16 | 0.01 | 0.04 | 0.00 | 9.23 | 0.14 | 48.79 | 0.11 | 0.00 | 0.01 | 0.26 | 99.75 | 90.40 |
| | FS13 | 40.95 | 0.02 | 0.04 | 0.03 | 9.69 | 0.15 | 48.88 | 0.09 | 0.01 | 0.00 | 0.24 | 100.08 | 90.00 |
| | FS14 | 40.91 | 0.01 | 0.04 | 0.02 | 9.73 | 0.13 | 48.55 | 0.07 | 0.02 | 0.01 | 0.21 | 99.70 | 89.89 |
| | FS16 | 41.21 | 0.01 | 0.03 | 0.03 | 8.42 | 0.14 | 50.02 | 0.04 | 0.01 | 0.00 | 0.24 | 100.16 | 91.37 |
| | FS17 | 40.87 | 0.00 | 0.02 | 0.02 | 8.88 | 0.16 | 48.95 | 0.05 | 0.03 | 0.01 | 0.26 | 99.24 | 90.77 |
| | FS18 | 40.09 | 0.02 | 0.04 | 0.04 | 10.07 | 0.15 | 49.52 | 0.12 | 0.00 | 0.00 | 0.36 | 100.42 | 89.76 |
| | FS19 | 40.94 | 0.01 | 0.04 | 0.01 | 9.68 | 0.14 | 48.70 | 0.10 | 0.01 | 0.01 | 0.23 | 99.85 | 89.97 |
| | FS21 | 40.93 | 0.01 | 0.03 | 0.02 | 9.80 | 0.14 | 48.51 | 0.05 | 0.02 | 0.00 | 0.25 | 99.76 | 89.82 |
| | FS23 | 41.15 | 0.00 | 0.02 | 0.04 | 9.14 | 0.12 | 48.99 | 0.09 | 0.01 | 0.01 | 0.24 | 99.82 | 90.52 |
| | FS24 | 40.48 | 0.00 | 0.01 | 0.01 | 8.82 | 0.14 | 50.61 | 0.04 | 0.00 | 0.00 | 0.43 | 100.56 | 91.09 |
| | FS26 | 40.84 | 0.00 | 0.01 | 0.02 | 9.89 | 0.14 | 48.40 | 0.04 | 0.00 | 0.00 | 0.23 | 99.58 | 89.72 |

Table 5.3 - Orthopyroxene major element composition in peridotite xenoliths from Subei basin

| Location | Sample | $SiO_2$ | $TiO_2$ | $Al_2O_3$ | $Cr_2O_3$ | FeO | MnO | MgO | CaO | $Na_2O$ | $K_2O$ | NiO | TOTAL | Mg# |
|---|---|---|---|---|---|---|---|---|---|---|---|---|---|---|
| Panshishan | PSS01 | 56.10 | 0.11 | 4.29 | 0.39 | 6.22 | 0.15 | 33.27 | 0.61 | 0.08 | 0.00 | 0.08 | 101.31 | 90.51 |
| | PSS02 | 56.49 | 0.08 | 4.24 | 0.37 | 6.25 | 0.16 | 33.59 | 0.61 | 0.08 | 0.00 | 0.10 | 101.97 | 90.55 |
| | PSS05 | 55.50 | 0.07 | 4.48 | 0.34 | 5.86 | 0.14 | 32.61 | 0.63 | 0.12 | 0.01 | 0.08 | 99.83 | 90.84 |
| | PSS07 | 57.71 | 0.11 | 3.66 | 0.21 | 6.57 | 0.17 | 31.51 | 0.43 | 0.06 | 0.00 | 0.07 | 100.49 | 89.53 |
| | PSS10 | 57.27 | 0.16 | 3.63 | 0.52 | 6.02 | 0.18 | 31.93 | 0.61 | 0.02 | 0.00 | 0.08 | 100.40 | 90.43 |
| | PSS11 | 55.34 | 0.10 | 3.66 | 0.31 | 6.19 | 0.16 | 34.30 | 0.43 | 0.05 | 0.00 | 0.11 | 100.66 | 90.81 |
| | PSS12 | 54.96 | 0.12 | 4.60 | 0.35 | 6.07 | 0.17 | 32.53 | 0.60 | 0.06 | 0.01 | 0.05 | 99.51 | 90.52 |
| | PSS13 | 57.85 | 0.06 | 3.61 | 0.24 | 5.75 | 0.15 | 31.39 | 0.51 | 0.05 | 0.00 | 0.09 | 99.71 | 90.68 |
| | PSS15 | 55.66 | 0.15 | 3.88 | 0.33 | 6.33 | 0.14 | 34.10 | 0.46 | 0.05 | 0.00 | 0.09 | 101.19 | 90.57 |
| | PSS16 | 56.67 | 0.11 | 4.82 | 0.34 | 6.36 | 0.16 | 30.48 | 0.78 | 0.13 | 0.00 | 0.08 | 99.93 | 89.52 |
| | PSS17 | 56.84 | 0.06 | 3.37 | 0.45 | 5.74 | 0.08 | 33.99 | 0.60 | 0.03 | 0.00 | 0.06 | 101.23 | 91.34 |
| | PSS18 | 55.58 | 0.10 | 3.65 | 0.21 | 6.52 | 0.17 | 33.07 | 0.37 | 0.00 | 0.00 | 0.06 | 99.73 | 90.04 |
| | PSS19 | 57.80 | 0.04 | 4.22 | 0.24 | 6.39 | 0.14 | 31.50 | 0.34 | 0.07 | 0.00 | 0.07 | 100.83 | 89.79 |
| | PSS20 | 55.79 | 0.16 | 3.58 | 0.39 | 6.33 | 0.14 | 34.31 | 0.46 | 0.03 | 0.00 | 0.09 | 101.28 | 90.63 |
| Lianshan | LS01 | 54.73 | 0.08 | 3.96 | 0.38 | 6.29 | 0.12 | 32.66 | 0.51 | 0.08 | 0.01 | 0.05 | 98.87 | 90.24 |
| | LS02 | 55.34 | 0.09 | 4.09 | 0.31 | 6.40 | 0.16 | 32.86 | 0.47 | 0.08 | 0.00 | 0.06 | 99.87 | 90.15 |
| | LS03 | 57.21 | 0.07 | 2.86 | 0.47 | 5.39 | 0.10 | 34.63 | 0.58 | 0.05 | 0.01 | 0.13 | 101.49 | 91.97 |
| | LS04 | 54.93 | 0.13 | 4.50 | 0.30 | 6.34 | 0.15 | 32.62 | 0.65 | 0.11 | 0.00 | 0.08 | 99.81 | 90.18 |
| | LS05 | 55.23 | 0.08 | 3.79 | 0.26 | 6.38 | 0.16 | 34.01 | 0.47 | 0.06 | 0.02 | 0.07 | 100.54 | 90.48 |
| | LS06 | 55.01 | 0.11 | 4.29 | 0.41 | 5.95 | 0.13 | 32.74 | 0.64 | 0.10 | 0.01 | 0.07 | 99.47 | 90.75 |
| | LS07 | 55.08 | 0.11 | 4.30 | 0.32 | 6.19 | 0.15 | 32.99 | 0.63 | 0.10 | 0.00 | 0.08 | 99.95 | 90.48 |
| | LS08 | 55.46 | 0.10 | 4.02 | 0.23 | 6.11 | 0.15 | 33.28 | 0.53 | 0.08 | 0.01 | 0.07 | 100.04 | 90.66 |
| | LS09 | 55.75 | 0.05 | 3.49 | 0.31 | 6.11 | 0.14 | 33.79 | 0.46 | 0.03 | 0.00 | 0.06 | 100.21 | 90.79 |
| | LS12 | 56.09 | 0.03 | 3.37 | 0.50 | 5.51 | 0.13 | 34.57 | 0.60 | 0.04 | 0.00 | 0.09 | 100.94 | 91.79 |
| | LS15 | 56.32 | 0.02 | 2.65 | 0.33 | 5.39 | 0.16 | 34.26 | 0.60 | 0.05 | 0.00 | 0.08 | 99.84 | 91.89 |
| | LS16 | 57.13 | 0.07 | 1.82 | 0.44 | 5.22 | 0.18 | 35.11 | 0.48 | 0.08 | 0.01 | 0.05 | 100.59 | 92.30 |

Table 5.3 continued

| Location | Sample | $SiO_2$ | $TiO_2$ | $Al_2O_3$ | $Cr_2O_3$ | FeO | MnO | MgO | CaO | $Na_2O$ | $K_2O$ | NiO | TOTAL | 92.05 |
|---|---|---|---|---|---|---|---|---|---|---|---|---|---|---|
| | LS17 | 56.13 | 0.03 | 2.72 | 0.54 | 5.44 | 0.15 | 35.33 | 0.65 | 0.04 | 0.00 | 0.06 | 101.08 | 92.05 |
| | LS19 | 55.63 | 0.06 | 2.93 | 0.48 | 5.94 | 0.14 | 33.95 | 0.52 | 0.05 | 0.01 | 0.07 | 99.77 | 91.06 |
| | LS20 | 56.75 | 0.05 | 3.61 | 0.54 | 6.05 | 0.09 | 33.91 | 0.64 | 0.14 | 0.00 | 0.12 | 101.90 | 90.91 |
| | LS21 | 56.29 | 0.04 | 1.88 | 0.24 | 5.34 | 0.13 | 34.09 | 0.48 | 0.07 | 0.01 | 0.07 | 98.64 | 91.93 |
| | LS22 | 54.61 | 0.15 | 4.10 | 0.22 | 6.60 | 0.16 | 32.47 | 0.55 | 0.07 | 0.01 | 0.06 | 98.99 | 89.77 |
| | LS23 | 56.17 | 0.13 | 4.49 | 0.31 | 6.45 | 0.16 | 33.37 | 0.59 | 0.06 | 0.01 | 0.05 | 101.79 | 90.22 |
| | LS24 | 54.97 | 0.10 | 4.39 | 0.26 | 6.32 | 0.15 | 33.00 | 0.58 | 0.09 | 0.00 | 0.08 | 99.94 | 90.30 |
| | LS26 | 56.01 | 0.00 | 2.29 | 0.47 | 5.63 | 0.14 | 34.33 | 0.57 | 0.01 | 0.00 | 0.08 | 99.54 | 91.58 |
| | LS30 | 54.75 | 0.10 | 4.32 | 0.27 | 6.32 | 0.11 | 31.71 | 0.67 | 0.11 | 0.02 | 0.08 | 98.46 | 89.94 |
| | LS31 | 55.36 | 0.13 | 3.71 | 0.24 | 6.75 | 0.14 | 33.04 | 0.41 | 0.06 | 0.01 | 0.06 | 99.90 | 89.72 |
| Fangshan | FS01 | 55.54 | 0.09 | 4.35 | 0.45 | 5.71 | 0.15 | 32.73 | 0.64 | 0.14 | 0.00 | 0.03 | 99.82 | 91.09 |
| | FS03 | 54.33 | 0.07 | 5.78 | 0.75 | 5.36 | 0.14 | 31.72 | 1.48 | 0.08 | 0.00 | 0.08 | 99.79 | 91.34 |
| | FS06 | 55.93 | 0.00 | 3.11 | 0.67 | 5.40 | 0.13 | 33.19 | 0.87 | 0.08 | 0.00 | 0.07 | 99.46 | 91.64 |
| | FS07 | 54.41 | 0.13 | 4.81 | 0.38 | 6.25 | 0.15 | 32.18 | 0.72 | 0.08 | 0.00 | 0.07 | 99.20 | 90.17 |
| | FS11 | 55.40 | 0.13 | 4.20 | 0.51 | 6.02 | 0.12 | 33.96 | 0.73 | 0.11 | 0.00 | 0.11 | 101.29 | 90.95 |
| | FS12 | 54.21 | 0.11 | 5.81 | 0.55 | 5.80 | 0.14 | 31.37 | 1.24 | 0.12 | 0.00 | 0.07 | 99.42 | 90.60 |
| | FS13 | 54.57 | 0.11 | 5.78 | 0.43 | 5.95 | 0.16 | 31.63 | 1.05 | 0.16 | 0.00 | 0.07 | 99.90 | 90.46 |
| | FS14 | 54.64 | 0.14 | 5.06 | 0.54 | 6.08 | 0.17 | 31.82 | 0.93 | 0.12 | 0.00 | 0.08 | 99.57 | 90.32 |
| | FS16 | 55.62 | 0.10 | 3.61 | 0.63 | 5.02 | 0.16 | 33.11 | 0.80 | 0.10 | 0.01 | 0.07 | 99.23 | 92.16 |
| | FS17 | 55.12 | 0.11 | 4.37 | 0.42 | 5.71 | 0.14 | 32.67 | 0.62 | 0.08 | 0.00 | 0.05 | 99.28 | 91.07 |
| | FS18 | 53.82 | 0.22 | 6.33 | 0.53 | 6.39 | 0.15 | 31.92 | 1.39 | 0.19 | 0.01 | 0.12 | 101.08 | 89.90 |
| | FS19 | 53.78 | 0.16 | 5.90 | 0.44 | 5.90 | 0.14 | 31.57 | 1.12 | 0.09 | 0.00 | 0.08 | 99.18 | 90.51 |
| | FS21 | 54.72 | 0.13 | 4.86 | 0.37 | 6.09 | 0.15 | 32.24 | 0.78 | 0.13 | 0.01 | 0.06 | 99.52 | 90.42 |
| | FS23 | 53.83 | 0.19 | 6.25 | 0.52 | 6.37 | 0.14 | 32.03 | 1.42 | 0.19 | 0.00 | 0.14 | 101.09 | 89.97 |
| | FS24 | 56.34 | 0.01 | 2.84 | 0.40 | 5.84 | 0.13 | 34.94 | 0.53 | 0.01 | 0.00 | 0.11 | 101.16 | 91.43 |
| | FS26 | 54.93 | 0.13 | 4.61 | 0.30 | 6.06 | 0.15 | 32.45 | 0.62 | 0.10 | 0.00 | 0.07 | 99.43 | 90.53 |

Table 5.4 - Clinopyroxene major element composition in peridotite xenoliths from Subei basin

| Location | Sample | $SiO_2$ | $TiO_2$ | $Al_2O_3$ | $Cr_2O_3$ | FeO | MnO | MgO | CaO | $Na_2O$ | $K_2O$ | NiO | TOTAL | Mg# |
|---|---|---|---|---|---|---|---|---|---|---|---|---|---|---|
| Panshishan | PSS01 | 53.09 | 0.58 | 6.53 | 0.85 | 2.56 | 0.07 | 15.14 | 20.38 | 1.60 | 0.01 | 0.05 | 100.85 | 91.34 |
| | PSS02 | 53.34 | 0.44 | 6.42 | 0.85 | 2.62 | 0.06 | 15.18 | 20.25 | 1.74 | 0.00 | 0.04 | 100.95 | 91.17 |
| | PSS05 | 52.22 | 0.42 | 7.03 | 0.85 | 2.46 | 0.09 | 14.64 | 20.13 | 1.70 | 0.00 | 0.02 | 99.56 | 91.39 |
| | PSS07 | 54.88 | 0.55 | 6.63 | 0.55 | 2.46 | 0.08 | 13.63 | 21.04 | 1.87 | 0.01 | 0.04 | 101.71 | 90.82 |
| | PSS10 | 54.71 | 0.53 | 4.48 | 0.78 | 2.27 | 0.08 | 14.95 | 22.13 | 1.06 | 0.00 | 0.05 | 101.05 | 92.16 |
| | PSS11 | 52.26 | 0.58 | 6.42 | 0.86 | 2.45 | 0.07 | 15.10 | 21.33 | 1.76 | 0.00 | 0.05 | 100.87 | 91.65 |
| | PSS12 | 51.89 | 0.57 | 6.77 | 0.73 | 2.62 | 0.11 | 14.88 | 20.38 | 1.58 | 0.01 | 0.01 | 99.53 | 91.02 |
| | PSS13 | 54.93 | 0.28 | 5.01 | 0.79 | 2.25 | 0.08 | 14.61 | 21.81 | 1.25 | 0.00 | 0.03 | 101.05 | 92.04 |
| | PSS15 | 52.23 | 0.62 | 6.16 | 0.82 | 2.41 | 0.08 | 15.28 | 21.71 | 1.65 | 0.00 | 0.04 | 101.00 | 91.89 |
| | PSS16 | 53.77 | 0.61 | 6.96 | 0.63 | 3.08 | 0.09 | 14.20 | 19.59 | 1.74 | 0.01 | 0.05 | 100.72 | 89.17 |
| | PSS17 | 53.41 | 0.21 | 4.23 | 1.05 | 2.25 | 0.07 | 16.33 | 22.30 | 0.85 | 0.00 | 0.03 | 100.75 | 92.84 |
| | PSS18 | 52.28 | 0.56 | 4.97 | 0.44 | 2.25 | 0.08 | 15.30 | 22.37 | 0.88 | 0.01 | 0.02 | 99.17 | 92.37 |
| | PSS19 | 54.88 | 0.30 | 7.38 | 0.65 | 2.08 | 0.08 | 13.04 | 20.82 | 2.17 | 0.01 | 0.02 | 101.43 | 91.79 |
| | PSS20 | 52.02 | 0.65 | 5.30 | 0.89 | 2.29 | 0.07 | 15.70 | 22.63 | 1.20 | 0.01 | 0.04 | 100.80 | 92.45 |
| Lianshan | LS01 | 51.88 | 0.47 | 5.74 | 0.78 | 2.42 | 0.07 | 14.76 | 21.10 | 1.61 | 0.01 | 0.04 | 98.87 | 91.59 |
| | LS02 | 52.42 | 0.51 | 6.51 | 0.81 | 2.53 | 0.08 | 14.77 | 21.05 | 1.73 | 0.01 | 0.04 | 100.45 | 91.22 |
| | LS03 | 54.29 | 0.11 | 3.87 | 1.11 | 2.24 | 0.09 | 16.22 | 21.82 | 1.14 | 0.00 | 0.06 | 100.96 | 92.82 |
| | LS04 | 51.76 | 0.63 | 7.01 | 0.76 | 2.90 | 0.08 | 14.72 | 20.03 | 1.76 | 0.01 | 0.02 | 99.67 | 90.04 |
| | LS05 | 51.80 | 0.48 | 6.58 | 0.81 | 2.41 | 0.09 | 14.79 | 21.23 | 1.88 | 0.01 | 0.04 | 100.10 | 91.62 |
| | LS06 | 51.79 | 0.52 | 6.40 | 0.92 | 2.52 | 0.08 | 14.84 | 20.29 | 1.69 | 0.00 | 0.05 | 99.10 | 91.31 |
| | LS07 | 51.88 | 0.51 | 6.38 | 0.75 | 2.63 | 0.08 | 14.94 | 20.38 | 1.67 | 0.00 | 0.03 | 99.25 | 91.01 |
| | LS08 | 52.49 | 0.42 | 5.93 | 0.64 | 2.31 | 0.08 | 14.73 | 20.60 | 1.85 | 0.01 | 0.04 | 99.10 | 91.89 |
| | LS09 | 52.65 | 0.19 | 4.99 | 0.79 | 2.19 | 0.08 | 15.41 | 22.32 | 1.16 | 0.00 | 0.03 | 99.81 | 92.62 |
| | LS12 | 53.01 | 0.13 | 4.17 | 0.88 | 2.33 | 0.08 | 16.52 | 22.24 | 0.94 | 0.00 | 0.03 | 100.33 | 92.65 |
| | LS15 | 53.52 | 0.03 | 3.27 | 0.54 | 2.12 | 0.08 | 16.60 | 22.42 | 0.94 | 0.00 | 0.04 | 99.57 | 93.32 |
| | LS16 | 53.99 | 0.25 | 3.65 | 1.48 | 1.86 | 0.06 | 15.84 | 21.08 | 1.93 | 0.01 | 0.03 | 100.18 | 93.81 |

Table 5.4 continued

| Location | Sample | $SiO_2$ | $TiO_2$ | $Al_2O_3$ | $Cr_2O_3$ | FeO | MnO | MgO | CaO | $Na_2O$ | $K_2O$ | NiO | TOTAL | Mg# |
|---|---|---|---|---|---|---|---|---|---|---|---|---|---|---|
| | LS17 | 54.06 | 0.04 | 3.36 | 1.16 | 2.11 | 0.07 | 16.94 | 22.25 | 1.22 | 0.00 | 0.02 | 101.23 | 93.46 |
| | LS19 | 52.79 | 0.22 | 4.36 | 1.29 | 2.18 | 0.07 | 15.56 | 21.52 | 1.43 | 0.01 | 0.04 | 99.46 | 92.72 |
| | LS20 | 53.97 | 0.31 | 5.54 | 1.32 | 2.65 | 0.13 | 15.52 | 20.33 | 1.79 | 0.01 | 0.03 | 101.61 | 91.27 |
| | LS21 | 53.50 | 0.17 | 2.98 | 1.38 | 2.02 | 0.07 | 15.76 | 20.87 | 1.57 | 0.00 | 0.04 | 98.36 | 93.28 |
| | LS22 | 51.17 | 0.72 | 6.15 | 0.61 | 2.62 | 0.09 | 14.90 | 21.09 | 1.39 | 0.00 | 0.04 | 98.80 | 91.01 |
| | LS23 | 53.01 | 0.63 | 7.05 | 0.73 | 2.79 | 0.03 | 14.92 | 20.32 | 1.71 | 0.01 | 0.04 | 101.24 | 90.50 |
| | LS24 | 51.69 | 0.63 | 6.79 | 0.50 | 2.77 | 0.09 | 14.81 | 20.41 | 1.65 | 0.00 | 0.04 | 99.39 | 90.50 |
| | LS26 | 53.31 | 0.01 | 2.11 | 0.63 | 2.10 | 0.09 | 17.61 | 23.85 | 0.16 | 0.00 | 0.04 | 99.90 | 93.72 |
| | LS30 | 51.89 | 0.44 | 6.30 | 0.66 | 2.71 | 0.08 | 14.65 | 20.22 | 1.63 | 0.00 | 0.03 | 98.61 | 90.59 |
| | LS31 | 51.78 | 0.52 | 6.48 | 0.57 | 2.40 | 0.08 | 14.32 | 21.07 | 1.70 | 0.00 | 0.02 | 98.95 | 91.37 |
| Fangshan | FS01 | 52.80 | 0.40 | 6.47 | 0.97 | 2.53 | 0.09 | 14.95 | 19.70 | 1.92 | 0.01 | 0.03 | 99.86 | 91.32 |
| | FS03 | 51.61 | 0.15 | 6.54 | 1.18 | 3.22 | 0.12 | 17.16 | 18.57 | 0.80 | 0.01 | 0.04 | 99.40 | 90.48 |
| | FS06 | 53.36 | 0.03 | 4.28 | 1.38 | 2.47 | 0.07 | 16.24 | 20.44 | 1.06 | 0.00 | 0.04 | 99.36 | 92.15 |
| | FS07 | 52.78 | 0.47 | 6.67 | 0.81 | 2.77 | 0.07 | 14.82 | 19.84 | 1.29 | 0.01 | 0.03 | 99.56 | 90.51 |
| | FS11 | 52.42 | 0.47 | 6.00 | 1.05 | 2.76 | 0.09 | 16.03 | 20.40 | 1.62 | 0.01 | 0.05 | 100.90 | 91.18 |
| | FS12 | 51.86 | 0.34 | 7.19 | 0.93 | 3.15 | 0.09 | 16.37 | 18.34 | 1.12 | 0.03 | 0.04 | 99.46 | 90.26 |
| | FS13 | 52.25 | 0.44 | 7.58 | 0.79 | 3.07 | 0.13 | 15.64 | 18.73 | 1.47 | 0.00 | 0.03 | 100.14 | 90.08 |
| | FS14 | 51.56 | 0.52 | 7.13 | 0.95 | 3.42 | 0.09 | 15.30 | 18.85 | 1.36 | 0.00 | 0.03 | 99.19 | 88.87 |
| | FS16 | 52.92 | 0.27 | 4.87 | 1.28 | 2.59 | 0.09 | 16.27 | 20.10 | 1.26 | 0.01 | 0.04 | 99.71 | 91.81 |
| | FS17 | 52.69 | 0.43 | 6.60 | 1.08 | 2.57 | 0.08 | 14.93 | 20.19 | 1.55 | 0.00 | 0.02 | 100.13 | 91.21 |
| | FS18 | 51.38 | 0.52 | 7.94 | 0.86 | 3.67 | 0.10 | 16.76 | 17.63 | 1.63 | 0.02 | 0.07 | 100.57 | 89.06 |
| | FS19 | 51.17 | 0.52 | 7.43 | 0.77 | 3.56 | 0.11 | 15.80 | 18.83 | 1.15 | 0.02 | 0.02 | 99.38 | 88.80 |
| | FS21 | 51.93 | 0.53 | 6.98 | 0.80 | 2.83 | 0.09 | 15.02 | 19.33 | 1.79 | 0.00 | 0.02 | 99.32 | 90.44 |
| | FS23 | 52.62 | 0.20 | 5.39 | 1.60 | 3.20 | 0.12 | 16.29 | 18.75 | 1.30 | 0.00 | 0.02 | 99.49 | 90.09 |
| | FS24 | 53.68 | 0.03 | 2.50 | 0.60 | 2.11 | 0.07 | 17.75 | 24.12 | 0.26 | 0.01 | 0.05 | 101.17 | 93.76 |
| | FS26 | 51.92 | 0.55 | 6.97 | 0.75 | 2.64 | 0.08 | 14.79 | 20.16 | 1.57 | 0.01 | 0.02 | 99.46 | 90.90 |

Table 5.5 - Spinel major element compositions in peridotite xenoliths from Subei basin

| Location | Sample | $SiO_2$ | $TiO_2$ | $Al_2O_3$ | $Cr_2O_3$ | FeO | MnO | MgO | CaO | $Na_2O$ | $K_2O$ | NiO | TOTAL | Cr# |
|---|---|---|---|---|---|---|---|---|---|---|---|---|---|---|
| Panshishan | PSS01 | 0.29 | 0.16 | 56.44 | 11.48 | 10.14 | 0.08 | 20.10 | 0.01 | 0.01 | 0.00 | 0.36 | 99.09 | 12.01 |
| | PSS02 | 0.28 | 0.11 | 56.05 | 12.07 | 10.79 | 0.15 | 19.78 | 0.02 | 0.00 | 0.01 | 0.28 | 99.53 | 12.62 |
| | PSS05 | 0.06 | 0.08 | 59.27 | 10.50 | 9.80 | 0.12 | 20.57 | 0.00 | 0.02 | 0.01 | 0.22 | 100.63 | 10.62 |
| | PSS07 | 0.04 | 0.06 | 58.63 | 8.94 | 10.66 | 0.09 | 19.67 | 0.00 | 0.02 | 0.00 | 0.33 | 98.44 | 9.27 |
| | PSS10 | 0.06 | 0.21 | 48.18 | 20.79 | 11.15 | 0.11 | 18.41 | 0.00 | 0.01 | 0.01 | 0.23 | 99.15 | 22.44 |
| | PSS11 | 0.02 | 0.09 | 56.52 | 10.57 | 10.61 | 0.06 | 21.85 | 0.01 | 0.00 | 0.00 | 0.38 | 100.11 | 11.15 |
| | PSS12 | 0.03 | 0.14 | 58.59 | 9.90 | 10.77 | 0.12 | 20.34 | 0.00 | 0.00 | 0.01 | 0.25 | 100.15 | 10.18 |
| | PSS13 | 0.05 | 0.07 | 53.37 | 15.16 | 10.46 | 0.11 | 19.18 | 0.00 | 0.00 | 0.00 | 0.28 | 98.69 | 16.00 |
| | PSS15 | 0.00 | 0.08 | 57.08 | 10.72 | 10.64 | 0.07 | 21.52 | 0.01 | 0.00 | 0.00 | 0.40 | 100.51 | 11.18 |
| | PSS16 | 0.07 | 0.17 | 57.44 | 9.11 | 11.09 | 0.11 | 19.61 | 0.00 | 0.01 | 0.00 | 0.31 | 97.93 | 9.62 |
| | PSS17 | 0.25 | 0.10 | 46.96 | 21.85 | 11.60 | 0.12 | 18.83 | 0.02 | 0.02 | 0.01 | 0.26 | 100.00 | 23.78 |
| | PSS18 | 0.01 | 0.08 | 55.17 | 14.30 | 11.33 | 0.16 | 19.28 | 0.00 | 0.00 | 0.01 | 0.17 | 100.51 | 14.81 |
| | PSS19 | 0.02 | 0.03 | 60.36 | 7.77 | 9.71 | 0.10 | 20.10 | 0.01 | 0.01 | 0.00 | 0.36 | 98.47 | 7.95 |
| Lianshan | LS01 | 0.05 | 0.09 | 53.62 | 14.39 | 11.46 | 0.13 | 19.96 | 0.00 | 0.01 | 0.00 | 0.30 | 100.02 | 15.25 |
| | LS02 | 0.07 | 0.05 | 58.37 | 10.12 | 10.14 | 0.12 | 20.95 | 0.00 | 0.02 | 0.01 | 0.31 | 100.17 | 10.42 |
| | LS03 | 0.27 | 0.13 | 39.33 | 28.33 | 13.20 | 0.21 | 17.98 | 0.01 | 0.00 | 0.01 | 0.23 | 99.69 | 32.57 |
| | LS04 | 0.07 | 0.14 | 58.01 | 9.42 | 11.14 | 0.09 | 20.94 | 0.00 | 0.00 | 0.00 | 0.32 | 100.14 | 9.82 |
| | LS05 | 0.05 | 0.07 | 57.67 | 9.57 | 10.72 | 0.06 | 21.11 | 0.01 | 0.00 | 0.00 | 0.37 | 99.61 | 10.01 |
| | LS06 | 0.06 | 0.11 | 55.24 | 12.48 | 10.53 | 0.12 | 20.57 | 0.00 | 0.01 | 0.00 | 0.31 | 99.43 | 13.16 |
| | LS07 | 0.09 | 0.12 | 55.78 | 12.37 | 10.72 | 0.12 | 20.69 | 0.00 | 0.01 | 0.00 | 0.29 | 100.19 | 12.95 |
| | LS08 | 0.04 | 0.07 | 54.28 | 13.83 | 11.18 | 0.11 | 20.35 | 0.00 | 0.01 | 0.01 | 0.29 | 100.16 | 14.59 |
| | LS09 | 0.04 | 0.03 | 55.68 | 12.96 | 11.09 | 0.14 | 20.38 | 0.00 | 0.01 | 0.01 | 0.29 | 100.62 | 13.50 |
| | LS12 | 0.03 | 0.07 | 46.28 | 21.88 | 12.14 | 0.08 | 19.51 | 0.00 | 0.01 | 0.00 | 0.30 | 100.29 | 24.08 |
| | LS15 | 0.08 | 0.02 | 36.94 | 33.18 | 12.87 | 0.20 | 17.50 | 0.00 | 0.01 | 0.00 | 0.14 | 100.93 | 37.60 |
| | LS16 | 0.01 | 0.24 | 29.89 | 39.97 | 14.05 | 0.17 | 15.97 | 0.01 | 0.04 | 0.01 | 0.14 | 100.46 | 47.28 |

Table 5.5 continued

| Location | Sample | $SiO_2$ | $TiO_2$ | $Al_2O_3$ | $Cr_2O_3$ | FeO | MnO | MgO | CaO | $Na_2O$ | $K_2O$ | NiO | TOTAL | Cr# |
|---|---|---|---|---|---|---|---|---|---|---|---|---|---|---|
| | LS17 | 0.01 | 0.03 | 37.07 | 31.91 | 12.19 | 0.00 | 18.44 | 0.01 | 0.00 | 0.00 | 0.22 | 99.89 | 36.60 |
| | LS19 | 0.04 | 0.10 | 44.19 | 25.97 | 12.66 | 0.16 | 18.71 | 0.00 | 0.02 | 0.00 | 0.19 | 102.07 | 28.27 |
| | LS20 | 0.22 | 0.10 | 47.24 | 20.81 | 12.11 | 0.11 | 18.68 | 0.00 | 0.00 | 0.01 | 0.25 | 99.53 | 22.81 |
| | LS21 | 0.04 | 0.14 | 29.62 | 41.27 | 13.98 | 0.23 | 16.04 | 0.00 | 0.01 | 0.00 | 0.09 | 101.41 | 48.31 |
| | LS22 | 0.06 | 0.09 | 57.51 | 9.76 | 10.85 | 0.12 | 20.21 | 0.00 | 0.01 | 0.00 | 0.28 | 98.90 | 10.22 |
| | LS23 | 0.06 | 0.13 | 59.68 | 8.40 | 10.56 | 0.15 | 20.47 | 0.00 | 0.01 | 0.01 | 0.39 | 99.87 | 8.63 |
| | LS24 | 0.05 | 0.11 | 58.78 | 8.76 | 10.35 | 0.12 | 21.15 | 0.00 | 0.01 | 0.01 | 0.31 | 99.65 | 9.09 |
| | LS26 | 0.04 | 0.03 | 34.59 | 35.70 | 14.55 | 0.19 | 16.82 | 0.00 | 0.02 | 0.00 | 0.16 | 102.10 | 40.90 |
| | LS30 | 0.08 | 0.10 | 56.02 | 11.77 | 10.59 | 0.11 | 20.16 | 0.00 | 0.01 | 0.00 | 0.32 | 99.15 | 12.35 |
| | LS31 | 0.03 | 0.06 | 58.10 | 8.94 | 11.24 | 0.12 | 20.35 | 0.00 | 0.00 | 0.00 | 0.33 | 99.19 | 9.35 |
| Fangshan | FS01 | 0.05 | 0.14 | 54.64 | 14.75 | 10.87 | 0.14 | 20.20 | 0.01 | 0.00 | 0.00 | 0.22 | 101.02 | 15.33 |
| | FS03 | 0.16 | 0.13 | 50.42 | 18.30 | 10.86 | 0.13 | 20.47 | 0.00 | 0.01 | 0.00 | 0.24 | 100.72 | 19.58 |
| | FS06 | 0.04 | 0.03 | 36.61 | 32.58 | 13.66 | 0.22 | 17.24 | 0.00 | 0.00 | 0.01 | 0.14 | 100.54 | 37.38 |
| | FS07 | 0.08 | 0.13 | 56.51 | 11.44 | 10.30 | 0.12 | 20.72 | 0.00 | 0.01 | 0.00 | 0.24 | 99.54 | 11.95 |
| | FS11 | 0.04 | 0.20 | 50.70 | 16.69 | 11.39 | 0.05 | 20.70 | 0.01 | 0.00 | 0.00 | 0.36 | 100.15 | 18.09 |
| | FS12 | 0.12 | 0.15 | 56.84 | 12.27 | 10.06 | 0.12 | 20.85 | 0.00 | 0.01 | 0.00 | 0.23 | 100.66 | 12.65 |
| | FS13 | 0.08 | 0.19 | 58.66 | 9.65 | 10.66 | 0.07 | 20.99 | 0.00 | 0.01 | 0.01 | 0.25 | 100.56 | 9.93 |
| | FS14 | 0.08 | 0.25 | 54.25 | 14.04 | 11.37 | 0.15 | 20.13 | 0.00 | 0.02 | 0.01 | 0.22 | 100.53 | 14.79 |
| | FS16 | 0.06 | 0.17 | 43.12 | 26.20 | 11.64 | 0.14 | 18.84 | 0.00 | 0.00 | 0.01 | 0.17 | 100.35 | 28.95 |
| | FS17 | 0.05 | 0.12 | 54.63 | 14.34 | 10.53 | 0.13 | 19.99 | 0.01 | 0.00 | 0.01 | 0.22 | 100.03 | 14.97 |
| | FS18 | 0.12 | 0.26 | 56.99 | 9.89 | 10.87 | 0.06 | 21.74 | 0.00 | 0.00 | 0.00 | 0.36 | 100.27 | 10.42 |
| | FS19 | 0.11 | 0.18 | 57.23 | 10.01 | 10.75 | 0.12 | 20.85 | 0.02 | 0.00 | 0.00 | 0.24 | 99.51 | 10.50 |
| | FS21 | 0.05 | 0.15 | 57.30 | 10.42 | 10.96 | 0.13 | 20.50 | 0.00 | 0.01 | 0.00 | 0.25 | 99.78 | 10.87 |
| | FS23 | 0.09 | 0.24 | 38.47 | 29.64 | 14.23 | 0.17 | 17.90 | 0.00 | 0.01 | 0.00 | 0.17 | 100.90 | 34.07 |
| | FS24 | 0.01 | 0.01 | 44.06 | 24.15 | 12.16 | 0.03 | 19.06 | 0.00 | 0.00 | 0.00 | 0.25 | 99.75 | 26.88 |
| | FS26 | 0.04 | 0.14 | 59.40 | 9.41 | 10.21 | 0.10 | 20.68 | 0.00 | 0.00 | 0.00 | 0.24 | 100.22 | 9.60 |

Table 5.6 - Clinopyroxene trace element analyses in peridotite xenoliths from Subei basin

| Location | Sample | n. | Sc | Ti | V | Co | Ni | Ga | Rb | Sr | Y | Zr | Nb | Ba |
|---|---|---|---|---|---|---|---|---|---|---|---|---|---|---|
| Panshishan | PSS01 | 6 | 64.6 | 2051 | 3021 | 20.9 | 363 | 4.17 | 0.01 | 59.1 | 19.3 | 27.6 | 0.12 | 0.01 |
| | PSS02 | 4 | 66.0 | 1646 | 2330 | 20.6 | 349 | 4.35 | 0.01 | 187 | 15.4 | 29.2 | 0.82 | 0.07 |
| | PSS05 | 5 | 62.0 | 1875 | 2780 | 21.0 | 360 | 4.35 | 0.03 | 81.5 | 18.2 | 37.0 | 0.29 | 0.00 |
| | PSS07 | 10 | 73.4 | 3101 | 286 | 19.1 | 323 | 4.20 | 0.21 | 45.3 | 19.0 | 23.9 | 0.05 | 0.82 |
| | PSS10 | 8 | 65.4 | 2370 | 1962 | 20.8 | 371 | 3.38 | 0.23 | 144 | 8.9 | 27.0 | 0.22 | 1.45 |
| | PSS11 | 5 | 61.8 | 2836 | 4315 | 19.3 | 325 | 4.64 | 0.01 | 95.6 | 19.5 | 36.2 | 0.28 | 0.07 |
| | PSS12 | 5 | 64.7 | 2086 | 3112 | 20.5 | 344 | 4.44 | 0.04 | 67.0 | 18.6 | 29.9 | 0.13 | 0.00 |
| | PSS13 | 12 | 73.3 | 1452 | 948 | 19.8 | 350 | 3.41 | 0.08 | 33.5 | 13.2 | 11.5 | 0.18 | 0.58 |
| | PSS15 | 9 | 67.8 | 3275 | 2627 | 20.4 | 470 | 4.21 | 0.14 | 89.1 | 19.5 | 36.9 | 0.26 | 0.14 |
| | PSS16 | 13 | 56.6 | 2977 | 1481 | 23.6 | 398 | 4.91 | 0.02 | 79.2 | 19.3 | 35.3 | 0.14 | 0.15 |
| | PSS17 | 8 | 63.0 | 1069 | 693 | 20.7 | 351 | 2.76 | 0.02 | 53.2 | 8.1 | 9.3 | 0.28 | 0.01 |
| | PSS19 | 9 | 54.0 | 1836 | 212 | 16.6 | 304 | 4.58 | 0.08 | 95.5 | 10.9 | 5.2 | 0.04 | 6.68 |
| Lianshan | LS01 | 5 | 65.6 | 2465 | 267 | 19.0 | 323 | 3.99 | 0.02 | 60.3 | 16.2 | 23.7 | 0.32 | 0.04 |
| | LS02 | 6 | 74.5 | 472 | 231 | 18.7 | 344 | 1.87 | 0.03 | 109 | 3.3 | 40.4 | 0.28 | 0.31 |
| | LS03 | 6 | 64.6 | 670 | 208 | 20.4 | 396 | 2.41 | 0.01 | 110 | 8.0 | 4.2 | 0.79 | 0.05 |
| | LS04 | 7 | 62.0 | 3498 | 270 | 21.3 | 357 | 4.70 | 0.02 | 81.9 | 19.5 | 35.0 | 0.12 | 0.03 |
| | LS05 | 9 | 66.4 | 2590 | 271 | 18.2 | 296 | 3.91 | 0.03 | 27.0 | 18.3 | 14.6 | 0.02 | 0.10 |
| | LS06 | 4 | 63.4 | 2853 | 253 | 21.0 | 352 | 4.09 | 0.02 | 77.0 | 17.2 | 32.4 | 0.11 | 0.06 |
| | LS07 | 6 | 62.2 | 2882 | 258 | 21.1 | 358 | 4.06 | 0.01 | 79.0 | 17.6 | 33.8 | 0.12 | 0.02 |
| | LS08 | 9 | 65.3 | 2412 | 265 | 18.5 | 312 | 4.01 | 0.20 | 104 | 15.6 | 26.0 | 0.18 | 0.18 |
| | LS09 | 16 | 64.9 | 993 | 938 | 18.9 | 308 | 3.05 | 0.02 | 3.1 | 11.4 | 1.4 | 0.01 | 0.23 |
| | LS12 | 5 | 63.0 | 750 | 217 | 21.0 | 397 | 2.72 | 0.01 | 63.1 | 8.8 | 2.5 | 0.14 | 0.01 |
| | LS15 | 5 | 85.8 | 503 | 256 | 20.2 | 372 | 2.11 | 0.02 | 224 | 3.4 | 45.5 | 0.25 | 1.88 |
| | LS16 | 5 | 119 | 1510 | 239 | 17.1 | 310 | 2.50 | 0.01 | 319 | 7.0 | 41.6 | 0.12 | 0.07 |

Table 5.6 continued

| Location | Sample | n. | Sc | Ti | V | Co | Ni | Ga | Rb | Sr | Y | Zr | Nb | Ba |
|---|---|---|---|---|---|---|---|---|---|---|---|---|---|---|
| Lianshan | LS17 | 4 | 84.5 | 247 | 221 | 18.7 | 346 | 1.94 | 0.02 | 172 | 3.4 | 41.6 | 0.24 | 8.60 |
| | LS19 | 8 | 87.0 | 1221 | 241 | 18.6 | 314 | 2.89 | 0.03 | 47.7 | 10.1 | 23.1 | 0.22 | 0.15 |
| | LS20 | 4 | 70.8 | 1474 | 250 | 20.0 | 351 | 4.54 | 0.02 | 210 | 14.6 | 45.8 | 0.76 | 0.01 |
| | LS21 | 6 | 107 | 1033 | 228 | 17.5 | 321 | 3.18 | 0.19 | 339 | 8.1 | 38.7 | 0.18 | 0.52 |
| | LS22 | 9 | 66.3 | 4325 | 294 | 19.4 | 308 | 5.02 | 0.03 | 91.3 | 20.5 | 38.2 | 0.15 | 0.22 |
| | LS23 | 4 | 62.4 | 3554 | 272 | 20.9 | 339 | 4.57 | 0.01 | 84.5 | 19.1 | 34.1 | 0.11 | 0.05 |
| | LS24 | 12 | 65.5 | 3554 | 281 | 21.0 | 343 | 5.28 | 0.14 | 85.2 | 19.5 | 35.2 | 0.08 | 0.67 |
| | LS26 | 16 | 58.5 | 166 | 160 | 20.3 | 350 | 1.14 | 0.05 | 14.9 | 1.5 | 2.0 | 0.06 | 0.15 |
| | LS30 | 11 | 63.6 | 2460 | 258 | 22.0 | 375 | 3.98 | 0.20 | 68.9 | 16.7 | 24.3 | 0.18 | 0.47 |
| | LS31 | 11 | 62.9 | 3110 | 272 | 18.5 | 306 | 4.52 | 0.16 | 55.4 | 20.3 | 27.6 | 0.07 | 1.94 |
| Fangshan | FS01 | 5 | 61.8 | 1636 | 2254 | 20.4 | 363 | 4.06 | 0.02 | 160 | 14.3 | 22.4 | 0.52 | 0.04 |
| | FS03 | 4 | 42.4 | 869 | 991 | 30.1 | 511 | 4.08 | 0.01 | 24.1 | 11.2 | 6.6 | 0.22 | 1.06 |
| | FS06 | 4 | 68.3 | 401 | 142 | 22.5 | 407 | 2.55 | 0.05 | 256 | 4.8 | 12.5 | 3.63 | 0.12 |
| | FS07 | 5 | 59.0 | 1792 | 2536 | 22.3 | 379 | 4.28 | 0.02 | 50.4 | 17.3 | 23.7 | 0.13 | 0.05 |
| | FS11 | 5 | 63.2 | 1758 | 2529 | 22.6 | 389 | 3.96 | 0.02 | 95.7 | 15.3 | 25.0 | 0.39 | 0.07 |
| | FS12 | 4 | 46.6 | 1306 | 1728 | 27.6 | 449 | 4.88 | 0.00 | 35.2 | 14.3 | 13.1 | 0.17 | 0.14 |
| | FS14 | 4 | 58.3 | 1870 | 2672 | 24.6 | 406 | 4.73 | 0.02 | 117 | 16.0 | 37.0 | 2.45 | 0.02 |
| | FS16 | 24 | 57.1 | 1244 | 403 | 21.3 | 368 | 2.93 | 0.03 | 239 | 8.7 | 18.6 | 2.34 | 0.15 |
| | FS17 | 4 | 62.3 | 1755 | 2354 | 20.9 | 368 | 4.02 | 0.01 | 73.1 | 15.0 | 24.2 | 0.75 | 0.00 |
| | FS19 | 5 | 51.9 | 1867 | 2689 | 26.0 | 411 | 5.13 | 0.01 | 84.1 | 16.7 | 28.3 | 0.88 | 0.08 |
| | FS21 | 5 | 60.9 | 1941 | 2843 | 22.3 | 366 | 4.18 | 0.01 | 118 | 17.9 | 29.2 | 3.79 | 0.07 |
| | FS23 | 5 | 52.0 | 919 | 1062 | 26.1 | 431 | 4.10 | 0.01 | 114 | 10.6 | 19.0 | 0.93 | 0.02 |
| | FS26 | 5 | 62.3 | 2198 | 3189 | 21.0 | 355 | 4.37 | 0.02 | 71.8 | 19.1 | 33.2 | 0.08 | 0.01 |
| | FS16 opx | 3 | 12.7 | 303 | 53 | 98.9 | 1799 | | 0.09 | 1.05 | 0.5 | 1.6 | 0.11 | 0.40 |

Table 5.6 continued

| Location | Sample | La | Ce | Pr | Nd | Sm | Eu | Gd | Tb | Dy | Ho | Er | Tm | Yb |
|---|---|---|---|---|---|---|---|---|---|---|---|---|---|---|
| Panshishan | PSS01 | 0.78 | 2.53 | 0.50 | 3.07 | 1.36 | 0.63 | 2.36 | 0.48 | 3.29 | 0.72 | 2.04 | 0.30 | 2.06 |
| | PSS02 | 9.66 | 19.9 | 2.27 | 9.16 | 1.88 | 0.76 | 2.40 | 0.43 | 2.63 | 0.59 | 1.58 | 0.22 | 1.56 |
| | PSS05 | 2.06 | 5.01 | 0.76 | 4.11 | 1.51 | 0.66 | 2.37 | 0.44 | 3.10 | 0.70 | 1.86 | 0.28 | 1.86 |
| | PSS07 | 0.30 | 1.66 | 0.39 | 2.89 | 1.44 | 0.64 | 2.47 | 0.47 | 3.22 | 0.73 | 2.04 | 0.29 | 1.94 |
| | PSS10 | 4.65 | 6.93 | 1.20 | 7.24 | 2.36 | 0.85 | 2.55 | 0.36 | 1.85 | 0.34 | 0.83 | 0.12 | 0.78 |
| | PSS11 | 2.06 | 6.15 | 1.05 | 6.22 | 2.25 | 0.95 | 3.21 | 0.54 | 3.61 | 0.75 | 1.98 | 0.27 | 1.85 |
| | PSS12 | 0.91 | 3.27 | 0.63 | 4.10 | 1.75 | 0.73 | 2.47 | 0.46 | 3.16 | 0.72 | 2.06 | 0.30 | 1.88 |
| | PSS13 | 0.87 | 2.25 | 0.35 | 1.97 | 0.84 | 0.36 | 1.52 | 0.31 | 2.16 | 0.52 | 1.54 | 0.21 | 1.47 |
| | PSS15 | 1.76 | 5.48 | 0.97 | 5.83 | 2.20 | 0.88 | 3.04 | 0.52 | 3.45 | 0.80 | 2.17 | 0.30 | 2.00 |
| | PSS16 | 1.08 | 3.86 | 0.72 | 4.55 | 1.83 | 0.76 | 2.73 | 0.52 | 3.49 | 0.75 | 2.03 | 0.30 | 1.93 |
| | PSS17 | 1.33 | 3.97 | 0.60 | 3.04 | 0.83 | 0.30 | 0.94 | 0.18 | 1.31 | 0.30 | 0.94 | 0.14 | 0.96 |
| | PSS19 | 0.80 | 2.62 | 0.38 | 1.92 | 0.77 | 0.56 | 1.42 | 0.29 | 2.00 | 0.44 | 1.22 | 0.17 | 1.13 |
| Lianshan | LS01 | 0.97 | 3.03 | 0.53 | 3.37 | 1.50 | 0.58 | 2.27 | 0.42 | 2.91 | 0.66 | 1.81 | 0.26 | 1.67 |
| | LS02 | 7.28 | 11.1 | 1.24 | 4.80 | 0.74 | 0.19 | 0.59 | 0.08 | 0.53 | 0.13 | 0.38 | 0.06 | 0.45 |
| | LS03 | 3.92 | 4.64 | 0.39 | 1.60 | 0.54 | 0.24 | 0.96 | 0.18 | 1.34 | 0.31 | 0.84 | 0.13 | 0.86 |
| | LS04 | 1.08 | 4.01 | 0.71 | 4.48 | 1.86 | 0.76 | 2.70 | 0.50 | 3.44 | 0.75 | 2.10 | 0.31 | 2.03 |
| | LS05 | 0.12 | 0.88 | 0.27 | 2.19 | 1.25 | 0.57 | 2.27 | 0.45 | 3.18 | 0.73 | 2.06 | 0.30 | 2.04 |
| | LS06 | 1.13 | 4.08 | 0.71 | 4.26 | 1.77 | 0.67 | 2.39 | 0.44 | 3.09 | 0.68 | 1.81 | 0.27 | 1.74 |
| | LS07 | 1.11 | 4.13 | 0.74 | 4.42 | 1.78 | 0.73 | 2.47 | 0.45 | 3.10 | 0.66 | 1.92 | 0.27 | 1.79 |
| | LS08 | 2.35 | 3.91 | 0.60 | 3.34 | 1.38 | 0.58 | 2.10 | 0.40 | 2.76 | 0.64 | 1.67 | 0.25 | 1.62 |
| | LS09 | 0.04 | 0.13 | 0.03 | 0.30 | 0.36 | 0.20 | 0.95 | 0.22 | 1.77 | 0.43 | 1.31 | 0.19 | 1.35 |
| | LS12 | 0.27 | 0.97 | 0.19 | 1.16 | 0.49 | 0.21 | 0.93 | 0.19 | 1.43 | 0.33 | 1.00 | 0.15 | 0.96 |
| | LS15 | 13.0 | 16.0 | 1.48 | 5.03 | 0.84 | 0.20 | 0.58 | 0.09 | 0.62 | 0.14 | 0.38 | 0.07 | 0.49 |
| | LS16 | 10.4 | 22.7 | 2.49 | 9.91 | 1.89 | 0.69 | 1.69 | 0.24 | 1.38 | 0.27 | 0.69 | 0.09 | 0.69 |

Table 5.6 continued

| Location | Sample | La | Ce | Pr | Nd | Sm | Eu | Gd | Tb | Dy | Ho | Er | Tm | Yb |
|---|---|---|---|---|---|---|---|---|---|---|---|---|---|---|
| Lianshan | LS17 | 10.8 | 13.2 | 1.37 | 5.20 | 0.72 | 0.18 | 0.60 | 0.09 | 0.60 | 0.13 | 0.37 | 0.06 | 0.51 |
| | LS19 | 0.95 | 2.21 | 0.35 | 2.03 | 0.79 | 0.39 | 1.26 | 0.24 | 1.68 | 0.39 | 1.13 | 0.16 | 1.05 |
| | LS20 | 8.98 | 20.8 | 2.70 | 12.28 | 2.94 | 1.05 | 2.92 | 0.49 | 2.85 | 0.58 | 1.45 | 0.21 | 1.46 |
| | LS21 | 11.6 | 28.2 | 3.41 | 13.90 | 2.75 | 0.94 | 2.27 | 0.32 | 1.61 | 0.31 | 0.77 | 0.10 | 0.72 |
| | LS22 | 3.24 | 10.4 | 1.76 | 9.55 | 2.92 | 1.10 | 3.53 | 0.58 | 3.72 | 0.79 | 2.14 | 0.30 | 1.98 |
| | LS23 | 1.18 | 4.27 | 0.77 | 4.65 | 1.82 | 0.77 | 2.73 | 0.50 | 3.38 | 0.73 | 2.08 | 0.30 | 1.99 |
| | LS24 | 1.23 | 4.46 | 0.80 | 4.96 | 1.90 | 0.79 | 2.68 | 0.50 | 3.39 | 0.76 | 2.14 | 0.31 | 2.07 |
| | LS26 | 0.36 | 0.86 | 0.12 | 0.65 | 0.17 | 0.07 | 0.22 | 0.04 | 0.24 | 0.06 | 0.19 | 0.04 | 0.27 |
| | LS30 | 1.37 | 2.85 | 0.49 | 3.26 | 1.29 | 0.58 | 2.09 | 0.40 | 2.93 | 0.65 | 1.84 | 0.26 | 1.72 |
| | LS31 | 0.33 | 1.77 | 0.43 | 3.30 | 1.58 | 0.73 | 2.76 | 0.50 | 3.61 | 0.81 | 2.21 | 0.33 | 2.22 |
| Fangshan | FS01 | 7.32 | 13.28 | 1.40 | 5.84 | 1.58 | 0.60 | 2.18 | 0.38 | 2.58 | 0.54 | 1.47 | 0.21 | 1.37 |
| | FS03 | 0.24 | 0.99 | 0.21 | 1.43 | 0.75 | 0.35 | 1.36 | 0.29 | 1.92 | 0.45 | 1.18 | 0.17 | 1.11 |
| | FS06 | 18.6 | 33.9 | 3.30 | 11.92 | 1.87 | 0.55 | 1.34 | 0.17 | 0.93 | 0.17 | 0.46 | 0.07 | 0.47 |
| | FS07 | 0.50 | 2.12 | 0.45 | 2.99 | 1.44 | 0.59 | 2.29 | 0.46 | 3.08 | 0.67 | 1.89 | 0.27 | 1.82 |
| | FS11 | 3.99 | 7.14 | 0.91 | 4.26 | 1.67 | 0.67 | 2.34 | 0.39 | 2.57 | 0.58 | 1.66 | 0.23 | 1.51 |
| | FS12 | 0.45 | 1.43 | 0.29 | 1.97 | 1.04 | 0.44 | 1.80 | 0.35 | 2.40 | 0.54 | 1.61 | 0.22 | 1.52 |
| | FS14 | 7.13 | 8.18 | 1.06 | 5.50 | 1.73 | 0.75 | 2.49 | 0.43 | 2.88 | 0.64 | 1.74 | 0.25 | 1.55 |
| | FS16 | 16.1 | 25.7 | 2.15 | 7.59 | 1.71 | 0.64 | 1.63 | 0.27 | 1.71 | 0.35 | 0.95 | 0.13 | 0.84 |
| | FS17 | 2.90 | 4.87 | 0.66 | 3.51 | 1.34 | 0.59 | 2.16 | 0.39 | 2.75 | 0.59 | 1.66 | 0.23 | 1.55 |
| | FS19 | 2.94 | 4.94 | 0.68 | 4.16 | 1.54 | 0.63 | 2.34 | 0.43 | 2.91 | 0.66 | 1.77 | 0.24 | 1.62 |
| | FS21 | 11.7 | 7.50 | 0.65 | 3.85 | 1.59 | 0.66 | 2.42 | 0.46 | 3.07 | 0.71 | 1.92 | 0.28 | 1.78 |
| | FS23 | 3.23 | 4.92 | 0.71 | 4.13 | 1.42 | 0.56 | 1.81 | 0.31 | 1.95 | 0.42 | 1.10 | 0.14 | 0.92 |
| | FS26 | 0.96 | 3.52 | 0.69 | 4.28 | 1.78 | 0.72 | 2.62 | 0.49 | 3.43 | 0.75 | 2.09 | 0.29 | 1.92 |
| | FS16 opx | 0.07 | 0.13 | 0.03 | 0.11 | 0.07 | 0.03 | | 0.02 | 0.16 | 0.03 | 0.07 | 0.01 | 0.15 |

Table 5.6 continued

| Location | Sample | Lu | Hf | Ta | Pb | Th | U | ∑REE | (La/Sm)N | (La/Yb)N | (Sm/Yb)N | Ti* | Zr* | Eu* |
|---|---|---|---|---|---|---|---|---|---|---|---|---|---|---|
| Panshishan | PSS01 | 0.30 | 0.87 | 0.00 | 0.03 | 0.03 | 0.01 | 20.41 | 0.37 | 0.27 | 0.73 | 0.41 | 0.93 | 1.06 |
| | PSS02 | 0.22 | 0.91 | 0.09 | 0.21 | 0.68 | 0.20 | 53.30 | 3.31 | 4.44 | 1.34 | 0.30 | 0.47 | 1.10 |
| | PSS05 | 0.27 | 0.97 | 0.04 | 0.12 | 0.90 | 0.21 | 25.00 | 0.88 | 0.79 | 0.90 | 0.37 | 1.02 | 1.07 |
| | PSS07 | 0.31 | 0.87 | 0.01 | 0.70 | 0.01 | 0.29 | 18.80 | 0.13 | 0.11 | 0.82 | 0.61 | 0.79 | 1.02 |
| | PSS10 | 0.11 | 1.03 | 0.02 | 0.22 | 1.95 | 0.22 | 30.17 | 1.27 | 4.26 | 3.35 | 0.39 | 0.45 | 1.06 |
| | PSS11 | 0.25 | 1.03 | 0.11 | 0.12 | 0.10 | 0.03 | 31.14 | 0.59 | 0.80 | 1.35 | 0.40 | 0.67 | 1.08 |
| | PSS12 | 0.29 | 0.96 | 0.01 | 0.24 | 0.02 | 0.01 | 22.73 | 0.34 | 0.35 | 1.03 | 0.38 | 0.76 | 1.08 |
| | PSS13 | 0.22 | 0.46 | 0.02 | 0.41 | 0.03 | 0.01 | 14.60 | 0.67 | 0.43 | 0.63 | 0.48 | 0.61 | 0.97 |
| | PSS15 | 0.29 | 1.13 | 0.09 | 3.80 | 0.08 | 0.06 | 29.68 | 0.51 | 0.63 | 1.23 | 0.49 | 0.71 | 1.04 |
| | PSS16 | 0.28 | 1.16 | 0.02 | 0.19 | 0.01 | 0.01 | 24.82 | 0.38 | 0.40 | 1.05 | 0.51 | 0.84 | 1.04 |
| | PSS17 | 0.13 | 0.27 | 0.02 | 0.06 | 0.03 | 0.01 | 14.94 | 1.03 | 1.00 | 0.97 | 0.50 | 0.40 | 1.03 |
| | PSS19 | 0.16 | 0.24 | 0.01 | 0.42 | 0.01 | 0.01 | 13.87 | 0.67 | 0.51 | 0.75 | 0.50 | 0.29 | 1.61 |
| Lianshan | LS01 | 0.24 | 0.71 | 0.03 | 0.06 | 0.05 | 0.02 | 20.24 | 0.42 | 0.42 | 1.00 | 0.52 | 0.72 | 0.97 |
| | LS02 | 0.08 | 1.00 | 0.03 | 0.23 | 2.63 | 0.37 | 27.62 | 6.37 | 11.62 | 1.82 | 0.35 | 1.38 | 0.84 |
| | LS03 | 0.11 | 0.19 | 0.00 | 0.30 | 0.58 | 0.18 | 16.05 | 4.69 | 3.25 | 0.69 | 0.34 | 0.32 | 1.03 |
| | LS04 | 0.29 | 1.11 | 0.02 | 0.11 | 0.02 | 0.01 | 25.02 | 0.37 | 0.38 | 1.02 | 0.60 | 0.83 | 1.04 |
| | LS05 | 0.28 | 0.65 | 0.00 | 0.13 | 0.00 | 0.01 | 16.58 | 0.06 | 0.04 | 0.68 | 0.56 | 0.59 | 1.03 |
| | LS06 | 0.25 | 0.98 | 0.02 | 0.03 | 0.01 | 0.00 | 23.28 | 0.41 | 0.47 | 1.13 | 0.56 | 0.81 | 0.99 |
| | LS07 | 0.25 | 1.03 | 0.01 | 0.04 | 0.01 | 0.00 | 23.83 | 0.40 | 0.45 | 1.11 | 0.53 | 0.83 | 1.06 |
| | LS08 | 0.24 | 0.80 | 0.03 | 0.89 | 0.48 | 0.28 | 21.84 | 1.10 | 1.04 | 0.95 | 0.54 | 0.83 | 1.04 |
| | LS09 | 0.20 | 0.10 | 0.00 | 0.02 | 0.00 | 0.00 | 7.48 | 0.06 | 0.02 | 0.30 | 0.55 | 0.25 | 0.99 |
| | LS12 | 0.13 | 0.13 | 0.01 | 0.04 | 0.01 | 0.00 | 8.42 | 0.36 | 0.20 | 0.56 | 0.41 | 0.22 | 0.95 |
| | LS15 | 0.09 | 1.15 | 0.02 | 0.40 | 4.69 | 0.57 | 38.95 | 10.00 | 18.82 | 1.88 | 0.36 | 1.45 | 0.82 |
| | LS16 | 0.10 | 1.09 | 0.07 | 1.50 | 1.21 | 0.40 | 53.22 | 3.55 | 10.83 | 3.05 | 0.34 | 0.64 | 1.16 |

Table 5.6 continued

| Location | Sample | Lu | Hf | Ta | Pb | Th | U | ∑REE | (La/Sm)N | (La/Yb)N | (Sm/Yb)N | Ti* | Zr* | Eu* |
|---|---|---|---|---|---|---|---|---|---|---|---|---|---|---|
| Lianshan | LS17 | 0.08 | 1.02 | 0.01 | 0.59 | 4.26 | 0.51 | 33.90 | 9.65 | 15.19 | 1.57 | 0.18 | 1.36 | 0.83 |
| | LS19 | 0.16 | 0.62 | 0.02 | 0.21 | 0.10 | 0.04 | 12.77 | 0.78 | 0.65 | 0.83 | 0.43 | 1.26 | 1.19 |
| | LS20 | 0.21 | 0.64 | 0.09 | 0.35 | 0.74 | 0.18 | 58.91 | 1.97 | 4.42 | 2.24 | 0.20 | 0.52 | 1.09 |
| | LS21 | 0.12 | 0.87 | 0.08 | 2.00 | 1.20 | 0.40 | 66.97 | 2.73 | 11.56 | 4.24 | 0.17 | 0.42 | 1.12 |
| | LS22 | 0.29 | 1.28 | 0.06 | 0.44 | 0.06 | 0.01 | 42.26 | 0.72 | 1.17 | 1.64 | 0.54 | 0.50 | 1.05 |
| | LS23 | 0.29 | 0.96 | 0.01 | 0.07 | 0.01 | 0.00 | 25.46 | 0.42 | 0.43 | 1.01 | 0.60 | 0.81 | 1.05 |
| | LS24 | 0.30 | 1.09 | 0.01 | 0.60 | 0.02 | 0.02 | 26.30 | 0.42 | 0.43 | 1.02 | 0.60 | 0.79 | 1.07 |
| | LS26 | 0.05 | 0.07 | 0.01 | 0.02 | 0.01 | 0.01 | 3.33 | 1.34 | 0.96 | 0.72 | 0.34 | 0.42 | 1.04 |
| | LS30 | 0.25 | 0.79 | 0.01 | 0.78 | 0.20 | 0.07 | 19.99 | 0.68 | 0.57 | 0.83 | 0.55 | 0.82 | 1.08 |
| | LS31 | 0.32 | 0.99 | 0.00 | 1.46 | 0.02 | 0.05 | 20.88 | 0.13 | 0.11 | 0.79 | 0.54 | 0.82 | 1.06 |
| Fangshan | FS01 | 0.20 | 0.69 | 0.02 | 0.17 | 0.62 | 0.16 | 38.95 | 2.98 | 3.82 | 1.28 | 0.35 | 0.51 | 0.98 |
| | FS03 | 0.16 | 0.29 | 0.00 | 0.03 | 0.01 | 0.00 | 10.61 | 0.21 | 0.16 | 0.75 | 0.31 | 0.43 | 1.04 |
| | FS06 | 0.08 | 0.04 | 0.54 | 0.54 | 1.93 | 0.43 | 73.83 | 6.44 | 28.20 | 4.38 | 0.11 | 0.17 | 1.02 |
| | FS07 | 0.26 | 0.79 | 0.01 | 0.13 | 0.02 | 0.02 | 18.82 | 0.23 | 0.20 | 0.88 | 0.38 | 0.77 | 0.99 |
| | FS11 | 0.22 | 0.77 | 0.02 | 0.15 | 0.32 | 0.08 | 28.14 | 1.54 | 1.90 | 1.23 | 0.34 | 0.65 | 1.04 |
| | FS12 | 0.23 | 0.46 | 0.01 | 0.02 | 0.01 | 0.00 | 14.31 | 0.28 | 0.21 | 0.76 | 0.36 | 0.61 | 0.97 |
| | FS14 | 0.22 | 1.04 | 0.14 | 0.11 | 2.64 | 0.55 | 34.54 | 2.66 | 3.31 | 1.24 | 0.34 | 0.83 | 1.10 |
| | FS16 | 0.11 | 0.47 | 0.18 | 0.20 | 2.03 | 0.51 | 59.83 | 6.05 | 13.68 | 2.26 | 0.30 | 0.35 | 1.15 |
| | FS17 | 0.22 | 0.80 | 0.03 | 0.08 | 0.42 | 0.13 | 23.43 | 1.40 | 1.34 | 0.96 | 0.38 | 0.77 | 1.06 |
| | FS19 | 0.23 | 0.96 | 0.04 | 0.02 | 0.36 | 0.10 | 25.09 | 1.23 | 1.30 | 1.06 | 0.38 | 0.77 | 1.01 |
| | FS21 | 0.26 | 0.99 | 0.01 | 0.57 | 1.72 | 0.47 | 36.91 | 4.77 | 4.73 | 0.99 | 0.38 | 0.81 | 1.03 |
| | FS23 | 0.14 | 0.38 | 0.02 | 0.03 | 0.50 | 0.10 | 21.76 | 1.47 | 2.50 | 1.71 | 0.22 | 0.54 | 1.06 |
| | FS26 | 0.28 | 1.04 | 0.01 | 0.02 | 0.01 | 0.00 | 23.82 | 0.35 | 0.36 | 1.03 | 0.39 | 0.83 | 1.02 |
| | FS16 opx | 0.02 | 0.06 | | 0.05 | 0.06 | 0.02 | 0.91 | 0.58 | 0.33 | 0.57 | 2.98 | 1.15 | 1.88 |

n. numbers of analysis  N indicate C1 chondrite normalization

$Ti^*=Ti_N/((Eu+Gd)_N/2)$  $Zr^*=Zr_N/((Nd+Sm)_N/2)$  $Eu^*=Eu_N/((Sm+Gd)_N/2)$

Table 5.7 - Oxygen isotopic analyses of xenoliths form Subei basin

| Location | Sample | OL | | OPX | | CPX | | SP | | Δopx-ol | Δcpx-ol | Δopx-cpx |
|---|---|---|---|---|---|---|---|---|---|---|---|---|
| | | $\delta^{18}O$ | 2δ | $\delta^{18}O$ | 2δ | $\delta^{18}O$ | 2δ | $\delta^{18}O$ | 2δ | | | |
| Panshishan | PSS01 | 5.71 | 0.18 | 6.36 | 0.27 | 5.69 | 0.20 | 4.84 | 0.26 | 0.65 | -0.02 | 0.67 |
| | PSS02 | 5.28 | 0.19 | 6.03 | 0.19 | 5.58 | 0.00 | 4.73 | 0.20 | 0.75 | 0.30 | 0.45 |
| | PSS05 | 5.36 | 0.44 | 6.29 | 0.23 | 5.70 | 0.41 | 5.10 | 0.24 | 0.93 | 0.33 | 0.60 |
| | PSS11 | 5.49 | 0.17 | 6.27 | 0.30 | 5.57 | 0.30 | 5.15 | 0.22 | 0.78 | 0.08 | 0.71 |
| | PSS12 | 5.30 | 0.04 | 5.87 | 0.21 | 5.38 | 0.11 | 4.36 | 0.04 | 0.57 | 0.09 | 0.49 |
| | PSS13 | 5.40 | 0.13 | 6.04 | 0.13 | 5.44 | 0.01 | 4.57 | 0.30 | 0.64 | 0.04 | 0.60 |
| | PSS15 | 5.37 | 0.17 | 5.94 | 0.38 | 5.47 | 0.44 | 5.37 | 0.11 | 0.57 | 0.10 | 0.46 |
| | PSS16 | 5.49 | 0.46 | 6.03 | 0.16 | 5.18 | 0.06 | 4.92 | 0.20 | 0.53 | -0.31 | 0.85 |
| | PSS17 | 5.78 | 0.25 | 6.53 | 0.32 | 6.15 | 0.29 | 4.11 | 0.47 | 0.75 | 0.37 | 0.38 |
| | PSS19 | 5.58 | 0.14 | 6.11 | 0.01 | 5.43 | 0.38 | 5.23 | | 0.53 | -0.15 | 0.67 |
| | Average | 5.48 | | 6.15 | | 5.56 | | 4.84 | | 0.67 | 0.08 | 0.59 |
| Lianshan | LS03 | 5.96 | 0.39 | 6.55 | 0.33 | 5.82 | 0.28 | 4.52 | 0.21 | 0.59 | -0.14 | 0.73 |
| | LS05 | 5.53 | 0.20 | | | 6.34 | 0.18 | 5.37 | 0.08 | | 0.81 | |
| | LS06 | 5.94 | 0.07 | 6.33 | 0.15 | 6.11 | 0.11 | 5.05 | 0.23 | 0.39 | 0.17 | 0.23 |
| | LS07 | 5.45 | 0.16 | 6.06 | 0.13 | 5.77 | 0.04 | 4.79 | 0.12 | 0.61 | 0.32 | 0.30 |
| | LS12 | 5.58 | 0.26 | 6.56 | 0.06 | 5.94 | 0.02 | 4.71 | 0.35 | 0.98 | 0.36 | 0.62 |
| | LS17 | 5.42 | 0.30 | 6.01 | 0.18 | 6.10 | 0.23 | | | 0.60 | 0.68 | -0.08 |
| | LS20 | 5.95 | 0.10 | 6.53 | 0.11 | 6.05 | 0.03 | 4.77 | 0.39 | 0.58 | 0.10 | 0.48 |
| | LS22 | 5.51 | 0.10 | 6.41 | 0.05 | 5.92 | 0.01 | 5.03 | 0.21 | 0.90 | 0.41 | 0.49 |
| | LS23 | 5.65 | 0.25 | 6.67 | 0.01 | 6.16 | 0.29 | 5.58 | 0.25 | 1.02 | 0.51 | 0.52 |
| | LS31 | 5.42 | 0.33 | 6.35 | 0.23 | 5.96 | 0.15 | 5.14 | 0.30 | 0.93 | 0.53 | 0.40 |
| | Average | 5.64 | | 6.39 | | 6.02 | | 4.99 | | 0.73 | 0.37 | 0.41 |

Table 5.7 continuied

| Location | Sample | OL | | OPX | | CPX | | SP | | Δopx-ol | Δcpx-ol | Δopx-cpx |
|---|---|---|---|---|---|---|---|---|---|---|---|---|
| | | $\delta^{18}O$ | 2δ | $\delta^{18}O$ | 2δ | $\delta^{18}O$ | 2δ | $\delta^{18}O$ | 2δ | | | |
| Fangshan | FS01 | 5.71 | 0.04 | 6.33 | 0.13 | 5.95 | 0.15 | 4.83 | 0.20 | 0.63 | 0.24 | 0.38 |
| | FS03 | 5.25 | 0.07 | 6.07 | 0.10 | 5.33 | 0.20 | | | 0.82 | 0.08 | 0.74 |
| | FS06 | 6.32 | 0.08 | 6.57 | 0.16 | 6.27 | 0.20 | | | 0.26 | -0.05 | 0.30 |
| | FS07 | 5.54 | 0.10 | 5.80 | 0.01 | 5.91 | 0.11 | 5.39 | 0.07 | 0.26 | 0.37 | -0.11 |
| | FS12 | 5.91 | 0.19 | 5.79 | 0.11 | 5.83 | 0.07 | | | -0.12 | -0.08 | -0.04 |
| | FS13 | 6.04 | 0.10 | 5.86 | 0.03 | 5.46 | 0.05 | 5.10 | 0.01 | -0.18 | -0.59 | 0.41 |
| | FS14 | 5.12 | 0.19 | | | | | 4.37 | 0.20 | | | |
| | FS16 | 5.26 | 0.11 | 6.54 | 0.50 | 5.46 | 0.04 | | | 1.28 | 0.20 | 1.08 |
| | FS17 | 5.79 | 0.11 | 6.48 | 0.41 | 6.31 | 0.25 | | | 0.69 | 0.52 | 0.18 |
| | FS19 | 5.64 | 0.20 | 6.00 | 0.30 | 5.44 | 0.20 | | | 0.36 | -0.20 | 0.56 |
| | FS23 | 5.37 | 0.01 | 5.82 | 0.05 | 5.80 | 0.20 | 4.84 | 0.14 | 0.45 | 0.43 | 0.02 |
| | FS26 | 5.44 | 0.11 | 6.05 | 0.08 | 5.87 | 0.06 | 5.07 | 0.10 | 0.61 | 0.43 | 0.18 |
| | Average | 5.61 | | 6.12 | | 5.78 | | 4.93 | | 0.46 | 0.12 | 0.34 |

Table 6.1 - Temperature, Pressure and Oxygen fugacity estimates of peridotite xenoliths from Subei basin

| Locality | sample | WR Mg# | Fo | Temperature(℃) | | | Pressure(kbar) | | Δlog fO2 |
|---|---|---|---|---|---|---|---|---|---|
| | | | | min | max | ΔTmax-min | min | max | |
| Panshishar | PSS01 | 92.70 | 89.85 | 1004 | 1025 | 21 | 20 | 24 | -3.9 |
| | PSS02 | | 89.84 | 979 | 1040 | 61 | 22 | 28 | -1.5 |
| | PSS05 | | 90.11 | 961 | 1015 | 54 | 22 | | -3.6 |
| | PSS07 | | 89.46 | 823 | 912 | 89 | | | |
| | PSS10 | | 90.36 | 849 | 910 | 61 | | | |
| | PSS11 | 91.51 | 90.38 | 831 | 905 | 74 | | | 0.0 |
| | PSS12 | | 89.74 | 933 | 1019 | 86 | | | -4.1 |
| | PSS13 | | 90.55 | 791 | 927 | 136 | | | |
| | PSS15 | 91.82 | 90.25 | 833 | 856 | 23 | 12 | | 0.3 |
| | PSS16 | | 89.64 | 1006 | 1061 | 55 | | | |
| | PSS17 | 93.03 | 90.51 | 917 | 927 | 10 | 26 | 24 | -1.0 |
| | PSS18 | | 90.31 | 819 | 836 | 17 | 21 | 29 | -2.3 |
| | PSS19 | | 90.03 | 805 | 828 | 23 | | | |
| | PSS20 | | 90.09 | 760 | 826 | 66 | | | |
| Lianshan | LS01 | | 90.10 | 810 | 870 | 60 | 18 | 23 | 0.0 |
| | LS02 | | 89.79 | 846 | 919 | 73 | | | -1.0 |
| | LS03 | 91.13 | 91.43 | 925 | 949 | 24 | 18 | 20 | 0.4 |
| | LS04 | | 89.56 | 982 | 988 | 6 | 16 | 26 | 0.0 |
| | LS05 | 91.10 | 90.38 | 740 | 881 | 141 | | | |
| | LS06 | 91.98 | 89.85 | 948 | 980 | 32 | 16 | 25 | -0.6 |
| | LS07 | 93.75 | 89.97 | 900 | 993 | 93 | | | |
| | LS08 | | 90.13 | 858 | 914 | 56 | 18 | 29 | -0.1 |
| | LS09 | | 90.31 | 726 | 829 | 103 | | | |
| | LS12 | | 91.76 | 889 | 906 | 17 | 14 | 27 | 0.6 |
| | LS15 | | 91.33 | 836 | 891 | 55 | 15 | 17 | -0.6 |
| | LS16 | | 91.83 | 807 | 840 | 33 | 9 | 16 | -0.3 |

Table 6.1 continued

| Locality | sample | WR Mg# | Fo | Temperature(℃) | | | Pressure(kbar) | | Δlog fO2 |
|---|---|---|---|---|---|---|---|---|---|
| | | | | min | max | ΔTmax-min | min | max | |
| Lianshan | LS17 | | 91.75 | 844 | 908 | 64 | 13 | | 0.2 |
| | LS19 | | 90.52 | 795 | 853 | 58 | 8 | 15 | -0.4 |
| | LS20 | 93.27 | 90.27 | 967 | 997 | 30 | 20 | 26 | -1.6 |
| | LS21 | | 91.50 | 832 | 878 | 46 | 11 | 23 | -2.5 |
| | LS22 | 90.57 | 89.23 | 891 | 903 | 12 | 16 | 26 | -0.5 |
| | LS23 | 91.42 | 89.62 | 981 | 988 | 7 | 19 | 27 | -1.1 |
| | LS24 | | 89.90 | 952 | 971 | 19 | 17 | 26 | -0.1 |
| | LS26 | | 90.93 | 819 | 822 | 3 | 12 | 20 | 0.0 |
| | LS30 | | 89.78 | 940 | 970 | 30 | 16 | 23 | -0.7 |
| | LS31 | | 89.32 | 777 | 909 | 132 | | | |
| Fangshan | FS01 | | 90.71 | 1009 | 1013 | 4 | 18 | 23 | -1.0 |
| | FS03 | | 90.57 | 1198 | 1219 | 21 | 21 | 25 | |
| | FS06 | | 90.86 | 1056 | 1059 | 3 | 22 | 26 | 0.0 |
| | FS07 | | 89.84 | 1058 | 1081 | 23 | 16 | 19 | -0.6 |
| | FS11 | 92.57 | 90.69 | 1006 | 1032 | 26 | 10 | 12 | 2.2 |
| | FS12 | | 90.40 | 1186 | 1193 | 7 | 15 | 23 | |
| | FS13 | | 90.00 | 1145 | 1148 | 3 | 15 | 24 | |
| | FS14 | | 89.89 | 1130 | 1135 | 5 | 20 | 26 | |
| | FS16 | | 91.37 | 1073 | 1074 | 1 | 31 | 33 | -0.4 |
| | FS17 | | 90.77 | 1025 | 1026 | 1 | 20 | 25 | -1.5 |
| | FS18 | | 89.76 | 1198 | 1213 | 15 | 21 | 23 | 0.2 |
| | FS19 | | 89.97 | 1160 | | | 15 | 25 | |
| | FS21 | | 89.82 | 1083 | 1088 | 5 | 16 | 20 | |
| | FS23 | | 90.52 | 1154 | 1156 | 2 | 14 | 24 | 0.6 |
| | FS24 | | 91.09 | 800 | 823 | 23 | | | 0.3 |
| | FS26 | | 89.72 | 982 | 1023 | 41 | 11 | 14 | -2.1 |

(a). Temperature were calculated using Brey and Kohler (1990) two pyroxenes geothermometer, with the pairs of cpx and opx, which equilibrium with lnKd vs 1000/T in the range of 10 and 50kbar

(b). Pressure were calculate with average of temperature, using Kohler and Brey (1990) with sample have the different of temperature less than 70 degree

Table 7.1 - Minerals and bulk rock water content of peridotite xenoliths from Subei basin

| Locality | Sample | $H_2O$ content (ppm, wt) | | | | | |
|---|---|---|---|---|---|---|---|
| | | cpx | n. | opx | n. | WR | cpx/opx |
| Panshishan | PSS01 | 95 | 10 | 26 | 13 | 21 | **3.59** |
| | PSS02 | 129 | 17 | 30 | 20 | 34 | **4.24** |
| | PSS05 | 161 | 15 | 34 | 15 | 36 | **4.74** |
| | PSS07 | 147 | 11 | 30 | 15 | 39 | **4.86** |
| | PSS10 | | | 16 | 14 | | |
| | PSS11 | 103 | 13 | 26 | 17 | 26 | **3.95** |
| | PSS12 | 183 | 20 | 56 | 22 | 52 | **3.26** |
| | PSS13 | 112 | 15 | 25 | 17 | 27 | **4.41** |
| | PSS15 | 64 | 14 | 17 | 16 | 15 | **3.67** |
| | PSS16 | 181 | 15 | 61 | 13 | 58 | **2.97** |
| | PSS17 | 177 | 12 | 50 | 17 | 31 | **3.54** |
| | PSS18 | 121 | 13 | 23 | 16 | 31 | **5.23** |
| | PSS19 | 145 | 11 | 23 | 18 | 33 | **6.40** |
| | PSS20 | 150 | 17 | 23 | 16 | 33 | **6.39** |
| Lianshan | LS01 | 55 | 15 | 18 | 16 | 13 | **3.00** |
| | LS02 | 41 | 13 | 13 | 14 | 15 | **3.08** |
| | LS03 | 41 | 13 | 17 | 16 | 10 | **2.39** |
| | LS04 | 56 | 16 | 28 | 15 | 27 | **1.97** |
| | LS05 | 90 | 11 | 34 | 14 | 24 | **2.61** |
| | LS06 | 73 | 12 | 32 | 16 | 19 | **2.29** |
| | LS07 | 96 | 14 | 30 | 17 | 26 | **3.18** |
| | LS08 | 42 | 12 | 15 | 14 | 12 | **2.81** |
| | LS12 | 78 | 13 | 32 | 16 | 18 | **2.43** |
| | LS17 | 37 | 13 | 17 | 16 | 8 | **2.20** |
| | LS19 | 89 | 15 | 45 | 18 | 25 | **1.97** |
| | LS20 | 84 | 11 | 34 | 14 | 18 | **2.46** |

Table 7.1 continued

| Locality | Sample | $H_2O$ content (ppm, wt) | | | | | |
|---|---|---|---|---|---|---|---|
| | | cpx | n. | opx | n. | WR | cpx/opx |
| | LS21 | | | 16 | 18 | | |
| | LS22 | 102 | 17 | 41 | 13 | 28 | **2.49** |
| | LS23 | 73 | 16 | 32 | 15 | 22 | **2.29** |
| | LS24 | 80 | 16 | 34 | 13 | 26 | **2.33** |
| | LS26 | 57 | 13 | 19 | 15 | 12 | **3.01** |
| | LS30 | 92 | 15 | 29 | 13 | 27 | **3.18** |
| | LS31 | 55 | 15 | 16 | 13 | 15 | **3.38** |
| Fangshan | FS01 | 64 | 14 | 25 | 16 | 22 | **2.52** |
| | FS03 | 167 | 16 | 68 | 12 | 50 | **2.46** |
| | FS06 | 170 | 19 | 61 | 20 | 43 | **2.79** |
| | FS07 | | | 60 | | | |
| | FS11 | 109 | 17 | 43 | 15 | 26 | **2.56** |
| | FS12 | 158 | 13 | 54 | 16 | 37 | **2.92** |
| | FS13 | 108 | 11 | 41 | 13 | 27 | **2.66** |
| | FS14 | 120 | 12 | 53 | 14 | 32 | **2.26** |
| | FS16 | 90 | 15 | 33 | 14 | 18 | **2.71** |
| | FS17 | 53 | 17 | 28 | 19 | 19 | **1.91** |
| | FS18 | | | 63 | | | |
| | FS19 | | | 74 | | | |
| | FS21 | 177 | 14 | 69 | 13 | 44 | **2.56** |
| | FS23 | 101 | 16 | 39 | 20 | 25 | **2.57** |
| | FS24 | 41 | 15 | 21 | 17 | 16 | **1.91** |
| | FS26 | 67 | 14 | 28 | 14 | 16 | **2.44** |

n. numbers of FTIR spectra which were used to made baseline and calculate the average water content of minerals. The whole rock (WR) $H_2O$ contents were calculated by assuming 2 ppm $H_2O$ for olivine of all samples.

Table 8.1 - Xenolith phase modal proportions (vol %) used in the models

| Phase | Start mode | Melt mode |
|---|---|---|
| olivine | 0.55 | 0.1 |
| opx | 0.25 | 0.2 |
| cpx | 0.18 | 0.68 |
| sp | 0.02 | 0.02 |
| | | |
| olivine | 0.55 | 0.13 |
| opx | 0.2 | 0.12 |
| cpx | 0.15 | 0.25 |
| grt | 0.1 | 0.5 |

Table 8.2 - Crystal/Liquid partition coefficients for modeling calculations

| Element | Partition coefficients | | | | |
|---|---|---|---|---|---|
| | olivine/melt | opx/melt | cpx/melt | sp/melt | grt/melt |
| La | 0.0008 | 0.0006 | 0.0536 | 0.0012 | 0.0003 |
| Ce | 0.0001 | 0.001 | 0.086 | 0.00002 | 0.005 |
| Pr | 0.0008 | 0.0032 | 0.14 | 0.01 | 0.02 |
| Nd | 0.002 | 0.01 | 0.1873 | 0.0008 | 0.052 |
| Sm | 0.0002 | 0.0082 | 0.291 | 0.00006 | 0.25 |
| Eu | 0.003 | 0.03 | 0.32 | 0.0009 | 0.4 |
| Gd | 0.008 | 0.034 | 0.4 | 0.01 | 0.61 |
| Tb | 0.01 | 0.045 | 0.42 | 0.01 | 1.03 |
| Dy | 0.012 | 0.045 | 0.442 | 0.0015 | 1.65 |
| Ho | 0.013 | 0.048 | 0.44 | 0.01 | 2.66 |
| Er | 0.025 | 0.06 | 0.467 | 0.003 | 3.6 |
| Tm | 0.009 | 0.071 | 0.449 | 0.01 | 5.26 |
| Yb | 0.008 | 0.086 | 0.43 | 0.00034 | 6.6 |
| Lu | 0.018 | 0.09 | 0.44 | 0.0007 | 8.5 |

Source of data: Fujimaki et al., 1984; McKenzie and O'Nions., 1991; Nielsen et al., 1992; Hart and Dunn, 1993; Dunn and Sen, 1994; Zack et al., 1997; Johnson, 1998; Green et al., 2000 ; Takazawa et al., 2000; Adam et al., 1994,2006; Elkins et al., 2008

Table 8.3 - Primitive mantle source and starting bulk composition (ppm) in spinel and garnet facies

| Element | Primitive mantl | Sp | | | Grt | | |
|---|---|---|---|---|---|---|---|
| | | $C^0$ | $D^0$ | P | $C^0$ | $D^0$ | P |
| La | 0.648 | 3.385 | 0.010 | 0.037 | 4.025 | 0.009 | 0.014 |
| Ce | 1.675 | 9.126 | 0.016 | 0.059 | 10.549 | 0.014 | 0.024 |
| Pr | 0.254 | 1.335 | 0.027 | 0.096 | 1.477 | 0.024 | 0.045 |
| Nd | 1.25 | 6.272 | 0.037 | 0.130 | 6.433 | 0.036 | 0.074 |
| Sm | 0.406 | 2.166 | 0.055 | 0.200 | 1.678 | 0.070 | 0.199 |
| Eu | 0.154 | 0.738 | 0.067 | 0.224 | 0.515 | 0.096 | 0.284 |
| Gd | 0.544 | 2.557 | 0.085 | 0.280 | 1.646 | 0.132 | 0.410 |
| Tb | 0.099 | 0.439 | 0.095 | 0.298 | 0.230 | 0.181 | 0.627 |
| Dy | 0.674 | 3.057 | 0.097 | 0.311 | 1.207 | 0.247 | 0.942 |
| Ho | 0.149 | 0.665 | 0.099 | 0.310 | 0.188 | 0.349 | 1.447 |
| Er | 0.438 | 1.812 | 0.113 | 0.332 | 0.449 | 0.456 | 1.927 |
| Tm | 0.068 | 0.294 | 0.104 | 0.321 | 0.050 | 0.613 | 2.752 |
| Yb | 0.441 | 1.836 | 0.103 | 0.310 | 0.254 | 0.746 | 3.419 |
| Lu | 0.0675 | 0.266 | 0.112 | 0.319 | 0.031 | 0.944 | 4.373 |

Table A1 EMPA for olivine core and rim

Table A2 EMPA for opx core and rim

Table A3 EMPA for cpx core and rim

Table A4 EMPA for sp core and rim

Table A5 trace element for average

FTIR spectra， they are include in CD.

Available upon request

## Related publications and manuscripts:

Costanza Bonadiman, **Yantao Hao**, Massimo Coltorti, Luigi Dallai, Barbara Faccini, Yu Huang and Qunke Xia. 2009. Water contents of pyroxenes in intraplate lithospheric mantle. Eur. J. Mineral(21) 637-647.

Qunke Xia, **Yantao Hao**, Pei Li, Etienne Deloule, Massimo Coltorti, Luigi Dallai, Xiaozhi Yang and Min Feng. 2010. Low water content of the Cenozoic lithospheric mantle beneath the eastern part of the North China Craton. Submitted to JGR-Solid Earth

Qunke Xia, Xiaozhi Yang, **Yantao Hao**, Yingming Sheng and Pei Li. 2007. Water: distribution and circulation in the deep Earth, Earth Science Frontiers, 14(2): 10-23. (in Chinese with English abstract)

**Yantao Hao**, Massimo Coltorti, Costanza Bonadiman, Luigi Dallai, Barbara Faccini and Qunke Xia. 2008. Petrology of mantle xenoliths and water determination in NAMs from Subei basin (central-eastern China). 33 IGC, Oslo, 6-14 Agosto, 2008.

Costanza Bonadiman, **Yantao Hao**, Massimo Coltorti, Luigi Dallai, Barbara Faccini, Yu Huang and Qunke Xia. 2009. Tectonic settings and water distribution in mantle pyroxenes. AGU, S.Francisco, U.S.A., 13-17 Dec. 2009. Abstract.

Costanza Bonadiman, **Yantao Hao**, Massimo Coltorti, Luigi Dallai, Barbara Faccini, Yu Huang and Qunke Xia. 2009. Water contents in pyroxenes of intraplate lithospheric mantle. Goldschmidt 2009 - June 21-26. Davos, Switzerland